Neutrino–nuclear responses for astro-neutrinos, single beta decays and double beta decays

H. Ejiri [a],[*], J. Suhonen [b], K. Zuber [c]

[a] Research Center for Nuclear Physics, Osaka University, Ibaraki, Osaka, Japan
[b] University of Jyvaskyla, Department of Physics, P.O. Box 35, FI 40014, Finland
[c] Institut für Kern- und Teilchenphysik, Technische Universität Dresden, Zellescher Weg 19, D-01069 Dresden, Germany

ARTICLE INFO

ABSTRACT

Neutrino–nuclear responses associated with astro-neutrinos, single beta decays and double beta decays are crucial in studies of neutrino properties of interest for astro-particle physics. The present report reviews briefly recent studies of the neutrino–nuclear responses from both experimental and theoretical points of view in order to obtain a consistent understanding of the many facets of the neutrino–nuclear responses. Subjects discussed in this review include (i) experimental studies of neutrino–nuclear responses by means of single beta decays, charge-exchange nuclear reactions, muon- photon- and neutrino–nuclear reactions, and nucleon-transfer reactions, (ii) implications of and discussions on neutrino–nuclear responses for single beta decays, for astro-neutrinos, and for astro-neutrino nucleosynthesis, (iii) theoretical aspects of neutrino–nuclear responses for beta and double beta decays, for nuclear muon capture and for neutrino–nucleus scattering, and (iv) critical discussions on nucleonic and non-nucleonic spin–isospin correlations and renormalization (quenching or enhancement) effects on the axial weak coupling. Remarks are given on perspectives of experimental and theoretical studies of the neutrino–nuclear responses and on future experiments of double beta decays.

© 2018 Elsevier B.V. All rights reserved.

Contents

* Corresponding author.
    E-mail addresses: ejiri@rcnp.osaka-u.ac.jp (H. Ejiri), jouni.suhonen@phys.jyu.fi (J. Suhonen), zuber@physik.tu-dresden.de (K. Zuber).

1. Introduction

1.1. Neutrino–nuclear responses and neutrino studies in nuclei

The neutrino is a key particle for astro-nuclear physics, particle physics and cosmology. It is the elementary particle that has only a weak charge and has no electric charge and no color charge. Thus, neutrino interactions with nuclei are extremely weak and experimental studies related to the neutrino are hard.

The neutrino has been extensively studied experimentally and theoretically in the recent 4–5 decades, but some fundamental properties of the neutrino and the astro-neutrino–nuclear interaction are still not well understood. Several basic questions about the neutrino remain yet unsolved. Some of them are as follows:

1. The nature of the neutrino, whether it is a Majorana particle (neutrino = antineutrino) or a Dirac particle (neutrino $\neq$ antineutrino).

2. The absolute mass scale and the mass hierarchy (spectrum), whether it is the normal or the inverted mass hierarchy.

3. The lepton-sector CP phases, the Majorana phases, and the leptogenesis for the baryon asymmetry.

4. The solar-neutrino sources and the fluxes, in particular the CNO-neutrino flux and production.

5. The supernova-neutrino intensities, spectra, flavors and oscillations. Supernova-neutrino–nuclear interactions and nucleosynthesis.

These questions can be studied well by investigating neutrino-related weak processes in nuclei, such as single beta decays (SBDs) and electron captures (ECs), inverse beta decays (IBDs) and neutrinoless double beta decays (DBDs). The neutrino–nuclear responses are crucial for these SBD/EC, IBD and DBD neutrino studies in nuclei.

Historical reviews and extensive previous works on the neutrino–nuclear responses are given in [1–5] and references therein, those on astro-neutrinos in, e.g. [6–14] and references therein, and reviews on DBDs are given in, e.g. [15–24] and references therein. The solar neutrinos, supernova neutrinos and DBDs are also discussed in [25,26], and nuclear weak interactions and β/γ decays are treated in monographs [27–29]. The various aspects of the renormalization of the weak axial–vector coupling in beta and double beta decays have been treated in the review [30]. Actually, we reviewed in Physics Reports effective couplings for $\beta-\gamma$ transitions in 1978 [1], nuclear-structure aspects in DBDs [2] and neutrino physics [15] in 1998 and low-energy neutrino–nuclear responses [4] in 2000.

Nuclei are used as femto (10^{-15} m) laboratories to study neutrinos, as described in the DBD review articles [4,16,18]. In the nuclear femto laboratory, the nucleons are in the good quantum states of energy, spin, parity and isospin. Thus, the energy and the multipolarity of the weak transitions involved in SBDs/ECs, IBDs and DBDs are well defined. In practice, the nuclear femto laboratories with a large enhancement for neutrino signals and severe reduction for background (BG) signals are selected for neutrino studies since the neutrino signals are extremely rare. The neutrino charged current (CC) processes of SBD/EC, IBD and neutrinoless DBD in a nuclear femto laboratory are schematically illustrated in Fig. 1.

Astro-neutrinos are studied by measuring astro-neutrino charged current (CC) interactions in nuclei. The neutrino-induced IBD is given by $A + \nu_e \rightarrow B + \beta^-$, with ν_e and β^- being the astro-neutrino and the β^- ray. The interaction rate $R(\nu)$ is expressed as

$$R(\nu) = g_W^2 G^\nu B(\nu) I(\nu) \quad \text{with} \quad B(\nu) = (2J_i + 1)^{-1} |M^\nu|^2 , \tag{1}$$

where g_W is the weak coupling constant, G^ν is the phase-space (kinematic) factor, $I(\nu)$ is the astro-neutrino flux, $B(\nu)$ is the nuclear response, M^ν is the nuclear matrix element (NME) and $2J_i + 1$ is the spin factor with J_i being the spin of the initial state. The β^- (electron) energy E_e is given by using the incident astro-neutrino energy E_ν as $E_e = E_\nu - Q_{EC}$, with Q_{EC} being the EC Q value as shown in Fig. 1. The neutrino flux is derived from the measured IBD rate and the nuclear response by using Eq. (1).

The nucleus (femto laboratory) to be used for the astro-neutrino study is the one with a large response $B(\nu)$, a large phase-space factor G^ν and a low Q value, Q_{EC}, to get a sufficient interaction rate and a large signal energy, well above the background. If the residual nucleus B is radioactive, the neutrino CC interaction (IBD) is followed by a successive SBD of B→C, as shown in Fig. 1. Then one may study the IBD β ray in delayed coincidence with the SBD β ray in order to select the rare
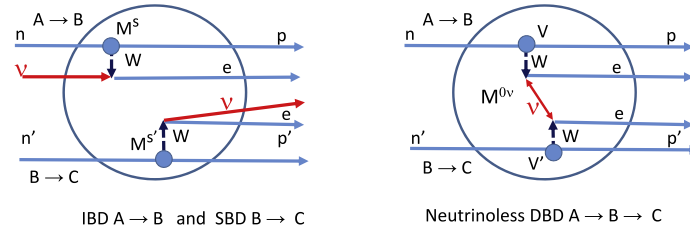
Fig. 1. Schematic CC-interaction processes in nuclear femto laboratories for IBD induced by astro-neutrinos followed by SBD (left figure) and neutrinoless DBD (right figure). The meaning of the symbols is: p=proton, n=neutron, e=electron, W=weak boson and ν = electron–neutrino. M^s and $M^{s'}$ are the IBD and SBD nuclear matrix elements (NMEs), respectively, and $M^{0\nu}$ is the neutrinoless DBD NME.

IBD signal. So, the nuclear femto laboratory is effective in the selection of the astro-neutrino signal and in the rejection of other background signals.

The neutrinoless DBD process is given by A $\rightarrow$ C + $2\beta^-$. The DBD transition rate for the light-neutrino mass mechanism is expressed as

$$R(0\nu) = g_A^4 \ln(2) G^{0\nu} B(0\nu)(m^{\text{eff}})^2 \quad \text{with} \quad B(0\nu) = (2J_i + 1)^{-1}|M^{0\nu}|^2, \tag{2}$$

where $G^{0\nu}$ is the phase-space (kinematic) factor, m^{eff} is the effective ν mass and $g_A = 1.27$ is the axial–vector weak coupling in units of the vector coupling g_V for a free nucleon. The rate is given by $\ln(2)/T_{1/2}$ with $T_{1/2}$ being the half-life, and the effective mass is expressed as $m^{\text{eff}} = |\sum U_{ei}^2 m_i|$ with m_i and U_{ei} being the ith neutrino mass eigenstate and the mixing amplitude [4,16,18], respectively. The nuclear response $B(0\nu)$ is given by the square of the DBD NME $M^{0\nu}$ in case of the $0^+ \rightarrow 0^+$ transition with $2J_i + 1 = 1$ and the sum energy E of the DBD electrons is given by the DBD Q value $Q_{\beta\beta}$.

The DBD transition rate is extremely small because it is mediated by a second-order weak process and a small neutrino mass, and the signal energy is only a couple of MeV. Then DBD nuclei (femto laboratories) to be used for the ν mass search are, like in the case of the astro-neutrino study, nuclei with a large response $B(0\nu)$, i.e. a large NME $M^{0\nu}$, a large phase-space factor $G^{0\nu}$ and a large signal energy $Q_{\beta\beta}$ to get an adequate DBD rate and a summed electron energy above the backgrounds.

In case of the light-Majorana-mass mode, the Majorana neutrino is exchanged between two nucleons in a DBD nucleus. The nucleons are located so close, within a few Fermi (10^{-15} m), that the exchange is enhanced by a factor 10^{4-5}. On the other hand, the single β decay is energetically forbidden to avoid the huge SBD background. So, the DBD femto laboratory acts as a microscope with a filter to enhance the DBD signal and to reject backgrounds.

Actual signal (event) rates for astro-neutrino interactions and DBDs are very small. In the case of astro-neutrino experiments with a large response of $|M^\nu|^2 = 0.6^2$ and a large phase space of $g_W^2 G^\nu = 10^{-44}$, the signal rate is around $R(\nu) = 40$/ton-year for the pp solar neutrinos including oscillations. In the case of the DBD experiment with a typical response of $|M^{0\nu}|^2 = 2^2$, including the renormalization (quenching) effect, and a large phase-space factor of $g_A^4 G^{0\nu} = 3 \times 10^{-14}$/y, the signal rate is around $R(0\nu) = 3$/ton-year for the effective ν mass of 25 meV. Therefore, multi-ton-scale detectors (femto laboratories) are required for both astro-neutrino and DBD experiments to get adequate signal rates. Here the neutrino–nuclear responses are key elements for high-sensitivity astro-neutrino and DBD experiments.

1.2. Neutral-current and charged-current neutrino–nucleus interactions

Nuclear responses for solar, supernova, and generally astro-neutrinos are mediated by scattering processes based on weak interactions. At the nuclear level, neutrino–nuclear responses can be considered as mutual interactions of the hadronic and leptonic currents mediated by the massive vector bosons Z^0 (neutral-current, NC, processes) and $W^\pm$ (charged-current, CC, processes) [31]. The leptonic and hadronic currents can be expressed as mixtures of vector and axial–vector contributions [32–34]. For a NC neutrino–nuclear process one has the leptonic current

$$J_{L,\mu} = \bar{\nu}_l(x)\gamma^\mu(1 - \gamma_5)\nu_l(x), \quad \text{(NC)} \tag{3}$$

and for the CC process one has

$$J_{L,\mu} = \bar{l}(x)\gamma^\mu(1 - \gamma_5)\nu_l(x) + \bar{\nu}_l(x)\gamma^\mu(1 - \gamma_5)l(x), \quad \text{(CC)} \tag{4}$$

where $l = e, \mu, \tau$ is either the electron, muon or tau lepton and ν_l are the corresponding neutrinos and γ^μ are the usual Dirac matrices with $\gamma_5 = i\gamma^0\gamma^1\gamma^2\gamma^3$. The weak vector and axial–vector coupling strengths g_V and g_A enter the theory when the hadronic current is renormalized at the nucleon level [35]. The conserved vector-current hypothesis (CVC) [32] and partially conserved axial–vector-current hypothesis (PCAC) [36,37] yield the free-nucleon values $g_V = 1.00$ and $g_A = 1.27$ [31] but for finite nuclei the value of g_A is usually modified in order to account for nuclear-model dependent modifications of transition operators when approximate many-body calculations are performed. Then a quenched or enhanced value might be needed to reproduce experimental observations [38–40].

Since the vector bosons Z^0 and $W^\pm$ have large mass and thus propagate only a short distance, the hadronic current and the leptonic currents (3) and (4) can be considered to interact at a point-like weak-interaction vertex with an effective coupling

strength G, which for the NC and CC processes has the value

$$G = G_F = 1.1664 \times 10^{-5}\,\text{GeV} \quad (\text{NC})\,; \quad G = \cos\theta_C G_F \approx 1.03 \times 10^{-5}\,\text{GeV}\,, \quad (\text{CC}) \tag{5}$$

where G_F is the Fermi constant and θ_C denotes the Cabibbo angle.

The parity non-conserving nature of the weak interaction forces the hadronic NC and CC current J_H^μ to be written at the quark level as a mixture of vector and axial–vector parts:

$$J_H^\mu = \bar{q}_f(x)\gamma^\mu(1 - \gamma_5)q_i(x)\,, \tag{6}$$

where q_i (q_f) is the initial-state (final-state) quark and the quark flavor changes in the CC processes and remains the same in the NC processes.

Renormalization effects of strong interactions and energy scale of the processes must be taken into account when moving from the quark level to the hadron level. Then the hadronic current between nucleons N_i and N_f takes the rather complex form

$$J_H^\mu = \bar{N}_f(x)[V^\mu - A^\mu]N_i(x)\,, \tag{7}$$

where the nucleon type changes (does not change) for the CC (NC) processes. The vector-current part can be written as

$$V^\mu = g_V(q^2)\gamma^\mu + ig_M(q^2)\frac{\sigma^{\mu\nu}}{2m_N}q_\nu \tag{8}$$

and the axial–vector-current part as

$$A^\mu = g_A(q^2)\gamma^\mu\gamma_5 + g_P(q^2)q^\mu\gamma_5\,. \tag{9}$$

Here q^μ is the 4-momentum transfer, q^2 its magnitude, m_N the nucleon mass (roughly 1 GeV) and the weak couplings depend on the magnitude of the exchanged momentum. For the vector and axial–vector couplings one usually adopts the dipole approximation

$$g_V(q^2) = \frac{g_V}{\left(1 + q^2/M_V^2\right)^2}\,; \; g_A(q^2) = \frac{g_A}{\left(1 + q^2/M_A^2\right)^2}\,, \tag{10}$$

where g_V and g_A are the weak vector and axial–vector coupling strengths at zero momentum transfer ($q^2 = 0$), respectively. For the vector and axial masses one usually takes $M_V = 840$ MeV [41] and $M_A \sim 1$ GeV [41–43] coming from the accelerator-neutrino phenomenology. For the weak magnetism term one can take $g_M(q^2) = (\mu_p - \mu_n)g_V(q^2)$ and for the induced pseudoscalar term it is customary to adopt the Goldberger–Treiman relation [44] $g_P(q^2) = 2m_N g_A(q^2)/(q^2 + m_\pi^2)$, where m_π is the pion mass and $\mu_p - \mu_n = 3.70$ is the anomalous magnetic moment of the nucleon in units of the nuclear magneton μ_N. It should be noted that the β decays are low-energy processes (few MeV) involving only the vector [first term in Eq. (8)] and axial–vector [first term in Eq. (9)] parts at the limit $q^2 = 0$ so that the q dependence of Eq. (10) does not play any role in the treatment of these processes in this chapter. Contrary to this, the $0\nu\beta\beta$ decays (see Section 5) and nuclear muon-capture transitions (see Section 2.4) involve momentum transfers of the order of 100 MeV and the full expression (7) is active with slow decreasing trend of the coupling strengths according to Eq. (10).

At this point it may be noted that the hadron currents (8)–(10), valid up to momentum transfers of about 400 MeV, can be derived in the context of chiral effective field theory. In addition, meson-exchange currents (two-body currents) are also predicted. For axial currents the first derivations were given by e.g. [45] and later in [46], extending to other currents. More complete derivations are performed in [47] and [48].

1.3. Nuclear responses for astro-neutrinos and neutrino nucleosynthesis

Astro-neutrinos, such as solar neutrinos and supernova neutrinos, are interesting in view of both neutrino physics and astrophysics. The observations of solar neutrinos provide evidences for the neutrino matter oscillations as well as nuclear fusion reactions in the sun, and those of the supernova neutrinos probe the explosion process, as described extensively in the review articles [6–10]. So, these observations have opened the new field of neutrino astronomy. Neutrino nucleosyntheses are found to be crucial for some isotopes, which are not produced otherwise, as described in the review articles [11–14].

High-precision studies of astro-neutrinos are important for investigating the matter oscillations in the sun and supernova explosions, the neutrino-production mechanisms for individual neutrino sources, the temperatures at the neutrino-production (clear-out) sites, and also for evaluating the possible neutrino-nucleosynthesis rates. Experimental studies of the astro-neutrinos are made by measuring neutrino interactions with atomic electrons and nuclei in astro-neutrino detectors.

The CC interactions with nuclei are used to study low- and medium-energy astro-neutrinos, depending on the CC threshold energy. Actually, the first observation of the solar neutrinos was made by measuring the CC interaction with ^{37}Cl [49]. We discuss in this review mainly neutrino–nuclear responses for the CC interactions with nuclei.

Neutrino and antineutrino CC interactions on a nucleus $_Z^A X$ leading to a residual nucleus $_{Z+1}^A X$ are expressed as

$$_Z^A X + \nu_e \rightarrow\, _{Z+1}^A X + e^- \quad (\text{NME } M^\nu) \tag{11}$$
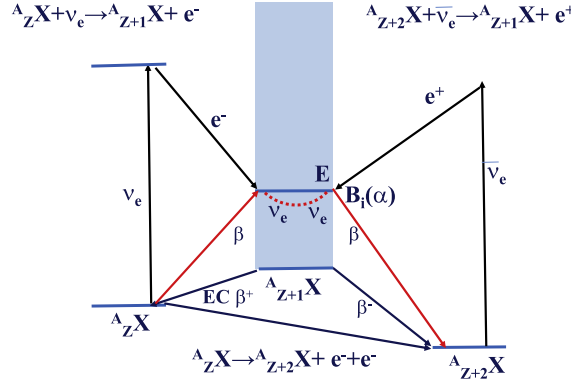
Fig. 2. Schematic diagrams for the neutrino and antineutrino CC interactions and the DBD process. Here $B_i(\alpha)$ is the neutrino response for the state i in the nucleus $_{Z+1}^{A}X$.

$$_{Z+2}^{A}X + \bar{\nu}_e \rightarrow {}_{Z+1}^{A}X + e^+ \quad (\text{NME } M^{\bar{\nu}}), \tag{12}$$

where M^ν and $M^{\bar{\nu}}$ are the corresponding NMEs. For the decay Q values, Q_ν and $Q_{\bar{\nu}}$, the corresponding threshold energies are given by $-Q_\nu$ and $-Q_{\bar{\nu}}$. The ν and $\bar{\nu}$ CC processes are inverse β^- and β^+ decays. The associated CC transitions are schematically illustrated in Fig. 2.

The pp, CNO and ^{7}Be solar neutrinos are low-energy neutrinos. The CC response is mainly the GT (Gamow–Teller $J^\pi = 1^+$) response $B(\text{GT})$. So, one needs a CC-interacting nucleus with a rather low threshold energy of sub-MeV and a large GT response. The ^{8}B solar-neutrino energy extends to 15 MeV and the supernova neutrinos to a couple of 10 MeV, depending on the temperature at the neutrino clear-out. Accordingly, the neutrino responses are $B(J^\pi)$ with $J^\pi = 0^+, 1^\pm, 2^\pm, 3^\pm$, depending on the ν and $\bar{\nu}$ energies.

The response for the ground-state transition may be obtained from the SBD/EC rate, while neutrino responses for excited states have to be measured by using various kinds of charge-exchange reactions (CERs). Since nuclear states (levels) in medium-heavy nuclei are located close to each other in energy, high energy-resolution experiments with $\Delta E/E =$ a few 10 keV are useful to study neutrino responses for individual states. The supernova-neutrino responses for excited states are also studied by measuring γ decays if the states are bound, or neutron emissions if the states are neutron-unbound. The NC interactions are also used to study astro-neutrinos by measuring γ rays and particles following inelastic nuclear scatterings.

1.4. Neutrino–nuclear responses for double beta decays

Interest on double beta decay has revived with the discovery of the neutrino oscillations [50] at the end of the 20th century, about 2 decades ago. The neutrino oscillations provide evidence for the mass difference between the neutrino mass eigenstates. The non-zero mass enables neutrinoless DBD if the neutrino is a Majorana particle in nature, i.e. a particle which is identical with its antiparticle. DBDs are well described in recent review papers [2,3,15–18,23,24] and references therein.

Two-neutrino DBDs ($2\nu\beta\beta$) are followed by two neutrinos to conserve the lepton number L in the standard electro-weak model (SM). On the other hand, neutrinoless DBDs ($0\nu\beta\beta$) with the lepton-number violation of $\Delta L = \pm 2$ are beyond SM, and open new astro- and particle-physics fields.

The $0\nu\beta\beta$ process is expressed as

$$_{Z}^{A}X \rightarrow {}_{Z\pm2}^{A}X + 2e^{\mp} \quad (\text{NME } M^{0\nu}), \tag{13}$$

where $M^{0\nu}$ is the neutrinoless DBD NME. The $0\nu\beta\beta$ process has several unique features from particle-physics and cosmology points of view.

(i) The neutrinoless DBD, if detected, provides evidence for the Majorana nature of the neutrino and the non-zero mass. It is a very sensitive probe to search for the Majorana mass, the lepton-sector CP phases , R-parity violating SUSY processes, heavy neutrinos, right-handed weak interactions, the leptogenesis and other processes, which are all beyond the SM.

(ii) In the light-neutrino exchange mechanism the effective neutrino mass m^{eff}, to be studied via $0\nu\beta\beta$ decays, depends on the neutrino-mass hierarchy: the normal-hierarchy (NH), the inverted-hierarchy (IH) or the quasi-degenerate (QD) mass pattern. The corresponding effective masses are around $1 - 5$ meV, $15 - 45$ meV, and $50 - 200$ meV respectively, depending on the neutrino-mixing phases. The QD mass may be constrained to be of the order of 100 meV or less by the cosmological mass density, depending strongly on the model for the mass density. The IH mass may be studied by current high-sensitivity $0\nu\beta\beta$ experiments with ton-scale DBD sources, depending largely on the values of the DBD NMEs.

(iii) The $0\nu\beta\beta$ effective mass depends on the mass hierarchy, the mixing phases and the minimum neutrino mass m_0. In other words, they are constrained to some extent by the $0\nu\beta\beta$-decay rate if the DBD NMEs are evaluated accurately enough.

(iv) The DBD process includes several mechanisms through which it can proceed. The mediators of the decay can be, e.g., the light Majorana mass, the heavy neutrino, SUSY mechanisms and right-handed weak currents. In the recent approach of the chiral effective field theory (χEFT) [51,52] new mechanisms, induced by lepton-number-violating operators up to dimension nine, are discussed. Related to this, the model-independent leading-order matrix elements of $\pi\pi ee$ operators have been evaluated in [53] using lattice-QCD methods. This was done in order to determine the related low-energy constants to be used, e.g. in the χEFT calculations on the nucleon and nucleus level in order to advance towards the NMEs of $0\nu\beta\beta$ decays. The different mechanisms are identified experimentally by investigating energy and angular correlations of the two β rays and the nucleus dependence of the DBD rates if the DBD NMEs are evaluated precisely enough.

(v) In case of the light ν-mass mechanism, the mass sensitivity (minimum m^{eff} that can be measured) is proportional to $(M^{0\nu})^{-1}$, while the DBD-detector mass (mass of the DBD source isotope) required for a given m^{eff} is proportional to $(M^{0\nu})^{-4}$ in realistic experiments [16,18]. Thus, one needs to know precisely the DBD NMEs in order to design the DBD detector for a given mass sensitivity and to extract the effective mass from the rate of the neutrinoless DBD, once the process is observed.

(vi) The DBD NMEs are very sensitive to nuclear physics involved in DBDs such as the nucleonic and non-nucleonic spin–isospin correlations, nuclear structure, nuclear models, nuclear medium effects, the renormalization (quenching) of the effective weak coupling in nuclei, and so on. Accurate theoretical calculations of DBD NMEs, including the effective weak coupling, however, are hard, and there are no experimental methods to directly measure them. Thus various experimental inputs relevant to the DBD responses are useful to help evaluate the DBD NMEs and to verify the correctness of the calculations.

The $0\nu\beta\beta$ NME for the Majorana-neutrino mediated mode is conventionally expressed as

$$M^{0\nu} = \left(\frac{g_A^{\text{eff}}}{g_A}\right)^2 \left[M_{\text{GT}}^{0\nu} + \left(g_V/g_A^{\text{eff}}\right)^2 M_F^{0\nu} + M_T^{0\nu}\right], \tag{14}$$

where $M_{\text{GT}}^{0\nu}$, $M_F^{0\nu}$ and $M_T^{0\nu}$ are the GT, Fermi and tensor NMEs and g_V/g_A^{eff} is the ratio of the vector to axial–vector weak couplings. The effective axial–vector coupling g_A^{eff} in units of the coupling g_A for a free nucleon stands for the renormalization (quenching) due to all kinds of nucleonic (many-body effects), non-nucleonic correlations and nuclear-medium effects that are not explicitly included in the model NMEs $M_{\text{GT}}^{0\nu}$ and $M_T^{0\nu}$.

In case of the light-ν-mass-mediated process, the NMEs are written as

$$M_{\text{GT}}^{0\nu} = \sum_k \langle t_\pm \boldsymbol{\sigma} h_{\text{GT}}(r_{12}, E_k) t_\pm \boldsymbol{\sigma}\rangle, \tag{15}$$

$$M_F^{0\nu} = \sum_k \langle t_\pm h_F(r_{12}, E_k) t_\pm\rangle, \tag{16}$$

$$M_T^{0\nu} = \sum_k \langle t_\pm h_T(r_{12}, E_k) S_{12} t_\pm\rangle, \tag{17}$$

where $h_K(r_{12}, E_k)$, K = GT,F,T, are the neutrino potentials with E_k being the intermediate-state energy and r_{12} being the distance between the two nucleons involved in the $0\nu\beta\beta$ decay, and S_{12} is the spin-tensor operator. The operator $\boldsymbol{\sigma}$ is the Pauli spin operator and $t_\pm$ is the isospin raising/lowering operator. The neutrino potential is approximately expressed in a Coulomb form of $1/r_{12}$. The magnitude of momentum $\mathbf{p}$ involved in the $0\nu\beta\beta$ transition is of the order of $1/r_{12} = 10 - 200$ MeV/c, and the involved angular momentum is in the range $l\hbar = 0 - 6\hbar$. Reliable evaluations of the NMEs $M_{\text{GT}}^{0\nu}$, $M_F^{0\nu}$ and $M_T^{0\nu}$, and g_A^{eff} are crucial for the DBD response of $B(0\nu) = |M^{0\nu}|^2$. The major NME in the neutrinoless NME $M^{0\nu}$ (Eq. (14)) is the first term of the axial–vector one $(g_A^{\text{eff}}/g_A)^2 M_{\text{GT}}^{0\nu}$, which is renormalized (quenched) much by the factor $(g_A^{\text{eff}}/g_A)^2$ due to the strong spin dependent correlations and nuclear medium effects. Then the second term $(g_V/g_A)^2 M_F^{0\nu}$ gets relatively important, and the reduction (quenching) factor for the $M^{0\nu}$ is somewhat modified, depending on the ratio $M_F^{0\nu}/M_{\text{GT}}^{0\nu}$.

DBDs to be studied in practice are the ground-state-to-ground-state $0^+ \rightarrow 0^+$ transitions in even–even nuclei. The transition process is schematically shown in Fig. 2. Here the paired neutrons (n_1, n_2) become paired protons (p_1, p_2) and a light Majorana neutrino is exchanged (neutrino emission and absorption) between the two neutrons in case of the Majorana ν-mass process. The light ν-mass DBD process is schematically expressed as a virtual-neutrino emission from $n_1: {}_{Z}^{A}X \rightarrow {}_{Z+1}^{A}X + \bar{\nu_e} + e^-$, and the re-absorption into $n_2: {}_{Z+1}^{A}X + \nu_e \rightarrow {}_{Z+2}^{A}X + e^-$, as shown in Fig. 2. This is possible in the case of a Majorana neutrino with non-zero mass, thus having both the right-handed and left-handed helicities. In this sense, the NME $M^{0\nu}$ is associated with ν and $\bar{\nu}$ (single $\beta^\pm$) NMEs for the neutrino emission and absorption processes. Accordingly, the SBD NMEs of $M(\nu)$ and $M(\bar{\nu})$ are used to help evaluate/verify the DBD NME $M^{0\nu}$. In other words, nuclear models with the

nuclear interactions and the effective weak coupling used for the $M^{0\nu}$ calculation should be able to reproduce the relevant ν and $\bar{\nu}$ (single $\beta^{\pm}$) NMEs.

It is to be noted that the $M^{0\nu}$ with the virtual-neutrino exchange is given by the sum of DBD NMEs $M_i^{0\nu}$ for all relevant intermediate states $|i\rangle$, and $M^{0\nu}$ is associated with the ν and $\bar{\nu}$ MNEs in the multipole and momentum ranges of $l\hbar$ with $l = 0 - 6$, and $p = 10 - 200$ MeV/c.

The $2\nu\beta\beta$ process is expressed as

$$^{A}_{Z}\mathrm{X} \rightarrow \,^{A}_{Z+2}\mathrm{X} + 2e^{-} + 2\bar{\nu}_e \,, \quad ^{A}_{Z+2}\mathrm{X} \rightarrow \,^{A}_{Z}\mathrm{X} + 2e^{+} + 2\nu_e \,, \quad (\text{NME } M^{2\nu}) \tag{18}$$

where $M^{2\nu}$ is the corresponding NME. It is expressed as

$$M^{2\nu} = \left(\frac{g_{\mathrm{A}}^{\mathrm{eff}}}{g_{\mathrm{A}}}\right)^2 \sum_i \left[\frac{M_i(\beta^-)M_i(\beta^+)}{\Delta_i}\right], \tag{19}$$

where $M_i(\beta^-)$ and $M_i(\beta^+)$ are GT NMEs for the ith intermediate state and $\Delta_i = E_i + Q(\beta\beta)/2$ is the energy denominator. In this case, the NMEs for the relevant single β decays may be used to help evaluate the DBD NME $M^{2\nu}$. In fact, one needs to take care of the relative phases of the single β NMEs, depending on the models as discussed in Section 5. The NMEs $M^{2\nu}$ are derived experimentally if the two-neutrino DBD rates are measured, and are used to help evaluate the $0\nu\beta\beta$ NMEs $M^{0\nu}$, in particular the $0\nu\beta\beta$ GT NMEs in the 1^+ intermediate channel and the information on the effective coupling $g_{\mathrm{A}}^{\mathrm{eff}}$ is obtained for the GT NME. Note the different momentum-exchange scales of the $0\nu\beta\beta$ and $2\nu\beta\beta$ NMEs since for the $2\nu\beta\beta$ the momentum-exchange scale is of the order of only few MeV.

1.5. Nucleonic and non-nucleonic correlations and nuclear medium effects

The neutrino CC and NC nuclear interactions involve nuclear spin ($\sigma/2$) and isospin ($\tau/2$) interaction operators, $\tau^{\pm}$ and τ^3, for the CC and NC interactions. The isospin weak interactions are of vector type and the isospin–spin interactions are of axial–vector type. Nuclear interactions via π, ρ and other mesons include appreciable σ and τ interactions and thus the neutrino–nuclear responses are necessarily sensitive to the nuclear τ and $\tau\sigma$ correlations in a given nucleus, as described in the reviews [1,4]. Accordingly, the vector and axial–vector nuclear responses in nuclei are modified from the single-quasiparticle (QP) responses due to the nucleonic and non-nucleonic τ and $\tau\sigma$ correlations and nuclear medium effects.

The τ and $\tau\sigma$ nuclear interactions are associated with the τ and $\tau\sigma$ symmetries, and thus are repulsive in nature. They push up the τ and $\tau\sigma$ strengths to the τ and $\tau\sigma$ giant resonances (GRs) in the high-excitation region. The GRs are collective (coherent) τ and $\tau\sigma$ vibrations of relevant nucleons [1,4,27–29]. Therefore, the τ and the $\tau\sigma$ responses for low-lying states are reduced with respect to the QP responses. They are discussed rather adequately by using a schematic particle–hole model with separable τ and $\tau\sigma$ interactions [1,4,54].

The isospin and spin transition (interaction) operators are expressed as

$$T_{SLJ} = h_{\alpha}\tau^{\pm}f_L(r)\big[\boldsymbol{\sigma}^S\mathbf{Y}_L\big]_J \,, \tag{20}$$

where $\alpha = S, L, J$ stands for the transition mode with S, L, J being the spin, the multipolarity, and the total angular momentum, respectively, and the square brackets stand for the angular-momentum coupling [55]. Then the isospin–spin nuclear interaction of $H = \chi_{\alpha}T_{\alpha} \cdot T_{\alpha}$ gives rise to the α-mode GR, as given by

$$[H_{\alpha}, T_{\alpha}] \approx E_{\alpha}T_{\alpha}, \quad |\mathrm{GR}_{\alpha}\rangle = T_{\alpha}|0\rangle \,, \tag{21}$$

where GR_{α} is the α-mode GR and E_{α} is the GR energy.

The simplest isospin GR is the Fermi GR with $T_{000} = T^-$, where T^- is the total isospin operator, and the commutation relation of Eq. (21) holds well because of the isospin symmetry. The Fermi GR is known as the sharp isobaric analogue state (IAS). The axial–vector GRs are Gamow–Teller GR (GTR) with T_{101}, isovector spin-dipole GR (IVSDR) with T_{112}, and so on. They are broad GRs, reflecting the incomplete super-multiplet ($\tau\sigma$) symmetry.

The reduction of the NMEs due to the τ and $\tau\sigma$ correlations is a kind of nuclear τ and $\tau\sigma$ core-polarization effect [1,4,54] due to the destructive coupling with the relevant GRs. Then the NME is schematically expressed as $M(T_{\alpha}) = k_{\alpha}^{\mathrm{eff}}M_{\mathrm{QP}}(T_{\alpha})$, where $k_{\alpha}^{\mathrm{eff}}$ stands for the effective weak coupling and $M_{\mathrm{QP}}(T_{\alpha})$ is the QP NME without the $\tau\sigma$ polarization. The coefficient $k_{\alpha}^{\mathrm{eff}}$ can be written by using the α-mode effective susceptibility.

It should be remarked that nucleons (proton, neutron) are dressed in meson clouds and thus their interactions are modified more or less in the nuclear medium due to correlations with other nucleons and mesons. Accordingly, the CC $p \leftrightarrow n$ NMEs in the nuclear medium are different from the NMEs for free nucleons since both the valence nucleons involved in the transition and the others in the core are modified through the CC transition. Actually, these effects are effectively included in the experimental NMEs.

The reduction of NMEs due to the spin–isospin correlations and the spin–isospin GRs are incorporated by the pnQRPA (proton–neutron quasiparticle random-phase approximation, see Section 3.1.1) through the spin–isospin interaction, while the non-nucleonic (Δ isobar, meson) and the nuclear-medium effects by the effective axial–vector coupling $g_{\mathrm{A}}^{\mathrm{eff}}$ are not. Experimental studies of the NMEs for low-lying states and the strength distributions for the relevant GRs are then important
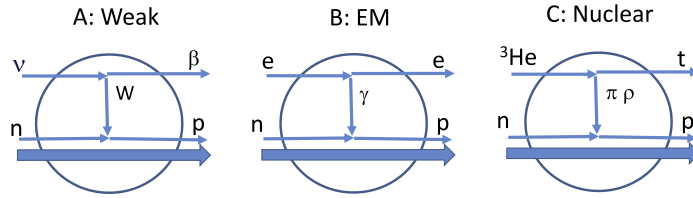
Fig. 3. Experimental probes for neutrino–nuclear responses. A: leptons with weak interaction, B: photons with EM interaction, C: nucleons and nuclei with strong/nuclear interaction. The notation is p: proton, n: neutron, e: electron, W: weak boson, γ: gamma ray, and π, ρ: mesons.

in order to understand the neutrino–nuclear responses in actual nuclei and to help realistic theoretical evaluations for the relevant NMEs by pinning down the nucleonic and non-nucleonic correlations and nuclear-medium effects.

Actually, neutrino responses for DBD and astro-neutrinos involve NMEs M in very wide excitation E, momentum q, angular-momentum J and nuclear-mass A ranges. The values for M, in particular those for the axial–vector NMEs, are sensitive to all kinds of nucleonic and non-nucleonic correlations and nuclear-medium effects. They are conventionally given as $M = (g_A^{\text{eff}}/g_A)M_m$, with M_m being the model matrix element and g_A^{eff}/g_A is the renormalization (quenching). The latter is the factor to incorporate such correlations and nuclear medium effects that are not explicitly included in the applied model, and it depends to some extent on the model and the ranges of E, q, J, A in the studied problem. Accordingly, extensive studies have recently been made and are currently under progress to measure the values for NMEs M by using various kinds of modern experimental probes and to evaluate them by more and more realistic and elaborate theoretical models and experimental and theoretical considerations on the ratio g_A^{eff}/g_A. The present article aims to review the present status of these studies from a wide perspective.

The review is organized as follows: In Section 2 various experimental ways to study neutrino–nuclear responses are described. They include single β/EC decays, nuclear CERs, muon-, photon- and neutrino-induced reactions and nucleon transfer reactions. Neutrino–nuclear responses for allowed and forbidden β/EC decays and the spin–isospin GRs are discussed in Section 3, in particular in the view of the quenching or enhancement of the axial coupling. Nuclear responses for astro-neutrinos and neutrino nucleosynthesis are described in Section 4. Section 5 reports on neutrino–nuclear responses for DBD, including tables on the recent NME calculations, and brief overviews of two-neutrino and neutrinoless DBD experiments. Summary and remarks are presented in Section 6 on perspectives of experimental and theoretical studies of the neutrino–nuclear responses and on future DBD experiments.

2. Experimental methods for neutrino–nuclear responses

Neutrino–nuclear responses are NC and CC weak responses for nuclei (see Section 1.2). They are discussed in terms of the responses for nucleons (protons and neutrons) embedded in nuclei which are described in terms of nucleon-based nuclear many-body models. In fact, nucleons are dressed in meson clouds and interact with neighboring nucleons in a nucleus, and accordingly the related neutrino responses are different from those for free nucleons. Therefore, neutrino–nuclear responses with weak couplings are sensitive to nuclear many-body correlations, non-nucleonic degrees of freedom (isobar and others), nuclear-medium effects (meson exchanges) and adopted nuclear models. Then experimental studies of the responses are valuable in order to obtain the true responses in the nucleus and to help/confirm the theoretical evaluations for the neutrino–nuclear responses, as discussed in the review articles [1,4,5,16,18,23]. It is remarked here that neutrino–nuclear responses and NMEs to be measured experimentally by SBDs, IBDs, two-neutrino DBDs, nuclear CERs, muon-photo and neutron reactions and others are real responses (NMEs) including effective weak coupling (renormalized/quenched g_A).

2.1. Experimental probes for neutrino–nuclear responses

The weak processes via astro-ν and astro-$\bar{\nu}$ can be expressed as ${}_Z^A X + \nu \rightarrow {}_Z^A X' + \nu'$ and ${}_Z^A X + \bar{\nu} \rightarrow {}_Z^A X' + \bar{\nu}'$ for NC processes, and ${}_Z^A X + \nu_e \rightarrow {}_{Z+1}^A X + e^-$ and ${}_{Z+1}^A X + \bar{\nu}_e \rightarrow {}_Z^A X + e^+$ for CC processes. The NC process is a nucleon excitation process of $N \rightarrow N'$ with N and N' being nucleons in the nucleus, while the CC process is a charge-exchange process of $p \leftrightarrow n$ with p and n being a proton and a neutron in the nucleus. The CC process for neutrinoless DBD is ${}_Z^A X \rightarrow {}_{Z\pm2}^A X + 2e^{\mp}$ with a two-nucleon charge exchange of $(n_1, n_2) \leftrightarrow (p_1, p_2)$ in the nucleus.

The nuclear responses are given by the product of the initial spin factor $1/(2J_i + 1)$ and the square of the NME for $N \rightarrow N'$ and $p \leftrightarrow n$ processes in cases of the astro-neutrino NC and CC interactions, and for $(n_1, n_2) \leftrightarrow (p_1, p_2)$ in case of the DBD. Here the DBD NMEs are associated indirectly with the NMEs for $p_1 \leftrightarrow n_1$ and $p_2 \leftrightarrow n_2$ via the neutrino potential in case of the neutrinoless DBD ($0\nu\beta\beta$) and directly with them in case of the two-neutrino DBD.

The weak responses for astro-neutrinos and DBDs have been studied experimentally by using various kinds of weak, electromagnetic (EM) and nuclear-interaction probes. They are schematically shown in Fig. 3.

Weak-interaction probes of ν and $\bar{\nu}$ beams are used as a direct way to study the weak (neutrino) responses. The neutrino cross section, however, is extremely small because of the weak interaction. It is of the order of $10^{-40} - 10^{-44}$ cm^2, depending

on the energy. Then high-flux neutrino beams of the order of $10^{13} - 10^{15}$/sec and multi-ton-scale detectors are required for the $\nu/\bar{\nu}$-beam experiments in order to achieve adequate signal rates.

The single beta decay (SBD) and electron capture (EC) provide the CC neutrino $n \leftrightarrow p$ responses. They are limited mostly to allowed and first-forbidden transitions from the ground and isomeric states to low-lying final states.

Negative muons are trapped in atomic orbits and are captured into nuclei via the weak interaction mostly in case of medium-heavy and heavy nuclei with atomic numbers $Z \geq 20$. Ordinary (non-radiative) muon-capture reaction of $^A_Z X + \mu^- \rightarrow {}^A_{Z-1} X + \nu_\mu$ is used to study the antineutrino $p \rightarrow n$ response in wide energy ($E = 1 - 70$ MeV) and momentum ($p = 30 - 100$ MeV/c) ranges.

Photons with EM interactions are also used to study the neutrino responses because the EM interactions have similar spin–isospin and multipole transition operators as the weak interactions. Electric and magnetic γ transitions are used to study vector and axial–vector weak responses, respectively.

Nuclear reactions with nuclear/strong interactions are useful for studying the neutrino–nuclear responses because of the large reaction/interaction cross section. The nuclear (strong) interaction itself is different from the weak interaction in strength, but the interaction operators include the spin, the isospin and the multipole terms in a similar fashion as the weak operators at the level of one-nucleon processes. This is not so in the case of processes involving two-body operators such as in the case of meson-exchange currents. The spin-flip and non-spin-flip inelastic scatterings of p, n, d, and light ions are used to study vector and axial–vector NC responses, respectively. Charge-exchange reactions (CERs) used for the CC-response studies are (p,n), (^{3}He,t) and others for ($n \rightarrow p$) responses and (n,p), (d,^{2}He), (t,^{3}He), (^{7}Li,^{7}Be) and others for ($p \rightarrow n$) responses.

High energy-resolution (^{3}He,t) reactions with the $0.42 - 0.45$ GeV ^{3}He beam at RCNP (Research Center for Nuclear Physics at Osaka University, Japan [56]) have been extensively used to study the $n \rightarrow p$ axial–vector responses since the spin–isospin interaction gets dominant at this medium energy. The projectile ^{3}He and the emitted t nucleus are charged particles, and thus high-precision energy analyses of them are possible by using a magnetic spectrometer. This means that one can carry out high energy-resolution measurements required to separate the individual final states. Nucleon-transfer reactions provide experimentally single-particle and single-quasiparticle properties of nucleons in a nucleus, which are, in turn, used to evaluate the neutrino–nuclear responses.

2.2. Single beta-decay and electron-capture experiments

2.2.1. Allowed and forbidden β/EC experiments

Single β and EC decays are used to study neutrino–nuclear responses. The current systematics of $\log ft$ values [57] for allowed and forbidden decays are shown in Fig. 4. In this section we briefly discuss three kinds of single-β and EC experiments relevant to neutrino-response studies, forbidden transitions in DBD nuclei, β spectrum shapes, and β spectra of radio-active impurities in neutrino detectors.

Neutrinoless DBDs involve NMEs with angular-momentum transfers of $\Delta J = 1 - 6$. Some of them are studied by measuring forbidden β and EC decays from intermediate nuclei. The decay scheme for ^{96}Zr is shown in Fig. 5. The ground-state-to-ground-state transition is $0^+ \rightarrow 6^+$. The phase-space and spin differences predict that the decay to the 5^+ state of ^{96}Nb is most likely and the estimated half-life is around 10^{20} years (see Section 3.5). Single β decay has been searched for and a lower limit of $t^\beta_{1/2} > 2.4 \times 10^{19}$ years has been given [58]. Additional constraints might be set by taking into account geochemical half-life determinations with all their uncertainties [59]. A similar case can be made for ^{48}Ca (see Section 3.5), see [60,61] for the first and recent $2\nu\beta\beta$ half-life data. A half-life limit of the β decay to the corresponding 5^+ excited state of ^{48}Ti results in a lower limit of $t^\beta_{1/2} > 2.5 \times 10^{20}$ years [62]. In both cases it seems that the β-decay half-life is longer than the one for $2\nu\beta\beta$ decay [61,63], see Section 3.5. In the case of DBD nuclei ^{130}Te and ^{136}Xe, the fourth-forbidden unique transition $5^+ \rightarrow 0^+$ is involved, see Section 3.3. The half life of $2.67 \times 10^{17} y$ and the limit of $> 1.9 \times 10^{19} y$ to the first excited states in ^{50}Ti and ^{50}Cr for ^{50}V with $\Delta J = 4$ give information on forbidden β transitions [64,65]. EC decays to the DBD nuclei ^{76}Ge, ^{100}Mo and others are of experimental and theoretical interest, as also the charge-exchange reactions populating states in the DBD intermediate nuclei, see Section 2.3.2.

Spectrum shapes for forbidden non-unique transitions provide information on axial–vector NMEs relative to vector NMEs, as discussed in Section 3.6. The very low energy region has an impact on the spectrum-shape determination as not all experiments will be able to measure the spectrum over the full range. The 4-fold non-unique forbidden decays of ^{113}Cd ($1/2^+ \rightarrow 9/2^+$) and ^{115}In ($9/2^+ \rightarrow 1/2^+$) are sensitive to the quenching of g_A because the spectral shape will change with the value of g_A [66]. A measurement of 44 individual detectors in the COBRA experiment indeed indicate a value for g_A in the ISM and MQPM models of 0.915 ± 0.021 and 0.911 ± 0.009 respectively [67], which is lower than the free value. Half-lives of $t^\beta_{1/2} = 8 \pm 0.11(\text{stat.}) \pm 0.24(\text{syst.}) \times 10^{15}$ years (^{113}Cd) [68] and $t^\beta_{1/2} = 4.41 \pm 0.25 \times 10^{14}$ years (^{115}In) [69] have been derived experimentally. The decay of ^{115}In to the first excited state of ^{115}Sn with the extremely small Q value is discussed in Section 3.4.1.

Various technologies are used for new measurements of the spectra. The KATRIN experiment measures the tritium spectrum in order to explore the neutrino mass [70]. Other technologies used are metallic magnetic calorimeters (MMC), working at low temperatures, and the Si-PIPS detectors.

The nuclei ^{40}K, ^{210}Bi, ^{39}Ar among others are well known as potential background components for neutrino and dark-matter searches. Then one needs the spectrum shape to evaluate contributions from them as discussed in Section 3.6.1. A β
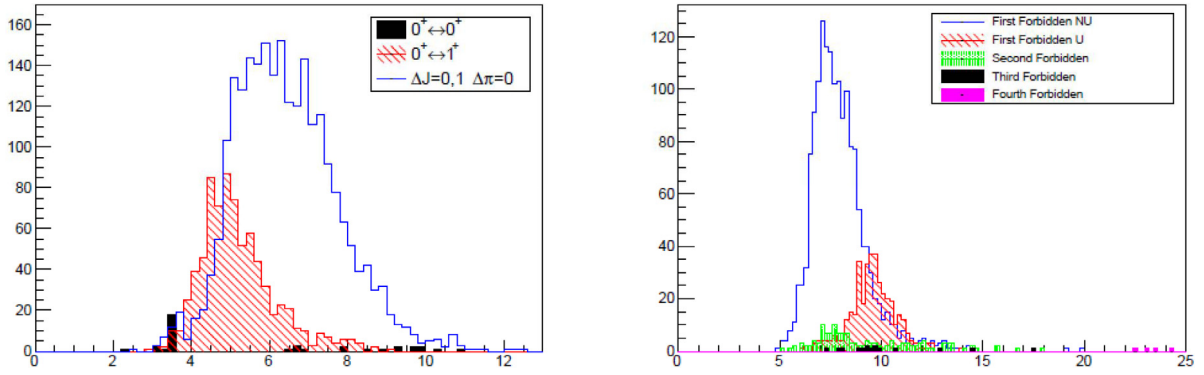
Fig. 4. Distribution of $\log ft$ values for allowed and super-allowed decays (left) and forbidden decays (right). The Data are from the IAEA database.
Source: Plots: Courtesy S. Turkat.
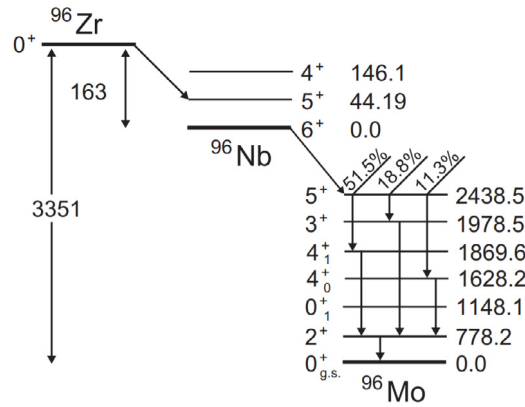
Fig. 5. Decay scheme of ^{96}Zr. The GT transition to the 5^+ state is most likely.
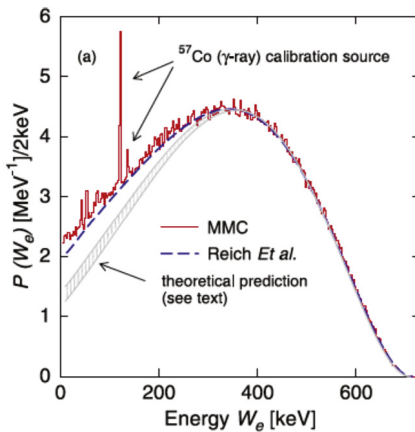
Fig. 6. Cryogenic MMC measurement of the β-decay spectrum of ^{36}Cl.
Source: taken from [71].

spectrum of the ^{36}Cl $2^+ \rightarrow 0^+$ transition, obtained by the MMC method, is shown in Fig. 6. More spectra, like for ^{241}Pu [72], have been obtained. Recently, calculated spectra of first-forbidden unique decays of ^{39}Ar and ^{42}Ar have been released [73], which allows to study backgrounds in large-scale argon-based experiments like DEAP searching for dark matter. On the other hand, there is now the opportunity to measure this shape with high precision.
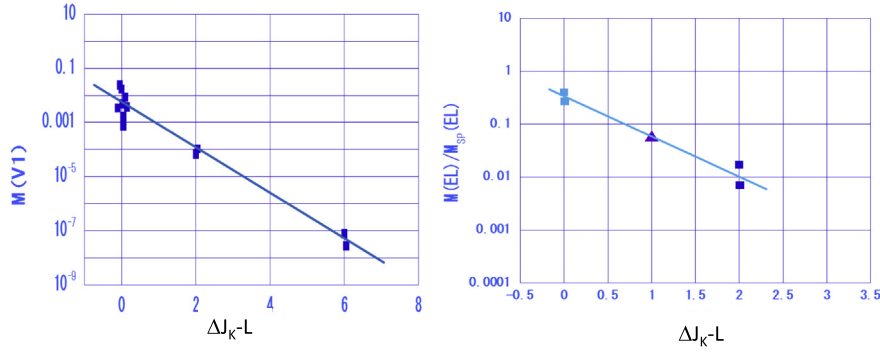
Fig. 7. Left side: NMEs for J_K-allowed and J_K-forbidden VL weak vector decays with $L = 1$ in $A = 170 - 182$ nuclei. Right side: NMEs in units of $M_{SP}(E L)$ for J_K-allowed and J_K-forbidden E3 ($L = 3$) and E5 ($L = 5$) transitions in $A = 164 - 186$ nuclei.

2.2.2. Single β/EC and γ transitions in deformed nuclei

Weak and electromagnetic decays in deformed nuclei are relevant for nucleosynthesis induced by supernova neutrinos. Open-shell nuclei with proton and neutron numbers far from magic numbers are likely deformed in shape due to the strong quadrupole interaction. In well-deformed nuclei, the J_K quantum number (projection of the angular momentum J on the intrinsic symmetry axis, note that J_K is conventionally denoted as K.) is a good quantum number. Then the J_K selection rule is effective for weak and EM transitions, as also for neutrino CC and NC responses in deformed nuclei. We first discuss briefly the J_K selection rules in β/EC and EM transitions in deformed nuclei around the mass number $A = 160 - 190$, and then discuss the J_K-hindered weak and EM responses for the ^{180m}Ta isotope of current astro-physics interest.

Experimental β/EC and EM transitions in the deformed nuclei are discussed in [74]. Recently the J_K selection rules for the β/EC and EM transitions in well-deformed nuclei have been derived [75]. The experimental NMEs M(V1) for vector transitions (VL) of $\Delta J = L = 1$, with J and L being the spin and the multipolarity, are obtained from the observed β/EC-decay rates, as shown in Fig. 7, left panel. The initial and final states involved in the transitions are simple two-quasiparticle (1 quasi-proton and 1 quasi-neutron) transitions in odd–odd nuclei. The J_K selection rule requires $\Delta J_K - L = 0$ with $L = 1$. The observed NMEs decrease as the deviation from $\Delta J_K - 1 = 0$ increases. The NMEs can be expressed as

$$M(V1) = M_0(V1) F^{\Delta J_K - 1}, \quad F \approx 0.15, \tag{22}$$

where $M_0(V1) \approx 7 \times 10^{-3}$ is the intrinsic V1 NME in natural units and F is the reduction factor. The V1 weak NMEs are reduced by a factor $F = 0.15$ and the transition rate (response) by a factor 0.023 with every one unit of deviation from the J_K selection rule.

The J_K-allowed and J_K-forbidden EM NMEs for E3 ($L = 3$) and E5 ($L = 5$) low-lying transitions are obtained. The values in units of single-particle NMEs [74,75] are shown in Fig. 7, right panel. The EL NMEs are expressed as

$$M(EL) = M_0(EL) F^{\Delta J_K - L}, \quad F \approx 0.16, \tag{23}$$

where $M_0(EL) \approx 0.35 M_{SP}(EL)$ is the intrinsic EL NME and F is the reduction factor. The EL NMEs are reduced by a factor $F = 0.16$ and the transition rate (response) by a factor 0.026 with every one unit of deviation from the J_K selection rule. The EL reduction factor is nearly the same as the factor for the weak V1 decays.

The ^{180}Ta isotope is of current interest from the astro-nuclear and neutrino-nucleosynthesis points of view. This is the rarest isotope with the probability of 2.4×10^{-12} per one Si atom and the very small isotopic abundance ratio of 1.2×10^{-4} [76]. This nucleus is not produced by ordinary s and r processes, but may possibly be produced by neutrino interactions. So the neutrino–nuclear responses associated with the ^{180}Ta production are interesting [77–80]. The ^{180}Ta ground state is unstable, but the 77 keV isomeric state is a long-lived state since the isomeric transitions are J_K-forbidden. The transition scheme is shown in Fig. 8.

The J_K-hindered β/EC and EL γ decays from the isomeric state in ^{180}Ta are evaluated by using the J_K selection rules. The evaluated β^- and EC NMEs are [75]

$$M(V3) = 3.8 \times 10^{-13} \ (\beta^-) \ ; \ M(V3) = 1.2 \times 10^{-12} \ (EC). \tag{24}$$

The $\log ft$ values and the half-lives are $\log ft = 29.9$ and $t_{1/2}(\beta^-) = 5.4 \times 10^{23}$ y for the β^- branch, and $\log ft = 28.9$ and $t_{1/2}(EC) = 1.4 \times 10^{20}$ y for the EC branch. The EM transition from the isomeric state with $J^\pi = 9^-, J_K = 9$ to the 40 keV state with $J^\pi = 2^+, J_K = 1$ is a J_K-forbidden E7 transition with $\Delta J_K - L = 1$. The E7 NME is evaluated as [75]

$$M(E7) = 1.3 \times 10^4 \, \text{fm}^7. \tag{25}$$

The γ-decay half-life is $t_{1/2}(\gamma) = 1.4 \times 10^{31}$ y, and the EM half-life, including the conversion electron emission, is $t_{1/2}(E7) = 8 \times 10^{18}$ y. The single β/EC and EM decay rates are, indeed, of the same order of magnitude as typical two-neutrino DBD rates. They have not been observed experimentally yet. Several groups have searched for the γ rays following
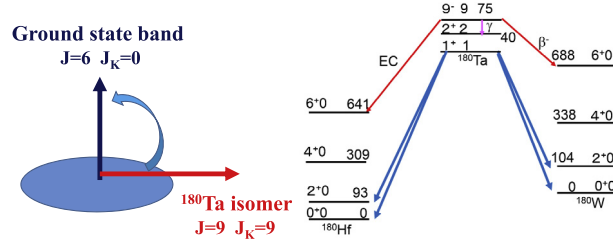
Fig. 8. Left side: Angular momentum J and its projection J_K on the symmetry axis. Right side: Beta- and gamma-transition scheme for the ground and isomeric states in ^{180}Ta. The spin–parity J^π, the projection J_K and the energy in units of keV are shown. The transitions (blue lines) from the ground state are J_K-allowed and the transitions (red lines) from the isomeric state are J_K-forbidden.

the β^-/EC decays as given in [81] and references therein. Lower limits of 2×10^{17} y and 5.8×10^{16} y for the EC and β^- decays, respectively, were recently reported [82].

2.3. Charge-exchange nuclear reactions

The nuclear (strong) interactions mediated by π, ρ and other mesons are different from the weak interactions carried by the weak bosons in strength and interaction range. On the other hand, they have common τ, σ and multipole-interaction operators, and accordingly have similar τ, σ and multipole-interaction NMEs and nuclear responses. Therefore, direct nuclear reactions induced by nuclear interactions are useful to study neutrino–nuclear responses induced by weak interactions.

2.3.1. Neutrino responses by charge-exchange nuclear reactions (CERs)

Various types of charge-exchange reactions (CERs) for CC-response studies are described in the review articles [4,16,18] and references therein. In this subsection we briefly discuss general features of CERs for neutrino-response studies and recent CER experiments for astro-neutrino and DBD responses. The nuclear reactions to be used for the neutrino-response studies are medium-energy light-ion reactions, with the projectile energy per nucleon of $E/A \approx$ sub-GeV and a mass range of $A \leq 20$, in order to avoid multi-step reactions and nuclear distortions. Merits of CERs for CC-response studies are as given below.

(i) A large cross section of the order of $10^{-26} - 10^{-28}$ cm^2/str for the nuclear reaction. This is $10^{15} - 10^{20}$ orders of magnitude larger than that for the neutrino reaction induced by the weak interaction. Then one can measure CER cross sections and nuclear responses for individual nuclear states with good energy resolution and good statistics.

(ii) Medium-energy projectiles are used to cover wide regions of excitation energy of $E \approx$ 0–40 MeV, the momentum of $p \approx$ 0–200 MeV/c and the angular momentum of $l\hbar \approx$ 0–6$\hbar$. The excitation energy and the spin of the final state are identified by measuring the energy and angular distributions of the emitted particles.

(iii) The CC τ^- responses are studied by using τ^- type CERs of (p,n), (^{3}He,t), (^{6}Li,^{6}He), (^{12}C, ^{12}B), etc., while CC τ^+ responses are studied by using τ^+ type CERs of (n,p), (d,^{2}He), (t,^{3}He), (^{7}Li,^{7}Be), (^{12}C,^{12}N), and so on.

(iv) Vector $\tau^\pm$ responses are studied by using CERs with isospin (τ) nuclear interactions, and axial–vector $\tau^\pm\sigma$ responses by CERs with isospin–spin ($\tau\sigma$) nuclear interactions. They are also identified by measuring spin observables and spin-flip excitations in nuclear reactions.

The nuclear interactions associated with the vector (isospin) and axial–vector (isospin–spin) excitations are the isospin V_τ and isospin–spin $V_{\tau\sigma}$ interactions. The interaction is expressed in terms of the central (C), spin–orbit (LS) and tensor (S^T) interactions as [83–85]

$$V^{\text{eff}} = V^{\text{C}} + V^{\text{LS}} + V^{\text{T}}, \tag{26}$$

$$V^{\text{C}} = V^{\text{C}}(r_{ij}) + V^{\text{C}}_\sigma(r_{ij})\boldsymbol{\sigma}_i \cdot \boldsymbol{\sigma}_j + V^{\text{C}}_\tau(r_{ij})\tau_i\tau_j + V^{\text{C}}_{\sigma\tau}(r_{ij})\boldsymbol{\sigma}_i \cdot \boldsymbol{\sigma}_j\tau_i\tau_j, \tag{27}$$

$$V^{\text{LS}} = \left[V^{\text{LS}}(r_{ij}) + V^{\text{LS}}_\tau(r_{ij})\tau_i\tau_j\right]\mathbf{L} \cdot \mathbf{S}, \tag{28}$$

$$V^{\text{T}} = \left[V^{\text{LS}}(r_{ij}) + V^{\text{LS}}_\tau(r_{ij})\tau_i\tau_j\right]S^T_{ij}. \tag{29}$$

The central, LS, and tensor interactions show characteristic dependencies on the energy E and the momentum transfer q as shown in Fig. 9. They are discussed in [83,85,86]. The isospin interaction V_τ becomes small as the incident energy E increases, and the isospin–spin interaction $V_{\tau\sigma}$ stays rather constant as a function of the projectile energy. Then interaction $V_{\tau\sigma}$ is of the same order of magnitude as V_τ at $E/A \approx$ 30 MeV, while the $V_{\tau\sigma}$ interaction is a factor 3–4 larger than V_τ at the medium energy $E/A \approx$ 140–180 MeV [87]. This feature is explained in terms of the π and ρ meson-exchange potentials and the second-order effects of tensor force [86]. In other words, the $\tau\sigma$ and τ excitations are identified by observing the cross sections as functions of the projectile energy. Noting that the cross section is proportional to the square of the interaction
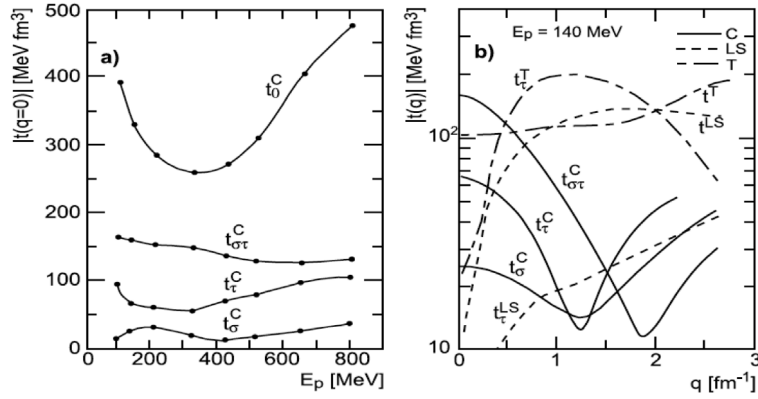
Fig. 9. Panel (a): Central interactions as function of the projectile energy. Panel (b): Central, tensor and LS interactions as function of the momentum transfer q [85].

strength, the medium-energy CERs with $E/A = 100$–300 MeV are used for preferentially exciting the $\tau\sigma$ mode as shown in Fig. 9. The distortion interaction (t_0^C) gets small at the medium energy.

The reaction proceeds mainly by the central interactions at forward angles with $q \approx 0$, while the tensor interaction gets important at backward angles with $q \approx 0.5$ fm$^{-1} = 100$ MeV/c, as seen in Fig. 9. Let us consider first the CER with the central spin–isospin interaction. The nuclear interaction for the CER of $A(a, b)B_i$ to excite an ith final state in B is expressed as

$$H_\alpha = \chi_\alpha Q_\alpha^\dagger Q_\alpha, \quad \alpha = TSLJ, \tag{30}$$

where χ_α is the interaction strength, $Q_\alpha^\dagger$ and Q_α are the projectile-nucleus and target-nucleus transition operators, and α stands for the transition mode of $TSLJ$ with T, S, L, J being the isospin, the spin, the orbital angular momentum and the total angular momentum, respectively. The transition operator is expressed as

$$Q_\alpha = \tau^\pm i^L f_L(r)\left[\mathbf{Y}_L \boldsymbol{\sigma}^S\right]_J, \tag{31}$$

where $S (= 0,1)$ is the spin and $f_L(r)$ is the radial function, given as $f_L(r) = r^L$ in the case of a low-energy (long-wave-length) EM transition. The square brackets denote angular-momentum coupling [55]. The Fermi (F, 0^+), Gamow–Teller (GT, 1^+), isovector spin-dipole (IVSD, 2^-) and isovector spin quadrupole (IVSQ, 3^+) transition operators are $Q_F = \tau^\pm$, $Q_{GT} = \tau^\pm \sigma^1$, $Q_{SD} = \tau^\pm i^1 f_1(r)\left[\mathbf{Y}_1 \sigma^1\right]_2$, and $Q_{SQ} = \tau^\pm i^2 f_2(r)\left[\mathbf{Y}_2 \sigma^1\right]_3$, respectively.

The cross section for the α-mode transition to the ith final state is expressed as

$$\frac{d\sigma_i}{d\Omega} = K_i(\alpha)F_i(\alpha, q)J_i(\alpha)^2 B_i(\alpha), \tag{32}$$

where $K_i(\alpha)$ is a kinematic factor, $F_i(\alpha, q)$, with q being the momentum transfer, is the q-dependent factor and J_α is the α-mode interaction integral. The nuclear response for the α-mode CER excitation of $A \rightarrow B_i$ is expressed by $B_i(\alpha) = (2J_i+1)^{-1}|M_i(\alpha)|^2$ with J_i and $M_i(\alpha)$ being the initial (target) state spin and the corresponding NME. The response for the projectile side $a \rightarrow b$ is included in the interaction integral. The momentum transfer q is a simple function of the angle θ of the emitted particle b, and the q-dependent factor $F_i(\alpha, q)$ stands for the angular distribution of the emitted particle b. Actually, the q-dependent factor is modified more or less by distortion potentials acting on the projectile a and the emitted particle b.

If the nuclear interaction, the initial and final wave functions involved in the CER and the optical potential for the projectile and the emitted particle are well known, one can calculate the cross section by means of a DWBA (distorted wave born approximation) code. The transferred angular momentum L is derived from the q-dependent factor $F_i(\alpha, q)$ (the angular distribution), and the α-mode response $B_i(\alpha)$ is obtained by comparing the DWBA and observed cross sections.

Experimental studies of the CERs for simple F and GT states have been performed extensively by using simple projectiles with $A \leq 3$ and so on, as shown in the review papers [4,16,18]. Among them, (p,n) and (n,p) CERs have been used widely as simple nucleon CERs [88,89]. Experimentally, the (p,n) and (n,p) reactions, however, involve the neutrons (neutral particles), which are measured by means of the TOF (time of flight) method. Then the energy resolution is limited to be of the order of a couple of sub-MeVs. Thus they are used to study isolated low-lying states and gross features of CER strength distributions.

Medium-energy ($E = 100$–200 MeV) (p,n) reactions have been used extensively at IUCF (Indiana University Cyclotron Facility, 1976–2010) and other laboratories to study IASs and GTRs and also some low-lying GT states. Here the q-dependent factor $F_i(GT, q)$ is given approximately by the square of a spherical Bessel function with $L = 0$. Then the cross sections at forward angles of $\theta \approx 0$ degrees, corrected for the kinematic factor $K_i(\alpha)$ and the q-dependent factor $F_i(GT, q)$, derived from the DWBA calculation, is given as

$$\frac{d\sigma_i}{d\Omega}K_i(GT)^{-1}F_i(GT, q)^{-1} = J_i(GT)^2 B_i(GT). \tag{33}$$
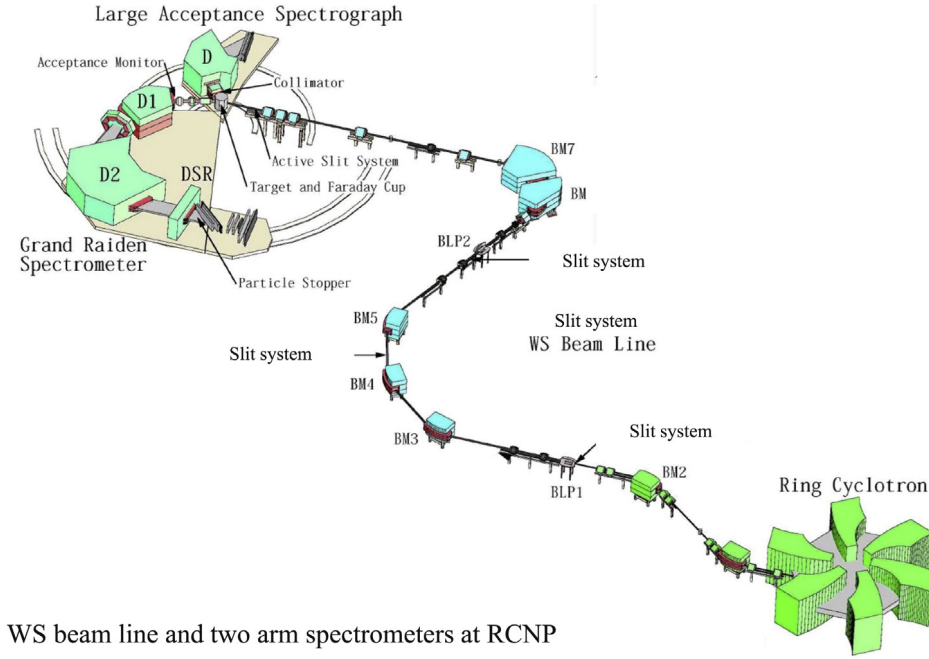
Fig. 10. The high energy-resolution beam line and the spectrometer at RCNP.

The coefficient $J_i(GT)^2$ is found to be nearly constant, being independent of the individual ith states in various nuclei in case of the simple GT states with large $B(GT) \geq 0.1$. They are illustrated for various kinds of CERs in the review article [4] and references therein. This is the so-called proportionality relation and is used to estimate the approximate response of $B_i(GT)$ for simple GT states from the measured cross section at $\theta = 0$. Here the proportionality coefficient $J_i(GT)^2$ is obtained from the measured cross section for a reference state with the $B(GT)$ known from the β-decay ft value in the neighboring nucleus.

The CERs of (^{3}He,t) and (t,^{3}He), with a charged projectile and a charged emitted particle, are much used for F and GT neutrino-response studies by means of magnetic analyzers for incident beams and emitted particles [4,90]. The cross sections, being corrected for the kinematic and the DWBA q-dependent factors, are approximately proportional to the nuclear response $B_i(\alpha)$, with the proportionality coefficient $J_i(\alpha)^2$. Then one can obtain the response from the measured cross section by using the proportionality coefficient derived from a reference state as in the case of the (p,n) and (n,p) reactions. The (p,n) and (^{3}He,t) reactions have been compared against each other in detail and they are consistent with each other after a momentum-dependent, yet trivial, adjustment [91].

The proportionality relation may be used if the ith state of interest is excited mainly by the central $\tau\sigma$ interaction and the interaction integral $J_i(\alpha)$ for the ith state of interest is the same as that for the reference state. This is the case for the simple spin-flip excitations with a large response of $M_i(\alpha) \geq 0.1$.

Actually, nuclear states are not simple single-particle configurations, but include mixtures of them. They are excited by the central $\tau\sigma$ interaction and the tensor-type interaction, and the NME is effectively expressed as

$$M(\alpha') = M(\tau\sigma) + k_t M'(\tau\sigma\mathbf{Y}_2),\tag{34}$$

where k_t is the tensor-interaction strength relative to the central one, and M' is the NME for the transition operator $\tau f(r)[\sigma\mathbf{Y}_2]_1$. The strength of the tensor interaction itself is of the order of $k_t \approx 0.1$. Then the second term of $M'(\tau\sigma\mathbf{Y}_2)$ gets important in case that the $\Delta l = 2$ excitation is appreciable and the first term is small. The contribution of the second term is seen in the $L = 2$ component of the angular distribution as discussed in Section 4.2.1.

2.3.2. High energy-resolution CERs for neutrino–nuclear responses

Nuclear responses for astro-neutrinos and DBDs are studied by CERs on individual nuclear states in the wide excitation and momentum regions of $E = 0$–40 MeV and $p = 0$–200 MeV/c, which are just the regions appropriate for astro-neutrinos and DBDs.

High energy-resolution studies of the charged-particle (^{3}He,t) CERs have been extensively carried out at RCNP, Osaka University [56] by using medium-energy ^{3}He projectiles with $E = 420$–450 MeV for selective $\tau\sigma$ excitations. The charged projectile ^{3}He and the charged emitted particle t are momentum-analyzed by means of the high energy-resolution beam line and the Grand Raiden spectrometer. The achieved energy resolution of $\Delta E/E \approx 5 \times 10^{-5}$ is an order of magnitude better than that for standard magnetic analyzers, and is just the resolution around 30 keV required for studying individual states. The beam line and the spectrometer at RCNP are shown in Fig. 10.
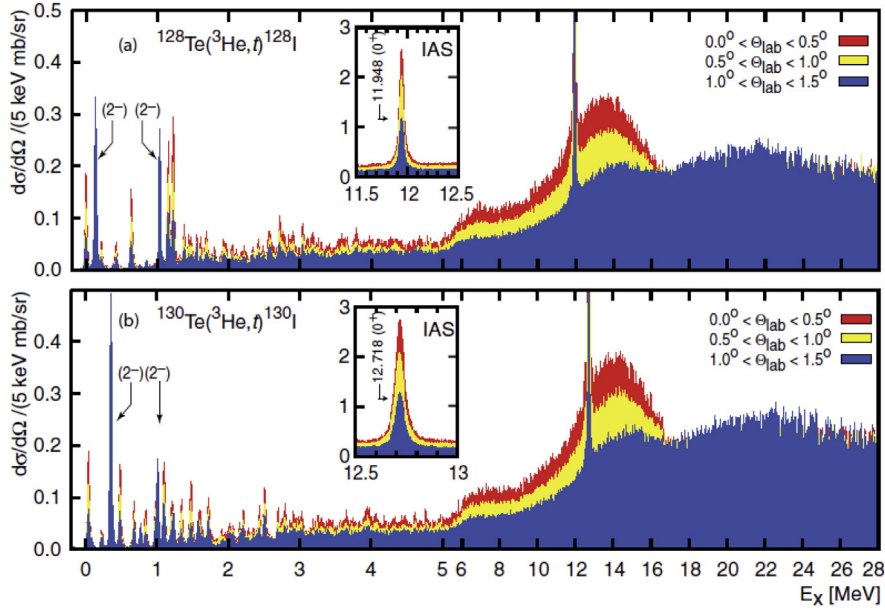
Fig. 11. Energy spectrum of the ^{128,130}Te(^{3}He,t)^{128,130}Xe CER [99].

Neutrino-response studies for the DBD nucleus ^{100}Mo and the solar-neutrino nucleus ^{71}Ga were carried out by using the (^{3}He,t) CERs in the 1990's at RCNP [92,93]. The (^{3}He,t) CERs have been shown to be useful for studying GT strengths [94]. Charged reaction particles are measured also in coincidence with γ rays to identify the final state.

The (^{3}He,t) CERs were measured on DBD nuclei of current interest for high-sensitivity DBD experiments. They are ^{76}Ge [95], ^{82}Se [96], ^{96}Zr [97], ^{100}Mo [92,98], ^{116}Cd [92], ^{128,130}Te [99], ^{136}Xe [100] and ^{150}Nd [101], which are all $\beta^-\beta^-$-decaying nuclei with a large phase-space factor and a large Q value $Q_{\beta\beta}$.

The energy spectra for the ^{128,130}Te(^{3}He,t)^{128,130}Xe at the emitted triton angles of $\theta \approx$ 0–4 degrees are shown in Fig. 11. Here the F (0^+) and GT (1^+) CERs with $\Delta L = 0$ are characterized by a large yield at the forward angles of $\theta = $ 0–0.5 degrees, while SD(2^-) with $\Delta L = 1$ and SQ(3^+) with $\Delta L = 2$ have large yields at larger angles of $\theta = 1 - 3$ degrees. Note that the Fermi giant state of IAS (isobaric analogue state) appears as IAR (isobaric analogue resonance) in the continuum region.

The observed spectra show discrete lines for GT, SD and SQ states at the low excitation region of $E = $ 0–4 MeV. The corresponding states are well excited by the $\sigma\tau$ interaction. At the high-excitation region one sees the strong F (Fermi IAR), GT and IVSD giant resonances of $E \geq $ 10 MeV, as discussed in Section 1. Most F, GT and IVSD strengths are pushed up into the GR regions. No Fermi states are seen at the low-excitation region since all of the F strength is concentrated in the IAS because of the good isospin symmetry. On the other hand some GT and SD strengths remain in the low-lying states since the spin–isospin symmetry is not fully realized in nuclei. These are common features of τ^--CERs on medium-heavy and heavy nuclei [1,4].

The observed angular distributions are analyzed to identify the angular-momentum transfer and the spin–parity to obtain the F, GT and SD strengths as shown in Fig. 12.

The GT strengths B(GT) are derived from the DWBA analyses of the angular distributions for individual states [95–101]. The strength distributions are plotted as function of the excitation energy in Fig. 13. The GT and SD states at the low-excitation region depend on valence nucleons in individual nuclei. The GRs (IAS, GTR, IVSDR) are nuclear-core vibrations, and thus are rather uniformly excited in all nuclei. The GT strengths are spread over the low-excitation region in cases of ^{76}Ge, ^{82}Se, ^{128,130}Te, ^{136}Xe and ^{150}Nd. Since the valence neutrons and the valence protons in these nuclei are in the same major shell of $N = 3$ or $N = 4$, there are many 1^+ states excited by the $\tau^- n \rightarrow p$ CER. On the other hand, there is only one GT state with the transition $(0g_{7/2})_n \rightarrow (0g_{9/2})_p$ in ^{96}Zr and ^{100}Mo since the neutrons and protons reside in the different major shells of $N = 3$ and $N = 4$, respectively.

The SD states play an important role for neutrino responses associated with the neutrinoless DBDs and medium-energy astro-neutrinos. They are well excited by the (^{3}He,t) CER, as shown in Fig. 11. The configuration of the lowest SD 2^- state is $(0g_{9/2})_n(0f_{5/2})_p$ for ^{76}Ge and ^{82}Se, and $(1d_{5/2})_n(1p_{1/2})_p$ for ^{96}Zr and ^{100}Mo, and $(0g_{7/2})_n(0h_{11/2})_p$ for ^{128,130}Te and ^{136}Xe.

The SD differential cross section with the angular-momentum transfer of $L = 1$ shows the typical pattern of $|j_1(qR)|^2$, where $j_1(qR)$ is the spherical Bessel function with q and R being the momentum transfer and the interaction nuclear radius. The cross section reaches its maximum at the angle $\theta_1 \approx 2$ degrees, corresponding to the momentum transfer $q_1 \approx 60$ MeV/c, as shown in Fig. 12.

If the experimental SD response B_G(SD) is proportional to the SD cross section σ(SD) at $\theta \approx 2$ degrees, as the GT response B(GT) is proportional to the GT cross section σ(GT) at $\theta \approx 0$ degrees, one gets B_G(SD) $= R[\sigma$(SD)$/\sigma$(GT)$] \times B$(GT), where
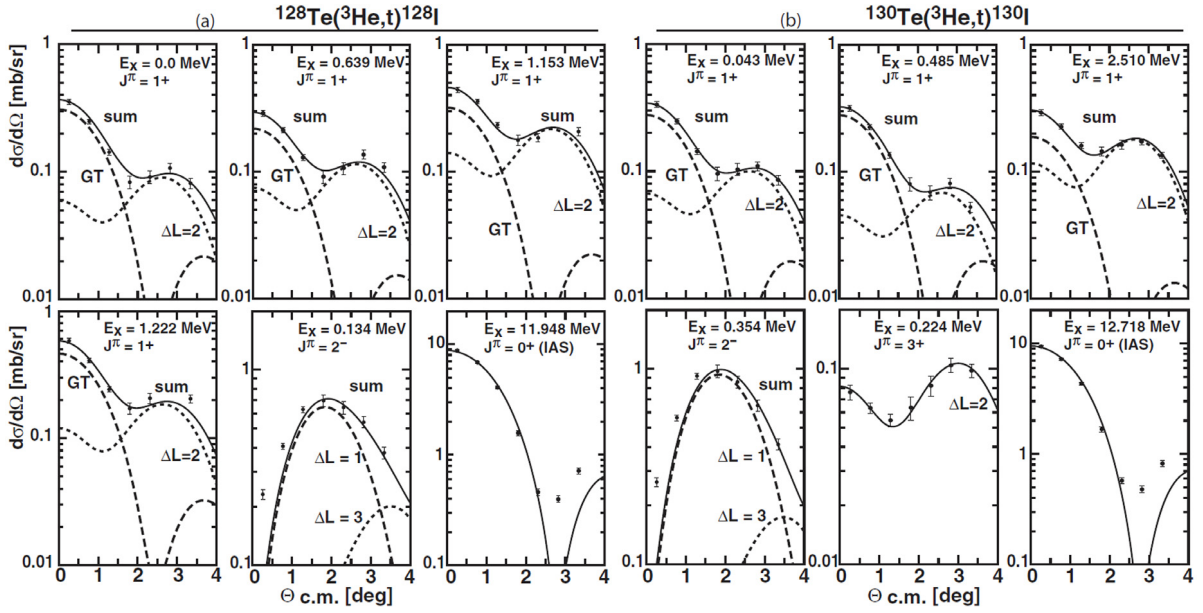
Fig. 12. Angular distributions of the GT, SD, SQ, and IAR states from the ^{128,130}Te(^{3}He,t)^{128,130}Xe reaction [99].
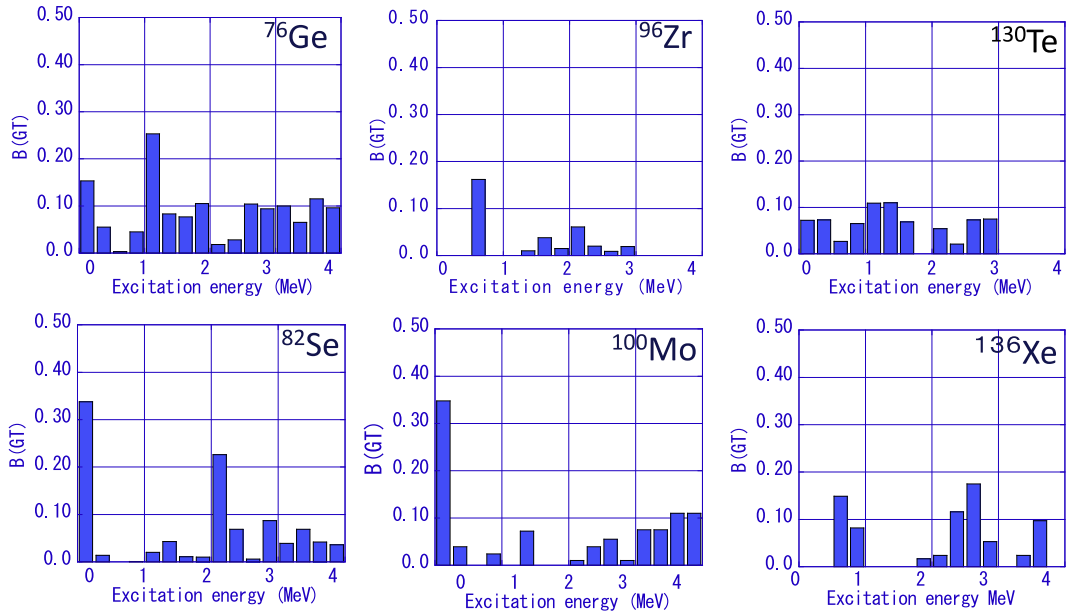
Fig. 13. GT strength (B(GT)) distributions plotted against the excitation energy for low-lying states in ^{76}Ge, ^{82}Se, ^{96}Zr, ^{100}Mo, ^{130}Te and ^{136}Xe.

R is the proportionality constant for the SD cross section with respect to the GT one. Using the observed cross sections of σ(SD), σ(GT) and the known B(GT), the values for B_G(SD)$/R$ were derived for the DBD nuclei [102]. The SD NMEs M_G(SD), derived as $[B_G$(SD)$]^{1/2}$, are indeed proportional to the model NMEs M(SD) as shown in Fig. 14, and thus CERs are used to get the SD NMEs.

Neutrino–nuclear responses associated with medium-energy supernova neutrinos and neutrinoless DBDs involve medium-momentum and angular-momentum transfers of $q = 20$–200 MeV/c and $\Delta l\hbar = 1 - 6\hbar$. Nuclear and muon CERs provide opportunities to study neutrino–nuclear responses in a wider momentum-transfer region. So, it is of interest to investigate how axial–vector responses with the axial–vector coupling are modified at the large momentum transfer of $q = 50$–100 MeV/c.
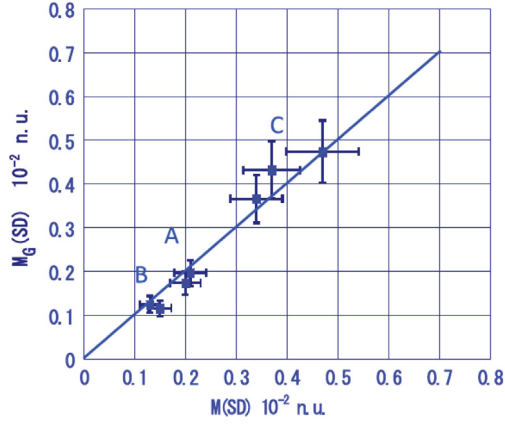
Fig. 14. Experimental SD NMEs M_G(SD) with $R^{1/2} = 0.86 \times 10^{-3}$ are plotted against the model (FSQP, Fermi-surface quasiparticle model, see Section 5.5.1) NMEs M(SD) for DBD nuclei of A: ^{76}Ge, ^{82}Se, B: ^{96}Zr, ^{100}Mo and C: ^{128}Te, ^{130}Te, ^{136}Xe [102].
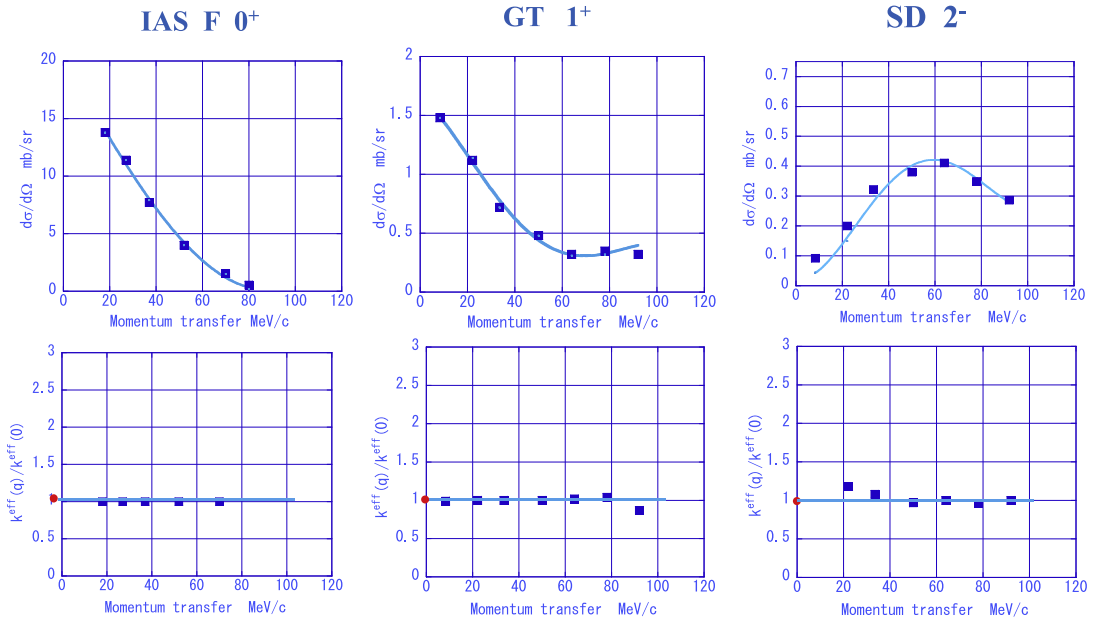
Fig. 15. Top: The ^{76}Ge(^{3}He,t) CER cross sections as functions of the momentum transfer q [95]. F 0^+: 8.31 MeV IAS, GT 1^+: the 0.12 MeV GT state, SD 2^-: the ground SD state. The solid lines are the DWBA calculations. Bottom: The ratio $k^{eff}(q)/k^{eff}(q = 0)$ for $\alpha =$ F (IAS), GT (1st GT state), and SD (ground) states. The red point is the normalization point at $q = 0$. See [103].

The (^{3}He,t) CERs on DBD nuclei were measured for F(IAS, 0^+), GT(1^+) and SD(2^-) states in the angular range of $\theta = 0$–4 degrees, corresponding to the momentum-transfer range of $q = 5 - 100$ MeV/c, to study the momentum dependence of the neutrino–nuclear responses [103]. The q-dependent cross section for the ith final state is expressed by modifying Eq. (32) as

$$\frac{d\sigma_i}{d\Omega} = K_i(\alpha)F_i(\alpha, q)J_i(\alpha)^2 \kappa^{eff}(q)^2 B_i(\alpha), \tag{35}$$

where $K_i(\alpha)$ and $J_i(\alpha)$ with $\alpha =$ F,GT,SD are the kinematic factor and the volume integral of the interaction, respectively. The kinematic q dependence is given by $F_i(\alpha, q) \approx |J_L(qR)|^2$ and the q-dependent response is effectively expressed as $\kappa^{eff}(q)^2 B_i(\alpha)$, with $B_i(\alpha)$ being the nuclear response at $q = 0$. The coefficient $k^{eff}(q)$ stands for the effective q-dependent coupling.

The kinematic q dependence $F_i(\alpha, q)$ is given by the DWBA calculation, and the q-dependent coupling $\kappa^{eff}(q)$ manifests as deviation of the observed q (angular) distribution from the DWBA calculation. Actually, the observed q dependencies (angular distributions) of the CER cross sections for $\alpha =$ F,GT,SD responses are well reproduced by the DWBA calculations with constant $\kappa^{eff}(q)^2$, as shown in Fig. 15. The GT and SD responses at the medium-momentum region of $q = 30$–100 MeV/c
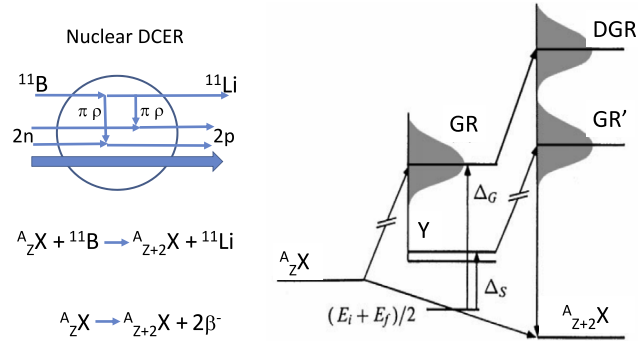
Fig. 16. Left side: Schematic diagrams of DCER of $^A_Z X(^{11}B,^{11}Li)^A_{Z+2}X$ and DBD of $^A_Z X \rightarrow \ _{Z+2}^A X + 2e^-$. Right side: DCER and DBD transition schemes: $^A_Z X$ and $^A_{Z+2}X$ are the DBD initial and final nuclei. The GR and DGR are the giant resonance and the double GR excited from the initial nucleus. GR' is the GR excited from the intermediate state [106].

are found to be the same as the responses at $q \approx 0$ [103]. The GT and SD NMEs at $q \approx 0$ for the DBD of other medium-heavy nuclei are experimentally available from β/EC data. They are quenched with respect to the pnQRPA NMEs by a factor $k_{NM}(0) \approx 0.6$ at the β/EC point of $q \approx 0$ [104,105]. Thus the axial–vector weak coupling is considered to be uniformly renormalized (quenched) by the coefficient $k_{NM}(q) \approx 0.6$ in the wide momentum region of $q = 0$–100 MeV/c, which is the region of the neutrinoless DBDs and the medium-energy supernova neutrinos.

2.3.3. Double charge-exchange nuclear reactions for DBD responses

Double charge-exchange reactions (DCERs) provide information on DBD responses, much like the single CERs on SBD (single beta decay) responses. The DCER to be used to study nuclear response for neutrinoless DBD is expressed as

$$^A_Z X + a \rightarrow \ _{Z\pm2}^A X + b , \tag{36}$$

where $^A_Z X$ and $_{Z\pm2}^A X$ are the DBD initial and final nuclei, and a and b are the DCER projectile and emitted nucleus. In case of $^A_Z X \rightarrow _{Z+2}^A X$ two neutrons in the initial nucleus $^A_Z X$ change to two protons in the final nucleus $_{Z+2}^A X$, while two protons in the projectile nucleus a turn to two neutrons in the emitted nucleus b.

The DCER and DBD involve common initial and final states, but their reaction and decay mechanisms are different. The interaction involved in DCER is the nuclear interaction via π, ρ and other mesons, while the one involved in DBD is the weak interaction via the exchange of a charged weak boson. Actually, the nuclear-interaction operators are different from the weak-interaction ones, depending much on the projectile energy and the momentum transfer. The projectile and emitted nuclei involved in DCER are distorted much by nuclear potentials. Therefore, it is not straightforward to relate the DCER cross section to the DBD transition rate. In case of a medium-energy projectile with $E/A =$ sub-GeV/nucleon, the $\tau\sigma$ central interaction dominates the nuclear interaction, and thus the double $\tau\sigma$ flip process gets dominant in DCER. Then one may get the double GT and double SD responses from the DCER cross section in the low-momentum-transfer region (forward angle), which may be used to help evaluate the DBD GT and SD responses.

The lightest-projectile DCER is the $(^3He,3n)$ reaction. This reaction involves 3 neutrons, which are hard to measure experimentally with good energy resolution. Light heavy-ion reactions to be used for DCERs are, e.g., $(^{11}B,^{11}Li)$ and $(^{18}O,^{18}Ne)$. DCER and DBD transition schemes for $^{100}Mo(^{11}B,^{11}Li)^{100}Ru$ and $^{100}Mo \rightarrow ^{100}Ru + 2e^-$ are shown in Fig. 16.

DCERs may excite strongly DIAS (double IAS), DGTR (double GTR), DIVSDR (double IVSDR) and other double GRs, like the single CERs excite strongly single IAS, GTR, IVSDR and other GRs. Thus DCERs may leave little strength to the ground and low-lying states, as single CERs do. Accordingly, one may expect a similar feature in case of the neutrinoless DBD and DCER responses, just as seen in the single β/EC and CER responses. The DBD followed by 2 neutrinos ($2\nu\beta\beta$ decay) is mainly a double-GT process, leaving little strength to the ground state [106]. The DGT GR and DBD were discussed from a theoretical point of view in [106,107].

Theoretical discussions are made on heavy-ion CERs [108] and on relation of DCERs to DBD responses in [109]. DBD NMEs $M^{0\nu}$ are shown theoretically to be related with DGT centroid energies in [110]. DCER experiments on medium-heavy DBD nuclei are interesting. So far DCER experiments are mainly performed on light nuclei [111].

The $(^{11}B,^{11}Li)$ DCER was studied at RCNP by using a medium-energy ^{11}B beam with $E/A = 80$ MeV [112]. The emitted nucleus ^{11}Li was analyzed by the high energy-resolution spectrometer Grand Raiden and was identified by TOF and PI measurements. The DCER on ^{56}Fe shows double IAR (isobaric analogue resonance) and large amount of strength in the high excitation region above 20 MeV, but no strength at the low-excitation region of $E = 0$–10 MeV. The cross-section ratio for the low- to high-excitation regions is less than 0.05. The DCER strengths are considered to be pushed up to the high-excitation double-GR region due to the repulsive $\tau\sigma$ interaction, like the single CER strengths are pushed up to the GR region (see Fig. 16). This suggests a reduction of the DBD strength for the ground-state transition.

Extensive programs of DCERs are under progress at INFN-LNS Catania (Laboratori Nazionali del Sud, [113]) to study DBD–neutrino responses [114]. The DCER of $^{40}\text{Ca}(^{18}\text{O},^{18}\text{Ne})^{40}\text{Ar}$ was measured by using the 0.27 GeV ^{18}O beam with $E/A = 15$ MeV [114]. The ground and low-lying states in ^{40}Ar were identified, and the angular distribution for the ground-state transition was measured. Medium-energy heavy-ion DCERs for isotopes with large T_z are interesting in order to see how the DCER strengths are concentrated in the possible double-GR regions.

2.4. Muon charge-exchange reactions for neutrino–nuclear responses

Muons ($\mu^{\pm}$, with mass $m_{\mu} = 105.66$ MeV) are charged heavy leptons with weak and EM interactions. They have been extensively used as massive charged particles with EM interactions to study EM responses in solid-state physics and also quarks and symmetries in particle physics. In the present subsection we discuss neutrino–nuclear responses studied by using negative muons as massive leptons for the studies of CC weak interaction. Possible usages of the muons to study nuclear weak responses are discussed in the review articles on DBDs [16,18,23] and usages to neutrino–nuclear responses in [115]. Ordinary muon capture (OMC)[1] reactions in nuclear physics are reviewed in [116].

Low-energy muon (μ^-) is trapped in one of the electron shells of the target atom, and then decays down to the lowest muon orbit in the atom. It stays there mostly for sub-μ seconds, and then decays via the weak interaction by two ways. One is the free decay into $\bar{\nu}_e + \nu_{\mu} + e$ and the other is the μ-capture reaction (mainly OMC) into the nucleus. In most medium-heavy and heavy nuclei with the atomic number $Z \geq 10$, the muon capture (MC) dominates.

2.4.1. Muon charge-exchange reactions for astro-neutrinos and DBDs

The OMC is a kind of muon charge-exchange reaction via the charged weak-boson W^+, where the muon becomes the muon neutrino and a proton in a nucleus turns to a neutron. The OMC is thus expressed as

$$_Z^A\text{X} + \mu^- \rightarrow \, _{Z-1}^A\text{X} + \nu_{\mu} \,, \tag{37}$$

where $_Z^A\text{X}$ is the target nucleus and $_{Z-1}^A\text{X}$ is the residual nucleus after the OMC. Then OMC is used to study the corresponding astro-antineutrino response for $_Z^A\text{X} + \bar{\nu}_e \rightarrow \, _{Z-1}^A\text{X} + e^+$ and the DBD β^+ response for $_Z^A\text{X} \rightarrow \, _{Z-1}^A\text{X} + \nu_e + e^+$ with $_{Z-1}^A\text{X}$ being the DBD intermediate nucleus, as discussed in Section 2.1. The muon response $B(\mu)$ is given by the OMC NME $M(\mu)$ and the spin factor $2J_i + 1$ for the initial state as

$$B(\mu) = (2J + 1)^{-1}|M(\mu)|^2 \,. \tag{38}$$

The OMC on $_Z^A\text{X}$ populates various kinds of excited states in $_{Z-1}^A\text{X}$ up to the Q value around the muon mass of 106 MeV, in principle. In real nuclei, the excitation energy extends up to around $E = 70$ MeV since excitations to higher states are suppressed by the small phase space and the small nuclear response. The transferred momentum is $p \approx 10$–40 MeV/c. The energy and the momentum are of the same order of magnitude as for the neutrinoless DBD virtual neutrinos and medium-energy supernova neutrinos. Therefore the muon responses provide useful information on the relevant DBD and supernova-neutrino responses [16,18,115] .

The excited states in the residual nucleus $_{Z-1}^A\text{X}$ decay by emitting γ rays to the ground state of $_{Z-1}^A\text{X}$ if they are particle-bound states, while they de-excite by emitting a number (x) of neutrons and/or protons if they are particle-unbound. Then the neutrino responses for the low-lying bound states are studied by measuring the γ transitions from the bound states, and those for the highly-excited states in the unbound region by measuring the emitted particles and/or the β–γ rays following the particle emissions. The OMC and decay scheme is illustrated in Fig. 17. The OMC γ-ray studies and the residual isotopes are discussed in the review article [116] and references therein.

2.4.2. Muon charge-exchange reactions for low-lying bound states

In this subsection we give a brief overview of the formalism of the OMC and calculations which are used to estimate capture rates to (low-lying) particle-bound states. In this review we do not discuss the total muon-capture rates since the review [116] is rather exhaustive in both the experimental and theoretical aspects of it. Theoretical approaches to the muon-capture problem have been devised in [117–121]. While the captures to individual states are rather complex to describe, the total capture rates are much easier to calculate [122,123]. An elegant and powerful theory formulation was introduced in Ref. [118] and there the total capture rate W was written as

$$W = 4P(\alpha Z m'_{\mu})^3 \frac{2J_f + 1}{2J_i + 1} \left(1 - \frac{q}{m_{\mu} + AM}\right) q^2 \,, \tag{39}$$

where A is the mass number of the initial and final nuclei, Z the atomic number of the initial nucleus[2], and $m'_{\mu} = AMm_{\mu}(m_{\mu} + AM)^{-1}$ the reduced muon mass. Furthermore, α denotes the fine-structure constant, M the average nucleon mass, $m_{\mu} = M_{\mu} - B_K$ is the muon mass M_{μ} corrected for the binding energy B_K of the μ-atomic K orbit, and q the

---

[1] To make a difference with the radiative muon-capture processes.

[2] Since the muon in μ-atomic K orbit penetrates the nucleus an effective value of Z should be used [117,118].
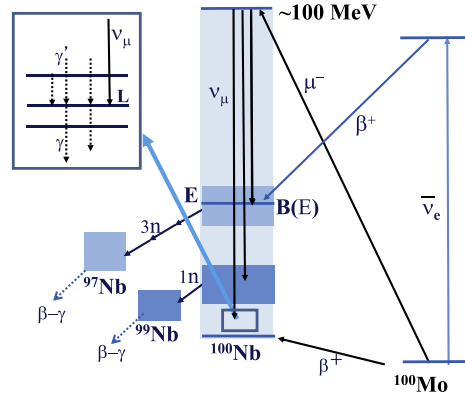
Fig. 17. CC excitation and neutron-emission scheme for OMC on ^{100}Mo. The low-lying states in ^{100}Nb decay by emitting γ rays to the ground state of ^{100}Nb. The highly-excited states around 30 MeV decay by emitting 3 neutrons and γ rays to the ground state in ^{97}Nb. Inset: excitation of a low-lying state (L) by OMC (ν_μ), γ decay (γ') to L, and γ decay (γ) from L.

muon-neutrino momentum. The term P contains the OMC NMEs, and can be written as

$$
\begin{aligned}
P = \sum_{\kappa u} \Big| & g_V \mathcal{M}[0lu] S_{0u}(\kappa)\delta_{lu} - \\
& + g_A \mathcal{M}[1lu] S_{1u}(\kappa) - \frac{g_V}{M}\mathcal{M}[1\bar{l}up] S'_{1u}(-\kappa) + \\
& + \sqrt{3}\frac{g_V q}{2M}\left(\sqrt{(\bar{l}+1)/(2\bar{l}+3)}\mathcal{M}[0\bar{l}+1u+]\delta_{\bar{l}+1,u} + \right. \\
& \left. + \sqrt{\bar{l}/(2\bar{l}-1)}\mathcal{M}[0\bar{l}-1u-]\delta_{\bar{l}-1,u}\right) S'_{1u}(-\kappa) + \\
& + \sqrt{\frac{3}{2}}\frac{g_V q}{M}(1-\mu_p-\mu_n)\left(\sqrt{\bar{l}+1}W(11u\bar{l},1\bar{l}+1)\mathcal{M}[1\bar{l}+1u+] + \right. \\
& \left. + \sqrt{\bar{l}}W(11u\bar{l},1,\bar{l}-1)\mathcal{M}[1,\bar{l}-1u-]\right) S'_{1u}(-\kappa) + \\
& - \frac{g_A}{M}\mathcal{M}[0\bar{l}up]S'_{0u}(-\kappa)\delta_{\bar{l}u} + \sqrt{\frac{1}{3}}\frac{(g_P-g_A)q}{2M}\times \\
& \times \left(\sqrt{\frac{\bar{l}+1}{2\bar{l}+1}}\mathcal{M}[1\bar{l}+1u+] + \sqrt{\frac{\bar{l}}{2\bar{l}+1}}\mathcal{M}[1\bar{l}-1u-]\right)\times \\
& \times S'_{0u}(-\kappa)\delta_{\bar{l}u}\Big|^2 ,
\end{aligned}
\tag{40}
$$

where $W(\dots)$ are the usual Racah coefficients, and the definitions for $\bar{l}$, the matrix elements $\mathcal{M}[kwu\binom{\pm}{p}]$ and the geometric factors $S_{ku}(\kappa)$ and $S'_{ku}(-\kappa)$ can be found in [118,124]. The coefficients g_V and g_A are the usual (effective) weak vector and axial–vector couplings. The CVC and PCAC hypotheses dictate for a free nucleon the values $g_V(0) = 1.00$ and $g_A(0) = 1.27$ at zero-momentum transfer and the dipole approximation [see Section 1.2, Eq. (10)] can be used for finite momentum transfer. For the induced pseudoscalar coupling g_P the Goldberger–Treiman relation [44] gives $g_P/g_A = 7.0$. The OMC Q value (momentum of the emitted muon neutrino) can be obtained from

$$
q = (m_\mu - W_0)\left(1 - \frac{m_\mu - W_0}{2(M_f + m_\mu)}\right) ,
\tag{41}
$$

where $W_0 = M_f - M_i + m_e + E_X$. Here M_f and M_i are the nuclear masses of the final and initial nuclei, and E_X is the excitation energy of the final-state nucleus.

Calculations for different mass regions of nuclei have been done along the years. In Table 1 a list of these calculations is given. The muon-capture transitions can be used to probe the right-leg (the β^+ side) virtual transitions of $0\nu\beta\beta$ decays and the value of the particle–particle interaction parameter g_{pp} of the pnQRPA (see Section 3.1.1), as discussed in [147–149]. The muon capture can also give information on the in-medium renormalization of the axial current (9) in the form of an effective g_A [132,139,141,150] and an effective g_P (in fact in most cases the ratio g_P/g_A) [119–121,127,128,135,137–143] at high (100 MeV) momentum transfers, relevant for the studies of virtual transitions of the $0\nu\beta\beta$ decays. A recent review on the renormalization of g_P is given in [151].

Table 1
List of OMC calculations of captures to low-lying bound states in nuclei.

Mass range	References
$A \leq 20$	[119,125–134],
	[135–137]
$A = 23 - 40$	[120,121,124,134,138–145]
$A = 36 - 62$	[134,145–147]
$A \geq 76$	[134,145,147–149]
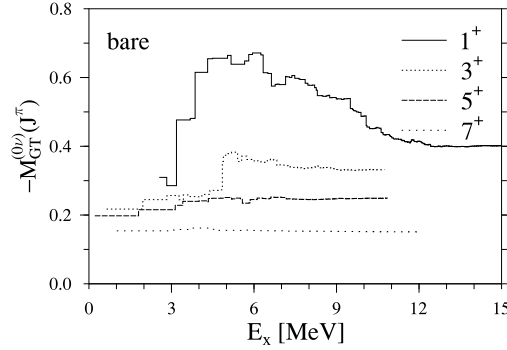
Fig. 18. Cumulative sums of the individual contributions, at energies E_x (excitation energy in the nucleus ^{48}Sc), to the multipole NMEs $M_{GT}^{0\nu}(J^\pi)$ for $J^\pi = 1^+, 3^+, 5^+, 7^+$. The word "bare" refers to the bare Gamow–Teller transition operator without contributions from core polarization and meson-exchange currents (see [147]).

As mentioned in Section 2.4.1, the OMC can be used as a probe for the $0\nu\beta\beta$ decays since the momentum exchanges in the two processes are of the same order of magnitude. The $0\nu\beta\beta$ NME can be decomposed in the form

$$M^{0\nu} = \sum_{J^\pi} M^{0\nu}(J^\pi), \tag{42}$$

where the multipole NMEs $M^{0\nu}(J^\pi)$ correspond to different multipole states J^π of the intermediate nucleus. Each of these NMEs consists of contributions stemming from the individual J_k^π states, at energy $E(J_k^\pi)$, where k denotes the kth state of multipolarity J^π in the intermediate nucleus. Summing these contributions over k gives the total multipole NME. In Fig. 18 a running sum of these individual k contributions is given as a cumulative $0\nu\beta\beta$ double Gamow–Teller NME (see Section 1.4, Eqs. (14) and Eqs. (15)) for the $0\nu\beta\beta$ decay of ^{48}Ca. The contributions are given as functions of the excitation energy in the intermediate nucleus ^{48}Sc. The intermediate-state wave functions have been calculated by using the ISM (interacting shell model, see Section 3.1.1) using the FPBP interaction [152] in the $1p - 0f$ single-particle space. In this space one can only construct positive-parity states (here $1^+ - 7^+$) and four of the contributions, $J^\pi = 1^+, 3^+, 5^+, 7^+$, are shown in the figure. It is seen that the 1^+ contributions are the largest having a saturation at around $\left| M_{GT}^{0\nu}(1^+) \right| \approx 0.4$.

In Fig. 19 a comparison of the contributions to the multipole NMEs $\left| M_{GT}^{0\nu}(J^\pi) \right|$, $J^\pi = 1^+, 2^+, 3^+, 4^+$, and the OMC rates to the same intermediate states has been performed. The comparison has been done in arbitrary units just to show that both the multipole NMEs and the OMC rates gather strong contributions from the same intermediate states in the nucleus ^{48}Sc. This means that the OMC can be used as a powerful probe of the strong intermediate contributions to the $0\nu\beta\beta$ NME (42). In other words, if a nuclear theory can predict the experimental OMC distribution it may also predict well the contributions to the $0\nu\beta\beta$ NME.

Finally, in Fig. 20, the ISM-computed capture rates to the low-lying $J^\pi = 1^+, 2^+, 3^+, 4^+$ states in ^{24}Na are shown. The ISM was used to compute also the energy spectrum in ^{24}Na and the rate of the Gamow–Teller decay from the first 1^+ state in ^{24}Na to the ground state of ^{24}Mg. Both the computed energy spectrum and the β-decay rate are in good agreement with the data. It is seen that the by far strongest capture branch is the OMC to the second 1^+ state. The corresponding experimental OMC rates will be measured at RCNP, Osaka.

Experimentally, neutrino responses for low-lying bound states are studied by measuring the emitted γ rays [153,154], as shown in the inset of Fig. 17. However, the low-lying states are populated not only directly by the OMC, but also by γ' decays from higher bound states excited by the OMC, and an accurate correction for the contributions from the higher states is hard to achieve in practice. Extensive studies of OMC γ rays from and to individual low-lying states are under progress by using the CAGRA γ-detector array at RCNP.

2.4.3. Muon-capture strength distributions and muon-capture giant resonances

The muon capture (MC) on $_Z^A$X populates excited states in a wide excitation region of the residual nucleus $_{Z-1}^A$X. They de-excite by emitting γ rays to the ground state of $_{Z-1}^A$X or by emitting the 1st neutron to a state in a nucleus $_{Z-1}^{A-1}$X, depending on
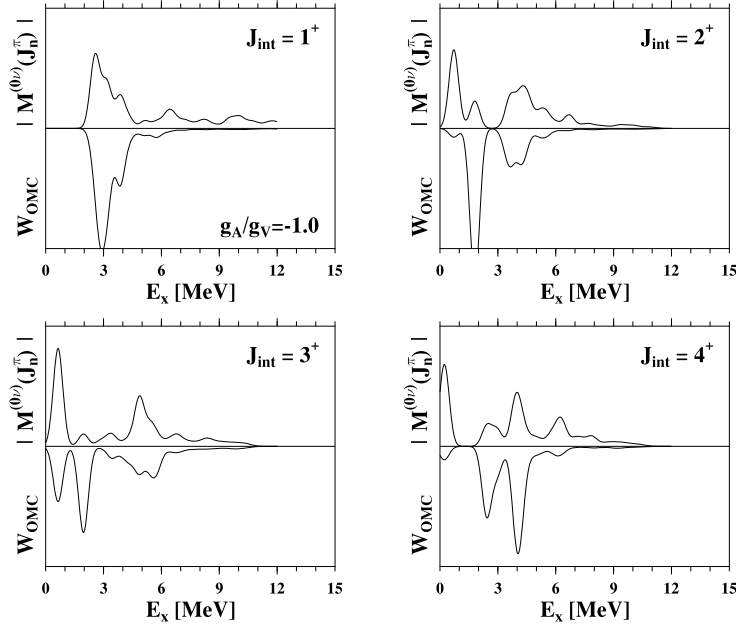
Fig. 19. Upper panels: Contributions to the multipole NMEs $\left|M_{GT}^{0\nu}(J^\pi)\right|$ for the intermediate states $J^\pi = 1^+, 2^+, 3^+, 4^+$ as functions of the excitation energy E_x in the nucleus ^{48}Sc. Lower panels: The OMC rates W_{OMC}, Eq. (39), to the low-lying states of the excitation energy E_x in the nucleus ^{48}Sc. A Gaussian smoothing of the $J^\pi = 1^+, 2^+, 3^+, 4^+$ contributions to the multipole NMEs and the OMC rates has been applied and arbitrary units are used for the NME and OMC-rate values. The values $g_A/g_V = 1.00$ and $g_P/g_A = 7.0$ were adopted in the calculations [147].
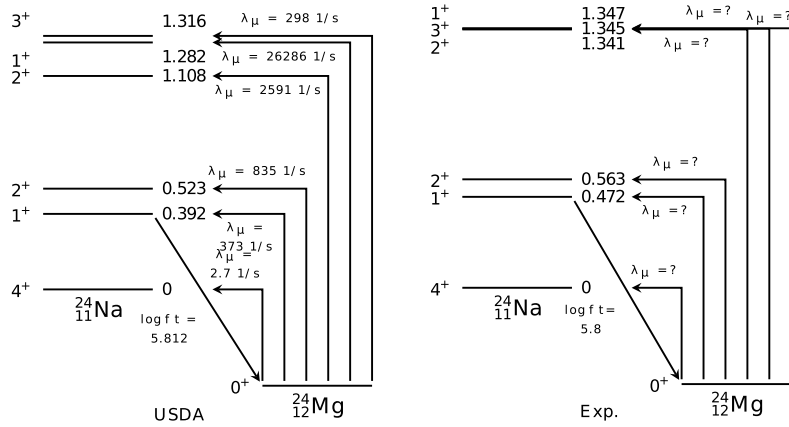
Fig. 20. OMC on ^{24}Mg. Shown are the ISM-calculated OMC rates to individual low-lying $1^+, 2^+, 3^+$ and 4^+ states in ^{24}Na (left panel). The computed excitation energies in ^{24}Na and the computed $\log ft$ of the Gamow–Teller $1_1^+ \rightarrow 0^+$ transition are compared with the available data (right panel). The values $g_A/g_V = 1.00$ and $g_P/g_A = 7.0$ were adopted in the calculations.

whether the excitation energy is below or above the 1st neutron-emission threshold energy. The residual nucleus $_{Z-1}^{A-1}$X, after the first neutron emission, de-excites by emitting γ rays to the ground state of $_{Z-1}^{A-1}$X or by emitting a 2nd neutron, depending on whether the excitation energy is below or above the 2nd neutron-emission threshold-energy, and so on. Then, one finally ends up with the residual isotopes of $_{Z-1}^{A-x}$Y with $x = 0,1,2,3, \ldots$, depending on the excitation energy E and the number x of the emitted neutrons, as shown in Fig. 17. Here proton emissions are suppressed by the Coulomb barrier in medium-heavy and heavy nuclei.

The neutron-number (x) and the mass-number $(A-x)$ distributions reflect the strength distribution $B(\mu, E)$ in the nucleus $_{Z-1}^{A}$X* after the MC [155]. The residual nucleus $_{Z-1}^{A-x}$X is identified by measuring prompt γ rays in $_{Z-1}^{A-x}$X and/or delayed γ rays from $_{Z-1}^{A-x}$X if it is radioactive.

The MC on ^{100}Mo was studied at the MuSIC beam channel at RCNP and the D2 beam channel in J-PARC MRL [156,157]. The nucleus ^{100}Mo is one of DBD nuclei, and is used also for solar- and supernova-neutrino studies [16,18,158,159]. The delayed γ-ray characteristics of the residual radioactive isotopes of $^{100-z}$Nb were measured as illustrated in Fig. 21 [156].
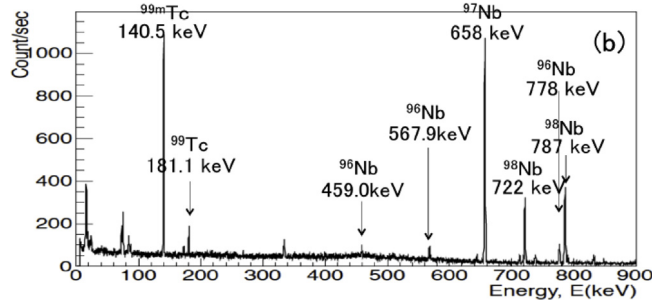
Fig. 21. Energy spectrum of delayed γ rays from long-lived Nb residual isotopes (RIs) produced by MC on ^{100}Mo [156].
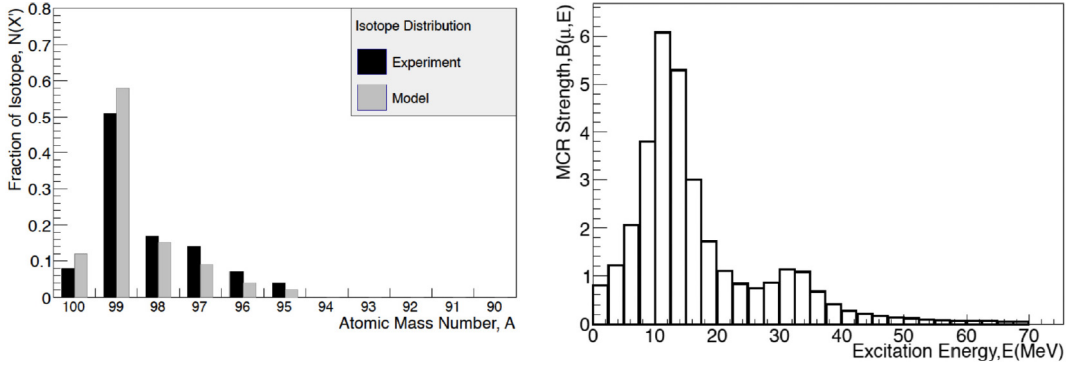
Fig. 22. Left side: Nb residual-isotope (RI) mass distribution for MC on ^{100}Mo. The black and gray histograms are the experimental and calculated relative yields. Right side: The MC strength distribution extracted from the experimental RI distribution. GR1 and GR2 are the MC GRs at around 11–14 MeV and 25–35 MeV [156].

The number of the Nb residual isotopes (RIs) $^{100-x}$Nb produced by the MC on ^{100}Mo was evaluated from the observed γ-ray yields. The RI-mass ($A - x$) distribution with x being the number of neutrons emitted from ^{100}Nb is shown in Fig. 22. The $^{100-x}$Nb yield at $x = 0$ is small, but jumps up at $x = 1$, and decreases gradually as x increases down to the mass $A = 95$ at $x = 5$.

MC excitations are expressed in terms of the vector excitations with the spin transfers of $\Delta J^\pi = 0^+, 1^-, 2^+$ and the axial–vector ones with $\Delta J^\pi = 1^+, 2^-$. Among them the 0^+ Fermi and the 1^+ GT excitations are reduced much since the $0\hbar\omega$ Fermi and GT excitations for the β^+ and antineutrino responses are blocked by the neutron excess in medium-heavy nuclei of the present interest.

The 1^- strength with $1\hbar\omega$ jump is considered to produce a MC GR, like the photon-capture (PC) can produce an E1 GR. The vector 2^+ and axial–vector 2^- strengths show broad GR-like distributions similarly to the IVSDR. Accordingly, the MC strength distribution $B(\mu, E)$ can be written as a sum of the two GR strengths of $B_1(\mu, E)$ and $B_2(\mu, E)$:

$$B(\mu, E) = B_1(\mu, E) + B_2(\mu, E), \tag{43}$$

$$B_i(\mu, E) = \frac{B_i(\mu)}{(E - E_{\text{GR}i})^2 + (\Gamma_i/2)^2}, \tag{44}$$

where E is the excitation energy, $E_{\text{GR}i}$ and Γ_i with $i = 1,2$ are the GR energy and the width for the ith GR.

The neutron-unbound state decays by emitting neutrons in the pre-equilibrium (PEQ) and equilibrium (EQ) stages [29]. The spectrum of the first neutron is expressed as

$$S(E_n) = k\left[E_n\exp\left(-\frac{E_n}{T_{\text{EQ}}(E)}\right) + pE_n\exp\left(-\frac{E_n}{T_{\text{PEQ}}(E)}\right)\right], \tag{45}$$

where E_n is the neutron kinetic energy, $T_{\text{EQ}}(E)$ and $T_{\text{PEQ}}(E)$ are the EQ and PEQ nuclear temperatures and p is the fraction of the PEQ-neutron emission. The neutron emission from the EQ stage is a kind of neutron evaporation from the thermal equilibrium phase. The EQ temperature is expressed as $T_{\text{EQ}}(E) = \sqrt{E/a}$ with a being the level-density parameter [29]. After the 1st neutron emission, neutrons are emitted at the equilibrium stage if the residual state is neutron-unbound. The observed RI mass-distribution is consistent with a calculation based on the MC strength distribution and the EQ/PEQ neutron-emission model. The MC GR1 energy is given as $E_{\text{G1}} \approx 33A^{-1/5}$ MeV.

MCs in other nuclei have been studied as discussed in the review papers [116,151]. The one-neutron emission is dominant in most MCs, being consistent with the observations on ^{100}Mo and with the strong population of the MC GR1. In other words, the dominance of the residual isotope of $^{A-1}_{Z-1}$X by one neutron emission reflects and supports the strong excitation of the GR1 around 12 MeV.

The RCNP MuSIC DC-muon beam and the J-PARC MLF pulsed-muon beam are promising for further studies of MC nuclear responses. Proton emission takes place, as well, in medium-heavy and heavy nuclei after several neutron emissions if the proton binding energy becomes lower than the neutron binding energy, and also in light nuclei where the Coulomb barrier gets lower. The MC lifetime measurements provide the absolute MC strength (square of the absolute MC NME). The absolute MC response, together with the MC strength distribution, helps theories to better evaluate the β^+ NMEs associated with the neutrinoless DBDs and the NMEs related to astro-antineutrinos.

2.5. Electromagnetic transitions and photo-nuclear reactions

EM interactions are given in terms of τ, σ and multipole operators, like the NC and CC weak interactions. Therefore, EM photon probes are well suited for studying neutrino–nuclear (weak) responses for astro-neutrinos and DBDs, as discussed in the review articles [16,18]. The EM and weak interactions and their transitions in nuclei are well described in [1,4,28,29,160] and references therein. We discuss in this subsection the EM transitions and the photo-nuclear reactions via IAS to study nuclear responses for astro-neutrinos and DBDs.

2.5.1. Electromagnetic interactions for neutrino–nuclear responses

The nuclear EM transitions and photo-nuclear reactions have the following specific features for studying neutrino–nuclear responses:

(i) The EM and weak interactions are fundamental interactions based on the electro-weak SU(3)×U(1) framework. The EM transition rates and the photo-nuclear cross sections are many orders of magnitude stronger than those of the weak interactions. It is realistic to carry out high-precision experiments of the EM transitions and the photo-nuclear reactions, while experiments with the weakly-interacting neutrino probes are hard, as discussed in Section 2.6.

(ii) The EM interaction is well known and the transition operator is expressed by the simple τ, σ and multipole operators. The lowest-multipole transition is dominant because of the long-wave-length nature of the photon. These features are different from the case of the nuclear probes, as discussed in Section 2.3.

(iii) High-intensity photons with linear and circular polarizations are available from polarized laser photons scattered off GeV electrons. High energy-resolution high-efficiency photon detectors are used for studying the EM transitions. The weak vector and axial–vector responses are studied by measuring electric and magnetic γ transitions, respectively.

(iv) EM transitions and photo-nuclear reactions via IAS provide unique opportunities for studying analogous weak transitions as discussed in [161] and these processes have been studied experimentally in several works [162–164]. Recently, photo-nuclear reactions via IAS are discussed theoretically to study DBD NMEs [165].

The weak transition operators to be studied by the EM transitions are expresses as [1,4,165],

$$T(VL) = g_V \tau^i r^L \mathbf{Y}_L,$$ (46)

$$T(AVL) = g_A \tau^i r^{L-1} \big[\boldsymbol{\sigma} \mathbf{Y}_{L-1}\big]_L,$$ (47)

where $T(VL)$ and $T(AVL)$ are the vector and axial–vector transition operators, respectively, and g_V and g_A are the vector and axial–vector couplings, respectively. Furthermore, L is the multipolarity, and the isospin operator is $\tau^i = \tau^3$ for the NC interactions and $\tau^i = \tau^\pm$ for the CC interactions. The square brackets denote angular-momentum coupling. Here we consider the unique axial–vector transition with the multipole L composed by the spin 1 and the orbital angular momentum $L - 1$.

The EM transition operators are expressed as

$$T(EL) = g_{EL} r^L \mathbf{Y}_L,$$ (48)

$$T(ML) = g_S r^{L-1}\big[\boldsymbol{\sigma}\mathbf{Y}_{L-1}\big]_L + g_l r^{L-1}\big[\mathbf{j}\mathbf{Y}_{L-1}\big]_L,$$ (49)

$$g_S = \frac{e\hbar}{2Mc}[L(L+1)]^{1/2}\left[\frac{g_s}{2} - \frac{g_l}{L+1}\right], \quad g_L = \frac{2g_l}{L+1},$$ (50)

where g_i with $i = EL, S$ and L are the effective charge, the effective spin g factor and the effective orbital g factor, respectively. The effective charge and g factors depend on the nucleon isospin τ^3, $\tau^3 = 1/2$ for neutron and $\tau^3 = -1/2$ for proton. In the second term of Eq. (49) $\mathbf{j} = \mathbf{l} + \mathbf{s}$ is the total angular momentum (sum of the orbital angular momentum and spin) and in case of spin-stretched transitions, $J_i \rightarrow J_f = J_i \pm 1$, it vanishes. Then we get good correspondence between the weak and EM transition operators in the case of one-body operators. Note this is not so if two-body operators are involved, such as in the case of the meson-exchange currents. GT $T(AV1)$, first-forbidden $T(V1)$ and unique first-forbidden $T(AV2)$ weak NMEs are
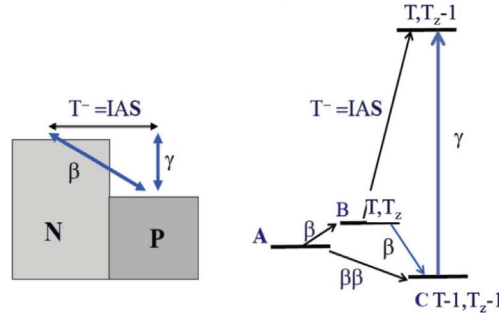
Fig. 23. Photo-nuclear reaction via IAS and DBD β transition schemes. A, B, and C are the DBD initial, intermediate and final states, respectively. The photo-nuclear reaction on C proceeds via IAS of B. T and T_z are the isospin and its third component in the state B.

derived from TM1, T(E1) and T(M2) γ-transition NMEs, respectively. The EM couplings g_i with $i = $ EL, S and L are expressed by using the isovector(τ^3) and isoscalar($\tau^0 = 1$) EM couplings as

$$g_i = \frac{g_i(\text{IV})}{2}\tau^3 + \frac{g_i(\text{IS})}{2}\tau^0, \tag{51}$$

where $g_i(\text{IV})$ and $g_i(\text{IS})$ are the effective isovector and isoscalar EM couplings, respectively. Experiments on the EM transition rates and the photo-nuclear cross sections provide the EM and the corresponding weak NMEs to help evaluate and verify the relevant neutrino responses.

2.5.2. Electromagnetic transitions and photo-nuclear reactions via IAS

EM transitions and photo-nuclear reactions via IAS are used to selectively study the isovector component of the EM NMEs, which are analogous to the weak (neutrino) interaction NMEs [162,163]. The weak (β) and EM (γ) NMEs are related by

$$\langle f|g_{\text{W}}m^\beta|i\rangle \approx \frac{g_{\text{W}}}{g_{\text{EM}}}K\langle f|g_{\text{EM}}m^\gamma|\text{IAS}\rangle, \tag{52}$$

where g_{W} is the weak coupling for a free nucleon and g_{EM} is its electromagnetic coupling. The β^+-side CC NME associated with DBD and astro-$\bar{\nu}$ responses is obtained by measuring the analogous EM γ NME from the IAS, as shown in Fig. 23.

The IAS in a medium-heavy nucleus is located in the same energy region as the broad E1 GR. Thus the IAS appears as IAR (isobaric analogue resonance) in the E1 GR region. Then the cross section is written as [162–164]

$$\frac{d\sigma}{d\Omega} = K|A_J^{\text{I}}|^2 + \Sigma_{J'}|A_{J'}^{\text{GR}}|^2 + 2\text{Re}(A_J^{\text{I}}A_J^{\text{GR}}), \tag{53}$$

where K is a kinematical factor, A_J^{I} is the IAR amplitude with J being the IAR spin, $A_{J'}^{\text{GR}}$ is the E1 GR amplitude with spin J' and $2\text{Re}(A_J^{\text{I}}A_J^{\text{GR}})$ is the interference term. The E1 GR contributions are corrected for to get the IAR component from the cross section. The IAR cross section at an energy E is given as

$$\frac{d\sigma}{d\Omega} = k(2J + 1)\frac{\Gamma_p\Gamma_\gamma}{(E - E_r)^2 + (\Gamma_t)^2/4}, \tag{54}$$

where Γ_p, Γ_γ and Γ_t are the proton, γ and total widths, respectively, and E_r is the IAR resonance energy.

Non-unique first-forbidden β decays with $\Delta J = 1$ include 3 NMEs: $M(\mathbf{r})$, $M(\mathbf{p}_e)$ (the velocity component) and $M(\boldsymbol{\sigma} \times \mathbf{r})$ [27], see operators in (96). Among them, $M(\mathbf{r})$ is derived from the IAS E1-γ NME M_{I}(E1), which is obtained by measuring the γ decay or the photo-nuclear reaction via the IAS.

The NME $M(\mathbf{r})$ for the first-forbidden transition of ^{141}Ce $\rightarrow$ ^{141}Pr was obtained by measuring the E1-γ transition from the IAS of ^{141}Ce [162,163]. Here the IAS is excited by the proton-capture reaction as a resonance (IAR) in the continuum region. The IAS EI-γ and the first-forbidden β transitions are schematically shown in Fig. 24.

The measured cross section was analyzed in terms of the IAR and E1 GR terms to obtain the γ width Γ_γ. The γ width is written in terms of the E1 NME M_{IA}(E1) as

$$\Gamma_\gamma = \frac{16\pi}{9}\left(\frac{E_\gamma}{\hbar c}\right)^3 e^2 B(\text{E1}); \quad B(\text{E1}) = \frac{1}{2J_i + 1}|M_{\text{IA}}(\text{E1})|^2, \tag{55}$$

where E_γ is the γ-ray energy and $J_i = 7/2$ is the IAR spin. The obtained γ NME is M_{IA}(E1) $= 0.18 \pm 0.2$ fm. Then the corresponding β NME is obtained by correcting for the isospin factor of $(2T)^{1/2} = 5$ as $M(r) = 0.9 \pm 0.2$ e fm.

The β NME is expressed on the basis of the ξ approximation of $\xi = \alpha Z/2R \gg E_\beta$ as

$$g_{\text{V}}M(\beta) = -g_{\text{V}}M(\mathbf{r})\left(\Lambda - \frac{g_{\text{A}}}{g_{\text{V}}}\Lambda_1 - 1\right); \quad \Lambda = \frac{iM(\mathbf{p}_e)}{\xi M(\mathbf{r})}; \quad \Lambda_1 = \frac{iM(\boldsymbol{\sigma} \times \mathbf{r})}{M(\mathbf{r})}, \tag{56}$$
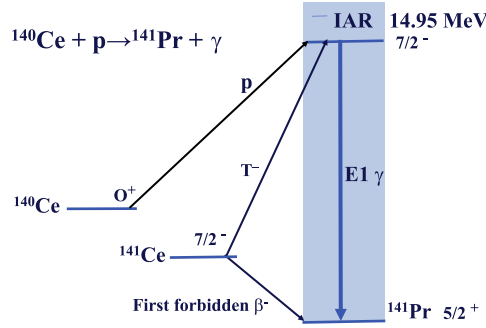
Fig. 24. Excitation of the IAS of ^{141}Ce by a proton-capture reaction on ^{140}Ce and E1 γ decay from the IAR to the ground state of ^{141}Pr [162,163].
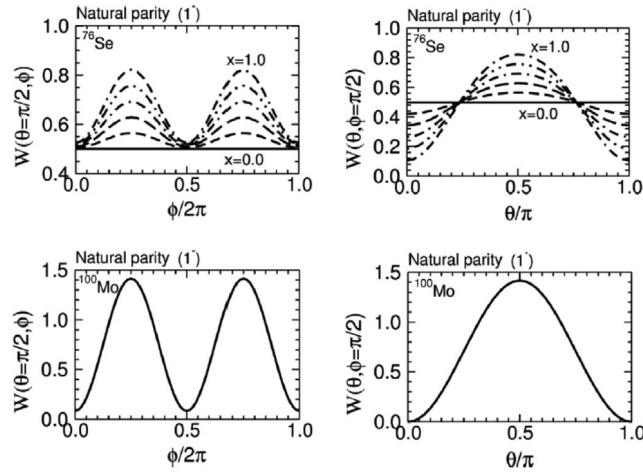
Fig. 25. Top: Angular distributions of the neutrons emitted from the photo-nuclear reactions via IARs in ^{82}Se. Bottom: As above in ^{100}Mo [165].

where $g_A/g_V = 1.27$ is the axial–vector coupling in units of the vector one, g_V. We use the experimental value $\Lambda = 2.6$ [166], which is consistent with the CVC value of $\Lambda = 2.4$. Inserting the present NME of $M(\mathbf{r}) = 0.9$ fm and the β-decay NME of $M(\beta) = 0.43$ into Eq. (56), one obtains the ratio $\Lambda = iM(\boldsymbol{\sigma} \times \mathbf{r})/M(\mathbf{r}) = 0.9$, and then the axial–vector NME of $M(\boldsymbol{\sigma} \times \mathbf{r}) = 0.8$ fm. The obtained β NME of $M(\mathbf{r})$ is reduced by coefficients of $k_{SP} = 0.21$ and $k_{QP} = 0.24$ with respect to the single-particle (SP) and quasiparticle (QP) NMEs, respectively, and $M(\boldsymbol{\sigma} \times \mathbf{r})$ is also reduced by the similar coefficients of $k_{SP} = 0.18$ and $k_{QP} = 0.21$.

The IAS E1 γ transitions were studied in other nuclei, and the IAS E1 γ NMEs and the corresponding β NMEs are shown to be reduced with respect to the QP NME by $k_{QP} \approx 0.25$ [1,4,162]. It is interesting to note that the non-unique and unique β MNEs and the E1 γ NMEs are all uniformly reduced by a coefficient around 0.20–0.25 with respect to the QP NMEs, suggesting uniform reduction effects due to the spin–isospin correlation and renormalization of the weak and EM couplings [1,4].

Nuclear responses for astro-neutrinos and DBDs are studied by measuring photo-nuclear reactions through IARs [165], as shown in Fig. 23. The IARs in DBD nuclei of current interest decay mainly by emitting one neutron. The energy-integrated cross section, being corrected for the interference with the E1 GR, is expressed as

$$\int \sigma(\gamma, n)dE = \frac{S(2J + 1)\pi^2}{k_\gamma^2} \frac{\Gamma_\gamma}{\Gamma_t} \Gamma_n ,$$ (57)

where $\sigma(\gamma, n)$ is the photo-neutron cross section, S is the spin factor, J is the IAS spin, k_γ is the photon momentum, and Γ_γ, Γ_n and Γ_t are γ, neutron and total widths, respectively. In the medium-heavy nuclei, the neutron emission dominates since the proton emission is suppressed. Then one can set $\Gamma_t \approx \Gamma_n$ and one gets Γ_γ from the integrated cross section. The EM NME is derived from the IAR Γ_γ as shown in Eq. (55).

Medium-energy polarized photons are obtained from laser photons scattered off GeV electrons. The spin and parity of the IAR are obtained from the angular distributions of the emitted neutrons with respect to the photon-polarization axis y and the direction z [165]. The distributions for E1 photo-nuclear reactions on ^{76}Se and ^{100}Mo are shown in Fig. 25. They are used to evaluate the spin–parity of the IAS and the analogous state in the intermediate nucleus B. Astro-neutrino and DBD responses for excited states in intermediate nuclei are studied by measuring photo-nuclear reactions via the IARs of the excited states.

2.6. Neutrino–nuclear reactions for neutrino–nuclear responses

Neutrino–nuclear reactions with neutrino beams are used to study neutrino–nuclear responses. The neutrino CC process is a kind of lepton CER, where the neutral lepton (neutrino) becomes a charged lepton (electron) via the charged weak-boson exchange (see Section 1.2). The neutrino CERs are free from uncertainties induced by nuclear-reaction mechanisms and nuclear interactions involved in the nuclear CERs as discussed in Section 2.3.

Neutrino CC and NC cross-sections, however, are extremely small because the gauge bosons are the heavy Z and W bosons. Therefore, one needs very intense ν and $\bar{\nu}$ beams and huge detectors to measure the neutrino reactions. The responses on ^{12}C have been studied by using the neutrino beams at the Rutherford laboratory [167] and LANL [168]. Neutrino-response studies by using intense neutrino beams extracted from high-intensity proton accelerators were discussed in [169,170], and those by using neutrinos from β beam in [171].

The neutrino reactions to be used for the NC and CC responses are

$$\nu + {}^{A}_{Z}\mathrm{X} \to \nu' + {}^{A}_{Z}\mathrm{X}_k, \quad \nu_e + {}^{A}_{Z}\mathrm{X} \to e^- + {}^{A}_{Z+1}\mathrm{X}_k, \tag{58}$$

$$\bar{\nu} + {}^{A}_{Z}\mathrm{X} \to \bar{\nu}' + {}^{A}_{Z}\mathrm{X}_k, \quad \bar{\nu}_e + {}^{A}_{Z}\mathrm{X}_k \to e^+ + {}^{A}_{Z-1}\mathrm{X}_k, \tag{59}$$

where ${}^{A}_{Z}\mathrm{X}$ is the target nucleus and ${}^{A}_{Z'}\mathrm{X}_k$ is the kth state in the residual nucleus ${}^{A}_{Z'}\mathrm{X}$.

The neutrino-reaction cross section is given as

$$\sigma_k(\alpha) = g_{\mathrm{W}}^2 K(E_\nu) F_k(E_\nu, Z') B_k(\alpha), \tag{60}$$

where g_{W} is the weak coupling for a free nucleon, $K(E_\nu)$ is a kinematic factor, E_ν is the neutrino energy, $F_k(E_\nu, Z')$ is a phase-space factor and $B_k(\alpha)$ is the α-mode response (strength) for the state k. Here the excitation modes to be considered are $\alpha =$ F(0^+), GT(1^+), D(1^-), SD(0^-, 1^-, 2^-), and so on. The NMEs are given by $M(\alpha) = [(2J+1)B(\alpha)]^{1/2}$.

Solar neutrinos are low-energy neutrinos with $E_\nu = 0.1 - 15$ MeV, while supernova-neutrino energies extend up to around $E_\nu = 40$–60 MeV, depending on the flavors and the temperatures in the neutrino spheres. The DBD is associated with virtual ν and $\bar{\nu}$ in the medium-energy region around 20–80 MeV. Accordingly, the neutrino beams used to study the nuclear responses for these neutrinos are low- and medium-energy ν and $\bar{\nu}$ beams.

The neutrino cross-sections are mainly the CC cross sections. It is given in units of cm^2 as

$$\sigma_k(\alpha) = 1.597 \times 10^{-44} p_e E_e F(Z, E_e) B_k(\alpha), \tag{61}$$

where p, E_e, and $F(Z, E_e)$ are the momentum, the total energy and the Fermi function for the electron from the CC interaction. The quantity $B_k(\alpha)$ is the α-mode response for the kth state in units of the weak vector coupling g_{V}. The Fermi and GT responses are given by

$$B_k(\alpha) = B_k(\mathrm{F}), \quad B_k(\alpha) = \left(\frac{g_{\mathrm{A}}}{g_{\mathrm{V}}}\right)^2 B_k(\mathrm{GT}), \tag{62}$$

where the axial–vector to vector coupling ratio is $g_{\mathrm{A}}/g_{\mathrm{V}} = 1.27$. The response $B_k(\mathrm{GT})$ is given as $(2J_k + 1)^{-1}|M_k(\mathrm{GT})|^2$. Thus the NME $M_k(\mathrm{GT})$, including the effective weak coupling $g_{\mathrm{A}}^{\mathrm{eff}}/g_{\mathrm{A}}$ (quenching), is derived from the observed cross section. The actual cross section for a typical GT state with $B(\mathrm{GT}) \approx 0.1$ is around 10^{-45} cm^2. Then very high-flux neutrino beams around 10^{14}/second and multi-ton-scale target isotopes are necessary for the neutrino-beam experiments.

Intense neutrino beams are obtained from $\pi - \mu$ decays. Here high-flux pions are produced by using high-intensity GeV-proton accelerators. The nuclear reaction is expressed as p + Hg $\to$ nπ^++X. Here several (n) pions are produced in addition to others mesons, nucleons and nuclei. The positive pions (π^+) stop and decay as

$$\pi^+ \to \mu^+ + \nu_\mu, \quad \mu^+ \to e^+ + \nu_e + \bar{\nu}_\mu. \tag{63}$$

Here the π^+-decay ν_μ shows a line spectrum at around 30 MeV, while the μ^+-decay ν_e and $\bar{\nu}_\mu$ show continuum spectra extending up to around 55 MeV, as shown in Fig. 26. These energy regions are just the regions of virtual neutrinos associated with the neutrinoless DBDs and astro-neutrinos. Hence, the ν_e, ν_μ and $\bar{\nu}_\mu$ beams are used to study the NC and CC nuclear responses for them.

The ν_e and $\bar{\nu}_\mu$ from the μ^+ decay are delayed by a couple of 100 nanoseconds and are separated in time from the fast component of the ν_μ and other nuclear reaction products by using pulsed proton beams [169,170,172]. A neutrino flux around 0.7×10^{15}/second is expected by using the SNS 1-GeV proton beam from the 1.6-MW accelerator [172], while neutrino beams of the order of 0.3×10^{15}/second may be obtained by using the 3-GeV proton beam from the 1-MW RCS J-PARC [170].

Low-energy antineutrinos from nuclear reactors are used for neutrino-oscillation studies. The ORNL reactor with 3 GW provides an intense $\bar{\nu}_e$ beam of around 6×10^{20}/second [172]. Natural neutrino sources such as the solar neutrinos and atmospheric neutrinos, which are used to study the neutrino oscillations and the solar nuclear reactions, are of interest for future neutrino-response studies with kilo-ton-scale detectors.

In fact, theoretical calculations for neutrino–nuclear responses on ^{12}C and on other nuclei of DBD and astro-physics interest depend much on the nuclear models, the nuclear parameters and the effective value of the axial–vector coupling g_{A}
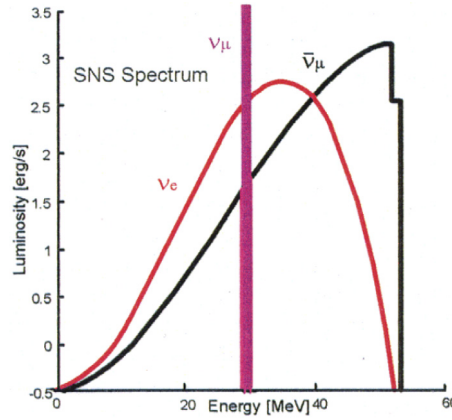
Fig. 26. Energy spectra for ν_μ from stopped π^+ decays and for ν_e and $\bar{\nu}_\mu$ from the μ^+ decay [169].

Table 2
Measured numbers of neutron holes and neutron particles in ^{76}Ge [176]. l is the orbital angular momentum [176].

l	Holes	Particles	Holes+Particles	Occupancy
1	1.12	4.83	5.97	4.87 ± 0.2
3	1.9	4.38	6.28	4.56 ± 0.4
4	3.41	6.27	9.68	6.48 ± 0.3

(see Section 4). Then direct experimental measurements of the responses by using neutrino beams are important in providing experimentally the NMEs, including the effective weak coupling [170].

2.7. Nucleon-transfer reactions for nucleon occupation and vacancy probabilities

Nucleon-transfer reactions have been used for studying valence nucleon properties such as single-QP occupancy and vacancy probabilities of V_j^2 and $U_j^2 = 1 - V_j^2$ in a j-shell orbit with j being the angular momentum. The V_j^2 and U_j^2 for quasi-neutrons are measured by using neutron-transfer (p,d) and (d,p) reactions, and those for quasi-protons by using proton-transfer (^{3}He,α), (^{3}He,d) and (α, t) reactions. They are described in the review paper [173] and references therein, as also in the recent works [174,175].

Nucleon-transfer reactions are analyzed by using a DWBA code to extract the orbital angular momentum l of the transferred nucleon and the spectroscopic factor S_F. Then one obtains $U_j^2 = \Sigma_i(S_F)^{add}/(2j+1)$ and $V_j^2 = \Sigma_i(S_F)^{rem}/(2j+1)$, where $(S_F)^{add}$ and $(S_F)^{rem}$ are the spectroscopic factors for the nucleon-adding and nucleon-removal reactions, respectively.

The V_j^2 and U_j^2 factors for the DBD nucleus ^{76}Ge are shown in Table 2 [176]. Here the V_j^2 and U_j^2 factors are given, respectively, by the ratios of the particle and hole numbers to the total number of $2j+1$, and the renormalization (quenching) factors around 0.55 are used to get $V_j^2 + U_j^2 = 1$.

The observed numbers for the holes and particles agree well with the numbers of the valence neutrons of 6 for $l = 1$ ($p_{1/2}, p_{3/2}$), 6 for $l = 3$ ($f_{5/2}$), and 10 for $l = 4$ ($g_{9/2}$). The sum of the observed occupancies is 16, which is consistent with the number of neutrons above the magic number 28. Thus the transfer reaction gives reasonable vacancy (hole) and occupancy (particle) numbers for the valence nucleons in the shell orbits, and thus are used to verify the pnQRPA and other nuclear models used for DBD NME calculations [177–183]. Actually, transfer reactions have been measured for several DBD nuclei as presented in a recent workshop [184].

The renormalization (quenching) factor to be used for getting S_F is discussed in detail in [185]. The quenching factors observed in various transfer reactions are shown against the transferred l in Fig. 27. The factors are uniformly distributed around 0.55 for all transfer reactions and transferred l values. The quenching factor is universal in a wide range $A = 16$–208 of the nuclear mass number. A similar quenching factor is found also in the EM proton knock-out reactions of (e,e'p) [186]. The universal renormalization (quenching) of the single quasi-nucleon at the nuclear surface (one major shell) is considered to be due to nucleonic and non-nucleonic correlations and nuclear medium effects. It is to be noted that similar renormalization factors around 0.5–0.6 appear in CERs and weak NMEs, as discussed in the following sections. Accurate evaluations of the short-range and other nucleonic and non-nucleonic correlations and the nuclear medium effects are important in order to understand how they affect the transfer reactions and the neutrino–nuclear responses.

In case of the $0^+ \rightarrow 0^+$ ground-state-to-ground-state DBD with (neutron pair)$\leftrightarrow$(proton pair), pairing correlations and pairing vibrations play a role in DBD NMEs. They are studied by using pair-transfer (p,t) and (t,p) reactions [187,188].
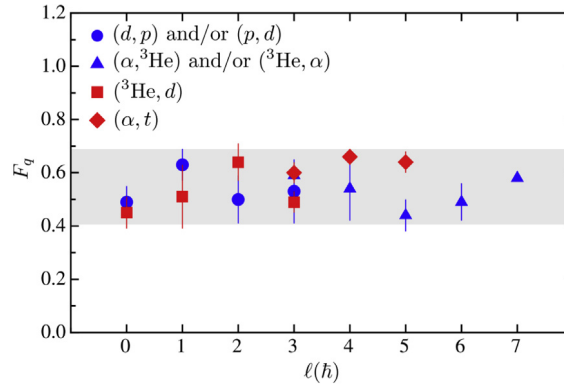
Fig. 27. Average of the quenching factor for different l transfers. The error bars stand for the rms of the spread in values. The gray band represents the $\pm 2\sigma$ deviation from the mean quenching. [185].

3. Neutrino–nuclear responses and single beta decays

The nuclear single beta decays, or simply β decays, are weak-interaction-mediated nuclear-disintegration processes where the atomic number of the decaying nucleus changes by one unit in the process. The atomic number either increases (β^- decays) or decreases (β^+ decays and/or electron captures (EC)). The processes can be schematically written as

$$^A_Z X \rightarrow \, ^A_{Z+1} Y + e^- + \bar{\nu}_e \,, \quad (\beta^- \text{decay}) \tag{64}$$

$$^A_Z X \rightarrow \, ^A_{Z-1} Y + e^+ + \nu_e \,, \quad (\beta^+ \text{decay}) \tag{65}$$

$$^A_Z X + e^- \rightarrow \, ^A_{Z-1} Y + \nu_e \,, \quad (\text{EC decay}) \tag{66}$$

where X (Y) denotes the decaying mother (resulting daughter) nucleus, e^- (e^+) is electron (positron) and ν_e ($\bar{\nu}_e$) is the corresponding neutrino (antineutrino). In the following we discuss neutrino–nuclear responses which relate to these decays and attract current interest.

3.1. The g_A problem for Gamow–Teller type of transitions

The quenching problem of the weak axial–vector coupling strength g_A has been known for several decades (see, e.g. the reviews [1,4]), mainly from the calculations of the Gamow–Teller and unique-forbidden β-decay transitions and isovector magnetic γ matrix elements in the framework of the nuclear shell model, or the interacting shell model, as it will be called in this review to distinguish it from the extreme simple non-interacting shell-model description of simple nuclear systems. The quenching factors due to spin–isospin correlations were discussed in terms of the effective weak couplings in [1,4]. Virtual Gamow–Teller transitions mediate also the two-neutrino $\beta\beta$ ($2\nu\beta\beta$) decay, so some degree of quenching is expected there as well. Below we summarize concisely the status of the quenching problem of g_A for the Gamow–Teller type of transitions in β and $2\nu\beta\beta$ decays.

3.1.1. Outline of the theory frameworks

In the analyses of the effective value of g_A the adopted many-body frameworks include the interacting shell model (ISM) [189], the quasiparticle random-phase approximation (QRPA) in its proton–neutron version, pnQRPA [19,55,190], and in its proton–proton-plus-neutron–neutron version (simply QRPA) [55,190]. To describe the odd-A nuclei a derivative of the QRPA, the microscopic quasiparticle–phonon model (MQPM) [191,192] has also been used. Also the framework of the microscopic interacting boson model (IBM-2) [193] and its odd-A version, the microscopic interacting boson–fermion model (IBFM-2) [194], have been used in the studies of the effective value of g_A. These theories have the following ingredients:

- *Many-body aspects of the ISM*: The ISM is a many-body framework that uses a limited set of single-particle states, typically one harmonic-oscillator major shell or one nuclear major shell, to describe nuclear wave functions involved in various processes. In the ISM one forms all the possible many-nucleon configurations in a given single-particle space, each configuration described by one Slater determinant, and diagonalizes the nuclear (residual) Hamiltonian in the basis formed by these Slater determinants. In this way the many-body features are taken into account exactly but only in a restricted set of single-particle states, typically leaving out one or two spin–orbit-partner orbitals from the model space. The pnQRPA calculations [180,181] and perturbative ISM calculations [195,196] suggest that inclusion of all spin–orbit-partner orbitals in the chosen single-particle model space is called for. This has been verified in the extended

ISM calculations where the missing spin–orbit partners have been included at least in an effective way [197,198]. A particular problem with the ISM is to find a suitable (renormalized) nucleon–nucleon interaction to match the limited single-particle space. Since this space is small, the renormalization effects of the two-body interaction become substantial.

- *Many-body aspects of the pnQRPA*: The proton–neutron version of the QRPA (pnQRPA) uses two-quasiparticle excitations that are built from a proton and a neutron quasiparticle. The pnQRPA wavefunctions are created on the QRPA vacuum, $|\mathrm{QRPA}\rangle$, by the phonon operator

$$|\omega M_\omega\rangle = Q^\dagger_{\omega M_\omega}|\mathrm{QRPA}\rangle\,, \qquad (67)$$

with the phonon structure

$$Q^\dagger_{\omega M_\omega} = \sum_{pn}\left[X^\omega_{pn}[a^\dagger_p a^\dagger_n]_{J_\omega M_\omega} + Y^\omega_{pn}[\tilde{a}_p\tilde{a}_n]_{J_\omega M_\omega}\right]\,, \qquad (68)$$

where $a^\dagger_p$ ($a^\dagger_n$) are the creation operators of quasiparticles in a proton (neutron) orbital with orbital quantum numbers $p = (n_p, l_p, j_p)$ [$n = (n_n, l_n, j_n)$], (n, l, j) being the triplet of principal, orbital angular momentum and total angular momentum quantum numbers for a given orbital. The corresponding annihilation operators for protons are defined as $\tilde{a}_\pi = (-1)^{j_p+m_\pi}a_{-\pi}$ with $-\pi = (p, -m_\pi)$, where m_π is the z projection of j_p, and correspondingly for the neutrons. Here J_ω is the angular momentum of the pnQRPA state and M_ω is its projection on the laboratory z axis. The sum in Eq. (68) runs over all possible proton–neutron configurations in the adopted valence space. The amplitudes X^ω and Y^ω can be found by solving the pnQRPA equations presented in [55].

The construction (67) enables description of odd–odd nuclei starting from an even–even reference nucleus where the quasiparticles are created, e.g., through the BCS procedure [55]. The advantage of the pnQRPA theory is that it can include large single-particle model spaces in the calculations: There arise no problems associated with spin–orbit-partner orbitals since they can easily be accommodated in the model space. On the other hand, the pnQRPA has a limited configuration space. Deficiencies of the pnQRPA formalism have been analyzed against the ISM formalism, e.g., in [199] by using a seniority-based scheme where the pnQRPA was considered to be a low-seniority approximation of the ISM. On the other hand, the ground-state correlations of the pnQRPA introduce higher-seniority components to the pnQRPA wave functions and the deficiencies stemming from the incomplete seniority content of the pnQRPA should not be so severe [200]. Schematic or G-matrix-based boson-exchange Hamiltonians have widely been used in the calculations. Extensions of the pnQRPA framework include the renormalized QRPA (RQRPA) [201,202] and similar "fully" renormalized schemes [203–205]. One particular problem with the pnQRPA calculations is the determination of the value of the particle–particle interaction parameter g_{pp}, used to scale the particle–particle part of the proton–neutron two-body interaction matrix elements [206,207]. The particle–hole parameter, g_{ph}, of the proton–neutron two-body interaction is usually determined by adjusting the parameter such that the phenomenological or experimental energy of the Gamow–Teller giant resonance is reproduced [208,209].

It should be noted here that the previous discussion pertains to the spherical form of the QRPA but most of the remarks are valid also for the deformed QRPA frameworks. Many of the double-beta-decaying nuclei (e.g., ^{150}Nd) are more or less deformed so that the use of a deformed QRPA framework would be preferable. The deformation effects, as also the associated overlap problem, are discussed in Section 5.3.6.

- *Many-body aspects of the MQPM*: The microscopic quasiparticle–phonon model (MQPM) is intended to description of states of odd-*A* nuclei starting from the adjacent even–even reference nuclei. The MQPM states are generated by combining proton or neutron one-quasiparticle excitations of the reference nucleus with three-quasiparticle excitations built by coupling a proton or neutron quasiparticle to a QRPA phonon. A QRPA phonon is a proton–proton-plus-neutron–neutron excitation of an even–even reference nucleus in the form

$$|\omega' M_{\omega'}\rangle = Q'^\dagger_{\omega' M_{\omega'}}|\mathrm{QRPA}\rangle\,, \qquad (69)$$

with the phonon structure

$$Q'^\dagger_{\omega' M_{\omega'}} = \sum_{a\leq b}\left[X^{\omega'}_{ab}N_{ab}(J_{\omega'})[a^\dagger_a a^\dagger_b]_{J_{\omega'} M_{\omega'}} + Y^{\omega'}_{ab}N_{ab}(J_{\omega'})[\tilde{a}_a\tilde{a}_b]_{J_{\omega'} M_{\omega'}}\right]\,, \qquad (70)$$

where the indices a, b run over all two-proton and two-neutron configurations within the chosen valence space, so that none of them is counted twice. N_{ab} is a normalization constant and the $X^{\omega'}_{ab}$ and $Y^{\omega'}_{ab}$ are amplitudes that can be solved from the QRPA equation of motion [55].

The MQPM creation operator creates a state $|kjm\rangle$ in an odd-*A* nucleus by the action

$$|kjm\rangle = \Gamma^\dagger_k(jm)|\mathrm{QRPA}\rangle\,, \qquad (71)$$

with the operator structure

$$\Gamma^\dagger_k(jm) = \sum_n X^k_n a^\dagger_{njm} + \sum_{a\omega'} X^k_{a\omega'}[a^\dagger_a Q'^\dagger_{\omega'}]_{jm}\,, \qquad (72)$$
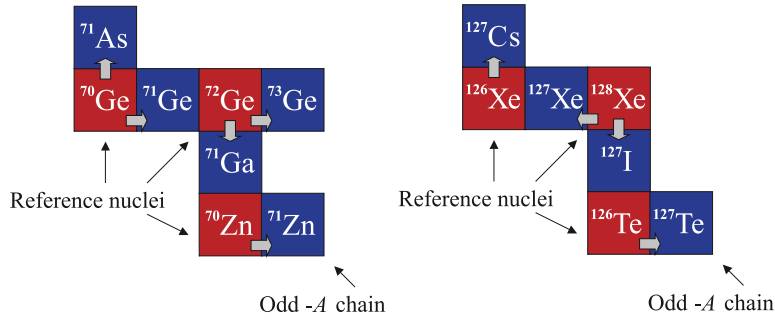
Fig. 28. Application of the MQPM procedure to description of states of odd-*A* germanium, gallium and iodine nuclei.

where Q' is the QRPA creation operator (70). Since the MQPM states (72) contain the three-quasiparticle components special care should be taken when solving the MQPM equations of motion for the amplitudes X_n^k and $X_{a\omega'}^k$ in order to handle the over-completeness and non-orthogonality of the quasiparticle–phonon basis. For details see [192].

Examples of the use of the MQPM are given in Fig. 28 for the solar-neutrino detectors based on ^{71}Ga [210] (left panel) and ^{127}I [211] (right panel). In the left panel the nucleus ^{71}Zn decays by β^- transitions to the ground state and excited states of ^{71}Ga, and the nucleus ^{71}Ge decays by electron capture to the ground state of ^{71}Ga. In the right panel the nucleus ^{127}Te decays by β^- transitions to the ground state and excited states of ^{127}I, and the nucleus ^{127}Xe decays by β^+/EC (electron capture) to the ground state and excited states of ^{127}I. Here the case of ^{71}Ga is particularly interesting due to the so-called "gallium anomaly" in the solar-neutrino scattering off ^{71}Ga to low-lying states in ^{71}Ge. The discrepancies associated with the comparison of the calculated and measured neutrino-scattering cross sections will be discussed in Section 4.4.4.

- *Many-body aspects of the IBM-2*: The interacting boson model (IBM) is a theory framework based on *s* and *d* bosons which have as their microscopic paradigms the 0^+ and 2^+ angular-momentum-coupled collective fermion pairs present in nuclei. An extension of the IBM is the microscopic IBM (IBM-2) where the proton and neutron degrees of freedom are explicit. The IBM-2 is a kind of phenomenological version of the ISM, containing the seniority aspect and the restriction to one magic shell in terms of the single-particle model space. The Hamiltonian and the transition operators are constructed from the *s* and *d* bosons as lowest-order boson expansions with coupling coefficients to be determined by fits to experimental data on low-lying energy levels and E2 γ transitions associated with the *s* and *d* bosons, but the fitting does not use the spin or isovector data available from β decays. One can also relate the bosons to the underlying fermion model space through a mapping procedure [212,213].

  The microscopic IBM can be extended to include higher-multipole bosons, like *g* bosons, as well. Further extension concerns the description of odd-*A* nuclei by the use of the microscopic interacting boson–fermion model (IBFM-2) [194]. The IBM concept can also be used to describe odd–odd nuclei by using the interacting boson–fermion–fermion model (IBFFM) and its proton–neutron variant, the proton–neutron IBFFM (IBFFM-2) [214]. Here the problems arise from the interactions between the bosons and the one or two extra fermions in the Hamiltonian, and from the transition operators containing a host of phenomenological parameters to be determined in some meaningful way.

  Recently a method was developed to calculate the IBM-2 occupancies of single-particle levels in nuclei [182]. This method was applied to calculate the occupancies in several nuclei of interest for $0\nu\beta\beta$ decay. An interesting study in the framework of the interacting boson model was carried out [215]. In this work it was examined whether neutron–proton pairing should be explicitly included as neutron–proton bosons in the IBM calculations of $0\nu\beta\beta$-decay NMEs.

The impact of the quenching of g_A on the half-lives of neutrinoless double beta ($0\nu\beta\beta$) decay has recently been discussed in the pnQRPA theory framework in Ref. [216]. The related decay rates are affected by the available phase space (Q values), the nuclear matrix elements (NMEs) and the value of g_A in its fourth power[3] [2,21,23,24]. In its simplest, in the light-neutrino mass mode (see Section 5), the $0\nu\beta\beta$ decay is mediated by light Majorana neutrinos and the measurements of the related half-lives offer access to the absolute mass scale of the neutrinos [2,23]. Quite a large number of nuclear models, including configuration-interaction based models like the ISM, pnQRPA and IBM-2 (Section 3.1.1), and various mean field models, have been adopted for the calculations [19,20,24] of $0\nu\beta\beta$ observables.

Lately some attention has been paid to the possible (large) quenching of g_A and its possibly strong impact on the sensitivities of the present and planned $0\nu\beta\beta$-decay experiments [16,18,30,216]. This deviation (quenching or sometimes enhancement) from the free-nucleon value $g_A = 1.27$ can arise from the *nuclear medium effects* and/or the *nuclear many-body effects*. The former contain quenching related to the presence of spin-multipole giant resonances [217], non-nucleonic degrees of freedom (like the Δ isobar [218,219]) and meson-exchange-related two-body weak currents [220–222]. The latter

---

[3] Actually, the dependence is exactly fourth power only if the Fermi NME is neglected. In practice, the Fermi NME is roughly one third of the Gamow–Teller one so that the dependence is not exactly fourth power.

Table 3
Mass ranges and effective values of g_A extracted from the works of the last column. For more information on the error bars etc., see the review [30].

Mass range	g_A^{eff}	Reference
Full $0p$ shell	$1.03^{+0.03}_{-0.02}$	[224]
$0p$ − low $1s0d$ shell	1.18 ± 0.05	[225]
Full $1s0d$ shell	$0.96^{+0.03}_{-0.02}$	[226] (see also [227])
	1.0	[228]
$A = 41 - 50$ ($1p0f$ shell)	$0.937^{+0.019}_{-0.018}$	[229] (see also [227])
^{48}Ca ($1s0d1p0f$ shells)	0.90	[230]
$1p0f$ shell	0.98	[228]
^{56}Ni	0.71	[228]
$A = 52 - 67$ ($1p0f$ shell)	$0.838^{+0.021}_{-0.020}$	[231]
$A = 67 - 80$ ($0f_{5/2}1p0g_{9/2}$ shell)	0.869 ± 0.019	[231]
$A = 63 - 96$ ($1p0f0g1d2s$ shell)	0.8	[232]
$A = 76 - 82$ ($1p0f0g_{9/2}$ shell)	0.76	[233]
$A = 90 - 97$ ($1p0f0g1d2s$ shell)	0.60	[234]
^{100}Sn	0.52	[228]
$A = 128 - 130$ ($0g_{7/2}1d2s0h_{11/2}$ shell)	0.72	[233]
$A = 130 - 136$ ($0g_{7/2}1d2s0h_{11/2}$ shell)	0.94	[235]
$A = 136$ ($0g_{7/2}1d2s0h_{11/2}$ shell)	0.57	[233]
$A = 136$ ($0g1d2s0h$ shell)	0.94	[198]

relates to deficiencies of the nuclear many-body approaches used to compute the wave functions involved in the decay transitions. The effective value of g_A can also depend on the energy scale of the process in question: the effective value can be different for β decays (zero-momentum-exchange limit) and $0\nu\beta\beta$ decays (high momentum exchanges, $\sim$ 100 MeV/c).

The effective value of g_A can be related to the *renormalization factor* q. In the case of quenching it is called *quenching factor*, see Section 3.1.2, and in the case of enhancement it is called *enhancement factor*, see Section 3.6.4. It is defined as the ratio

$$q = \frac{g_A}{g_A^{\text{free}}} ,\qquad(73)$$

where $g_A^{\text{free}} = 1.2723(23)$ [223] is the free-nucleon value of the axial–vector coupling as measured in neutron beta decay. Here g_A is the value of the axial–vector coupling derived from a given theoretical or experimental analysis. From (73) one can derive the *effective* value of g_A as

$$g_A^{\text{eff}} = q g_A^{\text{free}} .\qquad(74)$$

3.1.2. Quenching of g_A in Gamow–Teller beta decays

Gamow–Teller β decays are mediated by the Pauli spin operator σ [55] and they change the initial nuclear spin J_i by at most one unit in a given nuclear transition. The renormalization of g_A has long been studied for the Gamow–Teller β decays in the framework of the interacting shell model (ISM). In these calculations, reviewed in Table 3, it appears that the value of g_A is quenched, and the stronger the heavier the nucleus. The renormalization of g_A in the ISM includes all the possible sources of deficiency listed at the end of the previous section.

In Fig. 29 the results of Caurier et al. [233] (red horizontal bars indicating the mass range) and other ISM calculations are contrasted against those obtained by the use of the proton–neutron quasiparticle random-phase approximation (pnQRPA) in the works [104,236,237] (see also [238] and the review [30]). The pnQRPA results constitute the light-hatched regions in the background of the ISM results. The width of the regions reflects the rather large variation of the determined g_A^{eff} for β-decay transitions in different isobaric chains. Geometric mean of the β^- and β^+/EC transitions has been used. For more information on the analyses see the review [30]. As can be seen in the figure, the ISM results and the pnQRPA results are commensurate with each other, which is non-trivial considering the large differences in their many-body philosophy.

At this point it should be pointed out that there have been recent global studies of the allowed and first-forbidden β decays, in particular on the neutron-rich side, relevant for the description of the r-process and the associated matter flow. In [239] half-lives of allowed β decays of neutron-rich nuclei with charge-numbers $20 \leq Z \leq 50$ were studied using fully self-consistent proton–neutron QRPA based on the spherical relativistic Hartree–Fock–Bogoliubov framework. By introducing an isospin-dependent proton–neutron pairing in the isoscalar channel the experimental half-lives were reproduced by the choice $g_A^{\text{eff}} = 1.0$. In [240] 5409 β decays were analyzed within the framework of a fully self-consistent covariant density functional theory. The effective value $g_A^{\text{eff}} = 1.0$ was adopted for both the Gamow–Teller and first-forbidden decays and the gross features of the decay rates across the nuclear chart were reproduced. A similar level of global agreement with data was obtained in the global survey [241] where the charge-changing Skyrme–QRPA was utilized to compute allowed and first-forbidden β decays for axially-deformed nuclei. In this study the quenched value $g_A^{\text{eff}} = 1.0$ was used for the Gamow–Teller transitions and no quenching (bare g_A) was used for the first-forbidden transitions.
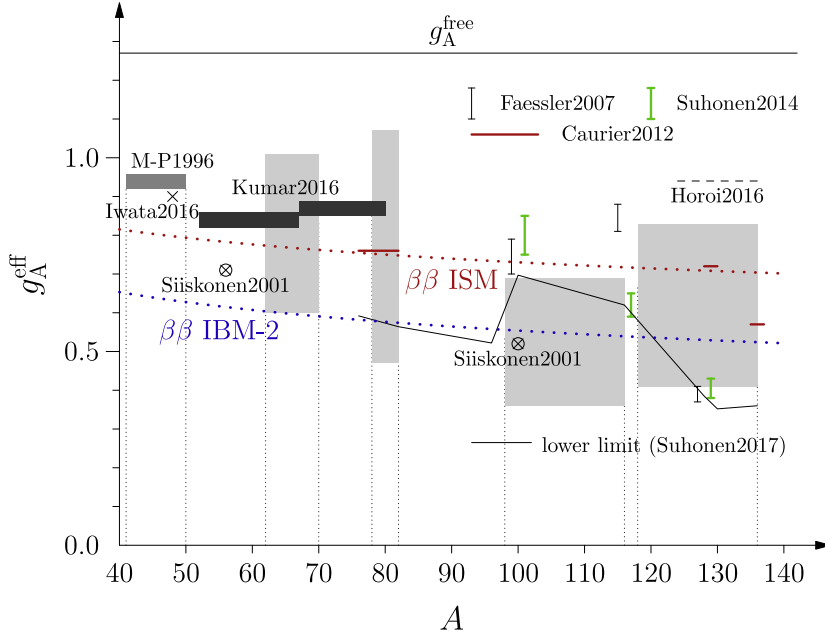
Fig. 29. Effective values of g_A in different theoretical β and $2\nu\beta\beta$ analyses for the nuclear mass range $A = 41 - 136$. The quoted references are *Suhonen2017* [216], *Caurier2012* [233], *Faessler2007* [242], *Suhonen2014* [243] and *Horoi2016* [235]. These studies are contrasted with the ISM β-decay studies of *M-P1996* [229], *Iwata2016* [230], *Kumar2016* [231] and *Siiskonen2001* [228]. For more information see the text and Table 3 in Section 3.1.2 and the text in Section 3.1.3.

3.1.3. Quenching of g_A in two-neutrino $\beta\beta$ decays

Recently the possibly decisive role of g_A in the half-life and discovery potential of the $0\nu\beta\beta$ experiments has surfaced [216,244]. In Barea et al. [244] a comparison of the experimental and computed $2\nu\beta\beta$ half-lives of a number of nuclei yielded the rather striking result

$$g_A^{eff}(\text{IBM-2}) = 1.269A^{-0.18} ; \quad g_A^{eff}(\text{ISM}) = 1.269A^{-0.12} , \tag{75}$$

where A is the mass number and IBM-2 stands for the microscopic interacting boson model (see Section 3.1.1). The IBM-2 results have been obtained by using the closure approximation for the analyzed $2\nu\beta\beta$ transitions since there are no spin–isospin degrees of freedom in the theory framework. Here one has to point out that the use of closure approximation for calculation of the $2\nu\beta\beta$ NMEs is not accurate and can be liable to large errors. The results (75), depicted in Fig. 29 as red (ISM) and blue (IBM-2) dotted curves, imply that strongly quenched effective values of g_A are possible, thus decreasing drastically the discovery potential of the $0\nu\beta\beta$ experiments.

Although the study [244] was the first to draw considerable attention in the experimental $0\nu\beta\beta$ community, it was not the first one to point to a possible strongly quenched value of g_A. Already the pnQRPA study of Faessler et al. [242] gave indications of a strongly quenched effective g_A, in the range $g_A^{eff} = 0.39 - 0.84$. These results, along with their 1σ errors, are shown in Fig. 29 as black vertical bars. Later a similar study was carried out in [243,245], with results comparable with those of [242] and depicted in Fig. 29 as green vertical bars. For more information see the review [30].

In Suhonen [216] a two-stage fit of the particle–particle parameter g_{pp} of the pnQRPA to the data on two-neutrino $\beta\beta$ decays was performed along the lines first introduced in Šimkovic et al. [246] and later used in Hyvärinen et al. [247]. The works [246,247] were extended in [216] to include also strongly quenched values of g_A. In this analysis it turned out that there is a minimum value of g_A for which the maximum NME can fit the $2\nu\beta\beta$-decay half-life. This lower limit of the possible g_A values is presented in Fig. 29 as a solid black line. It is seen that it is consistent with the thick green vertical bars of g_A ranges obtained in [243,245] and also commensurate with the thin black vertical bars obtained in [242]. However, the main message of Suhonen [216] is that no matter how quenched the value of g_A is, the half-lives of the present and future neutrinoless $\beta\beta$-decay measurements would only be affected by factors of 6 or less. This result is left for other theoretical approaches to be verified in the future.

In Section 3.6.4 an enhancement phenomenon of the g_A values in the context of the weak axial charge is discussed. For more information on the quenching of g_A in Gamow–Teller type of decays see the recent review [30]. See also Section 6.4 for the experimental $0\nu\beta\beta$ sensitivity and the NME with effective g_A.

Table 4
Change in angular momentum and parity for Kth forbidden unique β decays.

K	1	2	3	4	5	6	7
ΔJ	2	3	4	5	6	7	8
$\Delta \pi = \pi_i \pi_f$	-1	$+1$	-1	$+1$	-1	$+1$	-1

3.2. Forbidden beta decays

Forbidden β decays cover all β decays beyond the allowed Gamow–Teller (mediated by the $\boldsymbol{\sigma}$ operator) and Fermi (mediated by the unit operator) decays. In the allowed decays the maximum allowed change in angular momentum is $\Delta J = 1$ and the decay operator does not induce parity change, i.e. $\Delta \pi = \pi_i \pi_f = 1$, where π_i (π_f) is the parity of the initial (final) nuclear state. The forbidden decays can be divided into unique and non-unique decays. The unique decays have (essentially) universal β spectrum shapes (energy distribution of the emitted electrons in β^- decays or positrons in β^+ decays) with a weak nuclear-structure dependence. The non-unique decays can show strong dependence on the details of nuclear structure and hence the associated β spectra are not universal.

3.2.1. Forbidden unique beta decays

The forbidden unique β transitions are the simplest ones that mediate β decays of angular-momentum differences $\Delta J = |J_i - J_f| \geq 2$, where J_i (J_f) is the angular momentum of the initial (final) nuclear state. For a Kth forbidden ($K = 1, 2, 3, \ldots$) unique β decay the angular-momentum change is $\Delta J = K + 1$. At the same time the parity of the involved nuclear states changes in the odd-forbidden and remains the same in the even-forbidden decays [55]. The change in angular momentum and parity for different degrees of forbiddenness is presented in Table 4, and they obey the simple rule

$$(-1)^{\Delta J} \Delta \pi = -1 . \quad \text{(Forbidden unique decays)} \tag{76}$$

The half-lives $t_{1/2}$ of Kth forbidden unique β decays can be expressed in terms of reduced transition probabilities B_{Ku} and phase-space factors f_{Ku}. The B_{Ku} is given by the NME, which in turn is given by the single-particle NMEs and one-body transition densities. Then (for further details see [55])

$$t_{1/2} = \frac{\kappa}{f_{Ku} B_{Ku}} ; \quad B_{Ku} = \frac{g_A^2}{2J_i + 1} |M_{Ku}|^2 , \tag{77}$$

where κ is a constant with value [248]

$$\kappa = \frac{2\pi^3 \hbar^7 \ln 2}{m_e^5 c^4 (G_F \cos \theta_C)^2} = 6147 \text{ s} , \tag{78}$$

with G_F being the Fermi constant and θ_C being the Cabibbo angle. The phase-space factor f_{Ku} for the Kth forbidden unique $\beta^\pm$ decay can be written as

$$f_{Ku}^{(\pm)} = \left(\frac{3}{4} \right)^K \frac{(2K)!!}{(2K+1)!!} \int_1^{w_0} C_{Ku}(w_e) p_e w_e (w_0 - w_e)^2 F_0(\pm Z_f, w_e) dw_e , \tag{79}$$

where C_{Ku} is the shape factor for Kth forbidden unique β decays which can be written as (see, e.g., [55,249])

$$C_{Ku}(w_e) = \sum_{k_e + k_\nu = K+2} \frac{\lambda_{k_e} p_e^{2(k_e-1)} (w_0 - w_e)^{2(k_\nu-1)}}{(2k_e - 1)!(2k_\nu - 1)!} , \tag{80}$$

where the indices k_e and k_ν (both $k = 1, 2, 3 \ldots$) come from the partial-wave expansion of the electron (e) and neutrino (ν) wave functions. Here w_e is the total energy of the emitted electron/positron, p_e is the electron/positron momentum, Z_f is the atomic number of the daughter nucleus and $F_0(Z_f, w_e)$ is the Fermi function taking into account the Coulombic attraction/repulsion of the electron/positron and the daughter nucleus. It is to be noted that for positron emission the change $Z_f \to -Z_f$ has to be performed in $F_0(Z_f, w_e)$ and in $F_{k_e-1}(Z_f, w_e)$ in Eq. (81) below. The factor λ_{k_e} contains the generalized Fermi function F_{k_e-1} [250] as the ratio

$$\lambda_{k_e} = \frac{F_{k_e-1}(Z_f, w_e)}{F_0(Z_f, w_e)} . \tag{81}$$

The integration is performed over the total (by electron rest-mass) scaled energy of the emitted electron/positron, w_0 being the endpoint energy, corresponding to the maximum electron/positron energy in a given transition.

The NME in (77) can be expressed as

$$M_{Ku} = \sum_{ab} M^{(Ku)}(ab) (\psi_f \| [c_a^\dagger \tilde{c}_b]_{K+1} \| \psi_i) , \tag{82}$$

K	1	2	3	4	5	6	7
ΔJ	0,1	2	3	4	5	6	7
$\Delta\pi = \pi_i\pi_f$	-1	$+1$	-1	$+1$	-1	$+1$	-1

where the factors $M^{(Ku)}(ab)$ are the single-particle matrix elements and the one-body transition densities are $(\psi_f \| [c_a^\dagger \tilde{c}_b]_{K+1} \| \psi_i)$ with ψ_i being the initial-state wave function and ψ_f the final-state wave function. The operator $c_a^\dagger$ is a creation operator for a nucleon in an orbital a and the operator $\tilde{c}_a$ is the corresponding annihilation operator. The single-particle matrix elements are given (in the Biedenharn–Rose phase convention) by

$$M_{Ku}(ab) = \sqrt{4\pi}\left(a\|r^K[\mathbf{Y}_K\boldsymbol{\sigma}]_{K+1}i^K\|b\right), \tag{83}$$

where $\mathbf{Y}_K$ is a spherical harmonic of rank K, $\boldsymbol{\sigma}$ a vector containing the Pauli matrices as its components, r the radial coordinate, and a and b stand for the single-particle orbital quantum numbers. The NME (83) is given explicitly in [55].

3.2.2. Forbidden non-unique β decays

For the Kth forbidden ($K = 1, 2, 3, \ldots$) non-unique β decay the angular-momentum change is $\Delta J = K$ and the parity of the involved nuclear states changes in the same way as for the forbidden unique β decay (see Section 3.2.1). The rules for the change in angular momentum and parity for different degrees of forbiddenness are summarized in Table 5,[4] and they obey the rule

$$(-1)^{\Delta J}\Delta\pi = +1. \quad \text{(Forbidden non-unique decays)} \tag{84}$$

As seen in the table the first-forbidden non-unique decays are an exception, since there also the angular-momentum change $\Delta J = 0$ is possible owing to appearance of two additional NMEs, as discussed in Section 3.6.4.

The half-life of the forbidden non-unique β decays can be written in the form

$$t_{1/2} = \kappa/\tilde{C}, \tag{85}$$

where $\tilde{C}$ is the dimensionless integrated shape function, given by

$$\tilde{C} = \int_1^{w_0} C(w_e)p_e w_e(w_0 - w_e)^2 F_0(Z_f, w_e)\mathrm{d}w_e, \tag{86}$$

with the notation explained in Section 3.2.1. The general form of the shape factor of Eq. (86) is a sum

$$C(w_e) = \sum_{k_e, k_\nu, K} \lambda_{k_e}\left[M_K(k_e, k_\nu)^2 + m_K(k_e, k_\nu)^2 - \frac{2\gamma_{k_e}}{k_e w_e}M_K(k_e, k_\nu)m_K(k_e, k_\nu)\right], \tag{87}$$

where the factor λ_{k_e} has been given in (81) and Z_f is the charge number of the final nucleus. The indices k_e and k_ν ($k = 1, 2, 3\ldots$) are related to the partial-wave expansion of the electron (e) and neutrino (ν) wave functions, K is the order of forbiddenness of the transition, and $\gamma_{k_e} = \sqrt{k_e^2 - (\alpha Z_f)^2}$, $\alpha \approx 1/137$ being the fine-structure constant. The nuclear-physics information is hidden in the factors $M_K(k_e, k_\nu)$ and $m_K(k_e, k_\nu)$, which are complicated combinations of different NMEs and leptonic phase-space factors. For more information on the integrated shape function, see [66,250].

The shape factor $C(w_e)$ (87) can be decomposed into vector, axial–vector and mixed vector–axial–vector parts in the form [251]

$$C(w_e) = g_V^2 C_V(w_e) + g_A^2 C_A(w_e) + g_V g_A C_{VA}(w_e). \tag{88}$$

The same is true for the shape function of the forbidden unique decays (80) when the so-called next-to-leading-order terms are added to the leading ones [251,252]. Integrating Eq. (88) over the electron kinetic energy, one obtains an analogous expression for the integrated shape function (86)

$$\tilde{C} = g_V^2\tilde{C}_V + g_A^2\tilde{C}_A + g_V g_A\tilde{C}_{VA}, \tag{89}$$

where the factors $\tilde{C}_i$ in Eq. (89) are just constants, independent of the electron energy.

3.3. Studies of forbidden unique beta transitions

The first-forbidden unique β transitions are mediated by a rank-2 (i.e. having angular-momentum content 2) parity-changing spherical tensor operator [a special case of the operator (83)], schematically written as $\mathcal{O}(2^-)$. For these decays it is

---

[4] It is worth pointing out that for a given degree K of forbiddenness also lower ΔJ values participate but they are sub-dominant to forbiddenness $K - 2$ and thus unobservable.

customary to modify the general structure of Eqs. (77)–(79) by replacing the phase-space factor $f_{K=1,u}$ of (79) by a 12 times larger phase-space factor f_{1u}, i.e.

$$f_{1u} = 12 f_{K=1,u} , \tag{90}$$

yielding a factor log 12 = 1.079 times larger comparative half-lives than in the standard definition (77).

In the quenching studies it is simplest to study first-forbidden ground-state-to-ground-state β transitions, see the review [4]. In an early work [54] a systematic schematic analysis of the first-forbidden unique β decays was performed from the point of view of suppression factors stemming from the effect of E1 (electric dipole) giant resonance in the final odd–odd nucleus. In [253] the suppression mechanism of the first-forbidden and third-forbidden β decays of light nuclei ($A \leq 50$) was studied by using simple shell-model estimates and first-order perturbation theory. The hindrance of the decay transitions was traced to the repulsive $T = 1$ (isospin 1) particle–hole force. In the work [105] 19 first-forbidden unique ground-state-to-ground-state β-decay transitions were studied in the framework of the pnQRPA. In this study a central nucleus was defined and the computed β^-/EC (EC=electron capture) transitions to the left (corresponding to the left-side NME) and right (corresponding to the right-side NME) were compared with the available data. The geometric mean of the left-side and right-side NMEs was used in the analyses, making the analyses more stable. It was found that there is a strong quenching effect when going from the simple two-quasiparticle NME to the pnQRPA NME (a quenching factor $q \approx 0.4$), and finally from the pnQRPA NME to the experimental NME (a quenching factor $q \approx 0.45$). There the experimental NME was extracted from the data by using the free value $g_A^{free} = 1.27$ of the axial–vector coupling strength.

Early studies of the quenching in the second- and third-forbidden unique β decays were performed in [253,254]. The work of [253] was mentioned above, and in [254] these β decays were studied using a simple interacting shell model and the unified model (deformed shell model) for six β transitions in the $A = 10, 22, 26, 40$ nuclei. The interest in these studies derived from nuclear-structure considerations: how to explain in a nuclear model the hindrance phenomena occurring in certain measured β transitions. A later study of second-forbidden unique β decays in the mass range $A = 10$–54 was performed in [255] by using the ISM with newer shell-model interactions. A reasonable description of the experimental half-lives was achieved by using the bare value of the axial coupling g_A (but a quenched value would have improved the comparison). An interest beyond the single β decays is the double-beta decays: The $0\nu\beta\beta$ decays proceed via virtual intermediate states of all multipolarities J^π due to the multipole expansion of the Majorana-neutrino propagator (see, e.g., [2,23] and Section 5 for further information). A good part of these virtual transitions are forbidden unique transitions satisfying the selection rules given in Eq. (76) and Table 4. It is therefore of paramount importance to study the possible quenching effects associated with these β transitions.

The quenching related to the virtual β transitions of the $0\nu\beta\beta$ decay can be studied by using the theoretical machinery of Section 3.2.1. In [256] this machinery was applied to 148 potentially measurable second-, third-, fourth-, fifth-, sixth- and seventh-forbidden unique beta transitions. The calculations were done using realistic single-particle model spaces and G-matrix-based microscopic two-body interactions. The results of [256] could shed light on the magnitudes of the NMEs corresponding to the high-forbidden unique $0^+ \leftrightarrow J^\pi = 3^+, 4^-, 5^+, 6^-, 7^+, 8^-$ virtual transitions taking part in the $0\nu\beta\beta$ decays. In the work of [256] the *expected* half-lives of the studied β-decay transitions were derived by comparison with the analyses performed for the Gamow–Teller and first-forbidden unique β transitions in the works [104,105]. An example of such predictions is given in Fig. 30. In the figure one sees that the expected half-lives are long and hard to measure, even though the EC transition of interest exhausts 100% of the total electron-capture rate. This transition is, however, masked by the strong β^- branches to the excited states of ^{130}Xe. The implications of the studies of [256] for the observability of $0\nu\beta\beta$ decays are discussed in Section 5.

3.4. Low-Q-value beta decays for neutrino-mass studies

3.4.1. Low-Q-value beta decays for neutrino-mass measurements

The neutrino mass is measured by β-decay experiments, like in the case of the KATRIN experiment [70] (tritium decay) and the MARE experiment [259] (decay of ^{187}Re). The electron–neutrino mass is measured via the slight distortion of the electron end-point spectrum. To detect this distortion, β decays with small Q value are used. The tritium experiment measures an allowed decay with the Q value of 18.59 keV, while the rhenium experiment measures a first-forbidden unique transition with the Q value of 2.47 keV. The non-zero mass effect shows up as small deviation at the end point from the universal β-spectrum shape. (see Section 3.2.1).

One potentially interesting case is the β^- decay of the $9/2^+$ ground state of ^{115}In to the first excited state of ^{115}Sn with spin–parity $3/2^+$ (see Fig. 31). This decay transition is second-forbidden unique so that the β-spectrum shape of the decay is universal. What is interesting about this decay transition is that it has a world-record small Q value of 0.155(24) keV [260] so that it can be called "ultra-low" (i.e. below 1 keV). Measurement of such a small Q value is based on the Penning trap techniques [260,261]. The corresponding decay branch was measured first at LNGS in Italy to have a partial half-life of $(3.73 \pm 0.98) \times 10^{20}$ years [262] and at the HADES in Belgium to have a partial half-life of $4.3(5) \times 10^{20}$ yr [263]. It has been speculated that the decay branch could be used as a neutrino-mass detector [262]. Even more intriguing is that such an ultra-low Q value seems to enhance the interference of atomic effects in the nuclear decay, as discussed in [264,265] and further dwelled on in Section 3.4.2.
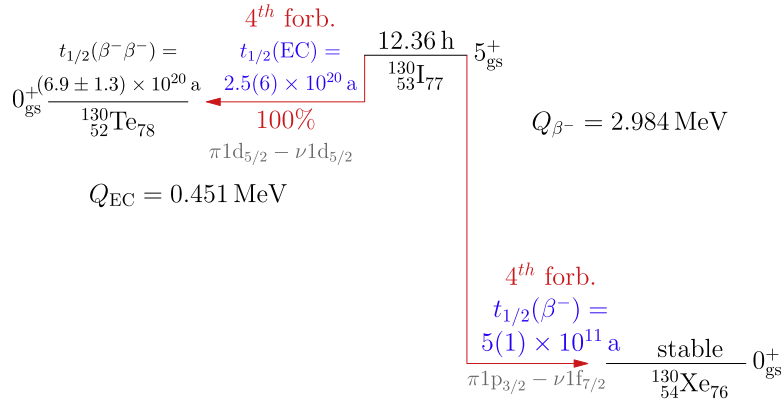
Fig. 30. Predicted half-lives and their error estimates (in parenthesis) for β^- and EC (electron-capture) transitions in the isobaric chain $A = 130$. The spin–parity assignment, life-time and decay energies (Q values) of the ground (gs) state of ^{130}I are experimental data and taken from [257]. The $2\nu\beta\beta$ half-life is taken from [258]. In addition to the half-lives the degree of forbiddenness and the leading single-particle transition are shown.
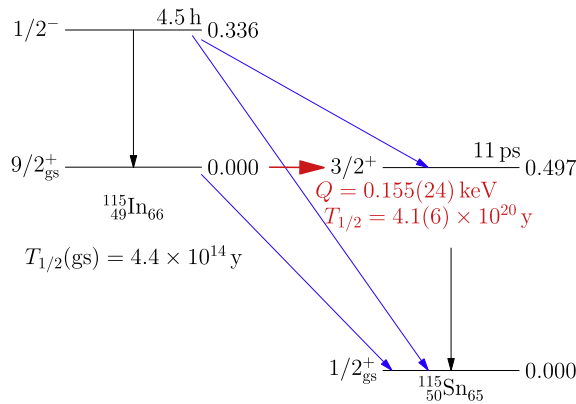
Fig. 31. β^- decay of the ground state of ^{115}In to the ground state and first excited state in ^{115}Sn. The numbers to the right of the energy levels are excitation energies in MeV.

An other possibility is the β^- decay of the $7/2^+$ ground state of ^{135}Cs to the first (and) second excited states of ^{135}Ba with spin–parities $1/2^+$ and $11/2^-$ which are second-forbidden and first-forbidden unique decays, respectively [266]. There are two half-life and Q-value measurements [267,268] that are in strong tension with each other. Depending on which one of the measurements is correct, either the decay to the first or to the second excited state can produce a transition with an ultra-low Q value [266]. So, accurate Penning trap measurement of the difference in masses between ^{135}Cs and ^{135}Ba is called for. Another potential low-Q-value candidate is the decay of ^{115}Cd discussed extensively in Ref. [269]. A list of other potential low-Q-value candidates is presented in Table 6. All the initial states of the first column of the table are ground states of the respective nuclei. In the table the decay type is either β^- or electron capture (EC).

A particularly interesting case is the allowed Gamow–Teller β^- decay of ^{131}I although the half-life of this candidate is rather short and thus experimentally challenging. There are also allowed Gamow–Teller (^{159}Dy) and Gamow–Teller/Fermi (^{161}Ho) electron-capture decays but especially ^{161}Ho is too short-lived. The first-forbidden unique β^- decay of ^{155}Eu is of high interest because of the rather long half-life of ^{155}Eu. The rest are short-lived and/or non-unique decays and depend on several nuclear matrix elements without a universal β-spectrum shape. All in all, it is desirable to perform high-precision Penning-trap mass measurements to improve the accuracy of the mass differences of the nuclei listed in Table 6.

3.4.2. Atomic effects in the low-Q-value beta decays

As mentioned in the previous section the low-Q-value β decays enhance the interference of atomic effects in nuclear decay processes. Evidence of such an interference was first pointed out in the context of the β^--decay transition ^{115}In($9/2^+$) $\rightarrow$ ^{115}Sn($3/2^+$) with a world-record small Q value [261] (see Section 3.4.1). There are at least four different effects of atomic origin that remain unknown for the decays with Q values this low [264]: the electron screening effect, the atomic overlap effect, the exchange effect and the effect of final-state interactions. According to the existing literature they are all known to become significant as the Q value decreases. While they are completely negligible for typical beta-decay Q

Table 6
Potential candidate transitions with ultra-low Q values. The first column gives the initial ground state of the listed nucleus and the second column gives the half-life of the nucleus. The third column gives the excited final state (f.s.) of interest for the low Q-value transition. The fourth column gives the experimental excitation energy with the experimental error. The fifth column gives the decay type and the last column the derived experimental decay Q value [257] in units of keV.

Initial state	$T_{1/2}$	low-Q f.s.	E^* (keV)	Decay type	Q (keV)
^{77}As$(3/2^-)$	38.8 h	^{77}Se$(5/2^+)$	680.1046(16)	1st non-unique β^-	2.8 ± 1.8
^{111}In$(9/2^+)$	2.805 d	^{111}Cd$(3/2^+)$	864.8(3)	2nd unique EC	-2.8 ± 5.0
		^{111}Cd$(3/2^+)$	866.60(6)	2nd unique EC	-4.6 ± 5.0
^{131}I$(7/2^+)$	8.025 d	^{131}Xe$(9/2^+)$	971.22(13)	allowed β^-	-0.4 ± 0.7
^{146}Pm(3^-)	5.53 yr	^{146}Nd(2^+)	1470.59(6)	1st non-unique EC	1.4 ± 4.0
^{149}Gd$(7/2^-)$	9.28 d	^{149}Eu$(5/2^+)$	1312(4)	1st non-unique EC	1 ± 6
^{155}Eu$(5/2^+)$	4.75 yr	^{155}Gd$(9/2^-)$	251.7056(10)	1st unique β^-	1.0 ± 1.2
^{159}Dy$(3/2^-)$	144 d	^{159}Tb$(5/2^-)$	363.5449(14)	allowed EC	2.1 ± 1.2
^{161}Ho$(7/2^-)$	2.28 h	^{161}Dy$(7/2^-)$	857.502(7)	allowed EC	1.4 ± 2.7
		^{161}Dy$(3/2^-)$	858.7919(18)	2nd non-unique EC	0.1 ± 2.7
^{188}W(0^+)	69.78 d	^{188}Re$((0, 1, 2)^+)$	346.580(7)	allowed β^- (?)	2.4 ± 3.0
^{189}Ir$(3/2^-)$	13.2 d	^{189}Os$(5/2^-)$	531.54(3)	1st non-unique EC	0.46 ± 13.00

values, they can contribute by several per cent to low-Q-value decays according to the existing theoretical estimates. The present status of these atomic corrections is as follows:

- *Electron screening*: Traditionally the Rose prescription [270] has been accurate enough to estimate the electron screening correction to the beta-decay half-life. For the ultra-low Q values it breaks down completely. The same holds true for the more accurate, completely relativistic expression derived by Lopez and Durand [271].
- *Atomic overlap*: The atomic overlap effect, caused by the fact that the bound electron states of the initial and final atom are slightly different, is another possible source of corrections. This effect has been theoretically studied for the allowed decays by Bahcall [272]. His estimates show that there is a trend of this effect to grow stronger as the Q value decreases. For the ^{241}Pu decay with a Q value of 21 keV, the estimated hindrance in the decay is 2%. However, those estimates break down for the Q values as low as a few hundred keV, and cannot be applied to the case of ultra-low Q values.
- *Atomic exchange*: The first approximation for the exchange effects was published by Bahcall in the same study as the atomic overlap effect [272]. That approximation suggests an additional reduction in the decay rate, 2% in the case of ^{241}Pu. Later theoretical work by Harston and Pyper [273] contradicts this result concluding that the exchange effect should actually enhance the decay rate. In the case of ^{241}Pu their calculation yielded a 7.5% enhancement of the decay rate. However, estimates derived in both works are inapplicable in the ultra-low-Q-value regime.
- *Final-state interactions*: The final-state interactions pose yet another theoretical challenge. The molecular final-state interactions have only been studied for the beta decay of tritium [274], where the atomic structure is simple compared to the heavier elements. The role of final-state interactions for heavier nuclei in a lattice is still deep in the terra incognita: Whether the chemical bonds of the atoms of a sample introduce a non-negligible correction to the decay channel with an ultra-low Q value or not remains yet another open question.

The developments of experimental techniques have now reached β decays with Q values so low that theoretical works on the atomic effects have become outdated. To improve the situation more studies, both theoretical and experimental, are necessary. Another challenge in the theoretical search for the true significance of the atomic contributions is the difficulty of experimental verification: The small corrections they induce to the usual low-Q-value beta decays are dwarfed by the uncertainties in the nuclear wave functions. Therefore a proper attack on the open questions may have to wait for the time when proper ab-initio nuclear-structure theory is available for the low-Q β transitions of interest. Still, this does not prevent from making theoretical estimates of the atomic effects for ultra-low-Q-value decays. If they proved to be as dramatic as the case of ^{115}In decay suggests there would be a realistic possibility to actually verify the existence of these atomic effects experimentally.

3.5. Competition of beta and double beta decays

Let us now discuss two interesting examples where extremely slow first-order weak processes (β decays) compete with second-order weak processes (double β decays). In Fig. 32 the mother nucleus ^{48}Ca decays to states in ^{48}Sc via extremely slow β-decay transitions, retarded by the large differences in angular momentum between the initial state (spin 0) and the final states (spins $4-6$). In addition to the ultra-slow β transitions there is an interesting ultra-slow second-order transition, the two-neutrino $\beta\beta$ ($2\nu\beta\beta$) decay, from ^{48}Ca directly to the ground state of ^{48}Ti. In this case the decay jumps past the nucleus ^{48}Sc and goes directly to the ground state of ^{48}Ti. These higher-order transitions form a class of transitions called generically the nuclear double beta decay, discussed more extensively in Section 5.

The half-lives of Fig. 32 have been calculated [275] by using the experimental Q values listed in the figure and by the use of the ISM in a model space consisting of the pf shell. The interaction GXPF1A [276] was adopted as the two-body interaction. These β decays have previously been discussed in [277] by the use of older two-body interactions. In the present case the
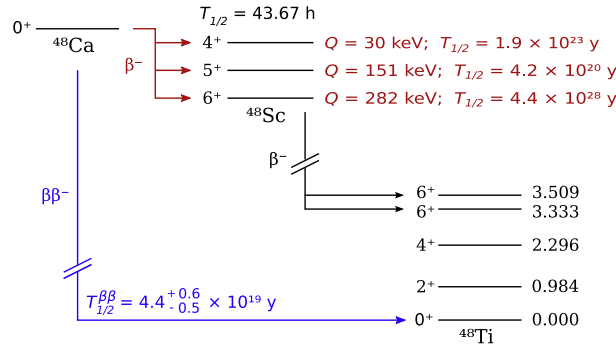
Fig. 32. Ultra-slow β-decay transitions from the ground state of ^{48}Ca to the lowest three states in ^{48}Sc, and the subsequent β decays to states in ^{48}Ti. The experimental Q values [257] and computed half-lives for $g_A = 1.0$ [275] are given to the right of the energy levels. Shown are also the experimental β-decay half-life of ^{48}Sc [257] and the measured half-life [258] of the direct $2\nu\beta\beta$-decay transition to the ground state of ^{48}Ti. The numbers to the right of the ^{48}Ti energy levels are excitation energies in MeV.

total beta-decay half-life, $T_{1/2}(\beta^-) = 4.2 \times 10^{20}$ y, is determined by the fourth-forbidden unique β^- transition to the 5^+ state in ^{48}Sc. The other transitions, the fourth-forbidden non-unique transition to the 4^+ state and the sixth-forbidden non-unique transition to the 6^+ state, do not play a role in the total β-decay half-life due to their long partial half-lives. The resulting total half-life depends now, in the leading order, on only one NME so that it can be written as

$$t_{1/2}^\beta = (4.2 g_A^{-2}) \times 10^{20} \text{ yr} . \tag{91}$$

It is interesting to note that the computed β^--decay half-life is roughly an order of magnitude longer than the experimental $\beta\beta$-decay half-lives (see Refs. [61,258]).

An exactly similar situation as for the ^{48}Ca decay occurs for the β and $2\nu\beta\beta$ decays of ^{96}Zr [278] in the decay chain ^{96}Zr $\rightarrow$ ^{96}Nb $\rightarrow$ ^{96}Mo (see Fig. 5 in Section 2.2.1). In a recent paper [59] the measured Q values were used to compute the following partial half-lives by adopting $g_A = 1.0$: $t_{1/2}^\beta(0^+ \rightarrow 6^+) = 1.6 \times 10^{29}$ yr, $t_{1/2}^\beta(0^+ \rightarrow 5^+) = 1.1 \times 10^{20}$ yr and $t_{1/2}^\beta(0^+ \rightarrow 4^+) = 7.5 \times 10^{22}$ yr. As can be seen, the total half-life is dictated by the fourth-forbidden unique β^- transition to the 5^+ final state. Again the resulting half-life depends in the leading order on only one NME so that it can be written as

$$t_{1/2}^\beta = (1.1 g_A^{-2}) \times 10^{20} \text{ yr} , \tag{92}$$

which is to be compared with the experimental [258] $2\nu\beta\beta$-decay half-life

$$t_{1/2}^{\beta\beta}(\text{exp.}) = (2.3 \pm 0.2) \times 10^{19} \text{ yr} . \tag{93}$$

Again we see that the β-decay half-life is clearly longer than the $2\nu\beta\beta$-decay half-life as mentioned in Section 2.2.1.

3.6. Shapes of beta spectra

Beyond the half-life analyses (see Section 3.1.2 for the Gamow–Teller transitions and Sections 3.3 and 3.5 for examples of forbidden transitions) also the β-spectrum shapes can be used to pin down the effective value of the weak axial–vector coupling strength g_A in forbidden non-unique β decays. In some forbidden non-unique β-decay transitions the shape of the β spectrum is sensitive to the variations in the value of g_A. This feature can be utilized in determining the value of g_A for forbidden β transitions. This method is coined the spectrum-shape method (SSM) and was introduced in [251]. Further systematic studies using the SSM were performed in [252,279,280]. The status of the effective values of g_A in β and $\beta\beta$ decays is summarized in [30] and the impact of the effective values of g_A on the sensitivies of the presently running and future $\beta\beta$-decay experiments has been discussed in [216] (see Section 3.1.3). Various applications of the SSM are discussed below in this section.

3.6.1. Backgrounds in rare-events searches

There is a long list of common background contaminants in dark-matter and rare-events experiments [281]. Usually the β-spectrum shapes of the corresponding β decays have not been measured or computed. Many of the $\beta\beta$ and dark-matter direct experiments may have cosmogenic backgrounds as discussed for Ge-based experiments [282]. Experimental ways to reduce such backgrounds are discussed in [16]. Also heavy nuclei like ^{214}Bi can be a dangerous background in $0\nu\beta\beta$ experiments. Below we give a few examples of the β spectra relevant for pinning down background contaminations in rare-event experiments.

The nuclei ^{39}Ar and ^{42}Ar are contaminants in experiments based on liquid argon (LAr). The applications of LAr-based detectors range from calorimetry in high-energy-physics experiments at the LHC (Large Hadron Collider at CERN) down to
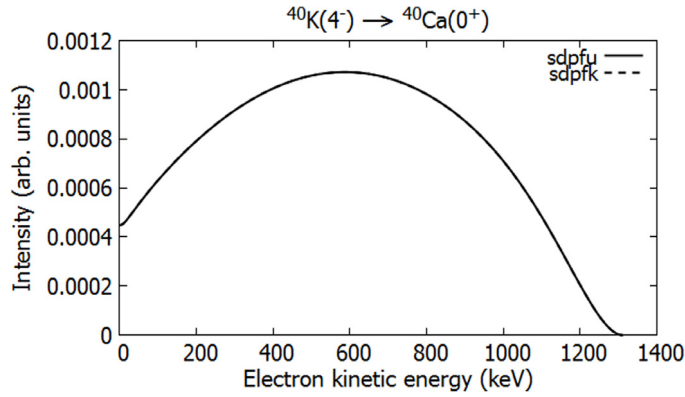
Fig. 33. Normalized β spectrum for the third-forbidden unique ground-state-to-ground-state β^- decay of ^{40}K calculated by using two different shell-model interactions. The value $g_V = 1.00$ was used in the calculations. Note the Coulomb shift of the β spectrum, see the text.
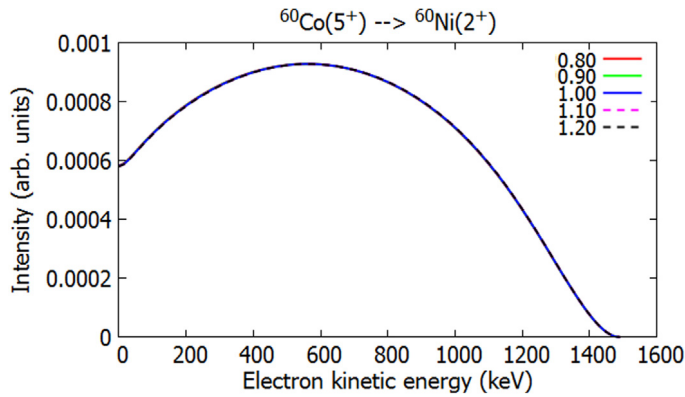
Fig. 34. Normalized β spectra for the second-forbidden unique β^- decay of ^{60}Co to the first 2^+ state in ^{60}Ni. The value $g_V = 1.00$ was used in the calculations and the color coding represents the different adopted values for g_A. Note the Coulomb shift.

large-scale low-background experiments for rare-events searches, in particular in quests for dark matter of the Universe (two particular examples are the running DEAP-3600 [283] and DarkSide-50 [284]). The related experimental problems and the β-spectrum shapes of ^{39}Ar and ^{42}Ar have been discussed in Ref. [73].

The long-lived potassium isotope ^{40}K is a common pollutant in the environment and in many materials. In Fig. 33 the normalized electron spectrum (the superficial area is normalized to unity) for the β^- decay of ^{40}K is presented. The dominant decay channel (89.28%) is the third-forbidden unique β^- decay to the ground state of ^{40}Ca [285]. The electron spectra have been computed by using the interacting shell model (ISM) with the effective interactions sdpfu [286] and sdpfk [287] in the proton sd model space and neutron $sdf_{7/2}$ model space, thus permitting configuration mixing for the doubly magic nucleus ^{40}Ca. The next-to-leading-order corrections [251] have been included in the calculation. An old measurement of the β-spectrum shape has been reported in [288]. At this point it should be noted that the β spectrum does not go to zero at electron kinetic energy zero due to the Coulomb effects affecting the shape factor (87) through the Fermi function $F_{k_e-1}(Z_f, w_e)$ of Eq. (81). This effect can be coined *Coulomb shift*.

The β^- decay of ^{60}Co is a common pollutant in the environment and in Ge-based experiments [282]. In Fig. 34 the normalized electron spectra for the second-forbidden unique β^- decay of ^{60}Co to the first 2^+ state in ^{60}Ni is shown for five different values for g_A. The β spectra have been calculated by using the ISM with the Horie–Ogawa interaction [289,290]. Due to the large number of valence nucleons in the pf shell the calculations were truncated to the proton-$0f_{7/2}$-neutron-$1p0f_{5/2}$ subspace. Though the dominant decay channel is the allowed decay to the first 4^+ state in ^{60}Ni there is a small branching (0.12%) to the first 2^+ state in ^{60}Ni [291]. The decomposition (88) suggests that the spectrum shape could be g_A dependent. It can be seen in the figure, however, that the next-to-leading-order corrections to the β-decay shape factor are not strong enough to make the spectrum shape appreciably g_A dependent. An old measurement of the β-spectrum shape has been reported in [292].

The ground state EC of ^{40}K, which is not known experimentally, might be used as an explanation for the claimed dark matter in the DAMA experiment [293].

Table 7
Summary of the most important (ground-state-to-ground-state) transitions of the ^{235}U cumulative β spectrum in the energy range around 4.0 MeV. Indicated are the β-decay Q value, the β-feeding branching ratio (BR), the multipolarities of the initial and final states and the contribution to the cumulative β spectrum (last column). The information of the table is taken from [309].

Nucleus	Q (MeV)	BR(%)	$J_{gs}^{\pi} \rightarrow J_{gs}^{\pi}$	Contr. (%)
^{88}Rb	5.3	77(1)	$2^- \rightarrow 0^+$	2.9
^{90}Rb	6.6	33(4)	$0^- \rightarrow 0^+$	3.4
^{92}Rb	8.1	95.2(7)	$0^- \rightarrow 0^+$	6.1
^{95}Sr	6.1	56(3)	$1/2^+ \rightarrow 1/2^-$	3.0
^{96}Y	7.1	95.5(5)	$0^- \rightarrow 0^+$	6.3
^{100}Nb	6.4	50(7)	$1^+ \rightarrow 0^+$	5.5
^{135}Te	5.9	62(3)	$(7/2^-) \rightarrow 7/2^+$	3.7
^{140}Cs	6.2	36(2)	$1^- \rightarrow 0^+$	3.4
^{142}Cs	7.3	56(5)	$0^- \rightarrow 0^+$	3.5
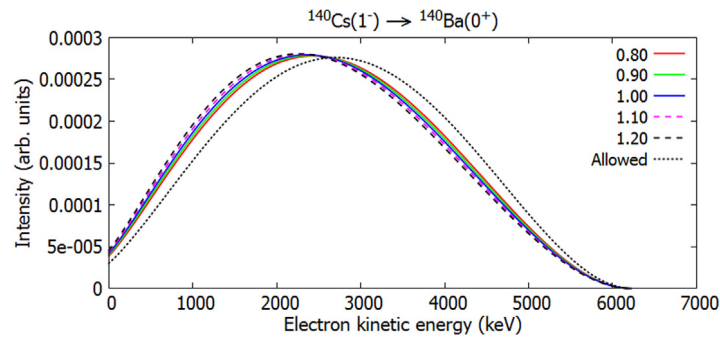
Fig. 35. Normalized β spectrum for the first-forbidden non-unique ground-state-to-ground-state β^- decay of ^{140}Cs. The value $g_V = 1.00$ was adopted in the calculations and the color coding represents the different adopted values for g_A. The allowed spectrum shape is plotted for comparison. Note the Coulomb shift.

3.6.2. The reactor-antineutrino anomaly

An interesting application of the β-spectrum studies is the reactor antineutrino anomaly (RAA) [294]. The antineutrino spectra in nuclear reactors result from the long uranium and plutonium α and β^- decay chains and the subsequent fission used as fuel to drive the energy production in the nuclear power plants. In the RAA the experimentally measured antineutrino flux is lower than what is expected from the β decays of the nuclear fission fragments deduced from nuclear data with some approximations [295]. In addition, there is a strange "bump" between 4 and 6 MeV in the antineutrino spectrum. The RAA and the spectral bump have been measured in the experiments Daya Bay [296], RENO [297] and Double Chooz [298]. The measured flux is some 6(2)% lower making this a rough 3σ deviation [299]. The method of virtual β branches [300–302] has been used to estimate the cumulative β spectra responsible for the theoretical antineutrino flux. The involved β decays go partly by forbidden transitions that cannot be assessed by the present nuclear data, but instead, could be calculated. Electron spectrum-shape calculations were done for first-forbidden β^- decays of ^{136}Te and ^{140}Xe in Ref. [303], and in general cases one can use the formalism introduced in [252,304]. Corrections to the leading contributions, like the finite-size, radiative and weak-magnetism corrections have been introduced in [252,300,301,305]. Possible shortcomings of the previously used analysis methods have been pointed out in [306].

While the actual cumulative β spectra, leading to the RAA and emerging from the decays of the fission fragments, are numerous, not all of them contribute in equal amounts. Then the cumulative β spectra can be nicely fit by just a limited number of virtual β spectra emerging from non-existent fictional β branches [300–302,307]. A shortcoming of this procedure is that all the virtual branches are assumed to be described by allowed β-spectrum shapes. Also adding information from the nuclear databases is not accurate enough due to deficiencies in this information. Out of the several thousand β branches taking part in the cumulative β spectra the majority are allowed decays but the contribution from the first-forbidden decay transitions is also considerable, in particular in the interesting region of the antineutrino spectrum, between 4 and 6 MeV [308]. On the other hand, forbidden decays become increasingly unlikely with increasing degree of forbiddenness.

The most important β branches taking part in the cumulative β spectra of the RAA were identified in [309] and they are given in Table 7. They also contribute to the observed spectral bump. The branchings of these decay transitions are between 33% and 96%. Here, as also in the analysis of [306], allowed β spectrum shapes were assumed also for the forbidden transitions, like the first-forbidden decays of Table 7. Thus, it is of paramount importance to compute the shapes of the β spectra associated with the above-listed key transitions and compare these spectra with the allowed shape to see the error made in the allowed approximation. The computation of the proper spectral shapes can be done by using the formalism of

Fig. 36. Normalized cumulative β spectra obtained by summing the individual β spectra associated to all the first-forbidden transitions of Table 7 by taking into account their branchings and relative contributions listed in the third and last columns of Table 7. The sum spectrum "allowed shape" corresponds to the assumed allowed shapes for all the individual β transitions, instead of the correct first-forbidden shapes, as computed by the use of the ISM and adopted for the sum spectrum "forbidden shape". The values $g_V = 1.00$, $g_A = 0.70$ and $\varepsilon_{MEC} = 1.7$ (see Section 3.6.4) were adopted in the calculations. Note the Coulomb shift.

Sections 3.2.1 and 3.2.2. An example of the application of the formalism is presented in Fig. 35 where the ISM-computed first-forbidden non-unique ground-state-to-ground-state β^- decay of ^{140}Cs is depicted and compared with the allowed spectrum shape. The used interaction is jj56pnb [310] in the proton $2s - 1d - 0g_{7/2}$ and neutron $2p - 1f - 0h_{9/2}$ single-particle model space. As can be seen there is a notable deviation from the spectrum shape of an allowed transition with the same Q value. In this case there is also some dependence of the β spectrum shape on the value of g_A, and in other key transitions this could be the case as well, as suggested by the decomposition (88). The effects stemming from the uncertainty in the values of g_A and the axial charge (see Section 3.6.4) have also been neglected in the analyses of the RAA thus far.

In Fig. 36 two cumulative sum spectra are presented. To obtain these spectra all the β spectra of the individual transitions of Table 7 have been summed by taking into account their branchings and their relative contributions (third and last columns of Table 7) to the total cumulative spectrum. For the "allowed shape" all the individual β spectra were assumed to be of the (unphysical) allowed shape and for the "forbidden shape" they were taken to be the ISM-computed shapes corresponding to the true first-forbidden β transitions. For the computed forbidden shapes the canonical value $g_V = 1.00$ was assumed, and for the axial–vector and axial-charge strengths the values $g_A = 0.70$ and $\varepsilon_{MEC} = 1.7$ (see Section 3.6.4) were adopted. The latter two values are rather realistic average values for nuclei in the mass range $A = 88 - 142$. The difference between the two spectra gives an idea about the importance of using the correct computed spectrum shapes, instead of the usually assumed allowed shapes, in the assessment of the confidence level of the RAA. From Fig. 36 it is seen that by assuming allowed shapes of the individual β spectra the average kinetic energy of the emitted electrons is slightly too high meaning that in the cumulative antineutrino spectrum the average antineutrino energy is a bit too low. This could have consequences for the confidence level of the RAA.

The RAA has been associated to disappearance of electron antineutrinos in short-baseline (10–100 m) reactor oscillation experiments. The disappearance can be explained quantitatively, e.g., by existence of sterile neutrinos. A $3 + 1$ scheme, with one sterile neutrino in eV mass scale, could explain the anomaly [311]. The same scheme could explain also the gallium anomaly [311], discussed in Section 4.4.4. An alternative explanation has been proposed recently [312,313]: the variations in the antineutrino fluxes stemming from the fissions of the nuclides ^{235}U and ^{239}Pu. The revaluation of these fluxes is proposed. In [308] it was found that both the effect of the RAA and the spectral "bump" is drastically mitigated by the ISM-calculated spectrum shapes for 29 key first-forbidden transitions and a subsequent Monte Carlo analysis for the rest of the first-forbidden transitions taking place in the fission products. This offers a possible nuclear-physics explanation of the RAA and the "bump".

3.6.3. Beta-spectrum shapes and the value of g_A

In [251] it was found that the shapes of β spectra could be used to determine the effective values of the weak coupling strengths g_V and g_A by comparing the computed spectrum with the measured one for forbidden non-unique β decays. This method was coined the spectrum-shape method (SSM). In this study also the next-to-leading-order corrections to the β-decay shape factor were included. In [251] the β-electron spectra were studied for the 4th-forbidden non-unique ground-state-to-ground-state β^- decay branches ^{113}Cd$(1/2^+) \rightarrow$ ^{113}In$(9/2^+)$ and ^{115}In$(9/2^+) \rightarrow$ ^{115}Sn$(1/2^+)$ using the microscopic quasiparticle–phonon model (MQPM, see Section 3.1.1) and the ISM. It was verified by both nuclear models that the β-spectrum shapes of both transitions are highly sensitive to the values of g_V and g_A and hence comparison of the calculated spectrum shape with the measured one opens a way to determine the values of these coupling strengths.[5] In

---

[5] In fact, the spectrum shape depends on the ratio g_V/g_A but the decay rate, and thus the half-life, depends on the absolute values of these weak couplings.

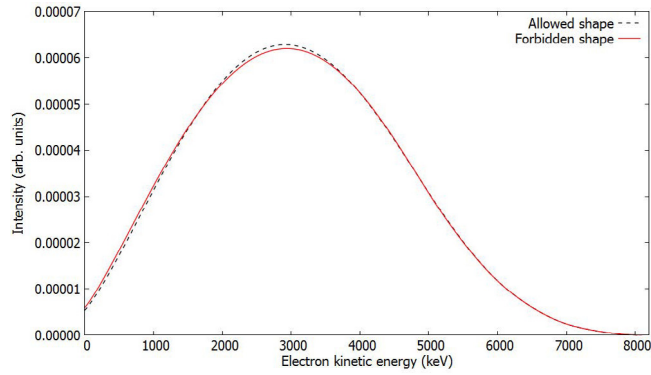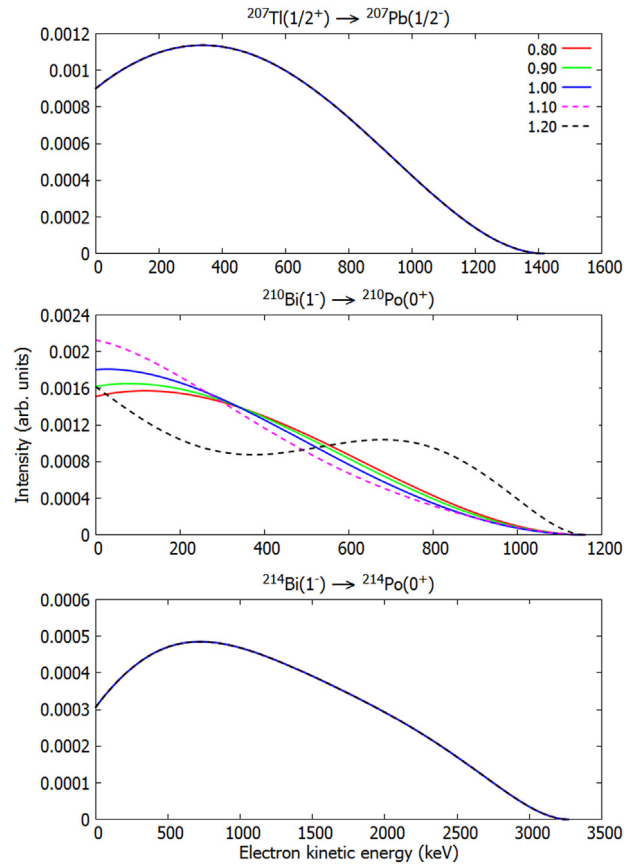**Fig. 37.** Normalized β spectra for the first-forbidden non-unique ground-state-to-ground-state β^- decays of ^{207}Tl [panel (a)], ^{210}Bi [panel (b)] and ^{214}Bi [panel (c)]. The value $g_V = 1.00$ was adopted in the calculations and the color coding represents the different adopted values for g_A (for the cases of panels (a) and (c) all the colored lines overlap in the adopted scales of the figures). Note also the Coulomb shift.

fact, this effect was overlooked in the earlier studies in Refs. [66,314]. In the study [251] it was furthermore noticed that the β-decay half-lives of the ^{113}Cd and ^{115}In nuclei could be reproduced with either relatively low or high values of g_A, the g_A values deduced from the spectrum shape being somewhere in the middle. This discrepancy may point to deficiencies in the nuclear models in this particular (A, Z) region of nuclei since in other regions, in particular in the region $60 \leq A \leq 140$, relevant for the RAA problem of the previous section, the half-lives of the nuclei could be reproduced by using g_A values that span the reasonable range of $0.6 \leq g_A \leq 0.9$. This was also noticed in the calculations referring to the axial-charge enhancement in Section 3.6.4. Future data on spectrum shapes will help analyze how consistently the SSM can reproduce the data of both spectrum shapes and the decay half-lives.

As a result of the studies in [251] it was found that for all values of g_A the best fits to spectrum-shape and half-life data were obtained by using the canonical CVC value $g_V = 1.0$ for the vector coupling strength. This finding contradicts to a certain extent the findings [303,315–317] for first-forbidden non-unique β decays, where strongly quenched values of g_V can be obtained in the fits to half-life data.[6] The work of [251] was extended to other nuclei and nuclear models in [252,279,280]. In particular, in [252] the microscopic interacting boson–fermion model (IBFM-2) (see Section 3.1.1) was used to analyze the β-spectrum shapes of the transitions ^{113}Cd$(1/2^+) \rightarrow {}^{113}In(9/2^+)$ and ^{115}In$(9/2^+) \rightarrow {}^{115}Sn(1/2^+)$. In all these studies it was found that the SSM is robust, not sensitive to the adopted mean field and nuclear model and its model Hamiltonian used to produce the wave functions of the participant initial and final nuclear states.

Examples of possible g_A dependencies are given in the previously discussed Fig. 35 and in the three-panel Fig. 37, where the ISM-computed first-forbidden non-unique ground-state-to-ground-state β^- decays of ^{207}Tl [panel (a)], ^{210}Bi [panel (b)] and ^{214}Bi [panel (c)] are depicted. The wave functions related to the decay of ^{207}Tl were calculated using the interaction khhe [319] in a valence space spanned by the proton orbitals $0g_{7/2}$, $1d$, $2s$ and $0h_{11/2}$, and the neutron orbitals $0h_{9/2}$, $1f$, $2p$

---

[6] It is, though, not excluded that different one-body operators in the complex expression (87) are renormalized with different values of g_V and g_A. This is a matter of future work and could also solve the problems in simultaneous matching of the half-life and spectrum-shape data in the case of the β decays of ^{113}Cd and ^{115}In.

Table 8

Selected forbidden non-unique β^--decay transitions and their sensitivity to the value of g_A. Here J_i (J_f) is the angular momentum of the initial (final) state, π_i (π_f) the parity of the initial (final) state, and K the degree of forbiddenness. The initial state is always the ground state (gs, column 2) and the final state is either the ground state (gs) or the n_f : *th*, $n_f = 1, 2, 3$, excited state (column 3) of the daughter nucleus. The branchings to the indicated final states are practically 100% in all cases. Column 4 indicates the sensitivity to the value of g_A, and the last column lists the nuclear models which have been used (thus far) to compute the β-spectrum shape. Here also references to the original works are given. The sensitivity "strong" refers to a similar g_A sensitivity as shown in Fig. 37, panel (b).

Transition	$J_i^{\pi_i}$ (gs)	$J_f^{\pi_f}$ (n_f)	K	Sensitivity	Nucl. model
^{87}Rb $\rightarrow$ ^{87}Sr	$3/2^-$	$9/2^+$ (gs)	3	Moderate	MQPM [279], ISM [280]
^{94}Nb $\rightarrow$ ^{94}Mo	6^+	4^+ (2)	2	Strong	ISM [280]
^{98}Tc $\rightarrow$ ^{98}Ru	6^+	4^+ (3)	2	Strong	ISM [280]
^{99}Tc $\rightarrow$ ^{99}Ru	$9/2^+$	$5/2^+$ (gs)	2	Strong	MQPM [279], ISM [280]
^{113}Cd $\rightarrow$ ^{113}In	$1/2^+$	$9/2^+$ (gs)	4	Strong	MQPM [251,279], ISM [251], IBFM-2 [252]
^{115}In $\rightarrow$ ^{115}Sn	$9/2^+$	$1/2^+$ (gs)	4	Strong	MQPM [251,279], ISM [252], IBFM-2 [252]
^{138}Cs $\rightarrow$ ^{138}Ba	3^-	3^+ (1)	1	Strong	ISM [318]
^{210}Bi $\rightarrow$ ^{210}Po	1^-	0^+ (gs)	1	Strong	ISM (this work)

Table 9

Dimensionless integrated shape functions $\tilde{C}$ (89) and their vector $\tilde{C}_V$, axial–vector $\tilde{C}_A$ and mixed components $\tilde{C}_{VA}$ for the β decays of Table 8. Also the nuclear model used to calculate $\tilde{C}$ is given. For the total integrated shape function $\tilde{C}$ the values of the coupling strengths were set to $g_V = g_A = 1.0$. The differences in the magnitudes of the components for different decay transitions reflect the differences in the (partial) half-lives associated to the transitions, and in particular the Bi→Po transition is fast.

Transition (Nucl. model)	$\tilde{C}_V$	$\tilde{C}_A$	$\tilde{C}_{VA}$	$\tilde{C}$
^{87}Rb($3/2^-$) $\rightarrow$ ^{87}Sr($9/2^+$) (MQPM)	1.531×10^{-13}	2.718×10^{-14}	-1.264×10^{-13}	5.39×10^{-14}
^{87}Rb($3/2^-$) $\rightarrow$ ^{87}Sr($9/2^+$) (ISM)	1.185×10^{-13}	2.082×10^{-14}	-9.734×10^{-14}	4.20×10^{-14}
^{94}Nb(6^+) $\rightarrow$ ^{94}Mo(4^+) (ISM)	1.598×10^{-8}	1.469×10^{-8}	-3.058×10^{-8}	1.03×10^{-10}
^{98}Tc(6^+) $\rightarrow$ ^{98}Ru(4^+) (ISM)	2.723×10^{-8}	2.544×10^{-8}	-5.254×10^{-8}	1.21×10^{-10}
^{99}Tc($9/2^+$) $\rightarrow$ ^{99}Ru($5/2^+$) (ISM)	2.240×10^{-9}	2.130×10^{-9}	-4.361×10^{-9}	8.78×10^{-12}
^{113}Cd($1/2^+$) $\rightarrow$ ^{113}In($9/2^+$) (MQPM)	1.925×10^{-19}	2.094×10^{-19}	-4.002×10^{-19}	1.38×10^{-21}
^{113}Cd($1/2^+$) $\rightarrow$ ^{113}In($9/2^+$) (ISM)	1.678×10^{-19}	1.825×10^{-19}	-3.494×10^{-19}	9.90×10^{-22}
^{113}Cd($1/2^+$) $\rightarrow$ ^{113}In($9/2^+$) (IBM-2)	3.228×10^{-20}	3.007×10^{-20}	-6.106×10^{-20}	1.28×10^{-21}
^{115}In($9/2^+$) $\rightarrow$ ^{115}Sn($1/2^+$) (MQPM)	6.503×10^{-18}	6.126×10^{-18}	-1.256×10^{-17}	6.49×10^{-20}
^{115}In($9/2^+$) $\rightarrow$ ^{115}Sn($1/2^+$) (ISM)	3.146×10^{-18}	3.851×10^{-18}	-6.939×10^{-18}	5.74×10^{-20}
^{115}In($9/2^+$) $\rightarrow$ ^{115}Sn($1/2^+$) (IBM-2)	5.531×10^{-19}	5.444×10^{-19}	-1.065×10^{-18}	3.25×10^{-20}
^{210}Bi(1^-) $\rightarrow$ ^{210}Po(0^+) (ISM)	0.9450	0.6368	-1.549	0.0332

and $0i_{13/2}$. For the heavier nuclei, ^{210}Bi and ^{214}Bi, the interaction khpe [319] was adopted. For ^{210}Bi the valence space was spanned by the proton orbitals $0h_{9/2}$, $1f$, $2p$ and $0i_{13/2}$, and neutron orbitals $0i_{11/2}$, $1g$ and $2d_{5/2}$.

The β-spectrum shapes of ^{207}Tl and ^{214}Bi are only slightly g_A dependent, but for ^{210}Bi the dependence is extremely strong. This makes ^{210}Bi an excellent candidate for the application of the SSM once new measurement(s), updating the old one [320], of the spectrum shape are performed. This is so far the only known first-forbidden β transition with a strong g_A dependence. Other thus far known strongly g_A-dependent decay transitions are listed in Table 8. Table 8 summarizes the exploratory works of [251,252,279,280] in terms of listing the studied β-decay transitions which are potentially measurable in rare-events experiments. An extended version of the table, including cases with strong g_A dependence but small branchings and vice versa, is given in [30]. A particularly interesting case is the decay of ^{138}Cs which will be elaborated further in Section 3.6.4. Usually only the non-unique forbidden β-decay transitions can be sensitive enough to g_A to be measured even when the next-to-leading-order terms are included in the β-decay shape factor [251].

In Table 9 the dimensionless integrated shape functions $\tilde{C}$ (89) have been decomposed into their vector $\tilde{C}_V$, axial–vector $\tilde{C}_A$ and mixed vector–axial–vector components $\tilde{C}_{VA}$ for the β decays of Table 8. A characteristic of the numbers of Table 9 is that the magnitudes of the vector, axial–vector, and mixed components are of the same order of magnitude, and the vector and axial–vector components have the same sign whereas the mixed component has the opposite sign. This makes the three components largely cancel each other and the resulting magnitude of the total dimensionless integrated shape function is usually a couple of orders of magnitude smaller than its components. Thus the integrated shape function becomes sensitive to the value of g_A, as seen in Fig. 37, panel (b), for the decay of ^{210}Bi.

For the β spectrum of the decays of ^{113}Cd and ^{115}In there are calculations available in three different nuclear-theory frameworks as shown in Tables 8 and 9. As visible in Table 9, an interesting feature of the components of the integrated shape functions $\tilde{C}$ is that the MQPM and ISM results are close to each other whereas the numbers produced by IBM-2 are clearly smaller. In spite of this, the total value of $\tilde{C}$ is roughly the same in all three theory frameworks leading to similar half-life predictions of the three nuclear models for $g_V = g_A = 1.0$.

3.6.4. Axial-charge enhancement

Here we discuss first-forbidden non-unique $\Delta J = |J_i - J_f| = 0$ type of transitions, where J_i (J_f) is the initial-state (final-state) spin of the mother (daughter) nucleus. In this particular case the shape factor (87) has to be supplemented with a term
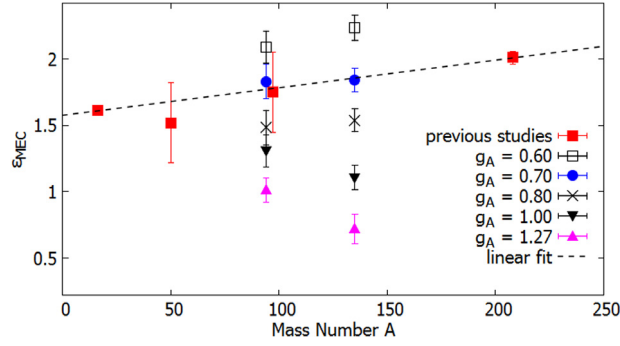
Fig. 38. Obtained enhancement factors ϵ_{MEC} of the previous studies and the present study as functions of the mass number A. The red squares represent the previous systematic studies done in the $A \approx 16$ and $A \approx 208$ regions and the separate studies done for ^{50}K and ^{96}Y. The other points represent the results of this study for different effective values of g_A. The linear fit is an error-weighted fit, where the results of the previous studies and the present study with $g_A = 0.70$ are used.

$C^{(1)}(w_e)$ [250,304,321,322]. Then the shape factor can be cast in the simple form [250,315,321]

$$C(w_e) = K_0 + K_1 w_e + K_{-1}/w_e + K_2 w_e^2 , \tag{94}$$

where the factors K_n contain the NMEs (6 different, altogether) of transition operators $\mathcal{O}$ of angular-momentum content (rank of a spherical tensor) $\mathcal{O}(0^-)$, $\mathcal{O}(1^-)$, and $\mathcal{O}(2^-)$, where the parity indicates that the initial and final nuclear states should have opposite parities according to Table 5. In the leading order in the non-relativistic reduction these operators contain the pieces [27]

$$\mathcal{O}(0^-) : g_A(\gamma^5)\frac{\sigma \cdot \mathbf{p}_e}{M_N} \; ; \; ig_A\frac{\alpha Z_f}{2R}(\sigma \cdot \mathbf{r}) , \tag{95}$$

$$\mathcal{O}(1^-) : g_V\frac{\mathbf{p}_e}{M_N} \; ; \; g_A\frac{\alpha Z_f}{2R}(\sigma \times \mathbf{r}) \; ; \; ig_V\frac{\alpha Z_f}{2R}\mathbf{r} , \tag{96}$$

$$\mathcal{O}(2^-) : \frac{i}{\sqrt{3}}g_A\,[\sigma\mathbf{r}]_2\,\sqrt{\mathbf{p}_e^2 + \mathbf{q}_\nu^2} , \tag{97}$$

where $\mathbf{p}_e$ ($\mathbf{q}_\nu$) is the electron (neutrino) momentum, $\mathbf{r}$ the radial coordinate, and the square brackets in (97) denote angular-momentum coupling. The matrix elements of the operators (95) and (96) are suppressed relative to the Gamow–Teller matrix elements by the small momentum $\mathbf{p}_e$ of the electron and the large nucleon mass M_N or the small value of the fine-structure constant α. The matrix element of (97) is suppressed by the small electron and neutrino momenta. The axial operator $\sigma \cdot \mathbf{p}_e$ and vector operator $\mathbf{r}$ trace back to the time component of the axial current A^μ in (9) and vector current V^μ in (8), and the rest of the operators stems from the space components of V^μ and A^μ.

In the case of the axial-charge NME, hereafter called the γ_5 NME, we are interested in the $\mathcal{O}(0^-)$ operator $\sigma \cdot \mathbf{p}_e$ of (95), i.e. the operator

$$g_A(\gamma_5)\sigma \cdot \mathbf{p}_e , \tag{98}$$

where $g_A(\gamma_5)$ is the corresponding coupling strength which can be written in the form

$$g_A(\gamma_5) = (1 + \varepsilon_{\mathrm{MEC}})g_A , \tag{99}$$

where the enhancement factor $\varepsilon_{\mathrm{MEC}}$ stems from the meson-exchange currents (MEC). Here the next-to-leading-order terms in the Behrens–Bühring expansion [250] are included, and the atomic screening effects and radiative corrections [252] are taken into account.

The enhancement of the axial-charge NME γ_5 due to nuclear medium effects in the form of meson-exchange currents was first suggested in Refs. [323–325]. An enhancement of 40%–70% over the impulse-approximation value was predicted based on chiral-symmetry arguments and soft-pion theorems. This enhancement seems fundamental in nature and insensitive to nuclear-structure aspects [326,327]. Systematic shell-model studies of the γ_5 matrix elements in the $A \approx 16$, $A \approx 40$, and $A \approx 208$ regions indicated enhancements of 60%–100% [328–330]. In [331] the exceptionally large enhancement of the γ_5 NME in heavy nuclei, witnessed in the shell-model studies of Warburton [330], was reproduced by introducing an effective Lagrangian incorporating approximate chiral and scale invariance of the QCD. The γ_5 NME is one of the two rank-zero matrix elements contributing to first-forbidden $\Delta J = 0, J^+ \leftrightarrow J^-$, transitions, highly relevant, e.g., for the RAA as shown in Table 7 of Section 3.6.2. It plays an important role in the decay rates of many of these transitions and therefore a significant enhancement of this matrix element can also affect the shapes of the corresponding beta spectra.

The previous systematic studies in the $A \approx 16$ [328] and $A \approx 208$ [330] regions have yielded enhancement factors 1.61 ± 0.03 and 2.01 ± 0.05, respectively. In addition, separate studies for ^{50}K [328] and ^{96}Y [332] yielded the enhancement
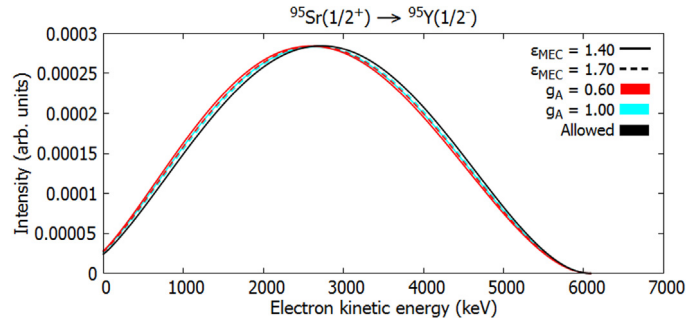
Fig. 39. Normalized β spectra for the first-forbidden non-unique ground-state-to-ground-state β^- decay of ^{95}Sr. The value $g_V = 1.00$ was adopted in the calculations and the color coding represents the different adopted values for g_A and the enhancement (ε_{MEC}) of the axial charge. For comparison also the allowed spectrum shape is shown.
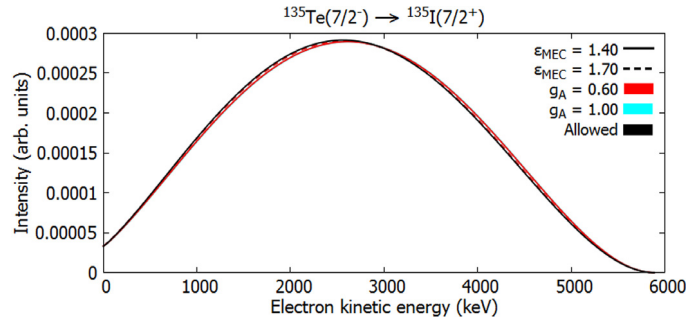
Fig. 40. Normalized β spectra for the first-forbidden non-unique ground-state-to-ground-state β^- decay of ^{135}Te. The value $g_V = 1.00$ was adopted in the calculations and the color coding represents the different adopted values for g_A and the enhancement (ε_{MEC}) of the axial charge. For comparison also the allowed spectrum shape is shown.

factors 1.52 and 1.75 ± 0.30. Calculating ϵ_{MEC} for different values of g_A in the $A \approx 95$ and $A \approx 135$ regions [318], and comparing with the previous results allows to access the mesonic enhancement as a function of mass number in different scenarios. The results are presented in Fig. 38. For ^{50}K the error is assumed to be 0.30 as it is for ^{96}Y. It is interesting that when the free-nucleon value $g_A = 1.27$ is adopted, no mesonic enhancement is obtained for $A \approx 95$ and for $A \approx 135$, and no renormalization of the axial-charge matrix element is needed to reproduce the experimental half-lives. For $g_A = 0.70$ one obtains a clear linear trend for the mass dependence of the mesonic enhancement factor:

$$\epsilon_{MEC} = 1.576 + 2.08 \times 10^{-3} A. \tag{100}$$

This finding suggests that the effective value $g_A \approx 0.7$ would be appropriate for the medium-mass nuclei, at least for the $J^+ \leftrightarrow J^-$ β-decay transitions.

An interesting by-product of the study of [318] is that the β spectrum of the decay of ^{138}Cs is rather strongly dependent on the value of g_A (see Table 8) but not at all on the mesonic enhancement ϵ_{MEC}. Thus the SSM can be used to determine the effective value of g_A in the $A \approx 135$ region. The study [318] shows that this value of g_A is in almost one-to-one correspondence with a value of ϵ_{MEC}, implying that the measurement of the β spectrum of the decay of ^{138}Cs not only gives the value of g_A but also the value of ϵ_{MEC} for the medium-heavy nuclei. This could have far-reaching consequences for, e.g., the analyses of the reactor-antineutrino anomaly discussed in Section 3.6.2.

Examples of possible g_A and $g_A(\gamma_5)$ dependencies of β spectra are given in Figs. 39 and 40 where the ISM-computed first-forbidden non-unique ground-state-to-ground-state β^- decays of ^{95}Sr and ^{135}Te are depicted. The related ISM calculations were performed in the following valence spaces: For the decay of ^{95}Sr a model space including the proton orbitals $0f_{5/2}$, $1p_{3/2}$, $1p_{1/2}$ and $0g_{9/2}$, and the neutron orbitals $1d_{5/2}$, $1d_{3/2}$ and $2s_{1/2}$ was used together with the interaction glbepn [332]. The interaction glbepn is a bare G-matrix interaction which also has an adjusted version glepn, where two-body matrix elements from Gloeckner [333] and Ji and Wildenthal [334] have been adopted. The decay of ^{135}Te was calculated using a model space spanned by the proton orbitals $0g_{7/2}$, $1d_{5/2}$, $1d_{3/2}$, $2s_{1/2}$ and $0h_{11/2}$, and the neutron orbitals $0h_{9/2}$, $1f_{7/2}$, $1f_{5/2}$, $2p_{3/2}$, $2p_{1/2}$ and $0i_{13/2}$ with the effective interactions jj56pnb [335].

It is seen that neither the effective value of g_A nor the enhancement (99) of $g_A(\gamma_5)$ affect the spectrum shape in an easily measurable way. Hence, in these cases the comparison with the experimental half-lives is the only way to pin down the amount of enhancement (99), and its possible mass dependence. Only a further exploratory work could tell if there are nuclear transitions where the β spectra are sensitive to the value of $g_A(\gamma_5)$. It should also be borne in mind that the
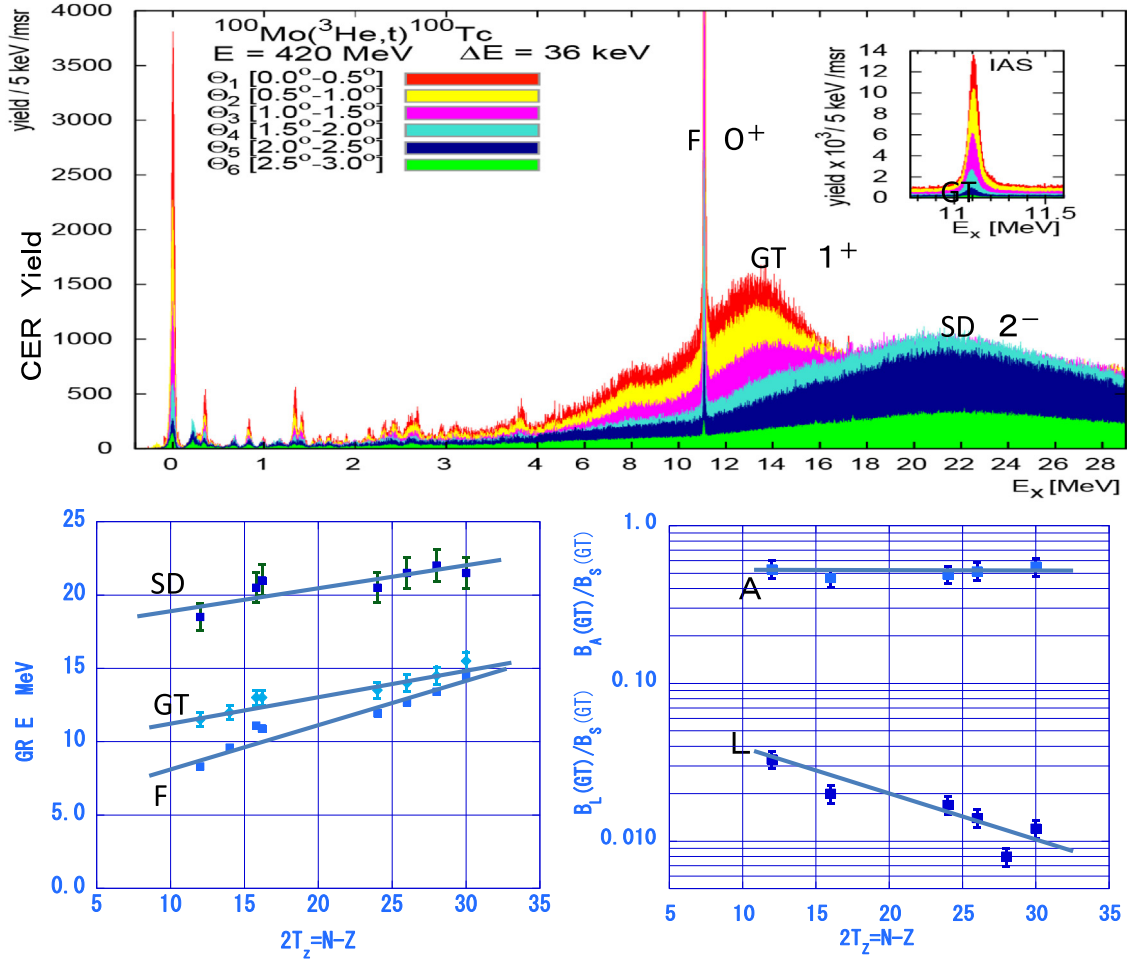
Fig. 41. Top: Energy spectrum of the (^{3}He,t) reaction on ^{100}Mo [97]. The spectra at the angle bins of θ_i with i =1,2,3,4,5,6 are overlaid to illustrate the angular distributions. Bottom left: Fermi (IAS), GTR and IVSDR energies in units of MeV for DBD nuclei as functions of $2T_z = N - Z$. To avoid the overlap, the ^{100}Mo and ^{96}Zr data at $N - Z = 16$ are plotted at $N - Z = 15.8$ and 16.2, respectively. Bottom right: Ratios of the summed GT strengths B_L(GT) and B_A(GT) to the sum-rule limit of B_S(GT) $= 3(N - Z)$ as functions of $2T_z = N - Z$.

spectrum shapes of $J^+ \leftrightarrow J^-$ transitions play an important role in the investigations of the validity of the RAA (see Table 7 in Section 3.6.2).

3.7. Axial–vector weak responses in low- and high-excitation regions

Neutrino–nuclear τ^- responses in a wide excitation region have been extensively studied by using high energy-resolution CERs at RCNP (Research Center for Nuclear Physics at Osaka University, Japan [56]), as discussed in Section 2.3. The (^{3}He,t) CERs at 0.42 GeV preferentially excite the axial–vector isospin–spin ($\tau^-\sigma$) states as studied in DBD nuclei [95–100]. In this section, we briefly discuss general features of axial–vector GT (0^+) and IVSD (isovector spin-dipole 2^-) strengths (responses) in low- and high-excitation regions on the basis of the observed CER data.

The energy spectra of the ^{100}Mo(^{3}He,t)^{100}Tc reactions at the angles from $\theta_i = 0$ degrees to $\theta_i = 3$ degrees are shown in Fig. 41. The spectra clearly show that (i): the Fermi (τ^-) strength is concentrated in the sharp IAS (the Fermi GR) at the high excitation region, leaving no Fermi strength in other regions, (ii): the GT ($\tau\sigma$) and IVSD ($\tau\sigma rY_1$) strengths are mostly concentrated, respectively, in the broad GTR and IVSDR at the higher-excitation region and (iii): the small GT and SD strengths are located at the low-excitation region, as discussed in Sections 1.4 and 2.3.

The Fermi GR (IAS), GTR and IVSDR are expressed as coherent (in-phase) τ^-, $\tau^-\sigma$ and $\tau^-\sigma f(r)Y_1$ excitations of all relevant neutron-hole–proton-particle states. The excitation energies are pushed up to the high excitation region due to the repulsive τ and $\tau\sigma$ interactions. The GR energies are derived from the observed peak energies of the resonances, being corrected for the contributions from the quasi-free (QF) charge-exchange scatterings in the higher-excitation region. They are shown as
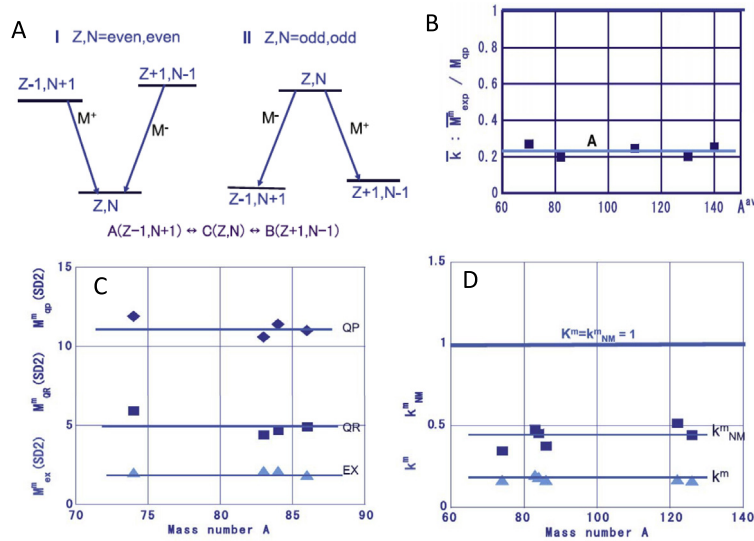
Fig. 42. Geometrical-mean NMEs M^m for GT and SD $\beta^\pm$ transitions. Panel A: Single $\beta^\pm$ decay schemes for even–even and odd–odd nuclei. Panel B: Average coefficients $\bar{k} = \bar{M}^m_{exp}/M_{qp}$ for the five discussed mass regions. $\bar{M}^m_{exp}$ is the average experimental GT NME, and M_{qp} is the quasiparticle GT NME. Panel C: Geometrical-mean SD NMEs for $0 \leftrightarrow 2^-$ decays. $M(SD2)$, $M^m_{qp}(SD2)$, and M^m_{QR} are the experimental, quasiparticle and pnORPA NMEs, respectively. Panel D: The ratio k^m of the observed to quasiparticle SD NMEs and the ratio k^m_{NM} of the observed to pnQRPA SD NMEs [104,105].

functions of $2T_z = N - Z$, with T_z being the isospin z-component, in Fig. 41. The IAS, GTR and IVSDR energies for DBD nuclei of current interest are expressed approximately as

$$E(\text{IAS}) \approx 5 + 0.6T_z \,, \quad E(\text{GT}) \approx 9 + 0.4T_z \,, \quad E(\text{SD}) \approx 16.5 + 0.4T_z \,, \tag{101}$$

where the energies are all in units of MeV.

The simple expressions of Eq. (101) reproduce the observed energies obtained in the recent CERs at RCNP and in other experiments [336–338] within 1 MeV, and are consistent with other empirical expressions [55,339] within around 1 MeV. Note that the IVSDR energy increases with the same slope as the GTR energy with increasing T_z, and the IVSDR is higher in energy than the GTR by $\hbar\omega \approx 7.5$ MeV, reflecting the effect caused by the radial operator **r** involved in the IVSD excitation. The energies of the IAS increase faster with increasing T_z than those of the GTR and IVSDR. The measured GTR and IVSDR energies are used to lend help to pnQRPA calculations for $0\nu\beta\beta$ NMEs, as recently discussed in [340].

Next we discuss the summed GT strengths, $B_L(\text{GT})$ for the low-lying GT states, and $B_A(\text{GT})$ for all GT states including the GTR. Here the GTR strength is obtained by assuming a Lorentzian shape of the GR and a quasi-free-scattering shape at the higher excitation region beyond $E \approx 20$ MeV. The GTR tail at $E = 3 - 4$ MeV in ^{76}Ge is corrected for. Fig. 41 shows the ratios of the summed strengths of $B_L(\text{GT})$ and $B_A(\text{GT})$ to the sum-rule limit of $B_S(\text{GT}) = 3(N - Z)$ as functions of $2T_z = N - Z$. Here the limit is practically exhausted by the τ^- strengths since in the presently discussed medium-heavy and heavy nuclei the τ^+ p→n contributions are blocked by the (large) excess of neutrons.

The summed strength $B_L(\text{GT})$ for the low-lying states is only $3 - 10\%$ of the sum-rule limit since the strength is mostly pushed up into the GTR. The reduction is partly due to the repulsive $\sigma\tau$ correlations [4,104,105]. The summed strength $B_A(\text{GT})$ for all GT states, including the GTR strength, is around 50–55% of the sum-rule limit, indicating a reduction of the GT strengths, as seen in other CERs [336,337,341].

Actually, the large CER cross section at forward angles in the higher excitation region of $E = 20$–50 MeV is a kind of quasi-free charge-exchange scattering to the unbound continuum region. The quasi-free contribution includes several (Δn) $\hbar\omega$ excitations associated with angular-momentum transfers of $\Delta l = 0$–$6\hbar$ and radial-node changes of $\Delta n = 2 - 6$, which are not GT strengths with $\Delta n = \Delta l = 0$. On the other hand, the pn CER experiments claim that the large $\Delta l = 0$ cross sections at the 30–50 MeV region are assigned mainly to the GT strength ($\Delta n = 0$) to be consistent with the sum-rule limit [342,343]. The GT strength in the continuum region above GTR is discussed in [344]. In fact, extraction of the absolute GT strength in the high-excitation region, if it exists, is a challenge. Theoretically, the interfering contributions from the isovector spin-monopole excitations to the GTR have been discussed in [345,346]. The isovector spin-multipole GRs have been discussed in [217] for several nuclei involved in $\beta\beta$ decays.

We note that the experimental single β GT and SD NMEs in the medium-mass and heavy-mass region are shown to be reduced with respect to the quasiparticle and pnQRPA NMEs by the reduction coefficients of $k \approx 0.4$ and $k_{NM} \approx 0.5$ (nuclear-medium effect), as shown in Fig. 42 [104,105].

The reduction of the GT strengths suggests some nuclear-medium and non-nucleonic (meson, isobar) effects [28,219]. The isobar effect is discussed for the first-forbidden β transitions in [347]. The reduction (quenching) of the summed GT
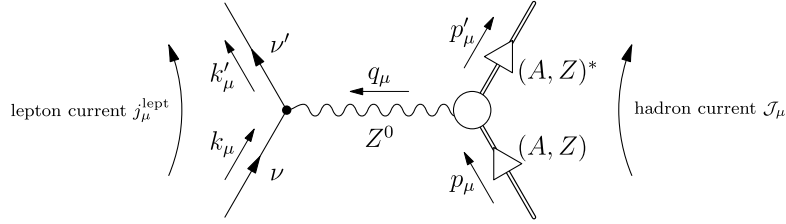
Fig. 43. Schematic presentation of a neutral-current neutrino–nucleus scattering off a nucleus (A, Z) mediated by the neutral weak boson Z^0. The transferred four-momentum is $q_\mu = k'_\mu - k_\mu = p_\mu - p'_\mu$.

strength is intriguing in view of the reduced effective g_A suggested for low-lying GT states, as discussed in Section 3.1.2, and low-lying SD states as discussed in Section 3.3. Also the two-neutrino and neutrinoless DBD NMEs can be affected by this quenching, as discussed in Sections 1.4 and 3.1.3, and recently in [216].

4. (Anti)neutrino–nuclear responses for astro-neutrino physics

The (anti)neutrino is a neutral particle introduced by Pauli in 1930 to restore the energy conservation in beta decay and given the name "neutrino" by Fermi in 1932. Since that time, the (anti)neutrino and its properties have attracted a great interest in theoretical and experimental studies of particle, nuclear and astro-neutrino physics. Neutrino-oscillation experiments have provided evidence on the non-zero neutrino mass in the form of neutrino-mass differences. However, the absolute value of the neutrino mass is still an open question [21,23]. Further questions, such as the nature of neutrino, i.e. it being either a Dirac or a Majorana particle, and the mass hierarchy still remain to be studied in future.

4.1. (Anti)neutrino–nucleus scattering cross sections

In this section a brief summary of the main points of the formalism of the neutral-current (NC) and charged-current (CC) (anti)neutrino–nucleus scattering is given. Measured cross sections of neutrino–nucleus scattering at energies relevant for supernova neutrinos ($\lesssim 80$ MeV) are available only for the deuteron [348], ^{12}C [349,350] and ^{56}Fe [350]. Theoretical predictions of astrophysical neutrino–nuclear responses for relevant nuclear targets are therefore indispensable [351,352]. The general framework for the treatment of semileptonic processes in nuclei, first introduced in Refs. [353–356] and summarized in [357], is followed. Further closed analytical expressions in the harmonic-oscillator basis was derived in [358]. Computations performed with this formalism (see e.g. [359]) show satisfying agreement between theory and experiment both for charged-current neutrino–nucleus scattering and for electron scattering for energies of the incoming particle of $E \lesssim 80$ MeV, appropriate for the majority of astro-neutrinos. However, it should be noted that for the treatment of neutrinos with energies of the order of several hundreds of MeV or larger, which are of interest e.g. for neutrino-oscillation experiments [360], extensions of the theory are required. Such extensions are the inclusion of competing mechanisms (e.g. pion production) and many-body correlations beyond the impulse approximation [360]. We refer to [361,362] for a more comprehensive treatment of the scattering problem.

4.1.1. General features of the NC and CC neutrino–nucleus scattering

In a NC reaction an (anti)neutrino is scattered from a nucleus (A, Z) leading to the ground state (elastic scattering) or an excited state of the same nucleus (A, Z) and the scattered (anti)neutrino:

$$\nu_l + (A, Z) \rightarrow (A, Z)^* + \nu'_l \,, \tag{102}$$

$$\bar{\nu}_l + (A, Z) \rightarrow (A, Z)^* + \bar{\nu}'_l \,, \tag{103}$$

where l stands for either an electron (e), muon (μ) or tau (τ) flavor, A is the nuclear mass number and Z the atomic number. Here the asterisk ($*$) stands for either the ground or excited state of the final nucleus. These reactions proceed via the exchange of a neutral Z^0 boson as depicted in the schematic diagram of Fig. 43. For an extensive discussion of the NC-current formalism see [357,363]. In the case of, e.g., lead isotopes we then have the reactions

$$\nu_l + {}^A\text{Pb} \rightarrow {}^A\text{Pb}^* + \nu'_l \,, \tag{104}$$

$$\bar{\nu}_l + {}^A\text{Pb} \rightarrow {}^A\text{Pb}^* + \bar{\nu}'_l \,. \tag{105}$$

In a CC reaction a neutrino [antineutrino] is scattered from a nucleus (A, Z) leading to a final nucleus $(A, Z+1)$ $[(A, Z-1)]$ and an emitted lepton [antilepton]:

$$\nu_l + (A, Z) \rightarrow (A, Z+1) + l^- \,, \tag{106}$$

$$\bar{\nu}_l + (A, Z) \rightarrow (A, Z-1) + l^+ \,. \tag{107}$$
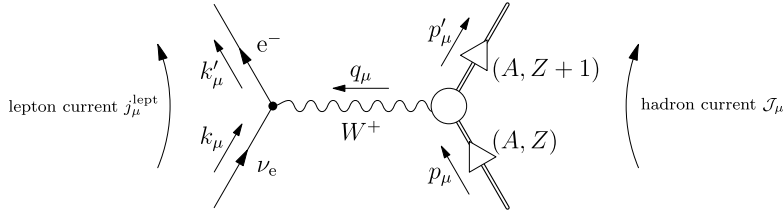
Fig. 44. Schematic presentation of a charged-current neutrino–nucleus scattering off a nucleus (A, Z) mediated by the positively-charged weak boson W^+. The transferred four-momentum is $q_\mu = k'_\mu - k_\mu = p_\mu - p'_\mu$.
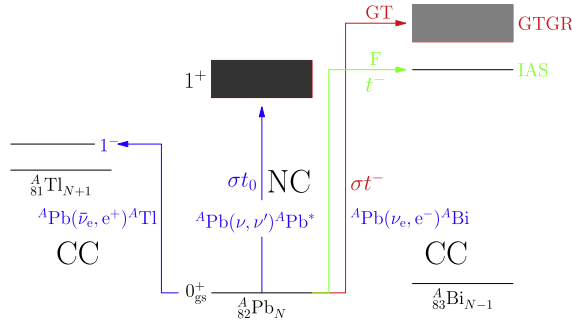
Fig. 45. Schematic presentation of the neutral-current and charged-current neutrino and antineutrino scatterings off lead targets.

These reactions proceed via the exchange of a charged W^+ or W^- boson as depicted in the schematic diagram of Fig. 44. In the case of the supernova neutrinos only the creation of an electron or a positron in the final state is possible due to the moderate energy ($E_\nu \lesssim 70$ MeV) of the incoming (anti)neutrino. A more complete treatise on the CC neutrino–nucleus scattering is given, e.g., in [361]. In the case of lead isotopes we then have the transitions

$$\nu_e + {}^A\text{Pb} \rightarrow {}^A\text{Bi} + e^- , \tag{108}$$

$$\bar{\nu}_e + {}^A\text{Pb} \rightarrow {}^A\text{Tl} + e^+ . \tag{109}$$

Both the NC and CC reactions for the lead targets are depicted in Fig. 45. If the residual nucleus in (106)–(109) is excited, it decays by emitting γ rays or particles, depending on whether the excitation energy is below or above the particle binding energy. Then the neutrino energy is obtained by measuring the CC electron energy and/or the emitted γ rays and the emitted particles.

4.1.2. NC and CC scattering cross sections

Here the energy of the impinging neutrino is assumed to be low, $E_\nu \lesssim 100$ MeV, and thus the transferred four-momentum is small compared to the mass of the exchanged weak boson, i.e. $Q^2 = -q_\mu q^\mu \ll M^2_{Z^0, W_\pm}$. In this case the corresponding matrix element of the effective Hamiltonian can be written in the form [361,363]

$$\langle f|H_{\text{eff}}|i\rangle = \frac{G}{\sqrt{2}} \int d^3 r l_\mu e^{-i\mathbf{q}\cdot\mathbf{r}} \langle f|J^\mu_H(\mathbf{r})|i\rangle , \tag{110}$$

where $J^\mu_H(\mathbf{r})$ denotes the hadronic current in Eq. (7) of Section 1.2 and l_μ is the leptonic matrix element

$$l_\mu = e^{i\mathbf{q}\cdot\mathbf{r}} \langle \ell|j_{L,\mu}(r)|\nu\rangle . \tag{111}$$

Here $j_{L,\mu}$ is the leptonic current (3) for NC scattering and (4) for CC scattering, defined in Section 1.2. For the NC and CC processes the coupling constant G is given in Eq. (5).

The final (f) and initial (i) states are assumed to have a well-defined angular momentum J and parity π. Then, the double differential cross section for (anti)neutrino scattering from an initial state $J^{\pi_i}_i$ to a final state $J^{\pi_f}_f$ is given by

$$\left[\frac{d^2\sigma_{i\rightarrow f}}{d\Omega dE_{\text{exc}}}\right]_{\nu/\bar{\nu}} = \frac{G^2|\mathbf{k}'|E_{\mathbf{k}'}}{\pi(2J_i + 1)} F_{\nu/\bar{\nu}} \left(\sum_{J\geqslant 0}\sigma^J_{\text{CL}} + \sum_{J\geqslant 1}\sigma^J_{\text{T}}\right), \tag{112}$$

where $E_{\text{exc}} = E_{\mathbf{k}} - E_{\mathbf{k}'}$ is the excitation energy with respect to the ground state of the target nucleus, $\mathbf{k}$ ($\mathbf{k}'$) is the three-momentum of the incoming neutrino (outgoing neutrino (NC)/lepton (CC)) and $E_{\mathbf{k}}$ ($E_{\mathbf{k}'}$) is the corresponding energy. For the

NC and CC scatterings we have the definitions

$$F_{\nu/\bar{\nu}} = 1 \quad \text{(NC scattering)}; \quad F_{\nu/\bar{\nu}} = F(\pm Z_f, E_{\mathbf{k}'}) \quad \text{(CC scattering)}, \tag{113}$$

where $F(\pm Z_f, E_{\mathbf{k}'})$ is the Fermi function, which accounts for the distortion of the final-state electron $(+Z_f)$ or positron $(-Z_f)$ wave function by the Coulomb field of the final nucleus of atomic number Z_f. Here σ_{CL}^J is the Coulomb-longitudinal component and σ_{T}^J is the transverse component defined as

$$
\begin{aligned}
\sigma_{\mathrm{CL}}^J =& (1 + a\cos\theta)|(J_f\|\mathcal{M}_J(q)\|J_i)|^2 \\
&+ (1 + a\cos\theta - 2b\sin^2\theta)|(J_f\|\mathcal{L}_J(q)\|J_i)|^2 \\
&+ \frac{E_{\mathbf{k}} - E_{\mathbf{k}'}}{q}(1 + a\cos\theta + c) \\
&\times 2\mathrm{Re}[(J_f\|\mathcal{L}_J(q)\|J_i)(J_f\|\mathcal{M}_J(q)\|J_i)^*],
\end{aligned}
\tag{114}
$$

and

$$
\begin{aligned}
\sigma_{\mathrm{T}}^J =& (1 - a\cos\theta + b\sin^2\theta) \\
&\times \left[|(J_f\|\mathcal{T}_J^{\mathrm{mag}}(q)\|J_i)|^2 + |(J_f\|\mathcal{T}_J^{\mathrm{el}}(q)\|J_i)|^2\right] \\
&\mp \frac{(E_{\mathbf{k}} + E_{\mathbf{k}'})}{q}\left(1 - a\cos\theta - c\right) \\
&\times 2\mathrm{Re}[(J_f\|\mathcal{T}_J^{\mathrm{mag}}(q)\|J_i)(J_f\|\mathcal{T}_J^{\mathrm{el}}(q)\|J_i)^*].
\end{aligned}
\tag{115}
$$

In the above expressions the minus sign refer to neutrino and the plus sign to antineutrino. In addition, we have introduced the notation

$$a = \sqrt{1 - \frac{m_f^2}{E_{\mathbf{k}'}^2}}, \tag{116}$$

$$b = \frac{a^2 E_{\mathbf{k}} E_{\mathbf{k}'}}{q^2}, \tag{117}$$

$$c = \frac{m_f^2}{q E_{\mathbf{k}'}}, \tag{118}$$

where the magnitude of the three-momentum transfer q is given by

$$q = |\mathbf{q}| = \sqrt{(E_{\mathbf{k}} - a E_{\mathbf{k}'})^2 + 2a E_{\mathbf{k}} E_{\mathbf{k}'}(1 - \cos\theta)}. \tag{119}$$

Here m_f is the mass of the final-state lepton, and thus $m_f = 0$ for the NC scattering.

The definition of the operators $\mathcal{T}_{JM} = \mathcal{M}_{JM}, \mathcal{L}_{JM}, \mathcal{T}_{JM}^{\mathrm{el}}, \mathcal{T}_{JM}^{\mathrm{mag}}$ is given in [362]. In general, these operators contain both vector and axial–vector pieces, i.e. $\mathcal{T}_{JM} = T_{JM}^{\mathrm{V}} - T_{JM}^{\mathrm{A}}$. They depend on the nuclear form factors $F_{1,2}^{\mathrm{V}}(Q^2)$ (Vector), $F^{\mathrm{A}}(Q^2)$ (axial–vector), and $F^{\mathrm{P}}(Q^2)$ (pseudo-scalar), which depend on the four-momentum transfer $Q^2 = -q_\mu q^\mu$ [361]. These form factors have been given for the NC processes in [363] and for the CC processes in [361]. For small momentum transfers the cross sections are typically dominated by Gamow–Teller-like transitions mediated by the operator $F^{\mathrm{A}}(q)j_0(qr)\boldsymbol{\sigma}$ and Fermi-like ones which proceed via the operator $F^{\mathrm{V}}(q)j_0(qr)\mathbf{1}$. Additionally, for supernova neutrinos, the spin-dipole-like transitions of the form $F^{\mathrm{A}}(q)j_1(qr)[\mathbf{Y}_1\boldsymbol{\sigma}]_{0^-,1^-,2^-}$ have turned out to be important.

The special case of coherent elastic neutrino–nucleus scattering is discussed later, in Section 4.5.1.

4.2. Solar-neutrino–nuclear responses

4.2.1. Solar-neutrino nuclear matrix elements and detection

Solar neutrinos provide unique opportunities to study physics of the sun and the neutrino oscillations, as discussed in detail in recent review articles [6,7] and references therein. The solar neutrinos are composed of the low-energy high-intensity pp neutrinos with $E \leq 0.42$ MeV, the medium-energy ^{7}Be, CNO and pep neutrinos with $E \approx 1$ MeV, and the higher-energy ^{8}B neutrinos with $E \approx 3 - 13$ MeV, see Fig. 46 for the energy-differential flux of solar neutrinos. The standard solar model (SSM) fluxes are given in [9] and measured fluxes are summarized in the reviews [6,7,10].

The solar neutrinos have been studied by measuring NC and CC weak interactions with atomic electrons and atomic nuclei. Here the NC and CC responses for atomic electrons and the deuteron are well known, and thus are used to study medium- and high-energy solar neutrinos. Studies of the solar neutrinos by measuring the NC and CC weak interactions with the atomic nuclei require accurate values for the neutrino–nuclear responses [4]. We discuss in this section the CC nuclear-responses for the solar neutrinos.
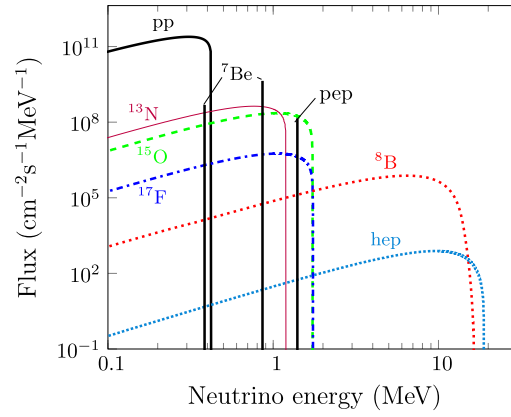
Fig. 46. Energy-differential flux for each different type of solar neutrino, as labeled in the figure. Also shown are the fluxes of the monoenergetic ^{7}Be neutrinos at 0.38 MeV and 0.86 MeV, and pep neutrinos at 1.44 MeV. The fluxes are based on the solar model BS05(OP) [364] and the energy spectra are taken from [365].

The CC interaction is expressed in this case as the inverse β decay

$$\nu_e + {}^A_Z X = e^- + {}^A_{Z+1}X, \tag{120}$$

where A and Z are the mass and atomic numbers of the initial nucleus. The weak interactions excite mainly the Fermi (F) 0^+ and GT 1^+ states, depending on the neutrino energy. The energy of the ^{8}B neutrinos extends to around $E_\nu \approx 13$ MeV, and thus can excite the isobaric analog state (IAS) [i.e. the Fermi giant resonance] and the Gamow–Teller giant resonance (GTR). They are mostly particle-unbound and thus decay by emitting protons and neutrons. The low- and medium-energy solar neutrinos excite mostly bound GT states in the low excitation region.

The CC cross section $\sigma_k(E_\nu)$ for the kth excited state is expressed by using the Fermi and GT responses $B_k(F)$ and $B_k(GT)$ as

$$\sigma_k(E_\nu) = \frac{G^2}{\pi} p_e E_e F(Z_f, E_e) \Big[B(F)_k + \Big(\frac{g_A}{g_V}\Big)^2 B(GT)_k \Big], \tag{121}$$

where E_e and p_e are the total energy and the momentum of the emitted electron, Z_f is the atomic number of the final nucleus, G is the effective coupling strength (5) for the CC processes, $g_A/g_V = 1.27$ is the axial–vector to the vector coupling ratio for a free neutron and $F(Z_f, E_e)$ is the Fermi function [see Eq. (113)]. The interaction rate is given by a sum over the rates of the accessible Gamow–Teller and Fermi states in the final nucleus as

$$R(\nu) = \sum_k \int \sigma_k(E_\nu) \phi_\nu(E_\nu) dE_\nu, \tag{122}$$

where $\phi_\nu(E_\nu)$ is the neutrino flux as a function of the neutrino energy E_ν.

The Fermi responses are concentrated mostly in the IAS, and the strength is given by

$$B(F) = \sum_k B(F)_k = N - Z. \tag{123}$$

The low- and medium-energy solar neutrinos are mostly captured into the low-lying GT states. The GT strength for the ground state is obtained from the ft value for the β^+/EC decay of ${}^A_{Z+1}X \to {}^A_Z X$, if available experimentally. Actually, GT states with known ft values are limited to the ground and isomeric states. Then charge-exchange reaction (CER) rates are used to evaluate the GT responses for excited states. The solar-neutrino responses have been studied by using β^+/EC decay rates and CER rates for various medium-heavy and heavy nuclei as described in the review [4] and [93] and [366].

The CC interactions on ^{37}Cl and ^{71}Ga nuclei have been used for off-line measurements of the low- and medium-energy solar neutrinos [4,6]. The first observation of the solar neutrinos is the Homestake experiment with ^{37}Cl [49]. The ^{37}Cl isotope with the threshold energy of $E_{\rm thr} = 0.814$ MeV is sensitive mainly to the ^{8}B and ^{7}Be neutrinos and partly to pep and CNO neutrinos. There are many GT states below the neutron threshold energy. The response for the ground state is known from the β-decay ft value, while those for the excited GT states are measured by the (p,n) CERs with a modest energy resolution [367]. The high energy-resolution measurements at RCNP are perfect to study the responses for the individual states in ^{37}Ar.

The CC interaction on ^{71}Ga with $E_{\rm thr} = 0.236$ MeV has been used to study the pp neutrinos and others because of the low threshold energy. A ground-state response of $B(GT) = 0.085$ has been evaluated from the β-decay rate. The GT responses for the excited states were studied by CERs on ^{71}Ga [93,366,368]. The energy spectrum and the angular distributions for the lowest-lying 3 states are shown in Fig. 47. The neutrino GT responses, $B(GT)$, with orbital angular momentum $L = 0$, for the excited states were derived from the DWBA analyses of the CER angular distributions. Here the non-GT $L = 2$ components
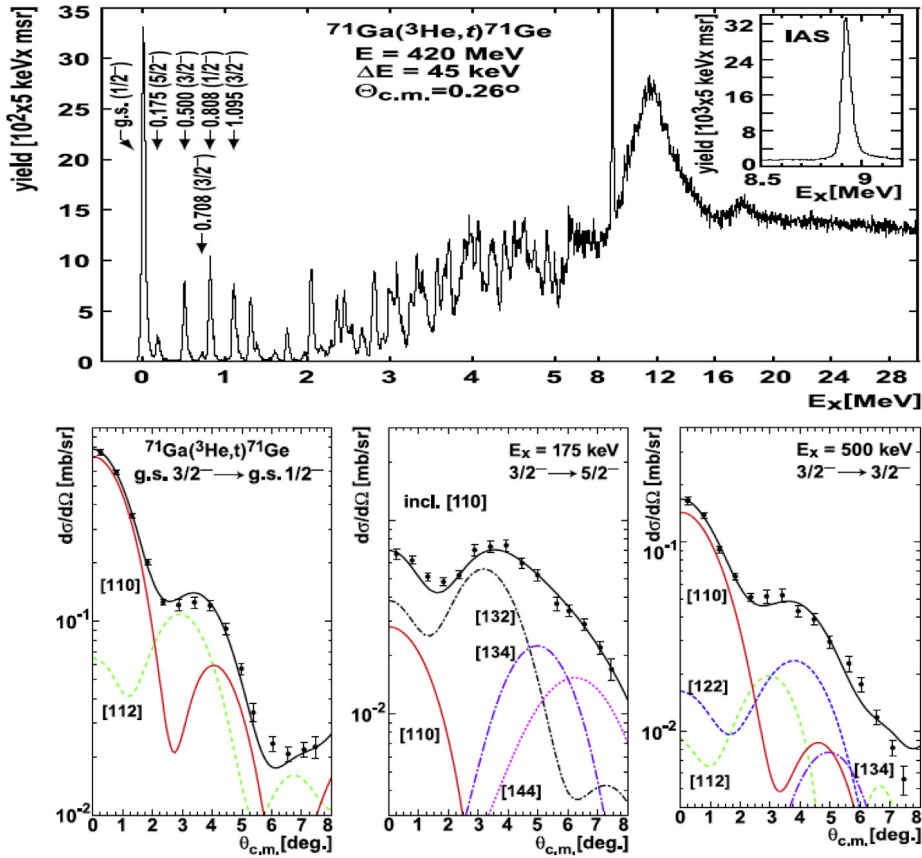
Fig. 47. Top: Energy spectrum of the (^{3}He,t) CER on ^{71}Ga. Bottom: Angular distributions of the (^{3}He,t) CERs populating the ground ($J^\pi = 1/2^-$), the 175 keV ($J^\pi = 5/2^-$) and the 500 keV ($J^\pi = 3/2^-$) states. Solid lines show the distributions for the GT (red line) and others with the projectile, target and relative angular momentum transfers of [$J_{pro}, J_{tar}, J_{rel}$] [366].

were corrected for [366]. The CERs for the ground ($1/2^-$) and 500 keV ($3/2^-$) states are mainly GT excitations with $L = 0$, but the CER for the 175 keV $5/2^-$ state includes a large fraction of non-GT excitation due to the tensor and $L = 2$ excitations. The solar-neutrino flux is estimated by measuring the EC rate of the product nuclei of ^{71}Ge. The neutron-unbound states near the binding energy contribute to the ν capture rate via γ rays to the ground state. The unbound state contribution is obtained to be around 0.34 SNU by measuring the (^{3}He,t) CER in coincidence with the decaying γ rays [93]. Recently, the ^{71}Ga responses for the low-lying states in ^{71}Ge have been under vivid discussion due to the possible support of the existence of sterile neutrino(s). This matter will be elaborated further in Section 4.4.4. The experimental set-up is shown in Fig. 48. This CER γ-coincidence system is used to study the spin and parity of states associated with CERs.

Real-time (on-line) measurements of the solar neutrinos are of great interest for studying the nuclear reactions in the sun. In particular, high-precision measurements of the real-time pp neutrinos, the main component of the solar neutrinos, are of interest in the studies of solar activities (see Ref. [369]). The real-time measurements of the CC nuclear interactions require coincidence measurement of the (ν_e, e) signal with $\beta - \gamma$ rays associated with the solar ν capture to reduce various kinds of backgrounds. The ^{115}In(ν_e, e)^{115}Sn reaction to the 612.8 keV $7/2^+$ state in delayed coincidence with the successive γ rays is one possible way [370]. The ^{176}Yb(ν_e, e)^{176}Lu reactions to the 339 keV 1^+ and 195 keV 1^+ states are also of potential interest for studying the ^{7}Be and pp neutrinos in coincidence with the 144 keV γ ray and in delayed coincidence with the 50 ns 72 keV γ ray [371]. The neutrino responses of $B(GT) = 0.11$ and 0.20 for the upper and lower GT states are measured by the CER (^{3}He,t) experiment [372].

The CNO neutrinos, which are interesting for studies of the composition of the sun, have not yet been identified experimentally. The current limit by the Borexino experiment is around 7.9×10^8/cm^2/s, while the low- and high-metallicity models predict 3.8×10^8/cm^2/s and 5.3×10^8/cm^2/s [6,7,10,373]. The standard solar model (SSM) predicts around 10 SNUs (solar neutrino unit) for the CNO-neutrino capture rate in ^{71}Ga. The solar-neutrino capture rate derived from the CER and the SSM neutrino fluxes [9] is 132 SNU, including around 11 SNU CNO flux [9], while recent RCNP CER data, with the improved energy resolution, reports 122 SNU without the CNO flux [374]. The CNO-flux study requires accurate measurements of the solar neutrinos. A 100-ton-scale Te detector with 32% abundance of the ^{128}Te isotope may be one option of the real-time CNO-flux experiments in coincidence with the decaying γ rays.
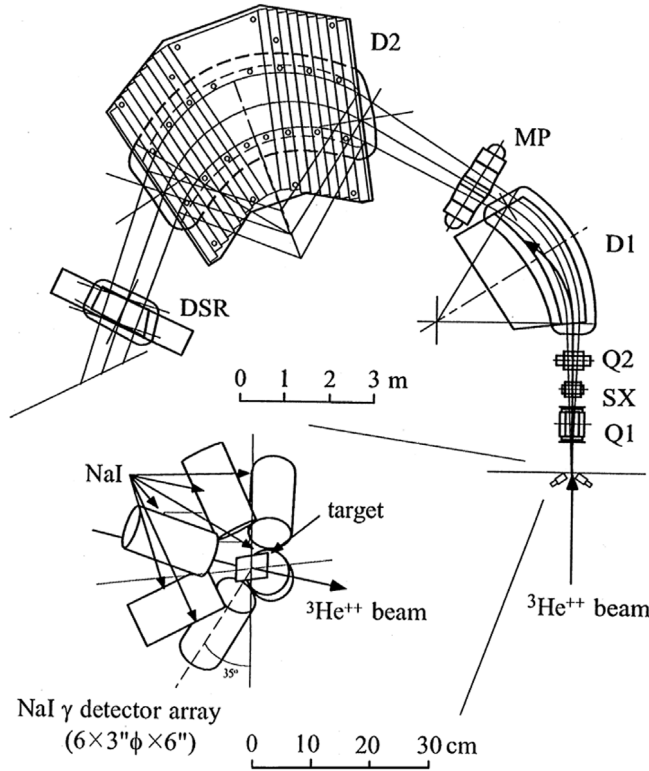
Fig. 48. RCNP spectrometer Grand Raiden and the γ-detector array. D1 and D2: dipole magnets. Q1 and Q2: quadrupole magnets. SX: sextupole magnet. SDR: dipole magnet for spin rotation. MP: multipole field magnet. NaI detector array is for γ detection in coincidence with CER particles [93].

4.2.2. Solar-neutrino responses for DBD nuclei

Double beta decay (DBD) nuclei with low threshold energy for CC interactions are of potential interest for the low- and medium-energy solar-neutrino experiments [16]. The solar-neutrino signal rate is of the same order of magnitude as the neutrinoless DBD rate in case of the inverted-hierarchy (IH) ν-mass spectrum and the solar-signal energy is in a similar MeV energy region as the DBD one. Thus, low-threshold DBD detectors may be used for solar-neutrino experiments if the solar-neutrino responses for the DBD nuclei are large, as discussed in [4,158,375,376]. Then, one may need to take into account the possible contributions of the solar-neutrino interactions to backgrounds in DBD experiments [377,378].

The weak transitions to be considered in the case of ^{100}Mo are the neutrinoless ($0\nu\beta^-\beta^-$) and two-neutrino ($2\nu\beta^-\beta^-$) DBDs with 2 electrons and γ(s), the single β decay (SBD) with an electron and γ(s), and the ν_e-CC interaction with an electron and γ(s). Here the γ(s) appear in the case of transitions to excited states. The Q values are given by $Q_{\beta\beta}$, Q_β, and Q_ν, for DBD, SBD and the CC reaction, respectively. The threshold energy for the solar-ν CC interaction is $E_{\mathrm{thr}} = -Q_\nu$. The decay and interaction scheme is shown in Fig. 49.

One crucial point for the solar-neutrino study with DBD nuclei is to eliminate the $2\nu\beta^-\beta^-$ backgrounds by means of the SSTC (signal selection by time correlation) and SSSC (signal selection by spacial correlation) [16]. The $2\nu\beta\beta$ rate is 6–8 orders of magnitude larger than the solar-neutrino CC rate.

The CC reaction ^{100}Mo(ν_e, e) ^{100}Tc with $Q_\nu = -168$ keV is for the first time shown to be usable for real-time pp and ^{7}Be neutrino experiments [158], as shown in Fig. 49. The neutrino response for the ground state is as large as $B(\mathrm{GT}) = 0.36$, and the pp, ^{7}Be and total solar-ν capture rates are 639 SNU, 206 SNU and 965 SNU, respectively, without taking into account the neutrino oscillations. The SSTC measurement of the CC electron in delayed coincidence with the β rays from the short-lived ^{100}Tc with the half-life of 16 s reduces the $2\nu\beta\beta$ and other background signals. An SSSC vertex resolution of the order of mm reduces the accidental coincidence of the 2 β rays. The nucleus ^{116}Cd has similar DBD, SB and solar-neutrino level schemes as ^{100}Mo, and thus it can also be used for solar-neutrino experiments [375].

Let us discuss contributions of the solar neutrinos to the background in the region of interest (ROI) for the $0\nu\beta\beta$ decay. The background was estimated for all DBD isotopes [379]. The CC interactions were studied by using the CER data on ^{76}Ge, ^{82}Se, ^{100}Mo, ^{130}Te, ^{136}Xe and ^{150}Nd [377,378]. These isotopes are of current interest for high-sensitivity DBD experiments. The actual solar-ν CC rates are evaluated by using the neutrino GT responses $B(\mathrm{GT})$ measured in recent RCNP CERs as shown in Table 10 [377,378].

The DBD nuclei can be classified into two groups: Group A: ^{82}Se, ^{100}Mo and ^{150}Nd, and group B: ^{76}Ge, ^{130}Te and ^{136}Xe. The group-A nuclei have low-lying GT states with a low threshold energy of $-Q_\nu$. They are strongly excited by the pp neutrinos
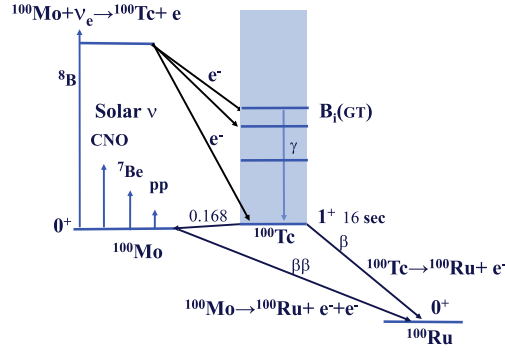
Fig. 49. Energy and transition scheme for the solar-neutrino CC reaction and the DBD of ^{100}Mo with $E_{thr} = 0.168$ MeV. Also the single β decay from the ground state of the intermediate nucleus ^{100}Tc is shown. See text [158].

Table 10
Solar-ν CC, SB and DBD rates. Q: Q values in units of MeV. S_{pp} and S_{tot}: pp and total solar-ν rates in units of SNU. B_{SB}: Background rate per ton-year for the single β decays. $B_{2\nu}$: Background rate per ton-year for $2\nu\beta\beta$ decay. An energy resolution of $\delta = 0.02$ is assumed. The solar-ν background rate B_{SB} is proportional to δ [378].

Isotope	$Q_{\beta\beta}$ (MeV)	Q_{ν} (MeV)	Q_{β} (MeV)	S_{pp}	S_{tot}	B_{SB}	$B_{2\nu}$
^{76}Ge	2.039	−1.010	2.926	0	6.3	0.03	0.005
^{82}Se	2.992	−0.172	3.093	257	368	4.42	0.15
^{100}Mo	3.034	−0.168	3.202	391	539	0.11	1.56
^{130}Te	2.528	−0.463	2.949	0	33.7	0.48	0.01
^{136}Xe	2.468	−0.671	2.548	0	68.8	0.55	0.003
^{150}Nd	3.368	−0.197	3.454	352	524	0.12	1.00

and their capture rates are as large as 300–500 SNU. The group-B nuclei have a large negative Q_{ν} value. Then the pp-νs are not captured and the total solar-ν capture rates are around 10–70 SNU. The solar-neutrino CC interaction with a DBD nucleus is followed by electron emission (e) and γ/β decays if the residual state is a bound excited state, and particle (p,n) decays if it is unbound [377].

We first consider DBD detectors where the sum energy for the e β/γ rays is measured. The SB events in the ROI are the major backgrounds. The SB background rates (counts per ton-year) in case of the energy resolution of $\Delta E/E = \delta = 0.02$ are shown in the 7th column of Table 10. The rates for ^{100}Mo and ^{150}Nd are as small as 0.1 /ton-year even though the solar-ν capture rates are high. This is because the DBD ROI is very close to the end-point energy of Q_{β}. The $2\nu\beta\beta$ tail (counts per ton-year) also contributes to background in the ROI, as shown in the 8th column of Table 10.

The DBD signal rate in a typical case of the IH neutrino mass of $m_{\nu} \approx 20$ meV and of the nuclear matrix element (NME) $M^{0\nu} = 2$ is around 0.1/ton-year for ^{76}Ge and 1/ton-year for others. Then good-energy-resolution detectors with $\delta \approx 0.01 - 0.02$ are required to avoid the solar-ν and/or $2\nu\beta\beta$ backgrounds. There are various ways to reduce the solar-ν backgrounds. In case of the nucleus ^{82}Se, the SB decays to the excited states are followed by γ rays. Thus they are reduced by the SSSC [16]. In case of the nucleus ^{100}Mo, the half-life of the intermediate nucleus ^{100}Tc is 16 s. Thus, the SSTC [16] is used to reduce the SB background from ^{100}Tc by anti-coincidence with the preceding CC electron.

The solar-neutrino CC and NC interactions with atomic electrons of DBD-detector components were studied in case of liquid scintillators in [379,380]. The interaction of the ^{8}B neutrinos with atomic electrons was evaluated for a liquid-scintillation detector with N tons of the scintillator and N' tons of the DBD isotopes dissolved into the scintillator. The neutrino–electron interaction rate per ton-year in the ROI is given by

$$B_e(E) \approx 0.15 \times Ef , \quad f = \delta/R , \tag{124}$$

where E is the ROI energy in units of MeV, $R = N'/N$ is the DBD-isotope concentration and $f = \delta/R$ is a kind of background efficiency. The background rate is around $B_e(E) \approx 0.3$ in high resolution and/or high concentration of $f \approx 0.5$ with $\delta \approx 1\%$ and $R \approx 2\%$. Noting that the DBD signal rate is around 1/ton-year for a typical case of mass $m_{\nu} = 20$ meV, NME $M^{0\nu} = 2$ and phase space $G = 5 \times 10^{-14}$/y, the required efficiency for the IH-mass studies is of the order of $f \leq 0.5$.

4.3. Supernova-neutrino–nuclear responses

Supernova neutrinos are electron (e), μ and τ neutrinos (ν_e, ν_μ, ν_τ) and their antineutrinos ($\bar{\nu}_e$, $\bar{\nu}_\mu$, $\bar{\nu}_\tau$) in the medium-energy region of $5 - 70$ MeV. They are experimentally studied by measuring the NC and CC interactions with atomic electrons and nuclei. The first observations of the supernova 1987A were made by measuring the CC interaction of $\bar{\nu}_e$ with protons [381–383]. The CC cross section of

$$\bar{\nu}_e + p \rightarrow e^+ + n \tag{125}$$

is large, but is limited to $\bar{\nu}_e$. In this section, we discuss supernova-neutrino NC and CC interactions with medium-heavy and heavy nuclei.

The (anti)neutrino–nuclear responses in the form of (anti)neutrino–nucleus cross sections are welcome information for any neutrino experiment. The knowledge of these cross sections offers a probe to investigate various questions in particle physics, astrophysics and astroparticle physics. Neutrinos and antineutrinos are produced in large quantities e.g. in supernova explosions initiated by the collapse of their iron cores (core-collapse type II supernovae) [384]. Nuclear responses to supernova neutrinos [385–387] are probes of the physics beyond the Standard Model [388,389], and important in investigations of the supernova mechanisms [390,391] and the nucleosynthesis of heavy elements [392–394]. Recent reviews on the core-collapse supernovae are, e.g. [395,396]. The estimations of (anti)neutrino–nucleus cross sections constitute a tool for detection of different (anti)neutrino flavors and exploring the structure of the weak interactions [4,394]. Also, the estimation of the charged-current (anti)neutrino–nucleus cross sections is important for the probing of the nuclear matrix elements for the neutrinoless double beta decay by exploiting the so-called neutrino beams [397].

(Anti)neutrinos interact only weakly with matter and (anti)neutrinos from astrophysical sources, such as supernovae, can therefore be detected by Earth-bound detectors via charged-current (CC) and/or neutral-current (NC) (anti)neutrino–nucleus interactions [4]. The final fate of massive type II stars at the end of their life cycle, when they have used up all their nuclear fuel, is their collapse to form a compact object such as a neutron star or a black hole. These stars radiate almost all of their binding energy in the form of (anti)neutrinos of all flavors and with energies of a few tens of MeV [398]. The emerging (anti)neutrino signal provides a great deal of information on the final stages of the supernova collapse for both particle and nuclear physics. Furthermore, the cross sections of the (anti)neutrino–nucleus scattering are sensitive to the details of nuclear structure, e.g. single-particle energies, locations of giant resonances etc.

In the NC experiments all the (anti)neutrino flavors, electron, muon and tau, can be detected whereas the CC experiments detect only electron–neutrinos (ν_e) and antineutrinos ($\bar{\nu}_e$) since the heavier flavors cannot be created in the final states of the scattering process due to the limited energy range ($E_\nu \lesssim 70$ MeV) of the supernova (anti)neutrinos. Several neutrino detectors around the world are being established and planned for such purpose, see e.g. [391] for an overview on supernova-neutrino detectors. One example of such a detector is the HALO (Helium and Lead Observatory) experiment [399] running at SNOLAB, Canada, and designed for observation of galactic core-collapse supernovae by a lead-based neutrino detector. The HALO experiment is complementary to other neutrino-detection experiments in that it is dominated by ν_e events over the $\bar{\nu}_e$ events since ν_e events are enhanced by the large neutron excess of the Pb nuclei and $\bar{\nu}_e$ events are suppressed by the Pauli blocking [400]. Hence, theoretical estimates of (anti)neutrino–nucleus responses for the stable lead targets are essential for the interpretation of the results from HALO and similar detection experiments. Other examples are the MOON experiment [401] using molybdenum isotopes and nEXO experiment [402] using ^{136}Xe as target material. In fact, the only observations of neutrinos from a supernova so far were the neutrinos from the extra galactic supernova SN1987a, observed by the Kamiokande II [381], IMB (Irvine–Michigan–Brookhaven) [382] and Baksan [383] detectors. In spite of the small number of the detected neutrinos (about 20 in total) these observations verified that neutrinos from supernovae are highly important probes of both supernova mechanisms and neutrino properties in general (see the review [403]).

4.3.1. Final-state Coulomb effects in CC reactions for supernova neutrinos

At this point it is appropriate to note on the treatment of the final-state Coulomb effects in case of the CC scattering [361]. These effects are represented by the Fermi function $F(\pm Z_f, E_{\mathbf{k}'})$ in (112) and (113) given in, e.g., Ref. [250]. The distortion is to be treated differently in the regions of small and large values of the so-called effective momentum

$$k_{\text{eff}} = \sqrt{E_{\text{eff}}^2 - m_{e\pm}^2}\,, \tag{126}$$

where $m_{e+}(m_{e-})$ is the positron (electron) rest mass and the effective energy is given by

$$E_{\text{eff}} = E_{\mathbf{k}'} - V_C(0)\,. \tag{127}$$

Here $V_C(0)$ is the Coulomb potential at the center of the final nucleus. For small values of k_{eff} we use the Fermi function but for large values of k_{eff} one can adopt the so-called modified effective momentum approximation (MEMA), introduced in [404]. Consequently, for large k_{eff} one drops the Fermi function from (112) and, instead, replaces the absolute value of the three-momentum and the energy of the outgoing electron/positron by their effective values (126) and (127). More details are given in [361].

4.3.2. Flux-averaged cross sections

The Earth-bound neutrino detectors are not measuring directly the (anti)neutrino–nucleus cross sections but, instead, the (anti)neutrino-flux-averaged cross sections, $\langle \sigma \rangle$, which are obtained by folding the (anti)neutrino–nucleus cross sections with an appropriate energy profile for the incoming (anti)neutrinos (e.g. the solar and supernova (anti)neutrinos). In theoretical calculations the energies of the supernova (anti)neutrinos can reasonably well be described by a two-parameter Fermi–Dirac distribution [405]

$$F_{\text{FD}}(E_{\mathbf{k}}) = \frac{1}{F_2(\alpha_\nu)T_\nu} \frac{(E_{\mathbf{k}}/T_\nu)^2}{1 + \exp(E_{\mathbf{k}}/T_\nu - \alpha_\nu)}\,, \tag{128}$$

where T_ν represents the effective (anti)neutrino temperature of the (anti)neutrino sphere and α_ν is the so-called degeneracy or pinching parameter. In (128) the constant $F_2(\alpha_\nu)$ normalizes the total flux to unity. For a given value of α_ν the temperature T_ν can be computed from the average neutrino energy $\langle E_\nu \rangle$ by using the relation

$$\langle E_\nu \rangle / T_\nu = \frac{F_3(\alpha_\nu)}{F_2(\alpha_\nu)} \,, \tag{129}$$

where the integrals are given as

$$F_k(\alpha_\nu) = \int \frac{x^k \mathrm{d}x}{1 + \exp(x - \alpha_\nu)} \,. \tag{130}$$

The folded cross section depends now on the parameters α and T. The values of these parameters and the corresponding average (anti)neutrino energies $\langle E_\nu \rangle$ depend on the adopted supernova model. Representative sets of these parameters can be found. e.g. in [398].

The supernova-(anti)neutrino energies reflect the (anti)neutrino-sphere temperatures T_ν. The average energies are $E(\nu_e) \approx 10$ MeV, $E(\bar{\nu}_e) \approx 15$ MeV and $E(\nu_x) \approx E(\bar{\nu}_x) \approx 25$ MeV with $x = \mu, \tau$. The ν_e and $\bar{\nu}_e$ energies are distributed in a wide energy region of $5 - 40$ MeV. Their energies in case of neutrino oscillations from ν_x and $\bar{\nu}_x$ spread in an even wider region of $5 - 70$ MeV. Accordingly, one needs to know the (anti)neutrino–nuclear responses in a wide energy region of $5 - 70$ MeV. They are studied experimentally by measuring CERs and the μ capture reactions, as discussed in Section 2. The low-energy (anti)neutrinos are captured into the low-lying GT states, while the medium-energy ones beyond 15 MeV are preferentially captured into giant resonances. The giant resonances involved are the Gamow–Teller resonance (GTR), the Fermi giant resonance (IAS) and isovector spin-dipole resonance (IVSDR).

The CER energy spectrum for ^{208}Pb shows the IAS, GTR and IVSDR responses. The one-neutron and two-neutron threshold energies are 6.9 and 15.0 MeV. Thus, medium-energy supernova (anti)neutrinos populating excited states above 7 MeV are studied by measuring neutrons from the neutron unbound states [406]. The number of neutrons reflects the excitation energy and thus the (anti)neutrino energy. The ratio of the two-neutron to one-neutron emissions is used to get the (anti)neutrino energy and the temperature of the (anti)neutrino sphere. Here the ratio is sensitive to the neutron energy, which depends on the neutron emission processes, the equilibrium evaporation or the pre-equilibrium emission [29]. Actually, an appreciably fast proton component from the IVSDR region suggests a fast neutron emission from the pre-equilibrium stage [407].

4.3.3. Flavor-conversion effects in supernova CC scattering

Because of the large muon and tau rest masses only electron–neutrinos and electron antineutrinos from supernovae can be detected by CC neutrino–nucleus scattering. Neutrinos can undergo flavor conversions due to interactions with the dense matter of the collapsing star. According to recent studies (see e.g. [408]) collective neutrino oscillations caused by neutrino–neutrino interactions could also have effects on the energy profiles of supernova neutrinos and antineutrinos. Assuming that the energy spectra of muon and tau (anti)neutrinos are the same it can be shown [409,410] that the three-neutrino mixing problem can be reduced to a two-neutrino problem of the form $\nu_y \leftrightarrow \nu_e$, where ν_y is a linear combination of ν_μ and ν_τ. The same is true for antineutrinos. Consequently, the energy profile for electron neutrinos which reach an Earth-bound detector can then be written in the form

$$F_{\nu_e}(E_\mathbf{k}) = p(E_\mathbf{k})F^0_{\nu_e}(E_\mathbf{k}) + (1 - p(E_\mathbf{k}))F^0_{\nu_y}(E_\mathbf{k}) =$$
$$p(E_\mathbf{k})F^0_{\nu_e}(E_\mathbf{k}) + (1 - p(E_\mathbf{k}))F^0_{\nu_x}(E_\mathbf{k}) \,, \tag{131}$$

where $p(E_\mathbf{k})$ represents the survival probability of electron–neutrinos and $F^0_{\nu_e}(E_\mathbf{k})$ $(F^0_{\nu_x}(E_\mathbf{k}))$ is the initial energy profile (128) of electron–neutrinos (non-electron–neutrinos). In Eq. (131) the last line follows from the assumption of equal initial energy profiles of muon and tau neutrinos. Similarly, for the electron antineutrinos one has

$$F_{\bar{\nu}_e}(E_\mathbf{k}) = \bar{p}(E_\mathbf{k})F^0_{\bar{\nu}_e}(E_\mathbf{k}) + (1 - \bar{p}(E_\mathbf{k}))F^0_{\bar{\nu}_x}(E_\mathbf{k}) \,. \tag{132}$$

One can use for the survival probability $p(E_\mathbf{k})$ $(\bar{p}(E_\mathbf{k}))$ of electron–neutrinos (electron antineutrinos) in the case of normal mass hierarchy (NH) the prescriptions [389,411]

$$p(E_\mathbf{k}) = 0 \,, \tag{133}$$

and

$$\bar{p}(E_\mathbf{k}) = \left\{ \begin{array}{ll} 1 & ; E_\mathbf{k} < \bar{E}_s \,, \\ 0 & ; E_\mathbf{k} > \bar{E}_s \,, \end{array} \right. \tag{134}$$

where $\bar{E}_s = 18.0$ MeV [411]. Similarly, for the inverted mass hierarchy (IH) one can use the survival probabilities

$$p(E_\mathbf{k}) = \left\{ \begin{array}{ll} \sin^2 \theta_{12} & ; E_\mathbf{k} < E_s \,, \\ 0 & ; E_\mathbf{k} > E_s \,, \end{array} \right. \tag{135}$$

and

$$\bar{p}(E_\mathbf{k}) = \cos^2 \theta_{12} \,, \tag{136}$$

Table 11
References for available neutrino–nucleus cross-section calculations performed for different nuclear targets.

Nucl.	Z	A	NC references	CC references
He	2	4	[413,414]	[414]
C	6	12	[414–418]	[131,133,414,416,417], [419–423]
C		13		[419,424]
O	8	16	[415,416,418]	[416,421,422,425,426]
Al	13	27		[419]
Ar	18	40	[427]	[427–431]
Fe	26	56	[417,418,432–434]	[417,422,426,432]
Ni	28	56	[417,418]	[417,433]
Zn	30	64,66	[435]	
Ge	32	82	[434]	
Zr	40	92		[436]
Nb	41	93	[436]	
Mo	42	98		[436]
		100		[159,426]
		92,94,96,98,100	[418,437]	[361]
		95,97	[438]	[439]
		92,94,95,96,97,98,100	[363,440,441]	[441]
Ru	44	99	[436]	
Cd	48	116	[442]	[442,443]
		106,108,110,111,112,113,114,116	[444]	[445]
Te	52	128,130	[351]	
Xe	54	136	[446]	[446]
		128,129,130,131,132,134,136	[447]	[448]
La	57	138	[78]	[78]
Ta	73	180	[78]	[78]
Pb	82	208	[432,449,450]	[422,426,432,449]
		204,206,208	[451]	[452]

for electron–neutrinos and electron antineutrinos, respectively. For the parameter values one can use $E_s = 7$ MeV [409] and $\sin^2 \theta_{12} \approx 0.306(0.312)$ [412], for the normal (inverted) hierarchy.

4.4. Neutrino–nucleus scattering calculations

Along the years a lot of different calculations of both NC and CC (anti)neutrino–nucleus scattering calculations for supernova (and solar) neutrinos have been performed. Also a host of different target nuclei have been addressed, in most calculations the light nuclei below the iron region $A = 56$ have been considered. A collection of these calculations, grouped by the target nuclei, are presented in Table 11. Here a division between the NC (column four) and CC (column five) calculations has been given for the convenience of the reader.

The neutrino–nucleus scattering cross sections have been calculated in a number of different theory frameworks. These theories include

ISM type of models:

- The ISM, used in [131,133,414,424,425,428,433,447]

(Q)RPA type of models:

- The Tamm–Dancoff approximation (TDA), used in [353].
- An RPA approach built up from single-particle states of an uncorrelated local Fermi sea, as applied in [419].
- Continuum random-phase approximation (CRPA), applied in [415,416,420,421].
- Hybrid model: The pn(Q)RPA plus the 1^+ channel treated by the ISM, as applied in [430,432].
- pnQRPA with a schematic δ force [159]
- RPA and pnRPA with Skyrme type of interactions, as used in [424,426,432,449]
- QRPA and pnQRPA (see Section 3.1.1 for more information) with Skyrme type of interactions [424,426,443,451,452]
- The QRPA and pnQRPA (see Section 3.1.1 for more information) with realistic Bonn one-boson-exchange based effective G-matrix interactions, as used in [351,361,363,435,437,440–442,444–448,450].
- The pnQRPA + QRPA with neutron–proton pairing and effective G-matrix interactions, as applied in [78,417,427,436].
- Consistent relativistic mean-field approach: relativistic Hartree–Bogoliubov model (RHFB) plus relativistic QRPA (RQRPA), as applied in [418,422].
- Projected QRPA (PQRPA) and relativistic QRPA (RQRPA), as applied in [423].
- Thermal QRPA (TQRPA) combined with Skyrme energy density functionals (Skyrme–TQRPA), as used in [434].

Quasiparticle–phonon coupling:

Table 12
Flux-averaged incoherent cross sections for the stable molybdenum isotopes in units of 10^{-42} cm^2. The calculations are done using the QRPA and MQPM nuclear-model frameworks [440]. The adopted neutrino parameters (T (MeV),α), T being the temperature, are: ν_e (3.6,2.1) ; $\bar{\nu}_e$ (3.8,3.2) ; ν_μ, ν_τ (4.8,0.8) ; $\bar{\nu}_\mu$, $\bar{\nu}_\tau$ (4.8,0.8).

flavor	$\langle\sigma\rangle^{92}$	$\langle\sigma\rangle^{94}$	$\langle\sigma\rangle^{95}$	$\langle\sigma\rangle^{96}$	$\langle\sigma\rangle^{97}$	$\langle\sigma\rangle^{98}$	$\langle\sigma\rangle^{100}$
ν_e	11.6	11.8	15.9	12.1	16.4	9.94	8.59
$\bar{\nu}_e$	17.3	17.6	23.0	17.9	23.7	15.1	13.1
ν_μ, ν_τ	25.5	25.3	31.5	25.6	32.3	22.1	19.9
$\bar{\nu}_\mu$, $\bar{\nu}_\tau$	22.7	22.7	28.6	23.0	29.4	20.0	17.7
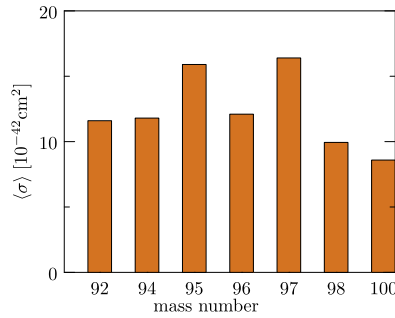
Fig. 50. Variation of the calculated flux-averaged NC electron–neutrino cross section with mass number for the Mo isotopes. The calculations are done using the QRPA and MQPM nuclear-model frameworks [440]. The adopted neutrino parameters (T(MeV),α), T being the temperature, are ν_e: (3.6,2.1).
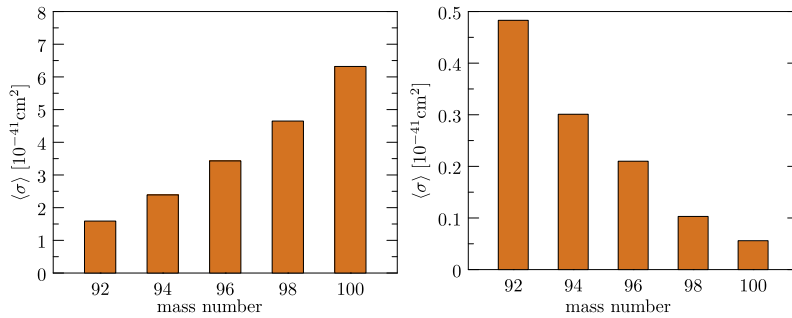
Fig. 51. Variation of the flux-averaged CC neutrino (left panel) and antineutrino (right panel) cross sections with mass number for the Mo isotopes. The calculations are done using the QRPA and MQPM nuclear-model frameworks [439,441]. The adopted neutrino parameters ($\langle E\rangle$(MeV),α), $\langle E\rangle$ being the average neutrino energy, are ν_e: (11.5,3.0) ; $\bar{\nu}_e$: (13.6,3.0).

- The MQPM approach for odd-A nuclei combined with the Bonn one-boson-exchange-based effective G-matrix interactions (see Section 3.1.1 for more information), as used in [363,439–442,444,445]

The ISM, pnQRPA, QRPA and MQPM theory frameworks have been briefly discussed in Section 3.1.1. The TDA and RPA, as also pnQRPA and QRPA model frameworks have been extensively discussed in the monograph [55].

4.4.1. Example: NC scattering off the stable molybdenum isotopes

In Fig. 50 the calculated flux-averaged NC electron–neutrino cross sections are displayed for the stable Mo nuclei. The cross sections of the even-A isotopes are computed [440] by the use of the QRPA and the odd-A isotopes by the use of the MQPM. There is no drastic dependence on the mass number although a decreasing trend of the cross sections is detectable for the heavy molybdenums. The two odd-mass isotopes stand out with their larger cross sections compared to the ones of even–even isotopes because of the larger phase space.

In Table 12 are listed the computed [440] flux-averaged (anti)neutrino cross sections for the different neutrino flavors. The mass dependence of the cross sections is qualitatively the same for all flavors. The cross sections for the heavy flavors are larger than for the electron flavor since the kinetic energy (temperature) of the heavy flavors is larger due to their early decoupling from the supernova environment. The results of [440] are in agreement with those of [418,437].

4.4.2. Example: CC scattering off the stable molybdenum isotopes

Fig. 51 displays the calculated [439,441] flux-averaged CC scattering cross sections for scatterings off the Mo isotopes separately for the electron–neutrinos and antineutrinos. There is a clear and opposite trend in the cross sections as
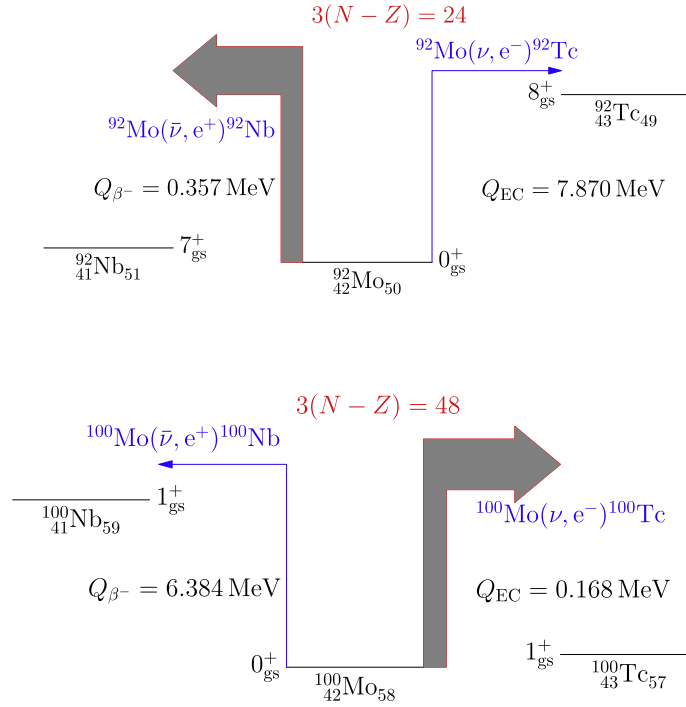
Fig. 52. Schematic figure of the threshold energies and Pauli blocking in the Mo chain of isotopes as taken from [441]. The spectroscopic data is from [257].

Table 13
Supernova-neutrino cross sections in units of 10^{-41} cm^2 for scattering off ^{100}Mo. J^π denotes spin–parity, ν_e denotes electron–neutrino, and ν_{xe} denotes electron–neutrino from μ and τ neutrino oscillations. The adopted neutrino parameters (T(MeV),α), T being the temperature, are ν_e: (3.5,0) ; $\bar{\nu}_e$: (5.0,0) ; ν_μ, ν_τ: (8.0,0) ; $\bar{\nu}_\mu, \bar{\nu}_\tau$: (8.0,0) [159].

J^π	0^+	0^-	1^+	1^-	2^+	2^-	3^+	3^-	4^+	4^-
ν_e	0.65	0.02	4.62	0.14	0.04	0.34	0.03	–	–	–
ν_{xe}	8.942	0.59	32.3	11.9	4.62	14.0	3.78	1.00	0.23	0.79

functions of the mass number: the neutrino cross sections increase and antineutrino cross sections decrease with increasing mass number. The reason for this is displayed in Fig. 52. There are two effects conspiring to the same direction: (a) the energy-threshold effect and (b) the Pauli-blocking effect. With increasing mass number the energy threshold increases for antineutrino scattering and decreases for neutrino scattering leading to a relative increase (decrease) in the neutrino (antineutrino) cross sections with increasing mass number. The Pauli blocking shows in the Ikeda $3(N - Z)$ sum rule for Gamow–Teller transitions: the larger the mass number, the larger the sum rule and the (p,n) type of Gamow–Teller transition strength (to the right in Fig. 52) which practically (more than 90%) exhausts the sum rule. The reverse happens to the (n,p) type of Gamow–Teller transition strength (to the left in Fig. 52).

4.4.3. Examples: Effects of flavor conversions

The supernova-neutrino CC rates and the electron spectra are evaluated for ^{100}Mo in [159] on the basis of the experimental responses [92]. Table 13 shows evaluated CC cross sections for electron–neutrinos and those converted from ν_μ and ν_τ through oscillations in the dense nuclear medium of the supernova.

It is noted that the electron–neutrinos ν_e are mainly captured into the GT(1^+) ground state and the GTR (1^+), and partially into the IAS (0^+) and the IVSDR (2^-), while the electron–neutrinos ν_{xe} from the μ and τ neutrino-flavor conversions are captured into the highly excited giant resonances with $J^\pi = 0^+, 2^\pm$ and $3^\pm$ in addition to the captures into GTR. The energy spectrum of the ν_e-CC electrons shows a broad bump in the region of $5 - 20$ MeV, while the spectrum for the ν_{xe}-CC electrons shows a broad bump in a higher energy region of 10–50 MeV. Then experimental studies of electron energy spectra give the temperature of the neutrino sphere and also information on the possible $\nu_e \rightarrow \nu_x$ oscillation.

The ν_e CC event rate for ^{100}Mo is around 3.5 per 100 tons in case of a supernova at a distance of 10 kpc (kiloparsecs) with 3×10^{53} ergs of total released energy, while the ν_{xe} CC one is around 22 per 100 tons [159]. The larger rate for ν_{xe} reflects a higher temperature of the μ- and τ-neutrino spheres than that for the electron–neutrino sphere.
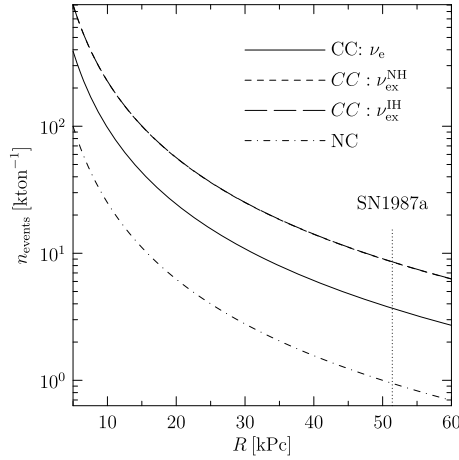
Fig. 53. Number of expected charged-current (CC) and neutral-current (NC) neutrino–nucleus scattering events per kiloton of ^{116}Cd as function of the distance to the supernova. In the figure is also shown the distance to the supernova SN1987a by a vertical dotted line. The results have been calculated in the QRPA nuclear-model framework [442].

If one assumes that the energy is equally partitioned between the neutrino flavors, then from (131) one obtains that the number of expected charged-current neutrino events in an Earth-bound detector per kiloton of target mass is given by

$$N_\nu^{CC}(R) = \frac{n_T}{4\pi R^2} \int \left[p(E_\mathbf{k}) N_{\nu_e} F_{\nu_e}(E_\mathbf{k}) + (1 - p(E_\mathbf{k})) N_{\nu_x} F_{\nu_x}(E_\mathbf{k}) \right] \sigma(E_\mathbf{k}) \mathrm{d}E_\mathbf{k} , \tag{137}$$

where n_T is the number of nuclei per kTon and R is the distance to the supernova. In (137) we have introduced

$$N_{\nu_e} = \frac{E_{\text{tot}}}{6 \langle E_{\nu_e} \rangle} , \tag{138}$$

and

$$N_{\nu_x} = \frac{E_{\text{tot}}}{6 \langle E_{\nu_x} \rangle} , \tag{139}$$

where E_{tot} is the total energy which is emitted as neutrinos. The non-electron–neutrinos which contribute to the second term in (137) are the ones which correspond to the linear combination ν_y (see discussion in Section 4.3.3). Hence, in the case of maximal mixing effectively half of the muon and tau neutrinos are affected by the $\nu_y \leftrightarrow \nu_e$ conversions. The case of antineutrinos is analogous.

Similarly, the number of neutral-current events in the detector can be written in the form

$$N_\nu^{NC}(R) = \frac{n_T}{4\pi R^2} \left(N_{\nu_e} \langle \sigma \rangle_{\nu_e} + 2 N_{\nu_x} \langle \sigma \rangle_{\nu_x} \right) . \tag{140}$$

In Fig. 53 the computed [442] number of CC and NC neutrino–nucleus scattering events per kiloton of ^{116}Cd as functions of the distance to the supernova is displayed. For the CC case results are shown for the non-oscillating case (ν_e) and for oscillating neutrinos for both the normal (NH) and inverted (IH) mass-hierarchy cases. The results for the normal and inverted mass hierarchies are similar and are thus not distinguishable in the figure. In the calculations a total energy of E_{tot} of $3.0 \cdot 10^{53}$ ergs has been assumed. The results can be easily re-scaled to other cases as well by changing the values of n_T in Eqs. (137) and (140) and E_{tot} in Eqs. (138) and (139). One can conclude that for a galactic supernova, i.e. $R \approx 10$ kPc, a detector with about 1 kTon could have several hundreds of events. Similarly, in Fig. 54 the results for the antineutrino reactions are shown. Most of the predicted events are neutral-current ones because of the large suppression of the charged-current antineutrino channel. The results in Figs. 53 and 54 depend strongly on the adopted energy profiles of the incoming neutrinos. Consequently, the computed numbers can vary with at least a factor of 2−3 depending on the employed supernova model.

4.4.4. Neutrino scattering off ^{71}Ga: the gallium anomaly

In some cases the description of neutrino scatterings involving low-lying states of nuclei requires special attention in terms of accurate nuclear wave functions. One interesting case is the CC scattering of monoenergetic neutrinos from EC (electron capture) decays of ^{37}Ar and ^{51}Cr on ^{71}Ga leading to the ground and 175 keV and 500 keV excited states in ^{71}Ge. The CC responses for higher-lying states induced by scattering of solar neutrinos off ^{71}Ga were discussed earlier in Section 4.2.1. The scattering cross sections for the mentioned three low-lying states can be estimated by using the data from charge-exchange reactions [366] or by using a microscopic nuclear model, like the ISM (see Section 3.1.1). In both cases it has
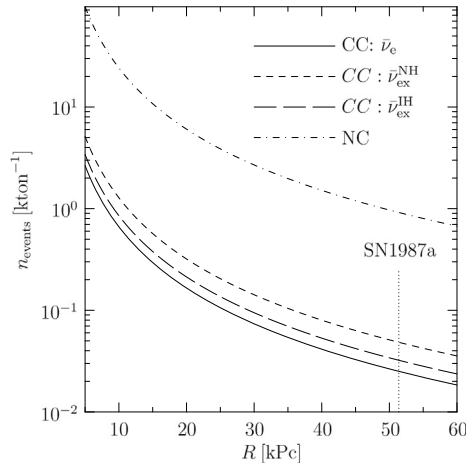
Fig. 54. Same as Fig. 53 but for the charged-current and neutral-current antineutrino scatterings off ^{116}Cd. The results have been calculated in the QRPA nuclear-model framework [442].

been observed that estimated cross sections are larger than the ones measured by the Ga experiments [453–455] and SAGE experiments [456–458]. The measured capture rates (cross sections) are 0.87 ± 0.05 of the rate based on the cross sections calculated by Bahcall [459]. The related model calculations and analyses based on them have been discussed in [311,460,461]. It should be noted that the response to the ground state is known from the EC ft value to be dominant ($>90\%$).

The discrepancy between the measured and theoretical event rates, the Ga anomaly, is at the level of about 3σ [311,460]. The missing neutrinos suggest that (i): the ν responses for the two excited states in ^{71}Ge are smaller than the values obtained in nuclear-structure studies, implying possible deficiencies in the nuclear-structure calculations or analyses of the (^{3}He,t) CER of [366] (see Fig. 47). (ii): the actual detector efficiency is smaller than the efficiency used in the evaluation or (iii): new physics is involved in the anomaly.

The point (iii) has been associated to the oscillation to a sterile neutrino in eV mass scale [311,460]. The same scheme could explain also the reactor-antineutrino anomaly [311], discussed in Section 3.6.2. Searches for the sterile neutrinos are under progresses in several laboratories. However, it should be remarked here that there is no accepted sterile neutrino model to explain the experimental anomalies consistently.

4.5. Coherent neutrino–nucleus scattering

Neutrinos can scatter off nuclei coherently [462], which practically means that the neutrino interacts with the nucleus as a whole instead of only a single nucleon. Coherent elastic neutrino–nucleus scattering (CEνNS) occurs whenever the inverse of the momentum transfer between the incoming neutrino and the nucleus (i.e. essentially the neutrino deBroglie wave length) is larger than or comparable to the size of the nucleus, i.e. $E_\nu \lesssim 50$ MeV. The process is a NC reaction that can be expressed as

$$\nu + (A, Z) \rightarrow \nu + (A, Z),\tag{141}$$

where the initial and final states of the nucleus of mass number A and atomic number Z are the same. CEνNS will become a nuisance in dark matter detectors (see the next section) in upcoming years, but it can also prove to be an important probe of beyond-standard-model physics.

4.5.1. Overview

Coherent neutrino–nucleus scattering is a special case of the more general neutral current process discussed in Section 4.1.2. The cross-section for coherent scattering is obtained from the general case by setting the initial and final states to be the same. Under the assumption of an even–even nucleus with a 0^+ ground state, no strange-quark contributions, and a vanishing neutron electric form factor, the angle-differential cross section for coherent neutrino–nucleus scattering predicted by the standard model is simply [462–464]

$$\frac{d\sigma}{d\cos\theta} = \frac{G_F}{8\pi}(1 + \cos\theta)E_\nu^2 \left[Z(4\sin^2\theta_W - 1)F_p(q^2) - NF_n(q^2) \right]^2,\tag{142}$$

where G_F is the Fermi coupling constant (5), E_ν the neutrino energy, θ_W is the Weinberg angle, and F_p and F_n are the nuclear form factors for protons and neutrons, respectively. As $4\sin^2\theta_W - 1$ is very small, the proton part is strongly suppressed and the coherent cross section effectively and characteristically scales as $\propto N^2$.

Typically, due to the coherent N^2 enhancement, the cross section for CEνNS is a few orders of magnitude larger than for the incoherent interactions [440]. Thus it is a little surprising that neutrinos scattering coherently and elastically off nuclei had been out of reach of experiments for decades. This is due to the fact that the measured signal is the recoil energy of the nucleus in some form, and the maximum recoil energy for CEνNS is

$$E_{\mathrm{R,max}} = \frac{2E_\nu^2}{M + 2E_\nu} \, , \tag{143}$$

where M is the mass of the target nucleus. Therefore detectors will need to have a low threshold energy: To go over 1 keV of recoil energy in, say, liquid xenon detectors ($A \approx 130$) would need a neutrino energy of at least 5 MeV. Moreover, the nuclear form factor in Eq. (142) vanishes rapidly with increasing recoil energy (or, equivalently, momentum transfer). This leads to the detectable recoil energies being of the order of a few keV. Translating a low recoil energy into a measurable signal is a challenge for experiments striving for a low threshold.

Although techniques to detect CEνNS were proposed decades ago [465], experimental techniques have only recently developed to the point that recoil energies of the order of $\sim$ keV can be detected. Indeed, CEνNS was finally detected recently [466] by the COHERENT experiment. This discovery by the COHERENT experiment seems to be consistent with the signal expected from the standard model at 1σ level [466]. After the initial discovery has now been made, further research can be done to investigate whether any evidence for beyond-standard-model physics, such as sterile neutrinos [467–469], a neutrino magnetic moment [470], or nonstandard interactions [471–474], can be found in this process.

4.5.2. Neutrinos in dark-matter detectors

Uncovering the nature of dark matter is one of the most pressing topics in modern physics. It has been convincingly argued, by unexpected galactic rotation curves [475–478], structure formation [479,480], and cosmic microwave background data [481,482], that large majority of matter in the Universe consists of nonbaryonic cold dark matter (CDM). The most compelling candidate for CDM is a Weakly Interacting Massive Particle (WIMP): a species of stable particles emerging in extensions to the standard model, that have a suitable relic density and have only weak couplings with ordinary matter. Such WIMPs appear for example in Kaluza–Klein models with universal extra dimensions [483,484], technicolor models [485,486], little Higgs models with T parity [487,488], and, perhaps the most famously, supersymmetric extensions to the standard model [489]. If dark matter indeed consists of WIMPs, it should in principle be possible to directly detect such a particle interacting with an atomic nucleus in an earthbound detector.

There has been a huge effort put into direct detection of WIMPs in the past decades, and there are many experiments currently running or proposed to start gathering data in the near future, for examples see Refs. [490–496]. Some of the current leading experiments use a liquid xenon target [497–502], which allows for easy scalability to larger and more sensitive detectors. One unique way to search for WIMPs is detection of nuclear gamma rays and atomic X rays [503,504], where the solar-neutrino NC-background contributions have to be considered.

With increasing detector mass and thus increasing sensitivity, the largest xenon detectors (and other detectors will follow) will soon face a possibly crippling problem when the detectors will start seeing coherent neutrino–nucleus scattering as background radiation [505,506]. This phenomenon is called the *neutrino floor* of the direct dark-matter experiments. The energy-differential flux of solar neutrinos is given in Fig. 46 in Section 4.2. It is expected that the first part of the neutrino floor encountered in direct detection experiments is caused dominantly by ^{8}B solar neutrinos as they have the largest flux out of neutrinos able to give a detectable recoil to a nucleus in a detector ($E_R \gtrsim 1$ keV) [507,508]. Other types of solar neutrinos also contribute, but they would require a lower detector threshold than what the next generation detectors will have. For atmospheric and diffuse-supernova-background neutrinos the spectra extend to higher energies than for solar neutrinos, but the expected fluxes are much smaller. It will require a long exposure to detect them with the next-generation detectors. It should be noted, that dark-matter detectors will also be sensitive to low energy neutrinos, such as the solar *pp* neutrinos, via electron recoils [506]. However, most detectors are able to discriminate between electronic and nuclear recoil events.

Once neutrinos are seen as background in dark-matter detectors, one cannot attribute a detected nuclear-recoil excess to a dark-matter particle unless the rate of this excess is larger than the uncertainty of the neutrino event rate. Moreover, neutrinos also effectively mimic nuclear recoil spectra expected from WIMPs, and at some select WIMP masses, the detection signal is predicted to be especially similar for WIMPs and neutrinos [506]. This leads to the neutrino floor in direct detection experiments. After reaching the neutrino floor the detection efficiency of the detector increases only marginally with increasing exposure.

As the neutrino background looms in the horizon for the next generation of dark matter direct detection experiments, it is of utmost importance to device a way to circumvent the neutrino floor to keep probing lower and lower cross sections for dark-matter interactions. One such possibility is the different-time signature of the neutrino and WIMP signals [509]. Due to the motion of the Earth around the Sun, the number of WIMP-induced recoils is expected to peak around June while for solar neutrinos the peak should be in January when the Earth is closest to the Sun. Using timing information in addition to spectral data can improve the exclusion limits of an experiment, depending on the WIMP velocity distribution [509].

Another possibility is to exploit the directional information of the nuclear recoil signal [510,511]. Dark-matter- and neutrino-induced recoils have a distinct favored event angle, which can be used to discriminate between the different signals. Most current detectors do not have directional sensitivity, however. Additional nuclear responses in a nonrelativistic effective field theory (EFT) [512,513] have also been suggested as a possible way to discriminate between neutrino and WIMP

Table 14
Valence space truncations made in the ISM calculations of $^{128-131}$Xe. The first column gives the nucleus in question, the following five columns give the minimum/maximum values of neutrons on the single-particle orbitals $0g_{7/2}$, $1d_{5/2}$, $1d_{3/2}$, $2s_{1/2}$ and $1h_{11/2}$, respectively. The calculations have been performed in the ISM nuclear-model framework [447].

Nucleus	$0g_{7/2}$	$1d_{5/2}$	$1d_{3/2}$	$2s_{1/2}$	$1h_{11/2}$
^{128}Xe	8/8	6/6	0/4	0/2	4/12
^{129}Xe	8/8	6/6	0/4	0/2	4/12
^{130}Xe	8/8	4/6	0/4	0/2	0/12
^{131}Xe	8/8	6/6	0/4	0/2	0/12
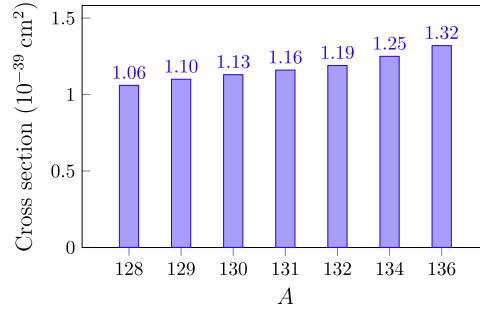
Fig. 55. Total coherent cross sections of ^{8}B solar neutrinos scattering off xenon isotopes. The calculations have been performed in the ISM nuclear-model framework [447].

recoil events. If the WIMP–nucleus interaction does not happen via the conventional spin-dependent or spin-independent channel, but via some other operator arising in the EFT framework, the recoil spectrum for WIMPs can be different from the one for neutrinos.

The total cross sections of solar ^{8}B neutrinos scattering coherently off the most abundant stable xenon isotopes, $^{128-132,134,136}$Xe, have been calculated recently [447]. The nuclear-structure calculations were made in the ISM using the shell-model code NuShellX@MSU [514] in the 50–82 major shell using the SN100PN interaction [515]. Calculations for ^{132,134,136}Xe were done in the fully unrestricted valence space, but for $^{128-131}$Xe truncations had to be made in the neutron valence space. The truncations made are shown in Table 14. For the even-A isotopes the experimental spectra are well reproduced by the ISM calculation. For the odd-A isotopes one gets the correct ground state and the low-lying positive-parity states are well reproduced, but the negative-parity states $9/2^-$ and $11/2^-$ are much lower in the computed spectrum than in the experimental one [447]. This is a feature in the SN100PN interaction, which has also been noticed elsewhere [516].

The total cross sections for the aforementioned xenon isotopes are given in Fig. 55. One can immediately see that the cross section becomes larger with increasing neutron number. Indeed, the cross section divided by the square of the neutron number is nearly a constant, as expected from (142).

4.6. Neutrino–nuclear responses for astro-neutrino nucleosynthesis

Gravitational energy gain in supernova collapse is carried away by the neutrino wind. Thus the neutrinos play an important role in the nucleosynthesis in the mantle of a core-collapse supernova. Actually, some nuclei are produced exclusively by the neutrino nucleosynthesis, and there are many nuclei which are produced partially by the neutrino–nuclear interactions. The neutrino nucleosynthesis and the neutrino effects on the supernova dynamics are described in recent research articles [11–14,517] and references therein. In this section, we briefly discuss neutrino–nuclear responses associated with the neutrino nucleosynthesis in a supernova.

Neutrino processes to be considered for the neutrino nucleosynthesis are CC^-, CC^+ and NC weak processes defined by

$$CC^- \ (\nu_e, e^- x), \quad CC^+ \ (\bar{\nu}_e, e^+ x), \quad NC \ (\nu_x, \nu_x' x), \tag{144}$$

where ν_x stands for a μ or a τ neutrino, and x for γ, β, neutron, proton, etc. following the neutrino interaction. The supernova neutrinos are mainly in the medium-energy region of $E_\nu = 5 - 40$ MeV and extend to higher energies around 50–70 MeV, depending on the temperature. This energy region is the same as that for $0\nu\beta\beta$ virtual neutrinos. The nuclear production rate for the neutrino nucleosynthesis is determined by the neutrino flux, the energy spectrum, the neutrino–nuclear cross section and the de-excitation process of the emitted particles x.

The neutrino cross section is given by the sum of the cross sections for residual states i with the excitation energy E_i. It is written as

$$\sigma(\nu) = \sum_i \sigma(E_\nu, E_i), \tag{145}$$
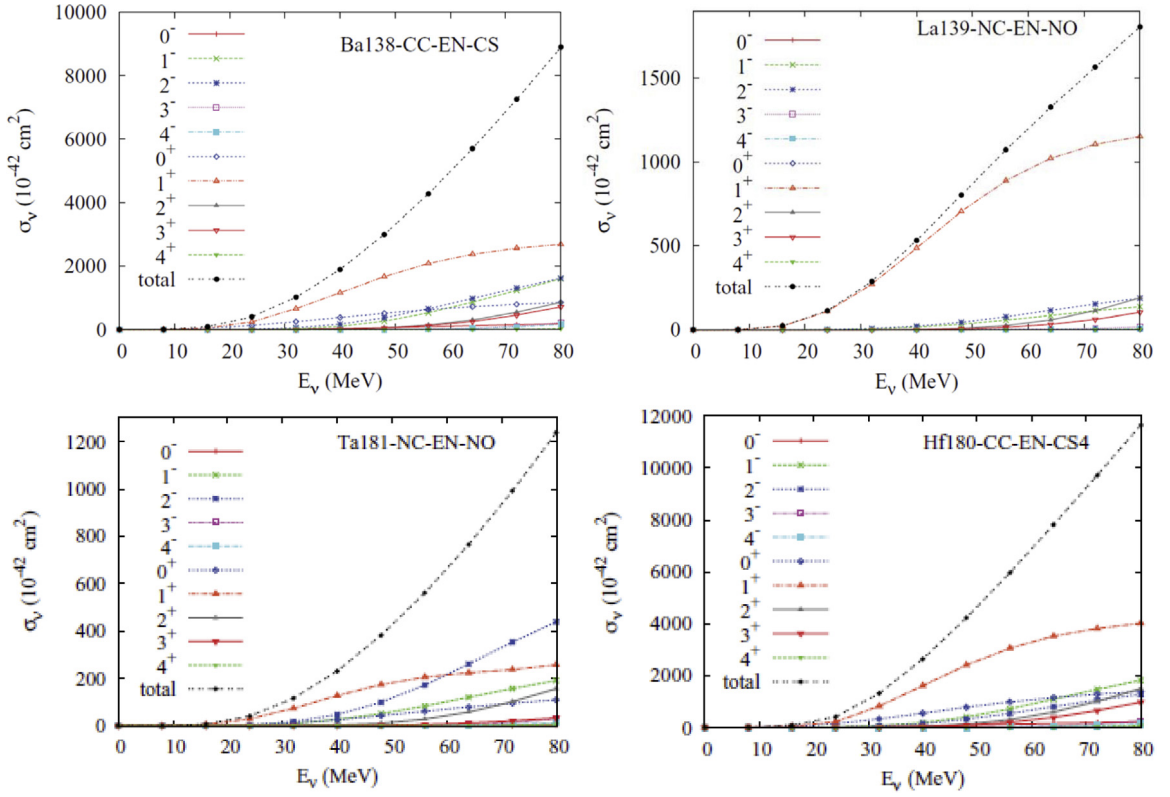
Fig. 56. Neutrino-nucleosynthesis cross sections as functions of the neutrino energy. Upper-left: CC interactions on ^{138}Ba, upper-right: NC interactions on ^{139}La, lower-left: NC interactions on ^{181}Ta, lower-right: CC interactions on ^{180}Hf [78].

where E_ν is the neutrino energy and $\sigma(E_\nu, E_i)$ is the cross section for the state i. The cross section for the scattering to the individual state i is

$$\sigma(E_\nu, E_i) = g_W K(E_\nu, E_i) B_i(J_i^\pi), \quad B_i(J_i^\pi) = (2J+1)^{-1}|M_i(J_i^\pi)|^2, \tag{146}$$

where g_W is the weak coupling, $K(E_\nu, E_i)$ is a kinematic (phase space) factor and $B_i(J_i^\pi)$ is the neutrino response for the state i with J^π being the spin and parity, and $M_i(J_i^\pi)$ is the NME.

The rate of neutrino nucleosynthesis (nuclear production rate) is sensitive to the neutrino flux, the neutrino energy spectrum and the nuclear response. The energy spectrum reflects the temperature of the neutrino sphere. Hence, one may get useful information on the neutrino flux and the nuclear temperature from the neutrino-synthesis rate. Here one needs the neutrino responses as functions of the neutrino energy and information on the nuclear decay processes in a wide excitation region.

The neutrino responses in the medium-energy region are mainly giant resonances with $J^\pi = 0^\pm$, $1^\pm$, $2^\pm$, $3^\pm$. In the high-excitation region above $E_\nu \geq 30$ MeV, quasi-free CC and NC scatterings get significant. The Fermi giant resonance (IAS 0^+), the GTR (1^+), the IVSDR (2^-) and the axial–vector CC quasi-free scattering responses have been studied using CERs, as described in Section 2.3.

The neutrino responses for light nuclei are evaluated based on the ISM, while those for the medium-heavy and heavy nuclei are evaluated by using the RPA [517]. In fact, accurate theoretical calculations of the neutrino CC and NC responses for nuclei in the needed wide excitation region are hard since they are sensitive to various kinds of nucleonic and non-nucleonic correlations and the renormalization (quenching) factors for the weak interactions. Some phenomenological values around $g_A^{\text{eff}}/g_A \approx 0.74$ are used for the quenching factor [14]. Experimentally the CC and NC neutrino responses in the wide excitation region are not well studied. Nuclear CERs, muon-capture reactions, photo-nuclear reactions, and neutrino-induced reactions in the future are encouraged to be performed in order to study the neutrino–nuclear responses relevant to the neutrino nucleosynthesis.

Nuclear de-excitation processes following the neutrino CC and NC interactions are calculated in order to get the final nuclear productions. Statistical models such as SMOKER [518] and others are used for particle and γ decays following the neutrino CC and NC interactions. Here we note that non-statistical particle emissions [29] at the pre-equilibrium stage of the reaction are necessary to be considered in addition to the statistical evaporation at the equilibrium stage, in particular for the energetic supernova neutrinos with $E_\nu \geq 30$ MeV. Note that γ and β decays in deformed nuclei, such as ^{180}Ta and others, are not just statistical decays, but are restricted by the J_K selection rules as discussed in Section 2.2.2.

Theoretical calculations of neutrino nucleosynthesis for ^{11}B, ^{19}F, ^{138}La and ^{180}Ta were made by using the ISM for light nuclei and RPA for heavy nuclei as given in the review [517] and references therein. The neutrino cross sections for electron–neutrinos are shown as functions of the temperature in [517]. The degeneracy parameter is set as $\alpha = 0$. The neutrino cross sections are dominantly CC cross sections, and increase as the temperature increases. The cross sections for ^{138}Ba show that the 0-neutron emission is dominant at low temperatures but the dominant process above 4 MeV is the 1-neutron emission and the 2-neutron emission gets appreciable at higher temperatures beyond 6 MeV. We note here that cross sections and the neutron cascades are sensitive to the CC strength distributions and the absolute values for the weak couplings (renormalization factors), which remain to be carefully verified by dedicated theoretical and experimental studies.

The NC and CC neutrino cross sections have been evaluated theoretically by using different nuclear models, as given in Table 11 and in the articles [13,396,517,518] and the references therein. QSM (quasiparticle shell model) NC cross sections on ^{139}La and ^{181}Ta and QRPA CC ones on ^{138}Ba and ^{180}Hf are shown in Fig. 56 [78]. The CC cross sections are larger by factors $4 - 5$ than the NC ones. They are predominantly the 1^+ GT cross sections up to 40 MeV, and the 1^- and 2^- contributions get appreciable above 40 MeV.

The neutrino energy spectra are sensitive to the nuclear temperatures of the neutrino spheres. The average energies are given as $\bar{E}_{SN} \approx 3T_{SN}$ with T_{SN} being the temperatures of 3.5 MeV, 5 MeV and 8 MeV, for the electron–neutrino, the electron antineutrino, and the μ, τ neutrinos, respectively [159]. The neutrino oscillations from μ and τ neutrinos to the electron–neutrino shift drastically the electron–neutrino spectrum to the higher-energy side, and accordingly increases the neutrino cross section (phase-space factor) and thus the synthesis rate. In other words, one may learn about the neutrino-mixing angles and the mass spectrum by investigating the effects of neutrino oscillations on the synthesis rates as discussed in [395] and references therein. Neutrino nucleosynthesis associated with two neutron-star mergers is interesting from astrophysics view points.

5. Neutrino–nuclear responses and double β decays

Neutrino–nuclear responses for double β decays (DBDs) have been a subject of intense study during the last decades. The subject was introduced in Section 1.4 of this review. The DBD has close connections to the physics beyond the standard model [519] and neutrino physics [520–522]. A comprehensive review of the nuclear matrix elements (NMEs) of the DBDs was published in 1998 [2]. In the same year an extensive review on the different mechanisms of DBD appeared [3]. These were complementary to the classical review [523] on the electron-emitting and reviews [524,525] on the positron-emitting modes of the DBD. Later reviews include [16–18,23,526]. A review on the Majorana-neutrino mixing was given in [527]. Some recent reviews on DBD theory, DBD experiments and nuclear responses for DBD are also given in Section 1.4.

Very recent reviews, appearing already earlier in this review, are [21,23,24]. Recent reviews about the DBD NMEs, covering part of the calculations, are [19,20]. A unique review on the effective value of the weak axial–vector coupling constant, g_A, was published recently [30].

5.1. Modes of double beta decays

There are several modes of DBDs and below we present those mediated by a light neutrino (two-neutrino DBD) or a light Majorana neutrino (neutrinoless DBD). We also briefly address the issue of the phase-space factors of these decays.

5.1.1. Light-neutrino-mediated DBDs

In Fig. 57 are shown schematic pictures presenting the concept of the two-neutrino DBD ($2\nu\beta\beta$ decay) with emission of two electrons and two antineutrinos. As mentioned in Section 1.4 the decay proceeds through two consecutive β^- decays (left figure) through the virtual 1^+ states of the intermediate nucleus, in this case ^{76}As (right figure).

In Fig. 58 is depicted the essential content of the neutrinoless DBD ($0\nu\beta\beta$ decay) with emission of two electrons. This $0\nu\beta^-\beta^-$ decay is mediated by the exchange of a light Majorana neutrino (left figure). A massive neutrino is needed in order to overcome the mismatch of the helicities of the emitted antineutrino ($\bar{\nu}$) and absorbed neutrino (ν). Since no antineutrinos are emitted, contrary to the case of the $2\nu\beta^-\beta^-$ decay, the lepton number is broken by two units ($\Delta L = 2$). In addition, the Majorana nature is needed in order to match the emitted $\bar{\nu}$ with the absorbed ν. The neutrino propagator between the two decay vertices produces a Coulomb-like, roughly $1/r$ (where r is the distance between the two decaying neutrons) type of potential, which can be decomposed into multipoles like the Coulomb field. These multipoles lead to virtual transitions through all possible multipole states J^π of the intermediate nucleus, in this case ^{76}As (right figure).

In Fig. 59 the neutrinoless double positron decay ($0\nu\beta^+\beta^+$ decay, left figure) and the neutrinoless positron/electron-capture ($0\nu\beta^+$EC decay, right figure) are shown schematically. In the latter decay only one positron (e^+) is emitted and a bound electron from an atomic orbital is captured, leaving a hole (H) in the orbital. The corresponding two-neutrino decays can be obtained from the diagrams by cutting the Majorana-neutrino propagator and letting the resulting two neutrinos fly free. The positron-emitting DBDs have recently been reviewed in [21].

In Fig. 60 we depict the two-neutrino double-electron capture (2νECEC, left side) and the radiative (R0νECEC, middle) and resonant (R-ECEC, right side) neutrinoless double-electron captures, discussed first in [528] and later in [529]. The resonant neutrinoless double electron capture (R-ECEC) has been reviewed in [21,530] and extensively studied in [531]. The R-ECEC
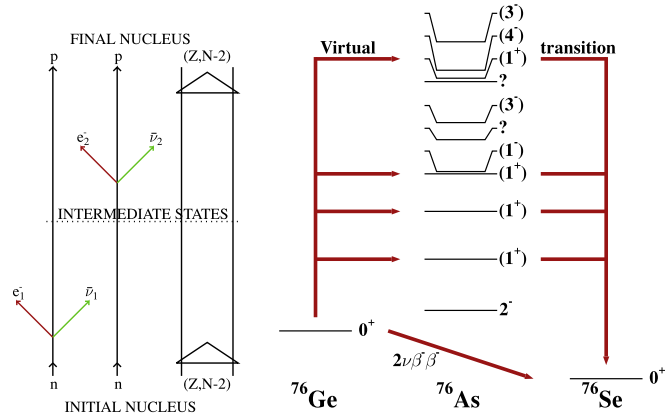
Fig. 57. Two-neutrino $\beta^-\beta^-$ decay of ^{76}Ge. Left side: Schematic diagram of the two consecutive β^- transitions of the $2\nu\beta^-\beta^-$ decay; Right side: Schematic level scheme and virtual transitions through 1^+ states of ^{76}As.
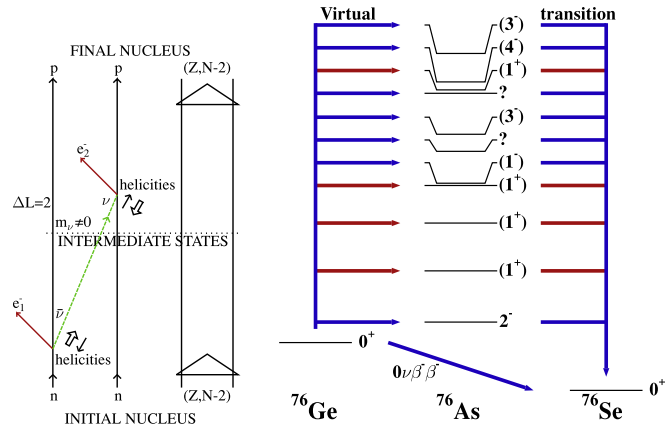
Fig. 58. Neutrinoless $\beta^-\beta^-$ decay of ^{76}Ge. Left side: Schematic diagram of the light-Majorana-neutrino-mediated $0\nu\beta^-\beta^-$ decay; Right side: Schematic level scheme and virtual transitions through J^π states of ^{76}As.
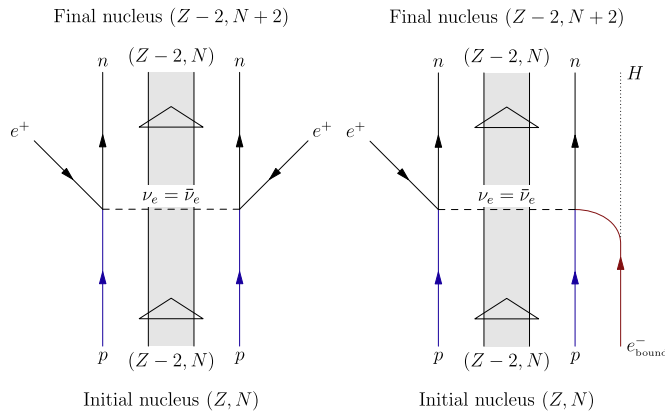
Fig. 59. Neutrinoless positron-emitting DBD. Left side: Schematic diagram of the light-Majorana-neutrino-mediated $0\nu\beta^+\beta^+$ decay. Right side: Schematic diagram of the light-Majorana-neutrino-mediated $0\nu\beta^+$EC decay. The symbol "H" denotes a hole left in the atomic orbital from which the electron was captured.

process is characterized by the possibility for a large resonance enhancement effect [529,532] by the coincidence of the energies of the initial and final states of the process.

In Fig. 61 we display the possible two-neutrino DBD transitions from the mother nucleus ^{124}Xe to the lowest four final states in the nucleus ^{124}Te. Along with the arrows are shown the possible modes of decay ($\beta^+\beta^+$, β^+EC and ECEC) and the
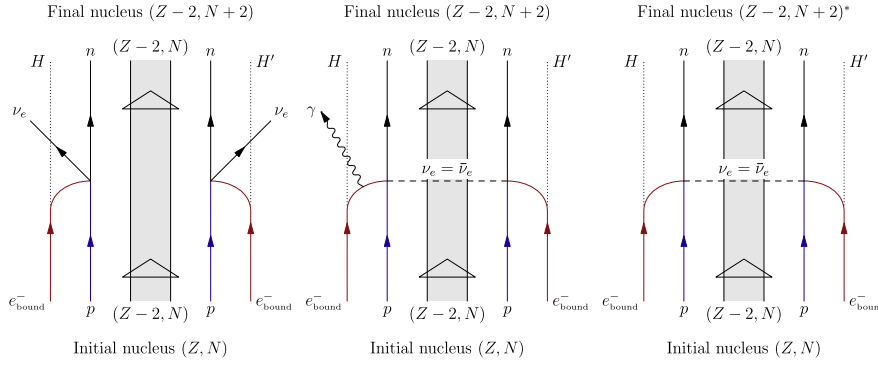
Fig. 60. Double-electron-capture (ECEC) decays. Left side: Schematic diagram of the two-neutrino ECEC decay (2νECEC). Middle: Schematic diagram of the light-Majorana-neutrino-mediated radiative neutrinoless ECEC decay (R0νECEC). Right side: Schematic diagram of the light-Majorana-neutrino-mediated resonant neutrinoless ECEC decay (R-ECEC). The symbols "H" denote holes left in the atomic orbitals from which the two electrons were captured.
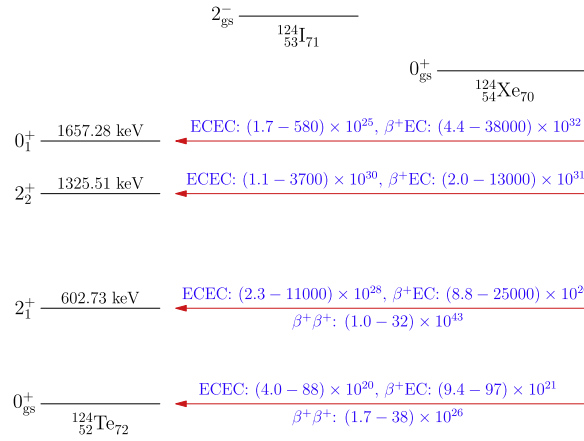
Fig. 61. Two-neutrino DBD of ^{124}Xe. Shown are the possible modes of positron-emitting decays and their computed half-lives in units of yr [533].

corresponding calculated half-lives [533]. Here it should be noted that the Q value of the ECEC mode (Q_{ECEC}) is always the largest, roughly[7] the nuclear mass difference between the mother and daughter nuclei plus $2m_ec^2$, where m_e is the electron rest mass. The Q value of the process β^+EC is smaller roughly by the energy $2m_ec^2$ and the Q value of the process $\beta^+\beta^+$ is smaller by roughly the energy $4m_ec^2$ than Q_{ECEC}. This is why in some cases only the ECEC mode is possible (see the tables of Section 5.4).

In Fig. 62 we show the leading neutrinoless DBD transitions between ^{124}Xe and ^{124}Te. The decays to the final 2^+ states are much suppressed [2] and are not included here. The Q values of the neutrinoless processes obey the same hierarchy as do the two-neutrino processes. Since in the R-ECEC process no leptons appear in the final state (see the right panel of Fig. 60) to carry away the decay energy, $Q_{ECEC} = m_i - m_f$, where m_i (m_f) is the *atomic* mass of the initial (final) atom, the decay can proceed only by a coincidence of the initial and final energies such that an excited final state with excitation energy $E = E^*$+electron binding, E^* being the *nuclear* excitation energy, has to be available such that the so-called degeneracy parameter $d = Q_{ECEC} - E$ is small enough to match the (nuclear plus atomic) width Γ of the excited final state. This width is presented in Fig. 62 as a shaded Lorentzian distribution. In the figure it is also shown that two atomic K-shell X-rays are emitted after the R-ECEC process. For more details on the R-ECEC mechanism and its relation to the NMEs, see the review [530].

5.1.2. Phase-space factors

Early compilations of the phase-space factors include Refs. [2,523–525], both for the electron- and positron-emitting modes of DBD. A rather comprehensive set of the $2\nu\beta^-\beta^-$ and $0\nu\beta^-\beta^-$ phase-space factors was compiled in [534]. The calculations were done by using exact Dirac wave functions with finite nuclear size (uniform charge distribution in a sphere), including electron screening in the Thomas–Fermi approximation. Single and summed electron spectra and their angular

---

7 The binding energies of the two captured electrons should be subtracted.
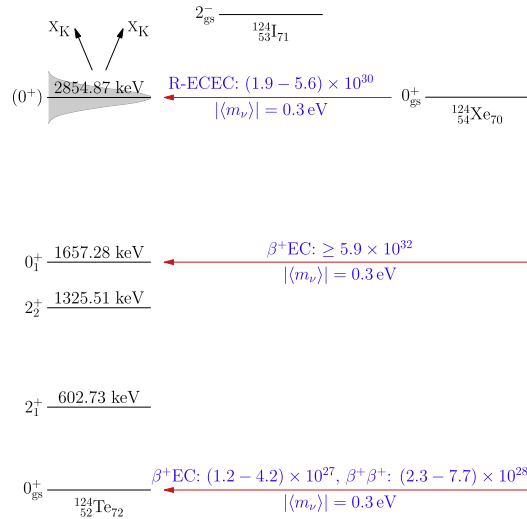
Fig. 62. Neutrinoless DBD of ^{124}Xe to the 0^+ finals states in ^{124}Te. Shown are the possible modes of positron-emitting decays and their computed half-lives in units of yr [533]. The resonant ECEC decay (R-ECEC) to the 2854.87-keV state is followed by two K-shell X-rays.

correlations were also given. In [535] phase-space factors for the $\beta^-\beta^-$ decays to the ground state and first 0^+ state were computed by solving numerically the Dirac equation for finite nuclear size and electron screening using a Coulomb potential derived from a realistic proton density distribution in the daughter nucleus.

In [536] the phase-space factors for positron-emitting modes of the two-neutrino and neutrinoless DBDs were computed by using the same calculational procedures which were used in the previous $\beta^-\beta^-$ paper [534]. In the work [537] the same authors computed the phase-space factors for the various $\beta^-\beta^-$ Majoron-emitting modes, and in [538] phase-space factors related to the ground-state and excited-state transitions in a left–right symmetric model were evaluated. In a recent work [539] the phase-space factors of the electron and positron-emitting modes of the two-neutrino DBD have been compiled by solving numerically the Dirac equation and including finite-nuclear-size and screening effects. In [236] a large number of phase-space factors for numerous $A \geq 100$ nuclei, both for the electron-emitting and positron-emitting $2\nu\beta\beta$ decays to the ground state and to many excited 0^+ and 2^+ final states was presented. In [540] a new method was introduced to compute the phase-space factors in an accurate way.

Many of the calculated phase-space factors in the above-mentioned works have been compared with earlier calculations, e.g. [2,523–525]. Consistency with these older results has been achieved and an improved accuracy, as well. Today the phase-space factors are accurately known due to accurate solvers of the Dirac equation and improved methods in handling the screening corrections and finite size of the nucleus. In addition, the decay Q values are better-known now than few decades ago.

5.2. Basic features of the $2\nu\beta\beta$ decays

The basic features of the $2\nu\beta\beta$ decays were briefly introduced in Section 1.4. As mentioned before, the virtual transition proceed through 1^+ state of the intermediate nucleus. The corresponding intermediate contributions can be presented, e.g., as running sums, i.e., as functions of the excitation energy in the intermediate nucleus, as done in Refs. [541,542]. The $2\nu\beta\beta$ strength functions and the associated Gamow–Teller running sums were given also in the ISM framework [235,543, 544]. The $2\nu\beta\beta$-decay strength functions of $A = 128,130$ nuclei were analyzed also in the framework of the microscopic interacting boson–fermion–fermion model (IBFFM-2) in the work [545]. Extremely large, two valence-shell ISM analysis of the $2\nu\beta\beta$ and $0\nu\beta\beta$ NMEs was performed in [230]. The pairing-vibrational aspects of the $2\nu\beta\beta$ decays of ^{128,130}Te were studied within the framework of a hybrid model in [546]. In [547] an effective theory to describe β and $\beta\beta$ decays was proposed. In this theory one can estimate the uncertainties based on power counting of the included degrees of freedom.

The relation of the $2\nu\beta\beta$ NMEs and $0\nu\beta\beta$ NMEs has been studied in [548] in the pnQRPA formalism and in [549] in an energy-density-functional formalism. The latter study was done in a chain of cadmium isotopes assuming fictitious DBD transitions. In the work [550] the two-neutrino Gamow–Teller and Fermi transitions were studied in an exactly solvable model, expressible using generators of the SO(8) group. The dependence of the energy denominator of the $2\nu\beta\beta$ NMEs on lepton energies was studied by using a Taylor expansion in [551]. The expansion possibly allows the determination of the effective value of the weak axial coupling g_A by $2\nu\beta\beta$ experiments.

A special class of theoretical approaches to the $2\nu\beta\beta$ decay is formed by the calculations resorting to the single-state-dominance hypothesis (SSDH) where the $2\nu\beta\beta$-decay half-life is dominated by the virtual transitions going through the lowest 1^+ state, in case it is the ground state of the DBD intermediate nucleus. Early studies of the feasibility of the SSDH were

Table 15
Effects of successive corrections to the magnitude of the pnQRPA $0\nu\beta^-\beta^-$ NMEs for decays of current experimental interest. Shown are the mother nucleus (column 1), the adopted value of the particle–particle strength (column 2) and the absolute value of the bare NME. The symbols denote A: induced currents (higher-order terms of the nucleonic current); B: effect caused by the form factors; C: Jastrow short-range correlations; D: UCOM short-range correlations for the Bonn-A nucleon potential [576,577].

Nucleus	g_{pp}	Bare value	+ A	+ A + B	+ A + B + C	+ A + B + D
^{76}Ge	1.00	8.529	7.720	6.356	4.723	6.080
^{82}Se	1.00	5.398	4.826	3.914	2.771	3.722
^{96}Zr	1.085	5.308	4.814	3.736	2.454	3.521
^{100}Mo	1.08	6.126	5.571	4.358	2.914	4.113
^{116}Cd	0.99	5.726	5.172	4.263	3.169	4.076
^{128}Te	0.905	7.349	6.673	5.260	3.563	4.979
^{130}Te	0.87	6.626	6.021	4.777	3.285	4.530
^{136}Xe	0.74	4.715	4.269	3.478	2.537	3.317

performed in [552–554], with further studies on the implications to the single-electron energy distributions and angular correlations of the outgoing electrons in [555]. A more comprehensive SSDH study was performed in [556]. All these studies were performed in the spherical pnQRPA framework. A study using pnQRPA based on a deformed Skyrme Hartree–Fock mean field was accomplished in [557].

The FSQP (Fermi Surface Quasi Particle model) is a semi-empirical model to evaluate the $2\nu\beta\beta$ NMEs [558–560]. Experimental single $\beta^\pm$/EC NMEs for Fermi-surface (low-lying) quasiparticle states in the intermediate nucleus are used. The FSQP NMEs reproduce well the observed NMEs. Experimental $2\nu\beta\beta$ NMEs are briefly described in Section 5.5.1, where the semi-empirical FSQP NMEs are also included for comparison.

5.3. Basic features of the $0\nu\beta\beta$ decays

The basic features of the $0\nu\beta\beta$ decays were briefly introduced in Section 1.4 and they have been partly discussed in the earlier reviews [2,18,21,23,24]. Specific attempts to describe the $0\nu\beta\beta$ NMEs include the quark-model-based model advocated in [561–563] and a formulation of the $0\nu\beta\beta$ problem in terms of nuclear moments, as devised in [564,565]. An interesting derivation of a general Lorentz-invariant parametrization for the long-range part of the $0\nu\beta\beta$ decay was done in [566] and for the short-range part in [567]. The $0\nu\beta\beta$-decay NMEs have been calculated also by considering the contributions coming from the right-handed weak currents (for a review of the old calculations see [2]). Some of the recent works for the decays to the 0^+ final ground state include [568] in the pnQRPA formalism and [569] in the ISM formalism. In the work [570] the feasibly of $0\nu\beta\beta$ decays to 2^+ excited final states was studied. There the light-Majorana-neutrino-mass mediated decay was found to be largely suppressed relative to decay to the final ground-state. In [571] the consequences of the assumption that the Pauli exclusion principle is violated for neutrinos and they obey, at least partially, the Bose–Einstein statistics was surveyed. In [572] and interesting new decomposition of the $0\nu\beta\beta$ NMEs was suggested, implying connection to the two-nucleon transfer experiments, and in [573] the importance of collective correlations in $0\nu\beta\beta$ decay were analyzed within a generator-coordinate method (GCM). In [574] the role of octupole correlations was analyzed for the $0\nu\beta\beta$ decay of ^{150}Nd using a relativistic energy-density functional formalism combined with the GCM.

5.3.1. Nucleonic currents and nucleon form factors

The nucleon-current form factors and additional nucleon-current contributions stemming from the induced currents (weak magnetism and pseudoscalar, see the form of the vector current (8) and axial–vector current (9) in Section 1.2) play a role in the neutrinoless $\beta\beta$ decays [575]. The nucleon-current form factors were present also in an earlier $0\nu\beta\beta$ model where they were derived from a quark model with harmonic confinement [561–563]. The effects of the higher-order terms in the nucleonic current and the nucleon-current form factors is shown in Table 15. It is seen that the higher-order terms (+ A) and the form factors (+ A+ B) successively reduce the absolute value of the $0\nu\beta\beta$ NME. In these calculations [576,577], as also in [575], the dipole form (10) has been adopted. A further study of these effects was performed recently [578].

5.3.2. Short-range correlations (SRC)

The traditional way [579] to include short-range correlations in the $0\nu\beta\beta$ NMEs was to introduce the Jastrow correlator function $f_J(r)$, where "J=Jastrow". The Jastrow function depends on the relative distance $r = |\mathbf{r}_1 - \mathbf{r}_2|$ of two nucleons, and in the Jastrow scheme one replaces the bare $0\nu\beta\beta$ operator $\mathcal{O}$ by a correlated operator $\mathcal{O}_J$ by the simple procedure

$$(0_f^+\|\mathcal{O}\|0_i^+) \rightarrow (0_f^+\|\mathcal{O}_J\|0_i^+) = (0_f^+\|f_J\mathcal{O}f_J\|0_i^+).\tag{147}$$

A typical choice for the function f_J is

$$f_J(r) = 1 - e^{-ar^2}\left(1 - br^2\right),\tag{148}$$

with $a = 1.1\,\text{fm}^{-2}$ and $b = 0.68\,\text{fm}^{-2}$. As a result, the Jastrow function effectively cuts out the small-r part from the relative wave function of the two nucleons. For this reason, the traditionally adopted Jastrow procedure does not conserve the norm
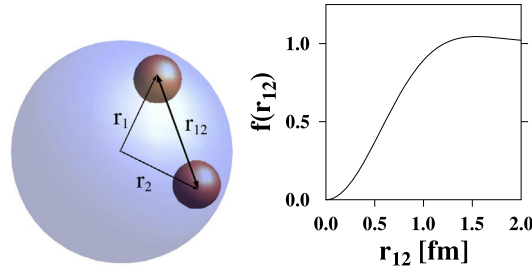
Fig. 63. Two nucleons in a nucleus. Left figure: Shown are their coordinates $\mathbf{r}_1$ and $\mathbf{r}_2$, and their relative coordinate $\mathbf{r}_{12} = \mathbf{r}_1 - \mathbf{r}_2$. Right figure: Jastrow correlator f as a function of the relative distance $|\mathbf{r}_{12}|$.
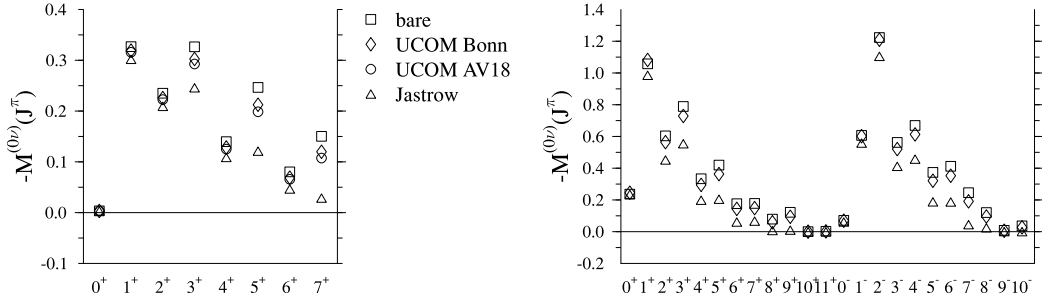
Fig. 64. Effects of various short-range correlators on the values of the $0\nu\beta^-\beta^-$ multipole NMEs $M^{0\nu}(J^\pi)$ of (42). Left panel: The ISM-computed NMEs for the decay of ^{48}Ca ; Right panel: The pnQRPA-computed NMEs for the decay of ^{76}Ge [581].

of the relative wave function. In the left panel of Fig. 63 are depicted two nucleons in a nucleus and their relative distance $r = |\mathbf{r}_1 - \mathbf{r}_2|$. The right panel presents the functional form (148) of the Jastrow correlator.

To circumvent the difficulties associated with the use of a Jastrow function one can adopt the more refined unitary correlation operator method (UCOM) [580]. The UCOM was first elaborated in the context of the DBD, within the pnQRPA framework, in [581] and later, e.g., in [576,577,582]. The UCOM SRCs were studied in the ISM framework in [199]. The UCOM creates the correlated many-nucleon state by a unitary correlation operator C:

$$|\tilde\Psi\rangle = C|\Psi\rangle, \quad C = C_\Omega C_r, \tag{149}$$

where C_Ω represents tensor correlations and C_r represents central correlations. In this scheme it is equivalent to use correlated states or correlated operators:

$$\langle\tilde\Psi|A|\tilde\Psi'\rangle = \langle\Psi|C^\dagger AC|\Psi'\rangle = \langle\Psi|\tilde A|\Psi'\rangle. \tag{150}$$

The exact form of the operator C is obtained by finding the minimum of the Hamiltonian matrix element $\langle\Psi|C^\dagger HC|\Psi\rangle$. Therefore, the choice of the two-body interaction in H affects also the form of C. Explicit expressions for the operators C_r and C_Ω can be found in Refs. [580,583]. The minimization has been done for the Bonn-A and Argonne AV18 potentials in [584] and the effects of the resulting UCOM SRCs for the Bonn-A potential are shown in Table 15.

The UCOM treats the SRCs smoothly and not as violently as the Jastrow method. This shows as a less drastic reduction in the values of the computed $0\nu\beta\beta$ NMEs, as is clearly visible in the numbers of Table 15 and in Fig. 64 where the multipole decomposition of Eq. (42) has been presented for the $0\nu\beta\beta$ decays of ^{48}Ca (left panel) and ^{76}Ge (right panel) for the mentioned two nuclear potentials. In fact, just adding the form factors (+ A+ B in Table 15) almost produces the final magnitude of the $0\nu\beta\beta$ NME (+ A+ B+ D in Table 15), without taking into account the SCRs.

In [585] the coupled cluster method (CCM) was used to evaluate the effect of the SRCs on the $0\nu\beta\beta$ NMEs since it provides directly the correlated two-body wave functions. To facilitate numerical calculations with the two adopted nucleon–nucleon (NN) potentials, the CCM SRCs were converted to a Jastrow-like analytical correlator function of the form

$$f_{\text{CCM}}(r) = 1 - ce^{-ar^2}\left(1 - br^2\right), \tag{151}$$

where now

$$a = 1.59\,\text{fm}^{-2}; \quad b = 1.45\,\text{fm}^{-2}; \quad c = 0.92 \quad \text{(for the Argonne NN potential)}, \tag{152}$$

$$a = 1.52\,\text{fm}^{-2}; \quad b = 1.88\,\text{fm}^{-2}; \quad c = 0.46 \quad \text{(for the CD-Bonn NN potential)}. \tag{153}$$
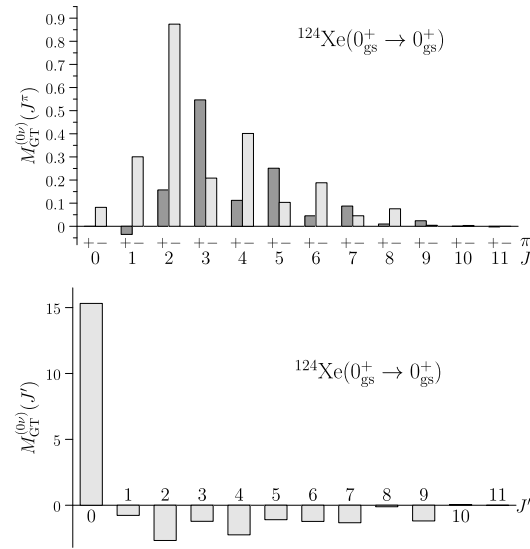
Fig. 65. Decomposition (42) [upper panel] and (154) [lower panel] of the GT NME for the ground-state-to-ground-state $0\nu\beta^+\beta^+$ decay of ^{124}Xe (based on calculations in [533]).

The effects of these SRCs were studied, e.g., in [586] using the ISM. A different type of study was performed in [587] where the nucleon–nucleon correlations were studied in both the coordinate and spin space for the $0\nu\beta\beta$ decay of ^{48}Ca. A 20% decrease of the associated NME relative to the ISM NME was recorded.

5.3.3. Decompositions of the $0\nu\beta\beta$ NMEs

The decomposition (42) for the ground-state-to-ground-state $0\nu\beta^-\beta^-$ decays of ^{48}Ca and ^{76}Ge are shown in Fig. 64. This type of decomposition was also discussed recently in [588]. The same decomposition is shown for the GT part of the total NME (this is the dominant NME) in the case of the ground-state-to-ground-state $0\nu\beta^+\beta^+$ decay of ^{124}Xe in the upper panel of Fig. 65. In the lower panel of the figure shown is the complementary decomposition

$$M^{0\nu} = \sum_{J'} M^{0\nu}(J'), \tag{154}$$

where J' is the angular momentum of the decaying nucleon pair. This decomposition has frequently been studied in the framework of the pnQRPA (see [589] for a review), but also in the ISM [590] and in the microscopic interacting boson model (IBM-2) [591]. The decomposition can also be probed by studying the angular momenta and parities of the neutron pairs that are changed into proton pairs in the $0\nu\beta^-\beta^-$ decay [200]. The usual multipole decomposition (42) has been studied in the case of the deformed QRPA in [592].

In Fig. 64 one may note the rather prominent role of the 1^+ and 3^+ contributions. The same can be concluded from the ISM study [588] for ^{48}Ca. In the right panel, for the $0\nu\beta^-\beta^-$ decay of ^{76}Ge, the 2^- contribution is the largest one. A similar trend continues for the $0\nu\beta^+\beta^+$ decay of ^{124}Xe, as seen in the upper panel of Fig. 65. For many other DBD systems the role of the mentioned multipoles is important for both the decays to the ground state (see, e.g., [247] for the pnQRPA and [544] for the ISM) and to the excited 0^+ states (see, e.g., [593]). In the decomposition (154), depicted in the lower panel of Fig. 65, the dominant contribution comes from a $J' = 0$ paired state and the contributions stemming from the higher J' pairs tend to cancel it in a coherent way. This is a general feature for all calculational frameworks and for all ground-state-to-ground-state neutrinoless DBD transitions (see, e.g., [582]). For the $0\nu\beta\beta$ transitions to excited 0^+ states this pattern no longer holds [593]. The decompositions for the heavy-Majorana-neutrino exchange have been analyzed in [247] for the pnQRPA and in [544] for the ISM.

In addition to the above decomposition analyses, the contributions from the intermediate J^π states can be presented as running sums, i.e., as functions of the excitation energy in the intermediate nucleus [594].

5.3.4. Radial dependence of the $0\nu\beta\beta$ NMEs

The radial dependence for the light-Majorana-neutrino-mediated $0\nu\beta\beta$ NME is presented in Fig. 66 [247]. The total NME is obtained by integration:

$$M^{0\nu} = \int_0^\infty M^{0\nu}(r)dr, \tag{155}$$
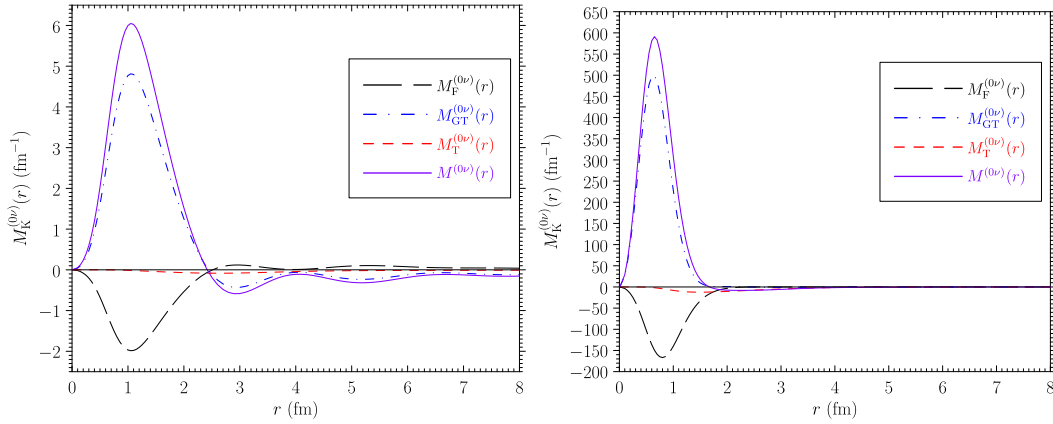
Fig. 66. Radial dependence of the Majorana-neutrino-mediated $0\nu\beta\beta$ NMEs $M_K^{0\nu}(r)$, $K = $ F, GT, T, and the total NME $M^{0\nu}(r)$ for the decay of ^{76}Ge [247]. Left panel: for light Majorana neutrino ; Right panel: for heavy Majorana neutrino.

where r is the relative distance between the decaying nucleons. The radial dependencies were also treated, e.g., in [582,585, 589] for the pnQRPA-based models and in [199] for the ISM. In [595] the $0\nu\beta^-\beta^-$ decays and in [596,597] the positron-emitting decays were studied for the radial dependence in the projected Hartree–Fock–Bogoliubov (PHFB) model for deformed nuclei. Different short-range correlations were added to the PHFB framework in [598] for the $0\nu\beta^-\beta^-$ emitters, and the corresponding radial dependencies were recorded.

In all these studies it is clear that the main contribution to the $0\nu\beta\beta$ NMEs is coming from short distances, below $2-3$ fm, and an accurate description of the physics involving distances $r \sim 1$ fm, or equivalently exchanged momenta $q \sim 200$ MeV, becomes important. Since such exchanged momenta occur at the Fermi surface of the many-nucleon system it is natural that the mentioned distances are the relevant ones, contributing most to the NMEs. In addition, since on average the distance between the nearest neighbors is[8] $r \sim 2$ fm it means that the nucleons participating in the $0\nu\beta\beta$ decay are mostly nearest neighbors.

5.3.5. Seniority truncation and the $0\nu\beta\beta$ NMEs

In [599] the effects of the seniority truncation on the value of the $0\nu\beta\beta$ NMEs were analyzed within the ISM framework. In this study the QRPA was considered to be a low-seniority approximation of the ISM, i.e. corresponding to seniorities of at most 4. Since the values of the $0\nu\beta\beta$ NMEs were found to decrease as functions of the included higher-seniority components it was concluded that the QRPA could overestimate the values of the $0\nu\beta\beta$ NMEs by several tens of percent. Similar results were obtained in the study ISM study of [199] and in the energy density functional (EDF) method study of [600]. Related to this, also the influence of the nuclear deformation has been addressed in [600], as also in [590] for the ISM and in [591] for the IBM-2.

5.3.6. Deformation effects

Nuclear deformation has clear effects on the values of the DBD NMEs, ranging from some 10% to several tens of percent for typical nuclei involved in $\beta\beta$ decays, the effect being strong for the $\beta^-\beta^-$ decay of ^{150}Nd. Deformation effects have been addressed in the shell-model like theories (with seniority degrees of freedom) in [543,590] for the ISM and in [591] for the IBM-2. In the Hartree–Fock(-Bogoliubov) type of calculations the effects of deformation have been addressed, e.g., in [557,596,601–605]. Usually the QRPA-type of models use a spherical formalism with a simple overlap factor with or without taking into account the different BCS occupation amplitudes of the mother and daughter nuclei. These spherical QRPA models have been extended to deformed QRPA approaches, e.g. in [592,606–612].

It has been found that deformation itself reduces the magnitudes of the DBD NMEs, and in particular the difference in the deformation of the DBD parent and daughter nuclei. In the QRPA-type of models the deformation difference is reflected in the overlap factor of the two sets of intermediate states, generated using separately the DBD initial and final nuclei (see, e.g., [606,610]). The overlap problem has been discussed extensively in [24,613–616].

In [617] a calculation of the $0\nu\beta\beta$ NMEs was performed by using a state-of-the-art Gogny-type energy density functional. The effects of deformation and difference in deformation were discussed in a comprehensive way. In a recent publication [183] the effects of axial and triaxial deformation were discussed for the $0\nu\beta^-\beta^-$ NMEs of ^{48}Ca, ^{76}Ge and ^{82}Se in a generator-coordinate framework using realistic shell-model interactions.

---

8 The radius of the nucleus is $R = 1.2A^{1/3}$ fm.

5.3.7. Partial restoration of the isospin symmetry

In the pnQRPA calculations of the $0\nu\beta\beta$ NMEs the g_{pp} parameter is usually adjusted by fitting the measured $2\nu\beta\beta$-decay half-lives, compiled recently in [258]. This procedure was followed in, e.g. [576,577,618,619]. Recently, an improved method was proposed in [246] where the NMEs corresponding to the exchange of light Majorana neutrinos were treated for the conservation of the isospin symmetry. There the particle–particle parts of the pnQRPA matrices were divided into isoscalar ($T = 0$) and isovector ($T = 1$) parts by the decomposition

$$
\begin{aligned}
g_{pp}\langle pn; J^\pi|V|p'n'; J^\pi\rangle \rightarrow\ & g_{pp}^{T=1}\langle pn; J^\pi; T = 1|V|p'n'; J^\pi; T = 1\rangle \\
& + g_{pp}^{T=0}\langle pn; J^\pi; T = 0|V|p'n'; J^\pi; T = 0\rangle\,.
\end{aligned}
\tag{156}
$$

One can now adjust the parameters $g_{pp}^{T=1}$ and $g_{pp}^{T=0}$ independently in the following way: The isovector parameter $g_{pp}^{T=1}$ can be adjusted such that the Fermi NME, similar to the Gamow–Teller NME of (19), but with intermediate Fermi transitions instead of Gamow–Teller ones, vanishes and thus the isospin symmetry is restored for the $2\nu\beta\beta$ decay. In this way practically all the Fermi strength goes to the double IAS (isobaric analog state), as it should. This procedure also leads [246] to the approximate isospin symmetry $g_{pp}^{T=1} \approx g_p^{pair} \approx g_n^{pair}$, where $g_{p,n}^{pair}$ are the pairing strengths adopted for protons and neutrons in the practical calculations. One can then keep this adjusted value of $g_{pp}^{T=1}$ in the further calculations for the $0\nu\beta\beta$ decay. One can independently vary $g_{pp}^{T=0}$ to reproduce the measured $2\nu\beta\beta$-decay half-life and again use this value in the calculation of the $0\nu\beta\beta$ NMEs.

In the ISM the isospin symmetry is automatically included in the formalism. As we saw above, this is not the case with the pnQRPA formalism. Also the IBM-2 formalism lacks isospin symmetry and it has to be restored explicitly, as done in the recent work [620]. In [600] the effects of the isospin symmetry were studied in the framework of the ISM and it was found that imposing isospin symmetry reduces drastically the magnitude of the Fermi NME but not the Gamow–Teller NME of the $0\nu\beta\beta$ decay, as was also found in the pnQRPA calculations in [246], and later in similar calculations by [247]. In [600] also an advanced, beyond-mean-field Gogny-based energy-density-functional (EDF) approach was used and its results were compared with the results of the ISM. It was found that due to the lack of isospin restoration in the EDF approach its $0\nu\beta\beta$ Fermi NME was large as compared with the Gamow–Teller NME. Lately a lot of effort has been put in developing isospin-invariant density-functional methods. In [621] an isospin invariant Skyrme EDF approach was developed and in [622] good isospin was achieved within a no-core configuration-interaction approach rooted in a multireference EDF theory.

5.3.8. Closure approximation

All theory frameworks, except the pnQRPA and some ISM calculations mentioned below, have to use the closure approximation when evaluating the $0\nu\beta\beta$ NMEs. In the closure approximation the sum over the intermediate J^π multipole states is removed by assuming an average excitation energy of these states so that the summation can be replaced by a unit operator. This was deduced to be a rather good approximation [623]. This approximation has recently been studied quantitatively both in the pnQRPA [548] and in the ISM [588] formalisms. In both studies it was found that the nonclosure $0\nu\beta\beta$ NMEs are about 10% larger than the closure ones. It was also found that the contribution from the 1^+ intermediate states mostly explains this difference. In [624] a method was suggested, based on the analysis of the $0\nu\beta\beta$ NMEs of ^{48}Ca, ^{76}Ge and ^{82}Se, to estimate the optimal value of the average closure energies at which the closure approximation gives the most accurate $0\nu\beta\beta$ NME. This work was extended to description of the ^{82}Se decay in [625] and further to the decay of ^{76}Ge in [626].

5.3.9. Chiral two-body currents

In [221] it was shown that the chiral two-body currents, built in the chiral effective field theory (χEFT), introduce a renormalization, $g_A^{eff}(q^2)$, that deviates from the one-body dipole $g_A(q^2)$ of (10) the less the higher the momentum exchange q is. The involved meson-exchange currents were consistently predicted by [45] and later extended and derived in [46–48]. In [221] it was estimated, by using the ISM many-body framework in the mass range $A = 48 - 136$, that the effect of the two-body currents on the value of the $0\nu\beta\beta$ NME is between -35% and 10% depending on the (uncertain) values of the χEFT parameters, the smallest corrections occurring for $A = 48$. In [627] the effect of the two-body currents was studied in the framework of the pnQRPA in the mass range $A = 48 - 136$, and a quenching effect of 10–22% was obtained for the $0\nu\beta\beta$ NMEs, the 10% effect pertaining to the case of ^{48}Ca. In a recent work [628] the quenching of the $0\nu\beta\beta$ NMEs was estimated by studying the contributions stemming from chiral two-body currents. The exact amount of quenching is, however, yet to be determined due to technical difficulties in the calculations.

5.3.10. Disentangling the decay mechanism

If the $0\nu\beta\beta$ decay will be detected then the question "What are the underlying mechanisms of $0\nu\beta\beta$ decay and how to identify them?" rises immediately. There are several possible mechanisms possibly contributing to the $0\nu\beta\beta$-decay amplitude in the general case of CP nonconservation: light Majorana-neutrino exchange, heavy left-handed and right-handed Majorana-neutrino exchanges, lepton-charge nonconserving couplings in supersymmetric theories with R-parity breaking, squark-neutrino mechanisms, leptoquark exchange, etc. [629–632]. In these cases measurements of two or more $0\nu\beta\beta$-decaying nuclei is necessary to (possibly) disentangle the different noninterfering or interfering mechanisms, the noninterfering case being simpler (e.g. light Majorana neutrino and heavy right-handed neutrino). It turns out that the measurements of the half-lives with rather high precision and the knowledge of the relevant NMEs with relatively small

uncertainties is needed to enable determination of the mechanism(s) of the $0\nu\beta\beta$ decay. In a later study [633] it was found that even to distinguish between the light and heavy Majorana-neutrino exchange is difficult due to the uncertainties in nuclear-structure calculations concerning the two-nucleon interaction, the mean field approximation and the poorly known effective value g_A^{eff} of the axial–vector coupling. In [538] the phase-space factors for the corresponding interference terms were derived for further analysis.

A more traditional way to try to distinguish between different $0\nu\beta\beta$-decay mechanisms is the observation and calculation of the single-electron/positron spectra and the angular correlations between the outgoing electrons/positrons. These spectra and correlations have been presented, e.g., in [523,534,568] for the $0\nu\beta^-\beta^-$ light Majorana-mass mode and in [523,568] also for the right-handed-currents modes. For the right-handed-currents modes the single-electron and correlation spectra depend on the NMEs and in [523] simple shell-model NMEs and in [568] QRPA-based NMEs were used. In [523,534] the spectra and correlations have been presented also for the $2\nu\beta^-\beta^-$ mode. In [537] the spectra and correlations have been presented for the Majoron-emitting $0\nu\beta^-\beta^-$ decay. The single-positron spectra and angular correlations between the outgoing positrons have been presented in [536] for both the $2\nu\beta^+\beta^+$ and $0\nu\beta^+\beta^+$ modes.

A thorough analysis of the angular correlations in the case of interference of the light Majorana-neutrino mass mode and the right-handed-currents mode was performed in [634] using NMEs based on the QRPA and ISM model frameworks, as also on the VAMPIR approach (see [623]). It was concluded that the only realistic way to obtain information on the interference of the mass mode and the right-handed modes is to perform a simultaneous analysis of a high-sensitive $0\nu\beta^-\beta^-$ experiment and a high-sensitive $0\nu\beta^+/\mathrm{EC}$ experiment. In [629] a formulation of the angular correlation of electrons emitted in $0\nu\beta\beta$ decay was presented for a general Lorentz-invariant effective Lagrangian containing leptonic and hadronic charged weak currents. As an example an analysis of the left–right symmetric models was performed and it was concluded that the sensitivity of the angular correlation to the mass of the right-handed W boson increases with decreasing value of the effective Majorana-neutrino mass m^{eff}. In [569] a survey of the interference effects of the light Majorana-neutrino mass mode and the right-handed-currents mode was performed for ^{82}Se decay by using NMEs calculated in the ISM framework. Conclusions in line with [523] were reached concerning the distinguishability between the mass mode and the right-handed λ and η modes: the single-electron spectrum is likely to be enough to distinguish between the mass mode and the λ mode, whereas one needs the angular correlations to distinguish between the mass mode and the η mode.

A clear conclusion of the above considerations is that much more theoretical and experimental work is needed in order to achieve the goal of disentangling the possible different mediating modes of the $0\nu\beta\beta$ decay. The $0\nu\beta\beta$ decay has not even been detected yet and the NMEs necessarily involved in the analyses are still too inaccurate to serve the purpose.

5.4. Survey of the calculations of two-neutrino and neutrinoless $\beta\beta$ decays

A lot of calculations have been performed for different nuclear isobaric systems, for both the $2\nu\beta\beta$ and $0\nu\beta\beta$ decays. Below we compile the available calculations for each DBD decay separately. We also give a brief description of the theory formalism behind the calculations (Section 5.3). It may be mentioned here that the $0\nu\beta\beta$ calculations can be greatly accelerated by the use of the Horie–Sasaki method [635], as done in, e.g., [561–563,636,637]. A further acceleration of the calculations can be achieved via recursive methods [637]. In [638] the proton–neutron pairing amplitudes and nuclear deformation were treated as generator coordinates to allow larger single-particle spaces than the ISM.

In Tables 16–18 we quote the available calculations of the NMEs for ground-state-to-ground-state DBD transitions in a comprehensive set of isobaric systems. In these calculations the light-Majorana-neutrino exchange was considered for the $0\nu\beta\beta$ mode of decay. The articles considering also the heavy-Majorana-neutrino exchange in the $0\nu\beta\beta$ decay are marked with an asterisk (*). In addition to the two $0\nu\beta\beta$-decay modes considered in Tables 16–18, also the NMEs for R-parity violating SUSY (supersymmetric) modes in the $0\nu\beta\beta$ decay have been calculated, e.g., in [639,640]. Furthermore, Majoron emission [595,641] and contributions of sterile neutrinos have been discussed as well [595,642].

In Tables 19–21 we compile the available calculations of the NMEs for ground-state-to-excited-state DBD transitions in a comprehensive set of isobaric systems and nuclear final states J_k^{π}, where π denotes the parity and k denotes the kth excited state of this particular multipolarity. The (nuclear) excitation energy of this state is denoted by E_{exc}. In these calculations the light-Majorana-neutrino exchange was considered for the $0\nu\beta\beta$ decay mode. Hereafter references cited in the tables are in chronological order.

The DBD NMEs of Tables 16–20 have been calculated in a number of different theory frameworks. These theories include the following:

Shell-model-like theories:

- The ISM, used in [179,198,199,235,543,544,569,578,590,624–626,643].
- Deformed shell model (DSM) based on Hartree–Fock states [644].
- Deformed pseudo-SU(3) model, advocated in [645,646].

Mean-field models:

- PHFB (projected Hartree–Fock–Bogoliubov) model for deformed nuclei [595–598,602,603,605,641,647,648].

Models based on fermions-to-bosons mapping:

- The microscopic interacting boson model (IBM-2) [244,591,620,649,650] and the microscopic interacting boson–fermion–fermion model (IBFFM-2) [545].

Table 16

References for available DBD calculations, performed since the previous comprehensive review [2], for different ground-state-to-ground-state DBD transitions. The 0ν-DBD results refer to the light- and/or heavy-Majorana-neutrino-mediated $0\nu\beta\beta$ decays. The references which consider also the heavy-Majorana-neutrino exchange are marked with an asterisk ($*$).

Transition	Decay mode	2ν-DBD references	0ν-DBD references
${}^{48}_{20}\text{Ca}_{28} \rightarrow {}^{48}_{22}\text{Ti}_{26}$	$\beta^-\beta^-$	[205,230,543,601,608], [615,643]	[199,230,246,565,581,590], [615,617], [620]*,[627], [649]*, [651,652]
${}^{58}_{28}\text{Ni}_{30} \rightarrow {}^{58}_{26}\text{Fe}_{32}$	β^+EC, ECEC	[620]	[620]*,[650]
${}^{64}_{30}\text{Zn}_{34} \rightarrow {}^{64}_{28}\text{Ni}_{36}$	β^+EC, ECEC	[620]	[620]*,[644,650]
${}^{70}_{30}\text{Zn}_{40} \rightarrow {}^{70}_{32}\text{Ge}_{38}$	$\beta^-\beta^-$	[237,612,653,654]	[654]
${}^{74}_{34}\text{Se}_{40} \rightarrow {}^{74}_{32}\text{Ge}_{42}$	β^+EC, ECEC		[644]
${}^{76}_{32}\text{Ge}_{44} \rightarrow {}^{76}_{34}\text{Se}_{42}$	$\beta^-\beta^-$	[205,601,607,612,653], [655,656]	[177,180,199,246], [247]*,[543], [565], [575]*,[576,581,590,591], [592,594], [616]*, [617,619], [620]*, [624], [626]*, [627,657–659], [660–662], [649]*,[651,663], [652]
${}^{78}_{36}\text{Kr}_{42} \rightarrow {}^{78}_{34}\text{Se}_{44}$	$\beta^+\beta^+$, β^+EC, ECEC	[620,664]	[620]*,[644,650,664]
${}^{80}_{34}\text{Se}_{46} \rightarrow {}^{80}_{36}\text{Kr}_{44}$	$\beta^-\beta^-$	[237,612,653]	
${}^{82}_{34}\text{Se}_{48} \rightarrow {}^{82}_{36}\text{Kr}_{46}$	$\beta^-\beta^-$	[205,601,607,612,653], [655]	[180,199,246], [247]*, [543,565], [575]*,[576,590,591], [594], [616]*, [617,619], [620]*, [625]*,[627,657], [658–661], [649]*, [651], [652]
${}^{84}_{38}\text{Sr}_{46} \rightarrow {}^{84}_{36}\text{Kr}_{48}$	β^+EC, ECEC		[644]
${}^{86}_{36}\text{Kr}_{50} \rightarrow {}^{86}_{38}\text{Sr}_{48}$	$\beta^-\beta^-$	[612,653,654]	[654]
${}^{92}_{42}\text{Mo}_{50} \rightarrow {}^{92}_{40}\text{Zr}_{52}$	β^+EC, ECEC		[665]
${}^{94}_{40}\text{Zr}_{54} \rightarrow {}^{94}_{42}\text{Mo}_{52}$	$\beta^-\beta^-$	[602,612,653,654]	[595,598,654]
${}^{96}_{40}\text{Zr}_{56} \rightarrow {}^{96}_{42}\text{Mo}_{54}$	$\beta^-\beta^-$	[205,601,602,608,612], [653]	[246], [247]*,[575]*, [577,594,595], [598,617,619], [620]*, [627,657], [659,666], [649]*, [651,652]
${}^{96}_{44}\text{Ru}_{52} \rightarrow {}^{96}_{42}\text{Mo}_{54}$	$\beta^+\beta^+$, β^+EC, ECEC	[620,667]	[596,597], [620]*, [650,665,667]
${}^{98}_{42}\text{Mo}_{56} \rightarrow {}^{98}_{44}\text{Ru}_{54}$	$\beta^-\beta^-$	[602,653]	[595,598]

Table 17

Continuation of Table 16: References for available DBD calculations, performed since the previous comprehensive review [2], for different ground-state-to-ground-state DBD transitions. The 0ν-DBD results refer to the light- and/or heavy-Majorana-neutrino-mediated $0\nu\beta\beta$ decays. The references which consider also the heavy-Majorana-neutrino exchange are marked with an asterisk ($*$).

Transition	Decay mode	2ν-DBD references	0ν-DBD references
${}^{100}_{42}\text{Mo}_{58} \rightarrow {}^{100}_{44}\text{Ru}_{56}$	$\beta^-\beta^-$	[236,237,601,602,608], [612,653,668,669]	[246], [247]*, [565], [575]*, [577,591], [594,595,598,617,619], [620]*, [627,659–661,668], [649]*, [651,652]
${}^{102}_{46}\text{Pd}_{56} \rightarrow {}^{102}_{44}\text{Ru}_{58}$	β^+EC, ECEC	[236]	[596,597]
${}^{104}_{44}\text{Ru}_{60} \rightarrow {}^{104}_{46}\text{Pd}_{58}$	$\beta^-\beta^-$	[205,236,237,602,608], [612,654,670]	[595,598,654]
${}^{106}_{48}\text{Cd}_{58} \rightarrow {}^{106}_{46}\text{Pd}_{60}$	$\beta^+\beta^+$, β^+EC, ECEC	[236,620,647,671,672]	[596,597], [620]*, [665,672,673], [650]
${}^{108}_{48}\text{Cd}_{60} \rightarrow {}^{108}_{46}\text{Pd}_{62}$	ECEC	[236]	
${}^{110}_{46}\text{Pd}_{64} \rightarrow {}^{110}_{48}\text{Cd}_{62}$	$\beta^-\beta^-$	[205,236,237,602,608], [612,654,670]	[246], [247]*, [543,594,595,598], [620]*,[627,654]
${}^{112}_{50}\text{Sn}_{62} \rightarrow {}^{112}_{48}\text{Cd}_{64}$	β^+EC, ECEC	[236]	
${}^{114}_{48}\text{Cd}_{66} \rightarrow {}^{114}_{50}\text{Sn}_{64}$	$\beta^-\beta^-$	[236,237]	
${}^{116}_{48}\text{Cd}_{68} \rightarrow {}^{116}_{50}\text{Sn}_{66}$	$\beta^-\beta^-$	[236,237,601,608,655], [674]	[246], [247]*, [543], [575]*, [577,594], [617,619], [620]*, [627,657,666], [659–661], [649]*, [651,652]
${}^{120}_{52}\text{Te}_{68} \rightarrow {}^{120}_{50}\text{Sn}_{70}$	β^+EC, ECEC	[236]	
${}^{122}_{50}\text{Sn}_{72} \rightarrow {}^{122}_{52}\text{Te}_{70}$	$\beta^-\beta^-$	[236,237]	
${}^{124}_{50}\text{Sn}_{74} \rightarrow {}^{124}_{52}\text{Te}_{72}$	$\beta^-\beta^-$	[235,236,654]	[199], [235]*, [246], [247]*, [543,590], [594,617], [620]*, [627,654,657], [649]*,[651,652]
${}^{124}_{54}\text{Xe}_{70} \rightarrow {}^{124}_{52}\text{Te}_{72}$	$\beta^+\beta^+$, β^+EC, ECEC	[236,533,603,620]	[533,596,597], [620]*, [657,665], [650]
${}^{126}_{54}\text{Xe}_{72} \rightarrow {}^{126}_{52}\text{Te}_{74}$	ECEC	[236,603]	
${}^{128}_{52}\text{Te}_{76} \rightarrow {}^{128}_{54}\text{Xe}_{74}$	$\beta^-\beta^-$	[205,236,237,545,601], [603,608,612,655,670]	[180,199,246], [247]*, [543,565], [575]*,[577,590,591,594,595], [598,617,619], [620]*, [659], [649]*, [651]

Table 18

Continuation of Table 17: References for available DBD calculations, performed since the previous comprehensive review [2], for different ground-state-to-ground-state DBD transitions. The 0ν-DBD results refer to the light- and/or heavy-Majorana-neutrino-mediated $0\nu\beta\beta$ decays. The references which consider also the heavy-Majorana-neutrino exchange are marked with an asterisk (*).

Transition	Decay mode	2ν-DBD references	0ν-DBD references
$^{130}_{52}\text{Te}_{78} \rightarrow {}^{130}_{54}\text{Xe}_{76}$	$\beta^-\beta^-$	[205,236,545,601,603], [608,612,670]	[180,199,246], [247]*,[543,544], [565], [575]*, [577,590,591,594], [595,598], [616]*, [617,619], [620]*, [627,657,659], [649]*, [651,663], [652]
$^{130}_{56}\text{Ba}_{74} \rightarrow {}^{130}_{54}\text{Xe}_{76}$	$\beta^+\beta^+$, β^+EC, ECEC	[236,603,620]	[596,597], [620]*, [650,665],
$^{132}_{56}\text{Ba}_{76} \rightarrow {}^{132}_{54}\text{Xe}_{78}$	ECEC	[236,603]	
$^{134}_{54}\text{Xe}_{80} \rightarrow {}^{134}_{56}\text{Ba}_{78}$	$\beta^-\beta^-$	[236,608,612,670]	[246], [620]*
$^{136}_{54}\text{Xe}_{82} \rightarrow {}^{136}_{56}\text{Ba}_{80}$	$\beta^-\beta^-$	[198,236,601,608,612], [670]	[180,199,246], [247]*, [543,544], [575]*,[577,590,594], [616]*, [617], [619], [620]*, [627,657,659], [649]*, [651,652,663]
$^{136}_{58}\text{Ce}_{78} \rightarrow {}^{136}_{56}\text{Ba}_{80}$	$\beta^+\beta^+$, β^+EC, ECEC	[236,620]	[620]*,[650,657,665]
$^{142}_{58}\text{Ce}_{84} \rightarrow {}^{142}_{60}\text{Nd}_{82}$	$\beta^-\beta^-$	[612,670]	
$^{146}_{60}\text{Nd}_{86} \rightarrow {}^{146}_{62}\text{Sm}_{84}$	$\beta^-\beta^-$	[670]	
$^{148}_{60}\text{Nd}_{88} \rightarrow {}^{148}_{62}\text{Sm}_{86}$	$\beta^-\beta^-$	[205,607,612,670]	[620]*,[649]*
$^{150}_{60}\text{Nd}_{90} \rightarrow {}^{150}_{62}\text{Sm}_{88}$	$\beta^-\beta^-$	[205,601,603,607,611], [670,674]	[574], [575]*, [591,592,595,598], [614], [616]*, [617], [620]*, [649]*,[651], [652,663,675]
$^{152}_{64}\text{Gd}_{88} \rightarrow {}^{152}_{62}\text{Sm}_{90}$	R-ECEC		[676,677], [678]*
$^{154}_{62}\text{Sm}_{92} \rightarrow {}^{154}_{64}\text{Gd}_{90}$	$\beta^-\beta^-$	[205,607,612,645]	[591], [620]*, [645], [649]*
$^{156}_{66}\text{Dy}_{90} \rightarrow {}^{156}_{64}\text{Gd}_{92}$	β^+EC, ECEC	[620,648]	[596,597], [620]*,[678]*
$^{160}_{64}\text{Gd}_{96} \rightarrow {}^{160}_{66}\text{Dy}_{94}$	$\beta^-\beta^-$	[205,607,612,645,646]	[592], [620]*, [645,646], [649]*
$^{164}_{68}\text{Er}_{96} \rightarrow {}^{164}_{66}\text{Dy}_{98}$	R-ECEC		[676,677], [678]*
$^{170}_{68}\text{Er}_{102} \rightarrow {}^{170}_{70}\text{Yb}_{100}$	$\beta^-\beta^-$	[645]	[645]
$^{176}_{70}\text{Yb}_{106} \rightarrow {}^{176}_{72}\text{Hf}_{104}$	$\beta^-\beta^-$	[612,645]	[645]
$^{180}_{74}\text{W}_{106} \rightarrow {}^{180}_{72}\text{Hf}_{108}$	R-ECEC		[676,677], [678]*
$^{198}_{78}\text{Pt}_{120} \rightarrow {}^{198}_{80}\text{Hg}_{118}$	$\beta^-\beta^-$		[620]*, [649]*
$^{232}_{90}\text{Th}_{142} \rightarrow {}^{232}_{92}\text{U}_{140}$	$\beta^-\beta^-$	[607,645]	[620]*,[645]
$^{238}_{92}\text{U}_{146} \rightarrow {}^{238}_{94}\text{Pu}_{144}$	$\beta^-\beta^-$	[607]	[620]*
$^{244}_{94}\text{Pu}_{150} \rightarrow {}^{244}_{96}\text{Cm}_{148}$	$\beta^-\beta^-$	[645]	[645]

Models based on energy-density functionals:

- A state-of-the-art Gogny-type energy density functional [549,617,651,676] with beyond-mean-field effects incorporated using the generating coordinate method (GCM) with particle-number and angular-momentum projection. Also shape mixing is included.
- Beyond-mean-field covariant density functional theory (BMF-CDFT), where correlations beyond the mean field are introduced by configuration mixing of both angular-momentum and particle-number projected quadrupole-deformed mean-field wave functions [675]. Also shape fluctuations are taken into account [652].
- A relativistic energy-density functional with generator coordinates [574].

(Q)RPA type of models:

- Spherical QRPA and pnQRPA (see Section 3.1.1 for more information) with realistic Bonn one-boson-exchange-based effective G-matrix interactions, as used in [177,180,236,237,246,247,533,576,577,581,619,654,660,661,664–668,671,684,685].
- Spherical pnQRPA with effective G-matrix interactions and with particle-number projection [684,686].
- Spherical renormalized pnQRPA (pn-RQRPA) with effective G-matrix interactions [681]. This extension of the pnQRPA was developed in [201,202] and further discussed, e.g., in [653,670,687,688]. A similar method, the self-consistent QRPA (SCQRPA or SRQRPA), was discussed, e.g., in [670,689,690], and a second quasirandom phase approximation in [659,672,691]. A fully renormalized QRPA approach was advocated in [203–205]. Schematic bosonic models to be tested in the context of Fermi-type of schematic DBDs were also considered [692,693].
- A higher QRPA scheme in the proton–neutron channel, pnMAVA (proton–neutron microscopic anharmonic vibrator approach) [656,669].
- Deformed QRPA based on deformed Wood–Saxon or deformed Skyrme Hartree–Fock mean fields [557,601,674]. Deformed QRPA with a realistic Bonn-CD force [541,610,677].
- Proton–neutron QRPA in angular-momentum-projected basis for deformed nuclei (deformed pnQRPA, pn-dQRPA) with schematic particle–hole and particle–particle forces [607–609,611,612,679].
- Continuum QRPA as discussed in [694].
- Axially deformed Skyrme–QRPA with the SkM* energy-density functional [663]

Table 19

References for available DBD calculations, performed since the previous comprehensive review [2], for different ground-state-to-excited-state DBD transitions. J_k^π denotes the kth excited state of multipolarity J^π and E_{exc} is the excitation energy (in MeV) of the J_k^π state in the daughter nucleus.

Transition	J_k^π	E_{exc}	Decay mode	2ν-DBD references	0ν-DBD references
$^{48}_{20}Ca_{28} \rightarrow {}^{48}_{22}Ti_{26}$	2_1^+	0.9835	$\beta^-\beta^-$	[609,679]	
	0_1^+	2.997	$\beta^-\beta^-$		[199], [620]*
$^{74}_{34}Se_{40} \rightarrow {}^{74}_{32}Ge_{42}$	2_1^+	1.204	R-ECEC		[680]
$^{76}_{32}Ge_{44} \rightarrow {}^{76}_{34}Se_{42}$	2_1^+	0.5591	$\beta^-\beta^-$	[609,679,681]	[570]
	0_1^+	1.122	$\beta^-\beta^-$		[181,199], [593]*, [594], [620]*, [640]*, [658,662]
$^{78}_{36}Kr_{42} \rightarrow {}^{78}_{34}Se_{44}$	2_1^+	0.614	$\beta^+\beta^+, \beta^-EC, ECEC$	[664]	
	2_2^+	1.309	$\beta^+EC, ECEC$	[664]	
	0_1^+	1.499	$\beta^+EC, ECEC$	[620,664]	[620]*,[650,664]
$^{82}_{34}Se_{48} \rightarrow {}^{82}_{36}Kr_{46}$	2_1^+	0.7765	$\beta^-\beta^-$	[609,681]	
	0_1^+	1.488	$\beta^-\beta^-$		[181,199], [593]*, [594], [620]*, [640]*, [658]
$^{86}_{36}Kr_{50} \rightarrow {}^{86}_{38}Sr_{48}$	2_1^+	1.077	$\beta^-\beta^-$	[654]	
$^{94}_{40}Zr_{54} \rightarrow {}^{94}_{42}Mo_{52}$	2_1^+	0.8711	$\beta^-\beta^-$	[605,654]	
$^{96}_{40}Zr_{56} \rightarrow {}^{96}_{42}Mo_{54}$	2_1^+	0.7782	$\beta^-\beta^-$	[605,609,679,681]	
	0_1^+	1.148	$\beta^-\beta^-$		[593]*, [594], [620]*, [666]
	0_2^+	1.330	$\beta^-\beta^-$		[593]*, [666]
$^{96}_{44}Ru_{52} \rightarrow {}^{96}_{42}Mo_{54}$	2_1^+	0.778	$\beta^+EC, ECEC$	[667]	
	0_1^+	1.148	$\beta^+EC, ECEC$	[620,667]	[620]*,[650,665,667]
	0_2^+	1.330	$\beta^+EC, ECEC$	[667]	[665,667]
	2_2^+	1.498	$\beta^+EC, ECEC$	[667]	
	2_3^+	1.626	$\beta^+EC, ECEC$	[667]	
	(0^+)	2.718	R-ECEC		[667]
$^{100}_{42}Mo_{58} \rightarrow {}^{100}_{44}Ru_{56}$	2_1^+	0.5396	$\beta^-\beta^-$	[236,605,609,681], [668,679]	[570]
	0_1^+	1.130	$\beta^-\beta^-$	[236,668,669]	[593]*,[594], [620]*, [640]*, [668]
	2_2^+	1.362	$\beta^-\beta^-$	[236,668]	
	0_2^+	1.741	$\beta^-\beta^-$	[668]	[593]*,[668]

Table 20

Continuation of Table 19: References for available DBD calculations, performed since the previous comprehensive review [2], for different ground-state-to-excited-state DBD transitions. J_k^π denotes the kth excited state of multipolarity J^π and E_{exc} is the excitation energy (in MeV) of the J_k^π state in the daughter nucleus.

Transition	J_k^π	E_{exc}	Decay mode	2ν-DBD references	0ν-DBD references
$^{102}_{46}Pd_{56} \rightarrow {}^{102}_{44}Ru_{58}$	2_1^+	0.4751	ECEC	[236]	
	0_1^+	0.9436	ECEC	[236]	
$^{104}_{44}Ru_{60} \rightarrow {}^{104}_{46}Pd_{58}$	2_1^+	0.5558	$\beta^-\beta^-$	[236,605,609,679], [654]	
$^{106}_{48}Cd_{58} \rightarrow {}^{106}_{46}Pd_{60}$	2_1^+	0.5119	$\beta^+\beta^+, \beta^+EC, ECEC$	[236]	
	2_2^+	1.128	$\beta^+EC, ECEC$	[236]	
	0_1^+	1.134	$\beta^+EC, ECEC$	[236,620,671]	[620]*,[650,665,673]
	0^+	2.766	R-ECEC		[673]
$^{110}_{46}Pd_{64} \rightarrow {}^{110}_{48}Cd_{62}$	2_1^+	0.6577	$\beta^-\beta^-$	[236,605,609,679], [654]	
	0_1^+	1.473	$\beta^-\beta^-$	[236,654]	[593]*,[594,654]
	2_2^+	1.476	$\beta^-\beta^-$	[236,654]	
$^{112}_{50}Sn_{62} \rightarrow {}^{112}_{48}Cd_{64}$	2_1^+	0.6174	$\beta^+EC, ECEC$	[236]	
	0_1^+	1.224	ECEC	[236]	
	2_2^+	1.312	ECEC	[236]	
	0^+	1.871	R-ECEC		[682]
$^{116}_{48}Cd_{68} \rightarrow {}^{116}_{50}Sn_{66}$	2_1^+	1.294	$\beta^-\beta^-$	[236,609,679,681]	
	0_1^+	1.757	$\beta^-\beta^-$	[236]	[593]*,[594], [620]*,[666]
	0_2^+	2.027	$\beta^-\beta^-$		[593]*, [666]
	2_2^+	2.112	$\beta^-\beta^-$	[236]	
$^{120}_{52}Te_{68} \rightarrow {}^{120}_{50}Sn_{70}$	2_1^+	1.172	ECEC	[236]	
$^{124}_{50}Sn_{74} \rightarrow {}^{124}_{52}Te_{72}$	2_1^+	0.6027	$\beta^-\beta^-$	[235,236,654]	
	2_2^+	1.326	$\beta^-\beta^-$	[236,654]	
	0_1^+	1.657	$\beta^-\beta^-$	[235,236,654]	[199], [235]*, [593]*, [594], [620]*, [654,665]
$^{124}_{54}Xe_{70} \rightarrow {}^{124}_{52}Te_{72}$	2_1^+	0.6027	$\beta^+\beta^+, \beta^+EC, ECEC$	[236,533]	
	0_1^+	1.156	$\beta^+EC, ECEC$	[236,620]	[620]*,[650,665]
	2_2^+	1.325	$\beta^+EC, ECEC$	[236,533]	
	0_2^+	1.657	$\beta^+EC, ECEC$	[533]	[533]
	0_5^+	2.855	R-ECEC		[533], [678]*

Table 21

Continuation of Table 20: References for available DBD calculations, performed since the previous comprehensive review [2], for different ground-state-to-excited-state DBD transitions. J_k^π denotes the kth excited state of multipolarity J^π and E_{exc} is the excitation energy (in MeV) of the J_k^π state in the daughter nucleus.

Transition	J_k^π	E_{exc}	Decay mode	2ν-DBD references	0ν-DBD references
$^{126}_{54}\text{Xe}_{72} \rightarrow\, ^{126}_{52}\text{Te}_{74}$	2^+_1	0.6663	ECEC	[236]	
$^{128}_{52}\text{Te}_{76} \rightarrow\, ^{128}_{54}\text{Xe}_{74}$	2^+_1	0.4429	$\beta^-\beta^-$	[236,605,609,679]	
$^{130}_{52}\text{Te}_{78} \rightarrow\, ^{130}_{54}\text{Xe}_{76}$	2^+_1	0.5361	$\beta^-\beta^-$	[236,605,679]	
	2^+_2	1.122	$\beta^-\beta^-$	[236]	
	0^+_1	1.794	$\beta^-\beta^-$	[236]	[199], [593]*, [594], [620]*, [665]
$^{130}_{56}\text{Ba}_{74} \rightarrow\, ^{130}_{54}\text{Xe}_{76}$	2^+_1	0.5361	β^+EC, ECEC	[236,609]	
	2^+_2	1.122	β^+EC, ECEC	[236]	
	0^+_1	1.794	ECEC	[236,620]	[620]*,[650]
$^{132}_{56}\text{Ba}_{76} \rightarrow\, ^{132}_{54}\text{Xe}_{78}$	2^+_1	0.6677	ECEC	[236]	
$^{134}_{54}\text{Xe}_{80} \rightarrow\, ^{134}_{56}\text{Ba}_{78}$	2^+_1	0.6047	$\beta^-\beta^-$	[236,609,679]	
$^{136}_{54}\text{Xe}_{82} \rightarrow\, ^{136}_{56}\text{Ba}_{80}$	2^+_1	0.8185	$\beta^-\beta^-$	[236,609,679]	
	2^+_2	1.551	$\beta^-\beta^-$	[236]	
	0^+_1	1.579	$\beta^-\beta^-$	[236]	[181,199], [593]*, [594], [620]*, [640]*, [665]
$^{136}_{58}\text{Ce}_{78} \rightarrow\, ^{136}_{56}\text{Ba}_{80}$	2^+_1	0.8185	β^+EC, ECEC	[236]	
	2^+_2	1.551	ECEC	[236]	
	0^+_1	1.179	ECEC	[236,620]	[620]*,[650]
	0^+	2.315	R-ECEC		[683]
$^{148}_{60}\text{Nd}_{88} \rightarrow\, ^{148}_{62}\text{Sm}_{86}$	2^+_1	0.5502	$\beta^-\beta^-$	[609]	
	0^+_1	1.427	$\beta^-\beta^-$		[620]*
$^{150}_{60}\text{Nd}_{90} \rightarrow\, ^{150}_{62}\text{Sm}_{88}$	2^+_1	0.3309	$\beta^-\beta^-$	[605,609]	
	0^+_1	0.7404	β^+EC, ECEC		[574], [620]*, [675]
$^{154}_{62}\text{Sm}_{92} \rightarrow\, ^{154}_{64}\text{Gd}_{90}$	2^+_1	0.1231	$\beta^-\beta^-$	[609]	
	0^+_1	0.6807	$\beta^-\beta^-$		[620]*
$^{156}_{66}\text{Dy}_{90} \rightarrow\, ^{156}_{64}\text{Gd}_{92}$	0^+_1	1.049	ECEC	[620]	[620]*, [678]*
$^{160}_{64}\text{Gd}_{96} \rightarrow\, ^{160}_{66}\text{Dy}_{94}$	2^+_1	0.0868	$\beta^-\beta^-$	[609]	
	0^+_1	1.275	$\beta^-\beta^-$		[620]*
$^{232}_{90}\text{Th}_{142} \rightarrow\, ^{232}_{92}\text{U}_{140}$	2^+_1	0.0476	$\beta^-\beta^-$	[609]	
	0^+_1	0.6913	$\beta^-\beta^-$		[620]*
$^{238}_{92}\text{U}_{146} \rightarrow\, ^{238}_{94}\text{Pu}_{144}$	2^+_1	0.0441	$\beta^-\beta^-$	[609]	
	0^+_1	0.9415	$\beta^-\beta^-$		[620]*

- An RPA-based hybrid model able to describe the interaction between neutrons in a superfluid phase and protons in a normal phase, with special application to the ^{128,130}Te isotopes [546].

The ISM, pnQRPA, QRPA, IBM-2 theory frameworks have been briefly discussed in Section 3.1.1. The pnQRPA and QRPA model frameworks have been extensively discussed in the monograph [55].

5.5. Overview of the DBD experiments

Neutrinoless DBD NMEs $M^{0\nu}$ are not known experimentally since the neutrinoless DBD rates and the neutrino mass are not yet measured. On the other hand, the two-neutrino DBD rates are measured experimentally for DBD nuclei of current interest, and thus their NMEs, $M^{2\nu}$, are known experimentally, as given in the review articles [4,16–18,23], and are summarized in [258]. Actually, the two-neutrino DBD and the neutrinoless DBD do not have the same transition operators and mechanisms, but their NMEs reflect some common nuclear features. Thus the observed two-neutrino NMEs are used to help evaluate the neutrinoless DBD NMEs.

5.5.1. Experimental NMEs for two-neutrino DBDs and FSQP

In this section, we discuss briefly experimental two-neutrino DBD NMEs and the FSQP (Fermi Surface Quasi Particle) NMEs based on experimental single-β NMEs [16,558–560]. Here the experimental and FSQP NMEs include the renormalization coefficient (g_A^{eff}/g_A) and all other nuclear effects. Features of theoretical two-neutrino NMEs are discussed in Section 5.2 and the calculated values are surveyed in Section 5.4.

The two-neutrino DBD NMEs are shown in Table 22. The $2\nu\beta^-\beta^-$ half-lives of nuclides with a Q value of at least 2 MeV, except for ^{110}Pd and ^{124}Sn, are known experimentally. The 2νECEC, $2\nu\beta^+$EC and $2\nu\beta^+\beta^+$ DBDs are not well studied because of the small involved phase space. Here we discuss the DBDs of ^{78}Kr, ^{106}Cd and ^{130}Ba, as shown in Table 22. The NME for $A(Z, N) \leftrightarrow C(Z + 2, N - 2)$ is expressed as

$$M^{2\nu} = \sum_i \frac{M_i^- M_i^+}{\Delta_i}, \tag{157}$$

Table 22

Two-neutrino NMEs for the $0^+ \rightarrow 0^+$ transitions to the 0^+ ground state and the first excited 0^+ state (*) [560]. $M^{2\nu}$(exp) denotes the experimental NME taken from a: Ref. [695], b: Ref. [696] and others: [258]. Furthermore, a': Ref. [697], b': Ref. [698], c': Ref. [699]. $M^{2\nu}$(FSQP) denotes the FSQP NME with c: Ref. [559], d: the present value in Ref. [560], and others in Ref. [558]. All NMEs are in units of $1/m_e$.

Transition	$M^{2\nu}$(exp)	$M^{2\nu}$(FSQP)
^{76}Ge $\rightarrow$ ^{76}Se	0.063^a	0.052^d
^{82}Se $\rightarrow$ ^{82}Kr	0.050	0.064^d
^{96}Zr $\rightarrow$ ^{96}Mo	0.049	0.045
^{100}Mo $\rightarrow$ ^{100}Ru	0.126	0.096
^{100}Mo $\rightarrow$ ^{100}Ru*	0.102	0.090
^{110}Pd $\rightarrow$ ^{110}Cd	$-$	0.145^d
^{116}Cd $\rightarrow$ ^{116}Sn	0.070	0.055
^{128}Te $\rightarrow$ ^{128}Xe	0.025	0.019
^{130}Te $\rightarrow$ ^{130}Xe	0.018	0.017
^{136}Xe $\rightarrow$ ^{136}Ba	0.010^b	0.012^c
^{78}Kr $\rightarrow$ ^{78}Se	$\leq 0.34^{a'}$	0.065^d
^{106}Cd $\rightarrow$ ^{106}Pd	$\leq 0.45^{b'}$	0.11^d
^{130}Ba $\rightarrow$ ^{130}Xe	$0.105^{c'}$	0.067^d

where M_i^- and M_i^+ are GT NMEs for the β^- A$(Z, N) \leftrightarrow$ B$(Z + 1, N - 1)$ and β^+ C$(Z + 2, N - 2) \leftrightarrow$ B$(Z + 1, N - 1)$ transitions via the ith 1^+ state in the intermediate nucleus B$(Z + 1, N - 1)$, and Δ_i is the associated energy denominator [16,18].

The $M^{2\nu}$ reflects directly the single-β NMEs M_i^- and M_i^+. As is well known [1,4], the single-β NME is much smaller than the simple quasiparticle (QP) NME due to nucleonic and non-nucleonic correlations and nuclear-medium effects. Accordingly, the two-neutrino DBD NMEs are also much smaller than the QP NMEs. The FSQP model is based on the experimental single-β NMEs [16,18,558,559]. In the model the $2\nu\beta\beta$ NME is expressed as a sum of the NMEs via the intermediate FSQP states. The QP configurations involved in the transition of A$(0^+) \leftrightarrow$ B$(1^+) \leftrightarrow$ C(0^+) are $(j_ij_i)_0 \leftrightarrow (j_ij_k)_1 \leftrightarrow (j_kj_k)_0$, where j_i and j_k are the spins of the ith neutron and kth proton.

The FSQP GT NMEs $M_i^\pm$ are simply expressed as [16,558,559],

$$M_i^\pm = k^\pm M_i^\pm(\text{QP}), \quad M_i^\pm(\text{QP}) = P_i^\pm M(J_ij_i), \tag{158}$$

where $M_i^\pm$(QP) is the quasiparticle (QP) NME, $k^\pm$ is the effective axial coupling constant in units of the unquenched axial coupling $g_A = 1.27g_V$ for the free nucleon [1,4] and $P_i^\pm$ is the pairing correlation coefficient for the $\beta^\pm$ transition, and $M(J_ij_i)$ is the single particle (SP) $J_i \leftrightarrow j_i$ GT NME. Since the same SP NME of $M(J_ij_i)$ is involved in both the M_i^- and M_i^+ NME, the product is positive and the sum in Eq. (157) is constructive. Here the $k^\pm$ coefficient takes into account the spin–isospin correlations and nuclear-medium effects as discussed in [1,4,18], and also recently on the context of the single β GT and SD NMEs in [104,105].

The GT NMEs for the FSQP states in the low-excitation region are based on the experimental GT responses (B(GT)) from CERs and/or the single $\beta^\pm$ decays. The FSQP NMEs are given in the 4th column of Table 22. The theoretical NMEs are discussed in Section 5.5.1. The experimental and FSQP NMEs for two-neutrino DBDs are discussed in the recent work [560].

The FSQP $M^{2\nu}$ NMEs have the following features:

(i) The single $\beta^\pm$ NMEs, including the effective weak coupling $k^\pm$ for the low-lying FSQP states, are given experimentally by CERs and β/EC rates. Contributions to the $M^{2\nu}$ from the GTR are evaluated to be much smaller than those from the low-lying QP states [106].

(ii) The FSQP NME $M_i^\pm$ is smaller than the SP NME by the pairing coefficient $P^\pm = 0.45 - 0.25$ and the effective coupling coefficient acquires values in the range $k^\pm = 0.3 - 0.2$ [4,16,18]. Thus NME $M^{2\nu}$ becomes smaller by the coefficient $k^-P^-k^+P^+ = 0.005 - 0.01$ with respect to the single-particle (SP) value.

(iii) The NME $M^{2\nu}$ depends on the shell structure as the pairing coefficient $P_i^\pm$ does [560]. The product $P_i^-P_i^+$ of the pairing factors is stable in the middle of the shell, but gets small near the shell closure because the vacancy amplitude U and the occupation amplitude V get small just before and after the shell closure, respectively.

In fact, it has long been believed that the actual $M^{2\nu}$ is much smaller than the QP $M^{2\nu}$ because the amplitudes involved in $M^{2\nu}$ cancel at the appropriate value of the particle–particle strength g_{pp} of the pnQRPA (see Section 3.1.1), while the NME $M^{0\nu}$ is not small because it is not sensitive to g_{pp}, and because it includes several multipole NMEs and thus is nearly the same for all nuclei.

The FSQP NMEs show that the NME $M^{2\nu}$ is much smaller than the QP NME $M_{QP}^{2\nu}$ by the reduction coefficient $(k^\pm)^2 = 0.05 - 0.1$ because the observed single-$\beta^\pm$ GT(1^+) NME $M^\pm$ is smaller than the single-QP NME $M_{QP}^\pm$(GT) by the coefficient $k^\pm = k^{\text{eff}} = 0.2 - 0.3$. The single-$\beta^\pm$ SD(2^-) NME $M^\pm$, which is one of the major components of $M^{0\nu}$, is smaller than the single-quasiparticle NME $M_{QP}^\pm$(SD) by a coefficient $k^\pm = 0.2 - 0.3$ [105], as in the case of the GT NME [104]. Accordingly, the axial–vector component of $M^{0\nu}$ may be much smaller than the QP NME $M_{QP}^{0\nu}$ by the coefficient $(k^{\text{eff}})^2 = 0.05 - 0.1$. Actually,
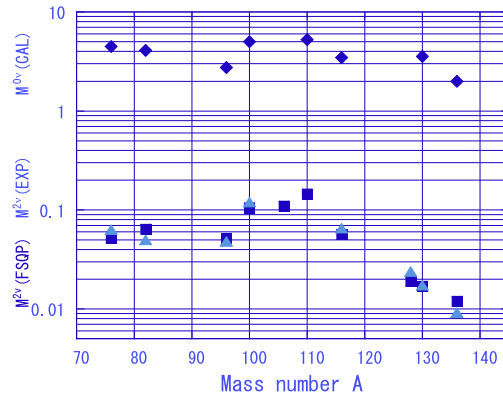
Fig. 67. Top: Average values (diamonds) for the QRPA NMEs $M^{0\nu}$ [23,627]. Bottom: The FSQP NMEs $M^{2\nu}$(FSQP) (squares) and the experimental NMEs $M^{2\nu}$(EXP) (triangles) in units of $1/m_e$ [560].

the values of $g_A^{eff}/g_A^{free} = 0.5 - 0.7$ are used in recent theoretical calculations such as in the ISM [229,233], pnQRPA [243,245] and IBM2 [244]. The theoretical NMEs are discussed in the previous subsections.

The $0\nu\beta^-\beta^-$ NMEs for the ground-state transitions have been calculated on various nuclei. The averaged value of the QRPA NMEs [23,627] for each DBD isotope of current interest is plotted against the mass number A in the top of Fig. 67. The experimental and FSQP values of $M^{2\nu}$ for the ground-state transitions are shown also for comparison in Fig. 67. Both the $M^{0\nu}$ and $M^{2\nu}$ values show similar dependence on the mass number, and are small at the shell closure of $A = 136$ (N=82). The shell closure at $N = 82$ blocks the $p \to n$ transition in both the $0\nu\beta\beta$ and $2\nu\beta\beta$ NMEs, resulting in a similar shell dependence for both the $M^{0\nu}$ and $M^{2\nu}$ NMEs. Interesting is to extend the $M^{2\nu}$ FSQP to the $0\nu\beta\beta$ NME $M^{0\nu}$. Higher-multipole single-β NMEs $M_i^{\pm}$ corresponding to transitions between low- and medium-energy QP states are involved in $M^{0\nu}$. Thus, experimental NMEs for them are useful for evaluation of the $M^{0\nu}$ NMEs.

5.5.2. Neutrinoless double-beta-decay experiments

In this section we briefly present the current status of the neutrinoless double-beta-decay experiments. The measured quantity is the half-life (or a limit on it) which can be linked with the effective Majorana-neutrino mass, m^{eff}, in case of the light ν-mass process, as discussed in Sections 1.4 and 5.1, and also in Refs. [4,16,23,520,521].

To observe this process, single β decay has to be forbidden by energy conservation or at least strongly suppressed due to a large change of the involved nuclear spins. For this reason only 35 potential double β^- emitters exist. The same number of source nuclides exists for the analogue process on the right side of the isobaric parabola in the form of double electron capture (ECEC) or decay modes with positron emission (see Section 5.1). Below a Q value of $2m_ec^2$ only the ECEC process is possible, between $2m_ec^2 - 4m_ec^2$ the ECEC and β^+/EC can occur and above $4m_ec^2$ the $\beta^+\beta^+$ decay channel opens (see an example in Fig. 62).

The phase space for $0\nu\beta\beta$ decay scales strongly with the Q value (in case of $0\nu\beta\beta$ with Q^5 and in case of $2\nu\beta\beta$ with Q^{11}). Thus experimental searches are typically using only nuclides with a Q value above 2 MeV, which reduces the list of suitable candidates to 11. They are listed in Table 23. From the experimental point of view an estimate of the half-life sensitivity depends on the fact whether the experiment is background-free or background-limited. In both cases the isotopic abundance and detection efficiency enter linearly. In the background-free case also the measurement time shows this linear behavior, while in a background-limited experiment it enters as a square-root. The square-root dependence is also valid for background level and energy resolution. The neutrinoless decay signal is the emission of two electrons with a total energy being identical to the decay Q value.

Various technologies are used and explored, the most common one is the "source = detector" approach. Given the fact that it is known by now that a potential half-life is beyond about 10^{26} years, this implies that a large amount of material, ideally isotopically enriched in the nuclide of interest, is needed and the disturbing background has to be reduced to lowest possible levels.

One experimental approach for the search is using semiconductors. This is realized for ^{76}Ge in germanium diodes produced with isotopically enriched material (GERDA [700], MAJORANA Demonstrator [701] and in the future LEGEND [702]) and CdZnTe for ^{116}Cd as used in COBRA [703].

Another detector technique is the usage of cryobolometers. The largest experiment of this type is CUORE [704], focusing on ^{130}Te using TeO$_2$ crystals. Several other cryobolometer approaches are studied worldwide, for example there is LUCIFER/ CUPID-0 using ZnSe (^{82}Se) [705], and AMoRE with CaMoO$_4$ (^{100}Mo) [706], where still a lot of additional R&D is done. For recent reviews on this topic see [18,23,707].

A further technology is based on scintillators, liquid and solid ones. KamLAND-Zen is loading a balloon filled with enriched xenon (^{136}Xe) [708]. The decay of ^{136}Xe is investigated in further experimental approaches: EXO-200 [709] and nEXO (Xenon-TPC with potential barium tagging [710]), general liquid Xenon detectors. The SNO+ experiment is using Te-loaded liquid

Table 23
Table of double β emitters with a Q value of at least 2 MeV, and the current lower limits on the half-life $T_{1/2}^{0\nu}$ for the transitions to the ground state and first excited 2^+ state. If more than one measurement is published, the best limit has been chosen. Shown are the isotope, its natural abundance (N.a.), the Q value, and the half-life limits.

Nuclide	N.a. (%)	Q value (keV)	$T_{1/2}(0_{gs}^+)$ (yrs)	$T_{1/2}(2_1^+)$ (yrs)
^{48}Ca	0.187	4262.96 ± 0.84	5.8×10^{22}	1.0×10^{21}
^{76}Ge	7.44	2039 ± 0.050	8.0×10^{25}	8.2×10^{23}
^{82}Se	8.73	2997 ± 0.3	2.4×10^{24}	1.0×10^{22}
^{96}Zr	2.80	3356 ± 0.086	9.2×10^{21}	9.1×10^{20}
^{100}Mo	9.63	3034.40 ± 0.17	1.1×10^{24}	1.6×10^{23}
^{110}Pd	11.72	2017.85 ± 0.64	6.0×10^{17}	2.9×10^{20}
^{116}Cd	7.49	2813.50 ± 0.13	1.9×10^{23}	6.2×10^{22}
^{124}Sn	5.79	2292.64 ± 0.39	2.0×10^{19}	9.1×10^{20}
^{130}Te	33.8	2527.518 ± 0.013	1.5×10^{25}	1.4×10^{23}
^{136}Xe	8.9	2457.83 ± 0.37	1.07×10^{26}	2.6×10^{25}
^{150}Nd	5.64	3371.38 ± 0.20	2.0×10^{22}	2.4×10^{21}

scintillators for the search (^{130}Te) [711] and solid scintillators are used in CANDLES with CaF$_2$ (^{48}Ca) [712] and by AURORA using CdWO$_4$ (^{116}Cd) [713].

Tracking devices have also been used in the various stages of the NEMO experiment (up to NEMO-3) and is planned for an upgrade to SUPERNEMO [714]. MOON, which is an extension of ELEGANT V, aims at a ton-scale DBD experiment with ^{100}Mo by using super-modules of multi-layer scintillators and tracking chambers [158,715]. NEXT plans to use a high-pressure Xe-gas TPC to study ^{136}Xe [716] as also PandaX-III for ^{136}Xe DBD [717].

A compilation of current half-life limits for the ground-state and the 2_1^+ transition is given in Table 23. The Q values are ^{48}Ca [718], ^{76}Ge [719], ^{82}Se [720], ^{96}Zr [59], ^{100}Mo [721], ^{110}Pd [722], ^{116}Cd [723], ^{124}Sn [724], ^{130}Te [723–725], ^{136}Xe [726], ^{150}Nd [727]. All relevant isotopes have a Q-value uncertainty of less than 1 keV. The half-life limits are taken from [700] for ^{76}Ge, from [728] for ^{82}Se, from [714] for ^{96}Zr, ^{100}Mo,^{150}Nd, from [713] for ^{116}Cd, from [704] for ^{130}Te, from [708] for ^{136}Xe, and for others from reviews [16,18,23,729,730] and references therein. See Section 6.4 for ^{124}Sn.

Things look different on the proton-rich side of the mass parabola. Here 35 potential ECEC candidates exist as well. However, abundances are in general lower and thus half-life limits obtained are lower as well. There are 6 candidates for double positron emission, but these decays suffer from phase-space reduction. None of these decays have been measured in the laboratory.

The signal for ground-state transitions in 2νECEC results from the corresponding de-excitation X-rays when filling the K-shell or from the emission of conversion electrons. This requires measurements below 100 keV unless heavier elements are involved. The corresponding 0νECEC would violate momentum conservation. Hence typically an L-shell capture is required to guarantee angular-momentum conservation. As signal, three processes have been considered [525]: pair production or internal bremsstrahlung in the nuclear field, the latter leading to a mono-energetic gamma ray, and internal conversion. This has been mentioned in [525] but is not worked out in detail. Potential detection signatures might improve for the modes containing one or two positrons but the associated phase spaces are reduced. Phase spaces for the individual processes are $\propto Q^5$ for 2νECEC, $\propto Q^8$ for 2$\nu\beta^+$/EC and $\propto Q^{11}$ for 2$\nu\beta^+\beta^+$. For 0$\nu\beta^+\beta^+$ the phase space scales with Q^5 and Q^2 for the mixed mode, while for 0νECEC this question has not been worked out.

It has been suggested, e.g., in [529] that a transition from the ground state to an excited state of the daughter, which is degenerate with the initial state, could lead to a resonant enhancement, but the resonance should be narrow, about 100–200 eV. This is the resonant neutrinoless ECEC decay, R-ECEC, discussed in Section 5.1.1. Penning-trap measurements on all potential candidates have found a decay, namely the decay of ^{152}Gd which shows a large enhancement [731]. However, this nuclide decays by α-emission with a half-life of 10^{14} years, which is about 13 orders of magnitude shorter than the R-ECEC half-life of ^{152}Gd for a mass 1 eV neutrino.

Double positron decay is only possible for 6 isotopes. From those isotopes ^{106}Cd can be studied by AURORA and COBRA and ^{124}Xe, as was suggested in [732], by using large-scale low-background Xe detectors aiming to search for dark matter. This approach has a good chance for the first detection of the 2νECEC decay. Selected half-life limits on some radiative 0νECEC decays (R0νECEC in Section 5.1.1) are ^{36}Ar: 3.6×10^{21} yrs [733], ^{58}Ni: 2.1×10^{21} yrs [734], ^{106}Cd: 4.2×10^{20} yrs [735]. Those on some 2νECEC decays are ^{124}Xe: 2.1×10^{22} yrs [736], ^{126}Xe 1.9×10^{22} yrs [736,737].

The current limits on the 0$\nu\beta\beta$ half-lives for ^{76}Ge [700,701], ^{130}Te [704] and ^{136}Xe [708,709] give effective ν-mass limits of an order of 100 meV, depending largely on the NMEs including the effective g_A. The effective ν masses are around 15–45 meV and 2–5 meV in cases of the inverted-hierarchy and normal-hierarchy mass spectra. Future high-sensitivity experiments to search for the effective ν masses are discussed in Section 6.4.

6. Concluding remarks and discussions

6.1. Summary of neutrino–nuclear responses

The width of the topic of this review article is quite exceptional, as testified by the number of pages and references collected under the umbrella of the topic of neutrino–nuclear responses. Neutrino–nuclear responses, which are crucial for neutrino and weak-interaction studies in nuclei, as described in Section 1, touch many areas of particle astro and nuclear physics. In this review we scan through the latest results in the fields from the experimental and theoretical points of view. Experimental approaches such as single β decays and electron captures, charge-exchange nuclear reactions (CER), muon, photon and neutrino reactions, and others are briefly discussed in Section 2. High energy-resolution CERs provide axial–vector multipole responses in wide energy and momentum regions. Then we review single β decays (the quenching problem of the axial–vector coupling constant g_A and its relation with the β spectrum shapes, etc. in Section 3), (anti)neutrino scattering on nuclei at low energies $E \leq 70$–80 MeV (solar and supernova neutrinos in Section 4) and the nuclear $\beta\beta$ decays (electron and positron emitting modes in Section 5). We also highlight the elastic coherent neutrino scattering in the context of the xenon-based dark-matter detectors (the neutrino-floor problem, Section 4.6).

The quenching of g_A has attracted attention lately due to its strong influence on the rates of the $\beta\beta$ decays. In particular, this strong sensitivity of the half-life of the neutrinoless $\beta\beta$ decay to the value of g_A deserves keen attention. The effective value of g_A, g_A^{eff}, has been studied much for low-momentum-exchange processes like β decays and two-neutrino $\beta\beta$ decays. In the context of β decays the value of g_A^{eff} has been studied in two major ways: (i) by comparing the computed β-decay half-lives with the experimental ones or lately (ii) by comparing the computed β spectrum shapes with the measured ones. In β decays the value of g_A seems to be quenched, i.e. $g_A^{\mathrm{eff}} < 1.27$, where $g_A = 1.27$ corresponds to the unquenched value obtained from the neutron β decay. An exception is the case of first-forbidden $J^+ \leftrightarrow J^-$ transitions where g_A seems to be enhanced (see Section 3.6.4). The low-energy quenching phenomenon can be associated with several sources: (i) non-nucleonic degrees of freedom (like Δ resonances), (ii) nuclear-medium effects (like meson-exchange/two-body currents), (iii) giant resonances that gather strength from the low-energy region and (iv) deficiencies in the many-body quantum mechanics used to describe atomic nuclei. These aspects of the effective value of g_A have been addressed in Section 3, and experimental reductions (quenchings) in the medium momentum and energy regions are studied in Section 2.3.

In addition to the g_A problem, there are interesting new phenomena associated to the β decays. One of them is the reactor antineutrino anomaly which has been discussed in Section 3.6.2. In this anomaly the antineutrino flux from nuclear reactor, measured by large-scale neutrino-oscillation experiments, is lower at short flight-length than what one expects by considering three-neutrino oscillations for the β decays of the fission fragments produced in the reactor. This deficit has been associated with oscillations into sterile neutrinos although the determination of the actual antineutrino flux based on the fission yields is not on a solid ground. Inspection of the β spectrum shapes of a handful of key nuclei in the process could help in checking the possible errors in the flux estimates. Another interesting subject are the ultra-low-Q-value β decays discussed in Section 3.4.1. Such tiny-Q-value decays could be used for direct determination of the neutrino mass since the β endpoint is not so overwhelmed by the tail of the electron spectrum, although the signal rate in coincidence with the emitted γ rays would be much smaller than the huge background of β and brems-γ rays to the ground state. On the other hand, such tiny Q-value β decay can also give information of the atomic effects interfering the nuclear decays in the form of electron screening, overlap of atomic clouds, exchange-interaction contributions and final-state interactions. These contributions have been discussed in Section 3.4.2. Also the influence of the isovector spin-multipole giant resonances on the low-energy decays of nuclei and on $0\nu\beta\beta$ decay is of great interest to study the reduction of the axial–vector strengths (see Section 3.7).

(Anti)neutrino–nucleus neutral- and charged-current scattering plays a key role in detection of solar, supernova and other neutrinos from astrophysical and cosmological sources. In particular, the flavor conversion effects in the dense nuclear medium of an exploding supernova are highly interesting, as discussed in Section 4.4.3. The future huge Earth-bound neutrino telescopes could say something about the neutrino mass hierarchy based on the conversion effects.[9] Neutrinos also contribute to the background of future DBD experiments. Of present interest is also the so-called gallium anomaly where the response of ^{71}Ga to the ^{37}Ar and ^{51}Cr electron-capture neutrinos has caused some confusion since the measured neutrino-scattering cross sections are smaller than the calculated ones, calling for the oscillations to sterile neutrino(s) as explanation of the difference (see Section 4.4.4 for the anomaly and Section 2.3.2 for the CER result on the neutrino responses for ^{71}Ga). Of recent interest is also the astro-neutrino nucleosynthesis discussed in Section 4.7.

The various modes of double β decays have been discussed in Section 5.1. Of particular interest has been the neutrinoless double electron capture with possible resonance enhancement. However, the mass measurements indicate that the resonance condition is hard to meet and not good candidates have been found thus far. The basic features of the double β decays have been discussed in Sections 5.2 and 5.3. These features include, e.g., induced-current contributions, nucleon form factors, short-range correlations, deformation effects, restoration of the isospin symmetry, validity of the closure approximation and chiral two-body currents.

A specific feature of the present review are the surveys of calculations for the nuclear muon-capture rates (Section 2.4.2, Table 1), neutrino–nucleus cross sections (Section 4.4., Table 11) and nuclear matrix elements for the neutrinoless double β decay (Section 5.4, Tables 16–21). Brief overviews are given on the present status of DBD experiments (see Section 5.5).

---

[9] The mass hierarchy, as also the CP-violating phases, can also be accessed by the future large neutrino-oscillation experiments, like NOνA, T2K, DUNE and HyperK, see the recent conference article [738].

6.2. Perspectives on experimental studies of neutrino–nuclear responses

Experimental studies of neutrino–nuclear responses shed light on weak-interaction aspects of nuclear structure and provide useful information on weak NMEs associated with astro-neutrinos and DBDs, as discussed in previous sections. In this section, we briefly discuss perspectives on experimental studies on the nuclear responses for astro-neutrinos and DBD virtual neutrinos.

The neutrino–nuclear responses to be studied are those in wide energy and momentum regions of $E \leq 70$ MeV and $p \leq 150$ MeV/c. Actually, the astro-neutrinos are in the low- and medium-energy region of $E = 0$–70 MeV, and the momentum associated with the neutrinoless DBD virtual neutrino is of the order of $p = 20$–150 MeV/c. Accordingly, various kinds of nuclear, photon and lepton probes are used to study the neutrino–nuclear responses. Here the nuclear responses extracted from the experimental transition rates and cross sections are $|M(\alpha)|^2/(2J_i + 1)$, where J_i is the initial-state spin and $M(\alpha)$ is the α-mode NME, including the effective (renormalized/quenched) weak coupling.

Single β/EC rates give directly the neutrino responses for the ground and isomeric states. So far, allowed and unique first-forbidden transitions are mainly investigated to study the GT (Gamow–Teller) and IVSD (isovector spin-dipole) responses. Further studies for β-ray spectrum shapes of non-unique transitions and transition rates of higher-forbidden β decays give information on high-multipole neutrino–nuclear responses, as discussed in Sections 2 and 3.

Nuclear CERs with medium-energy light ions have extensively been used to study neutrino–nuclear responses in wide energy and momentum regions. Among them, the high energy-resolution (^{3}He,t) CERs at RCNP are used to study the τ^- ($n \rightarrow p$) Fermi (0^+), GT (1^+) and IVSD (2^-) responses in nuclei of astro-neutrino and DBD interests, as discussed in Section 2.3. The CER experiments provide the GT and IVSD strength distributions, the strengths being pushed up and concentrated in the highly-excited giant resonances and leaving little strength at the low-lying states. It is worthwhile to extend the nuclear CERs to other multipole excitations with $J^\pi = 1^-, 2^+, 3^\pm, 4^\pm$, which are relevant to medium-energy supernova neutrinos and neutrinoless DBDs. High energy-resolution ($d,^2$He) and other τ^+ ($p \rightarrow n$) reactions are effective to study the β^+ NMEs. The (^{7}Li,^{7}Be) and other CERs to excited states, in coincidence with decaying γ-rays, are used to separate individual excited states and to identify the spin and parity for them. The high energy-resolution spectrometer combined with a Ge-detector array are promising for detailed studies of the neutrino–nuclear responses.

Muons are unique massive leptons used to study weak responses in wide energy and momentum regions, as discussed in Section 2.4. Ordinary muon-capture prompt-γ spectroscopy provides τ^+ ($p \rightarrow n$) responses for low-lying bound states. On the other hand, the delayed-γ spectroscopy for γ rays from radioactive isotopes produced by the (μ, xn) reaction gives the muon-capture strength distribution and the muon-capture giant resonances in the wide excitation region of $E = 5-70$ MeV. The obtained relative strength, together with the absolute strength from the muon-capture lifetime, is useful in the studies of τ^+ ($p \rightarrow n$) neutrino–nuclear responses.

Photo-nuclear reaction through IAS (isobaric analog state) provides τ^- (n→p) vector (1^-) and axial–vector (1^+) responses, as discussed in Section 2.5. The spin and parity are derived by measuring 1 neutron emission from photo-nuclear reactions with polarized photons. It is of great interest to study the vector ($\mathbf{r}$) and axial–vector ($\boldsymbol{\sigma} \times \mathbf{r}$) NMEs by using the E1-$\gamma$ transition rate derived from the IAS - γ decay rate and the corresponding first-forbidden β transition rate.

Nuclear-response studies by using ν projectiles are interesting even though they require high-flux ν beams and large-volume detectors, as discussed in Section 2.6. The ν-beam experiments may provide directly the neutrino responses, including the renormalization of the weak coupling, being free from complex nuclear interactions, and thus may elucidate the renormalization of the axial–vector weak coupling.

DCER (double charge-exchange reaction) is a new way to explore DBD responses as discussed in Section 2.3. The DCER (^{11}B,^{11}Li) with the medium-energy ($E/A \approx 0.1$ GeV) light ions from the RCNP cyclotron studies axial–vector DBD responses. The cross sections for low-lying states, however, are extremely small. The observed spectrum suggests that DCER strengths are mainly in the double giant-resonance regions. Heavy-ion DCERs at RIKEN and RCNP aim to explore DGT strengths to provide experimental input on nuclear structure relevant to DBD NMEs. The NUMEN project at LNS Catania studies neutrinoless DBD NMEs by using heavy-ion DCERs. In fact, the DCER transition operators depend on the energy of the heavy-ion projectile and the momentum transfer, and are different from the DBD ones. So, important is to study the energy and the momentum-transfer dependencies of the DCERs to extract NMEs relevant to neutrinoless DBDs. It is, however, a challenge to win useful information on neutrinoless DBD NMEs from DCER experiments.

Experimental axial–vector NMEs for the GT and IVSD transitions, and those for two-neutrino DBDs are reduced with respect to the simple quasi-particle NMEs due to (i) nucleonic spin–isospin correlations and other nuclear effects and (ii) non-nucleonic (isobar) correlations and nuclear-medium (meson) effects, as discussed in Section 3. The former effects are included in nuclear models with adequate model spaces and nucleonic correlations/interactions. On the other hand, the latter ones are not explicitly included in the earlier nucleon-based nuclear models and thus are incorporated by using an effective axial–vector coupling g_A^{eff}. However, modern many-body calculations, like the quantum Monte Carlo approach of [739], are able to include the meson-exchange and delta-resonance effects at least effectively. The results for light nuclei suggest that maybe no quenching of g_A is necessary. For heavier nuclei these "ab initio" methods are not yet available and for the presently available nuclear many-body approaches the observed GT and SD NMEs suggest an appreciable reduction of $g_A^{\text{eff}}/g_A \approx 0.6 - 0.7$ with $g_A = 1.27g_V$ for the free nucleon. Here important is to define explicitly the effective coupling g_A^{eff} in the nucleus and then to discuss the value experimentally and theoretically on a common physics basis.

The Δ isobar is strongly excited by the spin–isospin interaction on nucleons (N) in a nucleus to form the axial–vector GR (giant resonance), as discussed in Section 3.5. This is the GR associated with the quark spin–isospin flip, while the GTR and IVSDR are the GRs associated with the nucleon spin–isospin flip. The Δ isobar GR interferes destructively with the low-lying state to reduce the axial–vector NMEs with respect to the nucleon-based nuclear-model evaluations. The renormalization (quenching of g_A) effects are studied experimentally by measuring CER strengths for unnatural-parity excitations in the wide excitation region of $E = 0$–100 MeV.

Nucleons are modified in the nuclear medium due to various kinds of nucleonic and non-nucleonic correlations and nuclear-medium effects. The meson cloud (dress) around a free nucleon is different from that around a bound valence-nucleon in the nuclear medium. The valence nucleon and the nuclear core change more or less before and after the CC and NC interactions. These many-body and nuclear-medium effects and non-nucleonic (mesons, isobars) contributions manifest as deviations of the calculated values from the experimental ones for CC responses and nucleon-transfer cross sections. The deviations depend on how accurately these effects are incorporated in the calculational frameworks, as discussed in Sections 2.3, 2.7 and 3.5, and they are usually accounted for by the use of renormalization (quenching) factors in the computations.

It is remarked that accurate experimental studies of the detector efficiencies for low-energy ν and $\bar{\nu}$ are indispensable to understand the ^{71}Ga-ν and the reactor-$\bar{\nu}$ anomalies, which otherwise might suggest possible oscillations into sterile neutrinos.

6.3. Perspectives of theoretical studies of neutrino–nuclear responses

The neutrino–nuclear responses have thus far been calculated by using a host of different theoretical frameworks and formalisms (see Sections 4.4 and 5.4). These are usually formalisms where a restricted single-particle space or configuration space has been used. This produces imperfections in the calculations which have to be compensated, e.g., by an effective value of g_A.

The recent trend is that the "ab initio" calculations of nuclear structure will be available for heavier and heavier nuclear systems sometime in the future. Such calculations can be based, e.g., on lattice quantum chromodynamics [740–743] or advanced Monte Carlo shell model frameworks [739,744–747], or the coupled-cluster theory derived from the chiral effective field theory [748,749]. Other possibilities are the in-medium similarity renormalization group method [750,751] and density-matrix renormalization-group algorithm [752]. These theoretical approaches allow a systematic calculation of nuclear wave functions taking part in the weak-interaction processes in nuclei. In addition, a systematic estimation of the calculational errors becomes possible. It is anticipated that these advanced nuclear many-body frameworks reduce the amount of the needed renormalization of g_A in the calculations of neutrino–nuclear and other weak responses in the processes of interest to neutrino physics, astroparticle physics, nuclear astrophysics, etc.

In addition to the improved nuclear many-body frameworks, the contributions coming from the meson-exchange currents (two-body currents) can be taken into account in the calculations. These currents can be derived from the chiral effective field theory (χEFT) on the same footing as the many-body forces used in the nuclear Hamiltonians [45–48,221]. These calculations are able to account for the nuclear-medium effects and, in principle, compute the amount of in-medium renormalization of g_A, thus reducing the uncertainty associated with the value of g_A in various nuclear processes triggered by weak interactions. Weak processes, like the neutrinoless $\beta\beta$ decay, can also be approached from the point of view of the χEFT and new possible mechanisms of the decay can be devised [51,52], as also a new leading contribution which was not considered in previous $0\nu\beta\beta$ calculations [753], see also [754]. The low-energy constants related to the nucleon–pion short-range operators were computed from the lattice QCD in [53] in order to aid, e.g., the χEFT calculations towards the NMEs of $0\nu\beta\beta$ decays.

The advanced nuclear-structure calculations are in a position to probe accurately enough the weak-interaction processes from the nuclear side. For example, the computed neutrino–nucleus scattering cross sections can help pin down, e.g., supernova mechanisms once a supernova will be observed at a suitably close distance from the Earth. Accurate nuclear-structure calculations, combined with more and more advanced experiments, can also help learn about the astro-neutrino nucleosynthesis, neutrino mass and its hierarchy, astrophysical processes and origins of elemental and isotopic abundances.

6.4. Remarks on neutrinoless DBD experiments and neutrino–nuclear responses

Neutrino–nuclear responses are crucial for DBD-neutrino studies to design high-sensitivity DBD detectors and to extract the Majorana neutrino mass and other neutrino properties from the DBD experiments. In this section, we briefly discuss the neutrino-mass sensitivity for neutrinoless DBD experiments and perspectives for future DBD experiments from the neutrino–nuclear response point of view.

The neutrinoless DBD rate per ton-year (t-y) for the light Majorana-mass mechanism with the effective mass of m^{eff} is expressed as [16,18,23]

$$(T^{0\nu})^{-1} = \left(\frac{m^{\text{eff}}}{m_0}\right)^2 ; \quad m_0 = \frac{7.8A^{1/2}}{M^{0\nu}g_A^2(G^{0\nu})^{1/2}} , \tag{159}$$
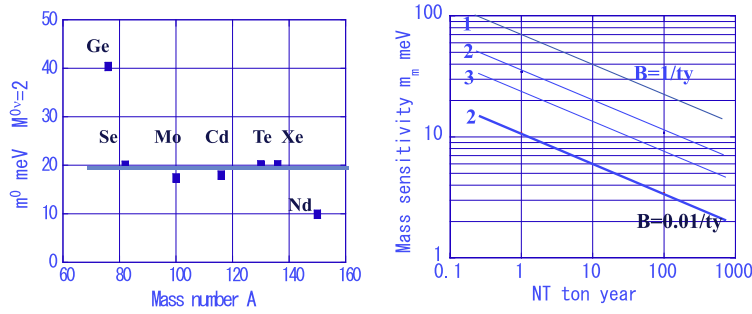
Fig. 68. Left side: Unit mass sensitivities m^0 (squares) in case of $M^{0\nu} = 2$ for ^{76}Ge, ^{82}Se, ^{100}Mo, ^{116}Cd, ^{130}Te, ^{136}Xe and ^{150}Nd, all with the enrichment of $r = 1$. Right side: Neutrino-mass sensitivities m_m for ^{130}Te with $\epsilon = 0.5$ as functions of the exposure NT in cases of the background rates of $B = 1/\text{t-y}$ (thin lines) and 0.01/(t-y) (thick line), respectively. The attached numbers 1, 2 and 3 stand for $M^{0\nu}$.

where m_0 is the nuclear sensitivity in units of meV, $g_A = 1.27$ is the axial–vector coupling in units of the vector coupling g_V for a free nucleon, $G^{0\nu}$ is the phase space in units of $10^{-14}\,\text{y}^{-1}$, A is the mass number, and $M^{0\nu}$ is the neutrinoless DBD NME. It is expressed as $M^{0\nu} = (g_A^{\text{eff}}/g_A)^2 M_M^{0\nu}$, with g_A^{eff} being the effective coupling to incorporate the renormalization (quenching) effect and $M_M^{0\nu}$ is the nuclear-model NME. Actually, $M^{0\nu}$ is sensitive to all kinds of nuclear and non-nuclear correlations, nuclear models and renormalization (quenching) coefficients of the weak couplings. Here the nuclear sensitivity m_0 is a characteristic of a given DBD nucleus. It corresponds to the ν mass required for the DBD rate of $(T^{0\nu})^{-1} = 1/\text{t-y}$.

The neutrino-mass sensitivity of a DBD experiment is defined as the minimum neutrino mass to be measured by using a DBD detector. It is written as

$$m_m = m_0\, d, \quad d = 1.3\, \epsilon^{-1/2} B^{1/4} (NT)^{-1/4}, \tag{160}$$

where d is the detector sensitivity, ϵ is the $0\nu\beta\beta$ peak efficiency, N is the total DBD-isotope mass in units of ton, T is the measurement time in units of y and B is the ROI (region of interest) background rate per t-y of NT. One gets the mass sensitivity of $m_m = m_0$ by using a detector with $d = 1$ (for example, a detector with $\epsilon = 1$, $NT = 3$ t-y and background rate of $B = 1/\text{t-y}$). The mass sensitivity depends on $(M^{0\nu})^{-1}$, $(NT)^{-1/4}$ and $B^{1/4}$. So it is sensitive to $M^{0\nu}$, but relatively less to the total isotope mass N and the background rate B.

Now we discuss DBD experiments to search for the IH (inverted hierarchy) mass of 20 meV and the NH (normal hierarchy) mass of 2 meV. DBD isotopes of ^{82}Se, ^{100}Mo, ^{116}Cd, ^{130}Te and ^{136}Xe, which are of current interest for high-sensitivity experiments, have large phase-space factors around $G^{0\nu} \approx 1.5$ in units of $10^{-14}\,\text{y}^{-1}$. The nuclear sensitivities m_0 are all around the IH ν-mass of 20 meV in case of a typical NME of $M^{0\nu} = 2$, as shown in Fig. 68. In other words, the kinematic factor $[A/G^{0\nu}]^{1/2}$ is more or less the same for all DBD nuclei. The mass sensitivity is inversely proportional to the NME $M^{0\nu}$, i.e. m_0 is around 30 meV in case of $M^{0\nu} = 1.5$.

The ν-mass sensitivities for ^{130}Te with $\epsilon = 0.5$, as a typical example, are shown as functions of the exposure NT in cases of $B = 1/\text{t-y}$ and $M^{0\nu} = 1, 2, 3$, and $B = 0.01/\text{t-y}$ and $M^{0\nu} = 2$ in Fig. 68. Exposures required for studies of the IH and NH ν-mass regions are $NT = 1 - 10$ t-y and $NT = 100$–1000 t-y in cases of $B = 1/\text{t-y}$, $M^{0\nu} = 2$ and $B = 0.01/\text{t-y}$, $M^{0\nu} = 2$, respectively. See also [755] for ^{124}Sn.

The ^{76}Ge isotope has the larger nuclear sensitivity around $m_0 = 40$ meV because of the smaller phase space of $G^{0\nu} \approx 0.2$ than the others, while the ^{76}Ge detector with excellent energy resolution has the small detector sensitivity d because of the small background rate in the region of interest.

The DBD mass sensitivity m_m is given by the product of the nuclear sensitivity m_0, proportional to $(M^{0\nu})^{-1}$, and the detector sensitivity d proportional to $N^{-1/4}$ and $B^{1/4}$. Using DBD nuclei with $M^{0\nu}$ smaller by 40% requires an order of magnitude more DBD isotope mass N or less background rate B in order to get the same mass sensitivity. It is crucial to know $M^{0\nu}$ in order to select the DBD isotopes with a high nuclear sensitivity (small m_0) in order to design high-sensitivity (small m_m) DBD detectors. The absolute and relative values of the NMEs, including the effective weak coupling (renormalization/quenching factor), have to be carefully considered in selecting the DBD isotopes to be used for future experiments.

Actually, several mechanisms such as the light ν-mass, the heavy ν-mass, the SUSY-mass, and others beyond the SM are possibly involved in the neutrinoless DBD, and the $M^{0\nu}$'s depend on the neutrinoless DBD mechanisms and nuclear structure. Accordingly, accurate $M^{0\nu}$ values are necessary to extract the effective ν mass in case of the light ν-mass mechanism and to identify the DBD mechanism once the rates are observed.

The DBD detector sensitivity required for the DBD experiment with the IH and NH ν-mass sensitivity is around $d = 1$ in a typical case of the NME of $M^{0\nu} = 2$ and the nuclear sensitivity of $m_0 = 20$ meV, assuming the realistic measurement (exposure) time of $T \approx 4$ y, multi-ton scale ($N \approx 1 - 5$ t) detectors with $\epsilon \approx 0.5$ and $B \approx 1/\text{t-y}$. Actually, the mass sensitivity depends on the enrichment r as $m_m \propto r^{-1/2}$. Multi-ton-scale DBD isotopes are needed even for the IH mass experiments, and such amounts of ^{76}Ge, ^{82}Se, ^{100}Mo, ^{116}Cd and ^{136}Xe are obtained by means of centrifugal isotope-separation plants.

The required background rates are of the orders of $B = 1/\text{t-y}$ and $B = 0.01/\text{t-y}$ for the IH and NH ν-mass studies. Background sources to be considered are the natural and cosmogenic RI impurities, cosmogenic muon and neutron interactions, solar-ν CC and NC interactions, high-energy $2\nu\beta\beta$ contributions, and others. Then DBD experiments are made by using high-purity (RI-free) DBD detectors at deep underground laboratories. Good energy resolution, combined with SSSC (single-site spacial correlation) and SSTC (single-site time correlation) analyses are used to reduce background rates as discussed in [16,18].

It is of vital importance to optimize the 3 key parameters for high-sensitivity DBD experiments: the NME $M^{0\nu}$, the total DBD-isotope mass N and the background rate B at the region of interest for high-sensitivity experiments through scientific and realistic discussions and to promote coordinated experimental and theoretical efforts for high-sensitivity DBD studies.

Acknowledgments

References

[1] H. Ejiri, J.I. Fujita, Effective coupling constants for beta and gamma transitions in medium and heavy nuclei, Phys. Rep. 38 (1978) 85–131.
[2] J. Suhonen, O. Civitarese, Weak interaction and nuclear structure aspect of nuclear double beta decay, Phys. Rep. 300 (1998) 123–214.
[3] A. Faessler, F. Šimkovic, Double beta decay, J. Phys. G. 24 (1998) 2139–2178.
[4] H. Ejiri, Nuclear spin isospin responses for low-energy neutrinos, Phys. Rep. 338 (2000) 265–351.
[5] H. Ejiri, Double beta decays and neutrino-nuclear responses, Prog. Part. Nucl. Phys. 54 (2010) 249–257.
[6] W.C. Haxton, R.G.H. Robertson, S.M. Serenelli, Solar neutrinos: status and prospects, Ann. Rev. Astron. Astrophys. 51 (2013) 21–61.
[7] M. Wurm, Solar neutrino spectroscopy, Phys. Rep. 685 (2017) 1–52.
[8] J.N. Bahcall, M.H. Pinsonneault, Standard solar models, with and without helium diffusion, and the solar neutrino problem, Rev. Modern Phys. 64 (1992) 885–926.
[9] J.N. Bahcall, M.H. Pinsonneault, G.J. Wasserburg, Solar models with helium and heavy element diffusion, Rev. Modern Phys. 67 (1995) 781–808.
[10] A. Ianni, Solar neutrinos and solar models, Phys. Dark Universe 4 (2014) 44–49.
[11] J.X. Prochaska, J.C. Howk, A.M. Wolfe, The elemental abundance in a galaxy at z=2.626, Nature 423 (2003) 57–59.
[12] K. Cunha, V.V. Smith, D.L. Lambert, K.H. Hinkle, Fluorine abundances in the large magnetic cloud and omega centauri: evidence for neutrino nucleosynthesis, Astron. J. 126 (2003) 1305–1311.
[13] G. Martinez-Pinedo, T. Fischer, L. Huther, Supernova neutrinos and nucleosynthesis, J. Phys. G: Nucl. Part. Phys. 41 (2014) 044008.
[14] K.G. Balasi, K. Langanke, G. Martinez-Pinedo, Neutrino-nuclear reactions and their role for supernova dynamics and nucleosynthesis, Prog. Part. Nucl. Phys. 85 (2015) 33–81.
[15] K. Zuber, On the physics of massive neutrinos, Phys. Rep. 305 (1998) 295–364.
[16] H. Ejiri, Double beta decays and neutrino masses, J. Phys. Soc. Japan 74 (2005) 2101–2127.
[17] F. Avignone, S. Elliott, J. Engel, Double beta decay, Majorana neutrino, and neutrino mass, Rev. Modern Phys. 80 (2008) 481–516.
[18] J. Vergados, H. Ejiri, F. Šimkovic, Theory of neutrinoless double-beta decay, Rep. Progr. Phys. 75 (2012) 106301.
[19] J. Suhonen, O. Civitarese, Double-beta-decay nuclear matrix elements in the QRPA framework, J. Phys. G: Nucl. Part. Phys. 39 (2012) 085105.
[20] J. Suhonen, O. Civitarese, Review of the properties of the $0\nu\beta^-\beta^-$ nuclear matrix elements, J. Phys. G: Nucl. Part. Phys. 39 (2012) 124005.
[21] J. Maalampi, J. Suhonen, Neutrinoless double β^+/EC decays, Adv. High Energy Phys. 2013 (2013) 505874.
[22] R. Sakyaan, Two-neutrino double beta decay, Ann. Rev. Nucl. Part. Sci. 63 (2013) 503–529.
[23] J. Vergados, H. Ejiri, F. Šimkovic, Neutrinoless double beta decay and neutrino mass, Internat. J. Modern Phys. E 25 (2016) 1630007.
[24] J. Engel, J. Menéndez, Status and future of nuclear matrix elements for neutrinoless double beta decay: a review, Rep. Progr. Phys. 60 (2017) 046301.
[25] Y. Totsuka, Experiments for solar neutrinos and supernova neutrinos, in: M. Fukugida, A. Suzuki (Eds.), Physics and Astrophysics of Neutrinos, Springer Verlag, Tokyo, 1994, pp. 625–693.
[26] H. Ejiri, Double beta decay and neutrinos, in: M. Fukugida, A. Suzuki (Eds.), Physics and Astrophysics of Neutrinos, Springer Verlag, Tokyo, 1994, pp. 500–519.
[27] A. Bohr, B.R. Mottelson, Nuclear Structure, vol. I, Benjamin, New York, 1969.
[28] A. Bohr, B.R. Mottelson, Nuclear Structure, vol. II, Benjamin, New york, 1975.
[29] H. Ejiri, M.J.A. de Voigt, Gamma-Ray and Electron Spectroscopy in Nuclear Physics, Clarendon press, Oxford, 1989.
[30] J. Suhonen, Value of the axial–vector coupling strength in β and $\beta\beta$ decays: A review, Front. Phys. 5 (2017) 55.
[31] E.D. Commins, P.H. Bucksbaum, Weak Interactions of Leptons and Quarks, Cambridge University Press, Cambridge, 1983.
[32] R.P. Feynmann, M. Gell-Mann, Theory of the fermi interaction, Phys. Rev. 109 (1958) 193–198.
[33] M. Gell-Mann, Test of the nature of the vector interaction in β decay, Phys. Rev. 111 (1958) 362–365.
[34] W.R. Theis, Eine rangordnung der einzelnen terme in den schwachen wechselwirkungen, Z. Phys. 150 (1958) 590–592.
[35] K. Zuber, Neutrino Physics, second ed, CRS Press, T & E group, Baca Raton, 2011.
[36] Y. Nambu, Axial vector current conservation in weak interactions, Phys. Rev. Lett. 4 (1960) 380–382.
[37] M. Gell-Mann, M. Lévy, The axial vector current in beta decay, Nuovo Cimento 16 (1960) 705–726.
[38] R.J. Blin-Stoyle, Renormalization of the axial–vector coupling constant in β-decays, Nuclear Phys. A 254 (1975) 353–369.
[39] F.C. Khanna, I.S. Towner, H.C. Lee, Quenching of axial–vector coupling constant in the β-decay of finite nuclei, Nuclear Phys. A 305 (1978) 349–356.
[40] W.C. Haxton, E.M. Henley, Symmetries and Fundamental Interactions in Nuclei, World Scientific, Singapore, 1995.
[41] A. Bodek, S. Avvakumov, R. Bradford, H. Budd, Vector and axial nucleon form factors: a duality constrained parametrization, Eur. Phys. J. C 53 (2008) 349–354.
[42] B. Bhattacharya, R.J. Hill, G. Paz, Model-independent determination of the axial mass parameter in quasielastic neutrino-nucleus scattering, Phys. Rev. D 84 (2011) 073006.
[43] J.E. Amaro, E. Ruiz Arriola, Axial-vector dominance predictions in quasielastic neutrino-nucleus scattering, Phys. Rev. D 93 (2016) 053002.
[44] M.L. Goldberger, S.B. Treiman, Form factors in β decay and μ capture, Phys. Rev. 111 (1958) 354–361.

[45] T.-S. Park, L.E. Marcucci, R. Schiavilla, M. Viviani, A. Kievsky, S. Rosati, K. Kubodera, D.-P. Min, M. Rho, Parameter-free effective field theory calculation for the solar proton-fusion and hep processes, Phys. Rev. C 67 (2003) 055206.

[46] M. Hoferichter, P. Klos, A. Schwenk, Chiral power counting of one- and two-body currents in direct detection of dark matter, Phys. Lett. B 746 (2015) 410–416.

[47] A. Baroni, L. Girlanda, S. Pastore, R. Schiavilla, M. Viviani, Nuclear axial currents in chiral effective field theory, Phys. Rev. C 93 (2016) 015501.

[48] H. Krebs, E. Epelbaum, U.-G. Meissner, Nuclear axial current operators to fourth order in chiral effective field theory, Ann. Phys. 378 (2017) 317–395.

[49] R. Davis Jr., D.S. Hammer, K.C. Hofman, Search for neutrinos from the sun, Phys. Rev. Lett. 20 (1968) 1205–1209.

[50] Y. Fukuda, et al., Evidence for oscillation of atmospheric neutrinos, Phys. Rev. Lett. 81 (1998) 1562–1567.

[51] V. Cirigliano, et al., Neutrinoless double beta decay in chiral effective field theory: lepton number violation at dimension seven, J. High Energy Phys. 12 (2017) 082.

[52] V. Cirigliano, W. Dekens, J. de Vries, M.L. Graesser, E. Mereghetti, A neutrinoless double beta decay master formula from effective field theory, arXiv:1806.02780 [hep-ph].

[53] A. Nicholson, et al., Heavy physics contributions to neutrinoless double beta decay from QCD, arXiv:1805.02634 [nucl-th].

[54] H. Ejiri, K. Ikeda, J.I. Fujita, Hindrance factors for beta decays of heavy nuclei, Phys. Rev. 176 (1968) 1277–1288.

[55] J. Suhonen, From Nucleons to Nucleus: Concepts of Microscopic Nuclear Theory, Springer, Berlin, 2007.

[56] Research Center for Nuclear Physics, Osaka University, http://www.rcnp.osaka-u.ac.jp.

[57] B. Singh, et al., Review of log ft values in β decay, Nucl. Data Sheets 84 (1998) 487–563.

[58] S.W. Finch, W. Tornow, Search for the β decay of ^{96}Zr, Nucl. Instrum. Methods A 806 (2016) 70–74.

[59] M. Alanssari, et al., Single and double beta-decay Q values among the triplet ^{96}Zr, ^{96}Nb, and ^{96}Mo, Phys. Rev. Lett. 116 (2016) 072501.

[60] A. Balysh, et al., Double beta decay of ^{48}Ca, Phys. Rev. Lett. 77 (1996) 5186–5189.

[61] R. Arnold, et al., (NEMO-3 collaboration), Measurement of the double-beta decay half-life and search for the neutrinoless double-beta decay of ^{48}Ca with the NEMO-3 detector, Phys. Rev. D 93 (2016) 112008.

[62] A. Bakalyarov, et al., Search for β^- and $\beta^-\beta^-$ decays of ^{48}Ca, Nuclear Phys. A 700 (2002) 17–24.

[63] J. Argyrlades, et al., (NEMO-3 collaboration), Measurement of the two neutrino double beta decay half-life of Zr-96 with the NEMO-3 detector, Nuclear Phys. A 847 (2010) 168–179.

[64] H. Dombrowski, S. Neumaier, K. Zuber, Precision half-life measurement of the 4-fold forbidden electron capture ^{50}V, Phys. Rev. C 83 (2011) 054322, M. Laubenstein, B, Lehnert, S.S. Nagorny, K. Zuber, A new investigation of half-lives for the decays of ^{50}V. arXiv:1812.04745.

[65] M. Haaranen, P.C. Srivastava, J. Suhonen, K. Zuber, β-decay half-life of ^{50}V calculated by the shell model, Phys. Rev. C 90 (2014) 044314.

[66] M.T. Mustonen, M. Aunola, J. Suhonen, Theoretical description of the fourth-forbidden non-unique beta decays of ^{113}Cd and ^{115}In, Phys. Rev. C 73 (2006) 054301; Phys. Rev. C 76 (2007) 019901, (erratum).

[67] L. Bodenstein-Dresler, et al., Quenching of g_A deduced from the -spectrum shape of Cd-113 measured with the COBRA experiment, arXiv:1806.02254.

[68] J. Dawson, et al., An investigation into the ^{113}Cd beta decay spectrum using a CdZnTe array, Nuclear Phys. A 818 (2009) 264–278.

[69] L. Pfeiffer, et al., Beta spectrum of ^{115}In, Phys. Rev. C 19 (1979) 1035–1041.

[70] S. Mertens, et al., KATRIN Collaboration, Status of the KATRIN experiment and prospects to search for KeV-mass sterile neutrinos in tritium β-decay, Physics Procedia 62 (2015) 267–273.

[71] H. Rotzinger, et al., Beta spectrometry with magnetic calorimeters, J. Low Temp. Phys. 151 (2008) 1087–1093.

[72] M. Loidl, et al., First measurement of the beta spectrum of ^{241}Pu with a cryogenic detector, Appl. Radiat. Isot. 68 (2010) 1454–1458.

[73] J. Kostensalo, J. Suhonen, K. Zuber, Spectral shapes of forbidden argon β decays as background component for rare-event searches, J. Phys. G: Nucl. Part. Phys. 45 (2018) 025202.

[74] F.G. Kondev, C.D. Dracoulis, T. Kibédi, Configurations and hindered decays of K isomers in deformed nuclei with $A \geq 100$, At. Data Nucl. Data Tables 103–104 (2015) 50–105.

[75] H. Ejiri, T. Shima, K-hindered beta and gamma transition rates in deformed nuclei and halflife of ^{180}Ta^m, J. Phys. G: Nucl. Part. Phys. 44 (2017) 065101.

[76] A. Andres, N. Grevesse, Abundance of the elements -meteoritic and solar, Geochim. Cosmochim. Acta 53 (1989) 197–214.

[77] A. Heger, E. Kolbe, W.C. Haxton, K. Langanke, G. Martínez-Pinedo, S.E. Woosley, Neutrino nucleosynthesis, Phys. Lett. B 606 (2005) 258–264.

[78] M.-K. Cheoun, E. Ha, T. Hayakawa, T. Kajino, S. Chiba, Neutrino reactions on ^{138}La and ^{180}Ta via charged and neutral currents by the quasiparticle random-phase approximation, Phys. Rev. C 82 (2010) 035504.

[79] A. Byelikov, et al., Gamow-Teller strength in the exotic odd-odd nuclei ^{138}La and ^{180}Ta and its relevance for neutrino nucleosynthesis, Phys. Rev. Lett. 98 (2007) 082501.

[80] T. Hayakawa, T. Kajino, S. Chiba, G. Mathews, New estimates for the time dependent thermal nucleosynthesis of ^{180}Ta^m, Phys. Rev. C 81 (2010) 052801(R).

[81] M. Hult, S.E.S. Wieslander, G. Marrisens, J. Gasparro, U. Wätjen, M. Misiaszek, Search for radioactivity of ^{180m}Ta using an underground HPGe sandwich spectrometer, Appl. Radiat. Isot. 67 (2009) 918–921.

[82] B. Lehnert, M. Hult, G. Lutter, K. Zuber, Search for the decay of nature's rarest isotope ^{180m}Ta, Phys. Rev. C 95 (2017) 044306.

[83] W.G. Love, M.A. Franey, Effective nucleon nucleon interaction for scattering at intermediate energies, Phys. Rev. C 24 (1981) 1073–1094.

[84] M.A. Franey, W.G. Love, Nucleon–nucleon t-matrix interaction for scattering at intermediate energies, Phys. Rev. C 31 (1985) 488–498.

[85] W.G. Love, M.A. Franey, F. Petrovich, The nucleon–nucleon interaction and nucleon–nucleus scattering, in: F. Petrovich, et al. (Eds.), Spin Excitation in Nuclei, Plenum, New York, 1982, pp. 205–231.

[86] G.E. Brown, J. Speth, J. Wambach, Energy dependence of the coupling potentials in (p, n) reactions, Phys. Rev. Lett. 46 (1981) 1057–1061.

[87] W.G. Love, Properties and applications of effective interactions derived from free nucleon–nucleon forces, in: C.D. Goodman, et al. (Eds.), The (p, n) Reaction and the Nucleon Nucleon Force, Plenum, New York, 1980, pp. 23–55.

[88] C.D. Goodman, et al., Gamow-Teller matrix elements for 0°(p, n) cross sections, Phys. Rev. Lett. 44 (1980) 1755–1759.

[89] C. Gaarde, et al., Excitation of giant spin–isospin multipole vibrations, Nuclear Phys. A 369 (1981) 258–280.

[90] M. Fujiwara, et al., Spin isospin resonances in nuclei, Nuclear Phys. A 599 (1996) 223c–244c.

[91] D. Frekers, P. Puppe, J.H. Thies, H. Ejiri, Gamow Teller strength extraction from (^{3}He, t) reactions, Nuclear Phys. A 916 (2013) 219–240.

[92] H. Akimune, et al., GT strengths studied by (^{3}He, t) reactions and nuclear matrix elements for double beta decays, Phys. Lett. B 394 (1997) 23–28, 665 (2011) 424–424 (erratum).

[93] H. Ejiri, et al., Spin–isospin responses of ^{71}Ga for solar neutrinos studied by ^{71}Ga(^{3}He, $t\gamma$)^{71}Ge reactions, Phys. Lett. B 433 (1998) 257–262.

[94] G.G. Zegers, et al., On the extraction of weak transition strengths via the (^{3}He, $t\gamma$) reactions at 420 MeV, Phys. Rev. Lett. 99 (2007) 202501.

[95] J.H. Thies, et al., The (^{3}He, t) reaction on ^{76}Ge, and double-β-decay matrix element, Phys. Rev. C 86 (2012) 014304.

[96] D. Frekers, et al., High energy-resolution measurements of the ^{82}Se(^{3}He, t)^{82}Br reaction for double-β decay and for solar neutrinos, Phys. Rev. C 94 (2016) 014614.

[97] J.H. Thies, et al., High-resolution ^{96}Zr(^{3}He, t) experiment and the matrix element for double-β decay, Phys. Rev. C 86 (2012) 054323.

[98] J.H. Thies, et al., High-resolution ^{100}Mo(^{3}He, t)^{100}Tc charge-exchange experiment and the impact on double-β decays and neutrino charged-current reactions, Phys. Rev. C 86 (2012) 44309.

[99] P. Puppe, et al., High resolution (^{3}He, t) experiment on the double-β decaying nuclei ^{128}Te and ^{130}Te, Phys. Rev. C 86 (2012) 044603.

[100] P. Puppe, et al., High resolution (^{3}He, t) reaction on the double-β decaying nucleus ^{136}Xe, Phys. Rev. C 84 (2011) 051305.
[101] C.J. Guess, et al., The ^{150}Nd(^{3}He, t) and ^{150}Sm(t, ^{3}He) reactions with applications to $\beta\beta$ decays of ^{150}Nd, Phys. Rev. C 83 (2011) 064318.
[102] H. Ejiri, D. Frekers, Spin dipole matrix elements for double beta decay nuclei by charge-exchange reactions, J. Phys. G: Nucl. Part. Phys. 43 (2016) 11LT01.
[103] H. Ejiri, Experimental studies of neutrino nuclear responses and nuclear structures for neutrino nuclear physics, in: CNNP, Catania, J. Phys.: Conf. Ser. 1056 (2018) 012019.
[104] H. Ejiri, J. Suhonen, GT neutrino-nuclear responses for double beta decays and astro neutrinos, J. Phys. G: Nucl. Part. Phys. 42 (2015) 055201.
[105] H. Ejiri, N. Soukouti, J. Suhonen, Spin-dipole nuclear matrix elements for double beta decays and astro-neutrinos, Phys. Lett. B 729 (2014) 27–32.
[106] H. Ejiri, H. Toki, Nuclear matrix elements for two-neutrino double beta decays, J. Phys. Soc. Japan Lett. 65 (1996) 7–10.
[107] N. Auerbach, L. Zamick, D.C. Zheng, Double Gammow-Teller strength in nuclei, Ann. Phys. 192 (1989) 77–84.
[108] M. Lenske, J.I. Bellane, M. Colonna, J.A. Lay, Theory of single charge exchange heavy ion reactions, arXiv:1803.06290v1.
[109] E. Santopinto, H. Garcia-Tecocoatzi, R.I. Magana-Vsevolodovn, J. Ferretti, Heavy-ion double charge-exchange and its relation to neutrinoless double-beta decay, arXiv:1803.03069v2.
[110] N. Shimizu, J. Menendez, K. Yako, Double Gammow-Teller transitions and its relation to neutrinoless $\beta\beta$ decay, Phys. Rev. Lett. 120 (2018) 142502.
[111] M. Takaki, et al., Heavy-ion double -charge exchange studiy via a ^{12}C(^{18}O,^{18}Ne)^{12}Be reaction, JPS Conf. Proc. 6 (2015) 020038.
[112] K. Takahisa, H. Ejiri, H. Akimune, H. Fujita, R. Matsumiya, T. Ohta, T. Shima, M. Tanaka, M. Yosoi, Double charge exchange (^{11}B,^{11}Li) reaction for double beta decay response, arXiv:1703.08264 [nucl-ex].
[113] www.lns.infn.it/en/.
[114] F. Cappuzzello, M. Cavallaro, C. Agodi, M. Bondi, D. Carbone, A. Cunsolo, A. Foti, Heavy-ion double charge exchange reactions: a tool toward 0$\nu\beta\beta$ nuclear matrix elements, Eur. Phys. J. A 51 (2015) 145.
[115] H. Ejiri, Nuclear responses for double-beta decays by hadron, photon and neutrino probes and MOON experiment, Czech. J. Phys. 56 (2006) 459–466.
[116] D.F. Measday, The nuclear physics of muon capture, Phys. Rep. 354 (2001) 243–409.
[117] H. Primakoff, Theory of muon capture, Rev. Modern Phys. 31 (1959) 802–822.
[118] M. Morita, A. Fujii, Theory of allowed and forbidden transitions in muon capture reactions, Phys. Rev. 118 (1960) 606–618.
[119] V. Gillet, D.A. Jenkins, Muon capture in oxygen-16, Phys. Rev. 140 (1965) B32–B41.
[120] R. Parthasarathy, V.N. Sridhar, Gamma-neutrino angular correlation in muon capture of ^{28}Si, Phys. Rev. C 18 (1978) 1796–1802.
[121] R. Parthasarathy, V.N. Sridhar, Gamma-neutrino angular correlations in muon capture by ^{28}Si. II, Phys. Rev. C 23 (1981) 861–868.
[122] J.R. Luyten, H.P.C. Rood, H.A. Tolhoek, On the theory of muon capture by complex nuclei (I), Nuclear Phys. 41 (1963) 236–274.
[123] J.R. Luyten, H.A. Tolhoek, On the theory of muon capture by complex nuclei (II), Nuclear Phys. 70 (1965) 641–657.
[124] T. Siiskonen, J. Suhonen, V.A. Kuz'min, T.V. Tetereva, Shell-model study of partial muon-capture rates in light nuclei, Nuclear Phys. A 635 (1998) 446–469; Nuclear Phys. A 651 (1999) 437-438 (erratum).
[125] I. Duck, Muon capture in the shell model, Nuclear Phys. 35 (1962) 27–48.
[126] G.H. Miller, M. Eckhause, F.R. Kane, P. Martin, R.E. Welsh, Negative muon capture in carbon leading to specific final states, Phys. Lett. 41B (1972) 50–52.
[127] M. Gmitro, S.S. Kamalov, F. Šimkovic, A.A. Ovchinnikova, Ordinary and radiative muon capture on ^{12}C, Nuclear Phys. A 507 (1990) 707–714.
[128] G. Jonkmans, et al., Radiative muon capture in hydrogen and the induced pseudoscalar coupling, Phys. Rev. Lett. 77 (1996) 4512–4515.
[129] T. Siiskonen, J. Suhonen, M. Hjorth-Jensen, Shell-model effective operators for muon capture in ^{20}Ne, J. Phys. G: Nucl. Part. Phys. 25 (1999) L55–L61.
[130] J. Govaerts, J.-L. Lucio-Martinez, Nuclear muon capture on the proton and ^{3}He within the standard model and beyond, Nuclear Phys. A 678 (2000) 110–146.
[131] A.C. Hayes, I.S. Towner, Shell-model calculations of neutrino scattering from ^{12}C, Phys. Rev. C 61 (2000) 044603.
[132] N. Auerbach, B.A. Brown, Weak interaction rates involving ^{12}C,^{14}N, and ^{16}O, Phys. Rev. C 65 (2002) 024322.
[133] A.C. Hayes, P. Navrátil, J.P. Vary, Neutrino-^{12}C scattering in the *abinitio* shell model with a realistic three-body interaction, Phys. Rev. Lett. 91 (2003) 012502.
[134] N.T. Zinner, K. Langanke, P. Vogel, Muon capture on nuclei: Random phase approximation evaluation versus data for $6 \le Z \le 94$ nuclei, Phys. Rev. C 74 (2006) 024326.
[135] D. Gazit, Muon capture on ^{3}He and the weak structure of the nucleon, Phys. Lett. B 666 (2008) 472–476.
[136] L.E. Marcucci, M. Piarulli, M. Viviani, L. Girlanda, A. Kievsky, S. Rosati, R. Schiavilla, Muon capture on deuteron and ^{3}He, Phys. Rev. C 83 (2011) 014002.
[137] L.E. Marcucci, A. Kievsky, S. Rosati, R. Schiavilla, M. Viviani, Chiral effective field theory predictions for muon capture on deureton and ^{3}He, Phys. Rev. Lett. 108 (2012) 052502.
[138] T.P. Gorringe, et al., Hyperfine effect in μ^- capture on ^{23}Na and g_p/g_a, Phys. Rev. Lett. 72 (1994) 3472–3475.
[139] E. Kolbe, K. Langanke, P. Vogel, Muon capture, continuum random phase approximation, and in-medium renormalization of the axial–vector coupling constant, Phys. Rev. C 50 (1994) 2576–2581.
[140] V. Brudanin, et al., Measurement of the induced pseudoscalar form factor in the capture of polarized muons by Si nuclei, Nuclear Phys. A 587 (1995) 577–595.
[141] B.L. Johnson, et al., Observables in muon capture on ^{23}Na and the effective weak couplings $\tilde{g}_a$ and $\tilde{g}_p$, Phys. Rev. C 54 (1996) 2714–2731.
[142] T. Siiskonen, J. Suhonen, V.A. Kuz'min, T.V. Tetereva, Erratum to: Shell-model study of partial muon-capture rates in light nuclei, Nuclear Phys. A 651 (1999) 437–438.
[143] T. Siiskonen, J. Suhonen, M. Hjorth-Jensen, Towards the solution of the C_P/C_A anomaly in shell-model calculations of muon capture, Phys. Rev. C 59 (1999) R1839–R1843.
[144] M. Kortelainen, M. Aunola, T. Siiskonen, J. Suhonen, Mean-field effects on muon-capture observables, J. Phys. G: Nucl. Part. Phys. 26 (2000) L33–L37.
[145] P.G. Giannaka, T.S. Kosmas, Detailed description of exclusive muon capture rates using realistic two-body forces, Phys. Rev. C 92 (2015) 014606.
[146] R.A. Eramzhyan, V.A. Kuz'min, T.V. Tetereva, Calculations of ordinary and radiative muon capture on ^{58,60,62}Ni, Nuclear Phys. A 642 (1998) 428–448.
[147] M. Kortelainen, J. Suhonen, Nuclear muon capture as a powerful probe of double-beta decays in light nuclei, J. Phys. G: Nucl. Part. Phys. 30 (2004) 2003–2018.
[148] M. Kortelainen, J. Suhonen, Ordinary muon capture as a probe of virtual transitions of $\beta\beta$ decay, Europhys. Lett. 58 (2002) 666–672.
[149] M. Kortelainen, J. Suhonen, Microscopic study of muon-capture transitions in nuclei involved in double-beta-decay processes, Nuclear Phys. A 713 (2003) 501–521.
[150] T.P. Gorringe, et al., Measurement of partial nuon capture rates in $1s - 0d$ shell nuclei, Phys. Rev. C 60 (1999) 055501.
[151] T. Gorringe, H.W. Fearing, Induced pseudoscalar coupling of the proton weak interaction, Rev. Modern Phys. 76 (2004) 31–92.
[152] W.A. Richter, et al., New effective interactions for the 0f1p shell, Nuclear Phys. A 523 (1991) 325–353.
[153] V. Egorov, et al., μCR42β: Muon capture rates for double-beta decay, Czech. J. Phys. 56 (2006) 453–457.
[154] D. Zinatulina, et al., OMC studies for the matrix elements in $\beta\beta$ decay, AIP Conf. Proc. 1572 (2014) 122–125.
[155] H. Ejiri, Isospin (spin) core polarization and charge exchange giant resonances, in: M. Torizuka (Ed.), Proc. Int. Conf. Nuclear Structure Studies using Electron Scattering and Photonuclear Reaction, Research Report Lab. Nucl. Sci. Tohoku Univ., vol. 5, 1972, pp. 261–271.

[156] I.H. Hashim, H. Ejiri, T. Shima, K. Takahisa, Y. Kuno, A. Sato, K. Ninomiya, N. Kawamura, Y. Miyake, Muon capture reaction on ^{100}Mo to study nuclear responses for double-β decays and neutrinos of astrophysics origins, Phys. Rev. C 97 (2018) 014617.
[157] H. Ejiri, et al., Nuclear γ rays from stopped muon capture reactions for nuclear isotope detection, J. Phys. Soc. Japan 82 (2013) 044202.
[158] H. Ejiri, J. Engel, R. Hazama, P. Krasyev, N. Kudomi, R.G.H. Robertson, Spectroscopy of double-beta decays from ^{100}Mo for neutrinos, Phys. Rev. Lett. 85 (2000) 2917–2920.
[159] H. Ejiri, J. Engel, N. Kudomi, Supernova-neutrino studies with ^{100}Mo, Phys. Lett. B 530 (2002) 27–32.
[160] T.W. Donnelly, J.D. Walecka, Electron scattering and nuclear structure, Ann. Rev. Nucl. Sci. 25 (1975) 329–405.
[161] J.I. Fujita, Further remarks on the extended Siegert theorem, Phys. Lett. B 24 (1967) 123–124.
[162] H. Ejiri, P. Richard, S. Ferguson, R. Heffner, D. Perry, Electric dipole transition from the 2f7/2 isobaric analogue resonance to the 2d5/2 ground state in ^{141}Pr, Phys. Rev. Lett. 21 (1968) 373–376.
[163] H. Ejiri, P. Richard, S. Ferguson, R. Heffner, D. Perry, The ^{140}Ce(p, γ)^{141}Pr reaction through isobaric analogue resonances in ^{141}Pr, Nuclear Phys. 128 (1969) 388–400.
[164] H. Ejiri, J.P. Bondorf, The (p, γ) reaction through isobaric analogue and giant dipole resonances, Phys. Lett. B 28 (1968) 304–307.
[165] H. Ejiri, A. Titov, M. Boswell, A. Young, Neutrino nuclear response and photonuclear reactions, Phys. Rev. C 88 (2013) 054610.
[166] H. Beekhuis, R.J. Van Duinen, Matrix element calculation in the beta decay of ^{141}Ce and ^{199}Au, Nuclear Phys. A 108 (1968) 382–400.
[167] B. Bodmann, et al., KARMEN Collaboration, Neutrino interactions with carbon: recent measurements and a new test of the ν_e, $\bar{\nu}_\mu$ universality, Phys. Lett. B 332 (1994) 251–257.
[168] C. Athanassopoulos, et al., (LSND collaboration), Measurements of the reactions ^{12}C(ν_e^-, e)^{12}N$_{g.s}$ and ^{12}C(ν_e^-, e)^{12}N*, Phys. Rev. C 55 (1997) 2078–2091.
[169] F. Avignone III, et al., (ORLaND Collaboration), ORLaND proposal, 1999, 2002.
[170] H. Ejiri, Neutrino studies in nuclei and intense neutrino sources, Nucl. Instrum. Methods Phys. Res. A 503 (2003) 276–278.
[171] N. Jachowicz, G.C. Mclaughlin, C. Volpe, Untangling supernova-neutrino oscillations with β-beam data, Phys. Rev. C 77 (2008) 05501.
[172] A. Galindo-Oribari, Neutrino physics at ORNL and PROSPECT experimental status, in: F. Cappuzzello (Ed.), CNNP, Catania, J Phys.: Conf. Proc. (2018).
[173] S.J. Freeman, J.P. Schiffer, Constraining the 0$\nu\beta\beta$ matrix elements by nuclear structure observables, J. Phys. G: Nucl. Part. Phys. 39 (2012) 124004.
[174] J.P. Entwisle, et al., Change of nucleon configurations in the neutrinoless double-β decays of ^{130}Te$\rightarrow^{130}$Xe and ^{136}Xe$\rightarrow^{136}$Ba, Phys. Rev. C 93 (2016) 064312.
[175] S.V. Szwec, et al., Rearrangement of valence neutrons in the neutrinoless double-β decays of ^{136}Xe, Phys. Rev. C 94 (2016) 054314.
[176] J.P. Schiffer, et al., Nuclear structure relevant to neutrinoless double β decay: ^{76}Ge and ^{76}Se, Phys. Rev. Lett. 100 (2008) 112501.
[177] J. Suhonen, O. Civitarese, Effects of orbital occupancies on the neutrinoless $\beta\beta$ matrix element of ^{76}Ge, Phys. Lett. B 668 (2008) 277–281.
[178] F. Šimkovic, A. Faessler, P. Vogel, 0$\nu\beta\beta$ nuclear matrix elements and the occupancy of individual orbits, Phys. Rev. C 79 (2009) 015502.
[179] J. Menéndez, A. Poves, E. Caurier, F. Nowacki, Occupancies of individual orbits, and the nuclear matrix element of the ^{76}Ge neutrinoless $\beta\beta$ decay, Phys. Rev. C 80 (2009) 048501.
[180] J. Suhonen, O. Civitarese, Effects of orbital occupancies and spin–orbit partners on 0$\nu\beta\beta$-decay rates, Nuclear Phys. A 847 (2010) 207–232.
[181] J. Suhonen, Effects of orbital occupancies and spin–orbit partners II: 0$\nu\beta\beta$ decays of ^{76}Ge,^{82}Se and ^{136}Xe to first excited 0$^+$ states, Nuclear Phys. A 853 (2011) 36–60.
[182] J. Kotila, J. Barea, Occupation probabilities of single particle levels using the microscopic interacting boson model: Application to some nuclei of interest in neutrinoless double-β decay, Phys. Rev. C 94 (2016) 034320.
[183] C.F. Jiao, J. Engel, J.D. Holt, Neutrinoless double-β decay matrix elements in large shell-model spaces with the generator-coordinate method, Phys. Rev. C 96 (2017) 054310.
[184] B.P. Kay, An overview of nucleon-transfer studies on 0$\nu\beta\beta$-decay candidates ^{76}Ge,^{130}Te and ^{136}Xe, APS Conf. Proc. 1894 (2017) 020013.
[185] B.P. Kay, J.P. Schiffer, S.J. Freeman, Quenching of cross sections in nucleon transfer reactions, Phys. Rev. Lett. 111 (2013) 042502.
[186] L. Lipikás, Quasi elastic electron scattering off nuclei, Nuclear Phys. A 533 (1993) 297–308.
[187] J.S. Thomas, et al., Neutron pair correlations in $A = 100$ nucleus involved in neutrinoless double-β decay, Phys. Rev. C 86 (2012) 047304.
[188] M.A. Rathman, M.S. Chowdhury, Nuclear structure of ^{100}Mo, Phys. Rev. C 73 (2012) 054311.
[189] E. Caurier, G. Martínez-Pinedo, F. Nowacki, A. Poves, A.P. Zuker, The shell model as a unified view of nuclear structure, Rev. Modern Phys. 77 (2005) 427–488.
[190] P. Ring, P. Schuck, The Nuclear Many-Body Problem, Springer, New York, 1980.
[191] J. Toivanen, J. Suhonen, Microscopic quasiparticle-phonon description of odd-A Xe isotopes, J. Phys. G: Nucl. Part. Phys. 21 (1995) 1491–1497.
[192] J. Toivanen, J. Suhonen, Microscopic quasiparticle-phonon description of odd-mass $^{127-133}$Xe isotopes and their beta decay, Phys. Rev. C 57 (1998) 1237–1245.
[193] F. Iachello, A. Arima, The Interacting Boson Model, Cambridge University Press, Great Britain, 1987.
[194] F. Iachello, P. Van Isacker, The Interacting Boson-Fermion Model, Cambridge University Press, USA, 1991.
[195] J.D. Holt, J. Engel, Effective double-β-decay operator for ^{76}Ge and ^{82}Se, Phys. Rev. C 87 (2013) 064315.
[196] A.A. Kwiatkowski, et al., New determination of double-β-decay properties in ^{48}Ca: High-precision $Q_{\beta\beta}$-value measurement and improved nuclear matrix element calculations, Phys. Rev. C 89 (2014) 045502.
[197] E. Caurier, F. Nowacki, A. Poves, Nuclear-structure aspects of the neutrinoless $\beta\beta$-decays, Eur. Phys. J. A 36 (2008) 195–200.
[198] M. Horoi, B.A. Brown, Shell-model analysis of the ^{136}Xe double beta decay nuclear matrix elements, Phys. Rev. Lett. 110 (2013) 222502.
[199] J. Menéndez, A. Poves, E. Caurier, F. Nowacki, Disassembling the nuclear matrix elements of neutrinoless $\beta\beta$ decay, Nuclear Phys. A 818 (2009) 139–151.
[200] A. Escuderos, A. Faessler, V. Rodin, F. Šimkovic, Contributions of different neutron pairs in different approaches for neutrinoless double-beta decay, J. Phys. G: Nucl. Part. Phys. 37 (2010) 125108.
[201] J. Toivanen, J. Suhonen, Renormalized proton–neutron qrpa and its application to double beta decay, Phys. Rev. Lett. 75 (1995) 410–413.
[202] J. Toivanen, J. Suhonen, Study of several double-beta-decaying nuclei using the renormalized proton–neutron quasiparticle random-phase approximation, Phys. Rev. C 55 (1997) 2314–2323.
[203] A.A. Raduta, C.M. Raduta, A. Faessler, W.A. Kaminski, Description of the 2$\nu\beta\beta$ decay within a fully renormalized RPA approach, Nuclear Phys. A 634 (1998) 497–524.
[204] C.M. Raduta, A.A. Raduta, Description of the 2$\nu\beta\beta$ decay within a fully renormalized proton–neutron quasiparticle random-phase approximation approach with a restored gauge symmetry, Phys. Rev. C 82 (2010) 068501.
[205] C.M. Raduta, A.A. Raduta, I.I. Ursu, New theoretical results for 2$\nu\beta\beta$ decay within a fully renormalized proton–neutron random-phase approximation approach with the gauge symmetry restored, Phys. Rev. C 84 (2011) 064322.
[206] P. Vogel, M.R. Zirnbauer, Suppression of the two-neutrino double-beta decay by nuclear-structure effects, Phys. Rev. Lett. 57 (1986) 3148–3151.
[207] O. Civitarese, A. Faessler, T. Tomoda, Suppression of the two-neutrino double β decay, Phys. Lett. B 194 (1987) 11–14.
[208] J. Suhonen, A. Faessler, T. Taigel, T. Tomoda, Suppression of the β^+ decays of ^{148}Dy, ^{150}Er and ^{152}Yb, Phys. Lett. B 202 (1988) 174–178.
[209] J. Suhonen, T. Taigel, A. Faessler, pnQRPA calculation of the β^+/EC quenching for several neutron-deficient nuclei in mass regions $A = 94 - 110$ and $A = 146 - 156$, Nuclear Phys. A 486 (1988) 91–117.

[210] E. Holmlund, J. Suhonen, Microscopic nuclear-structure calculations for the solar-neutrino detector ^{71}Ga and close-lying isobars, Nuclear Phys. A 714 (2003) 673–695.

[211] E. Holmlund, J. Suhonen, Gamow-Teller beta decays of the odd-mass neighbors of the solar-neutrino detector ^{127}I, Nuclear Phys. A 706 (2002) 335–350.

[212] T. Otsuka, A. Arima, F. Iachello, Nuclear shell model and interacting bosons, Nuclear Phys. A 309 (1978) 1–33.

[213] T. Otsuka, Microscopic basis of the interacting boson model, Progr. Theoret. Phys. Suppl. 125 (1996) 5–48.

[214] S. Brant, V. Paar, IBFFM yrast states in odd-odd nuclei associated with O(6) and SU(3) limits, Z. Phys. 329 (1988) 151–159.

[215] P. Van Isacker, J. Engel, K. Nomura, Neutron-proton pairing and double-β decay in the interacting boson model, Phys. Rev. C 96 (2017) 064305.

[216] J. Suhonen, Impact of the quenching of g_A on the sensitivity of $0\nu\beta\beta$ experiments, Phys. Rev. C 96 (2017) 055501.

[217] L. Jokiniemi, J. Suhonen, Isovector spin-multipole strength distributions in double-β-decay triplets, Phys. Rev. C 96 (2017) 034308.

[218] E. Oset, M. Rho, Axial currents in nuclei: The Gamow-Teller matrix element, Phys. Rev. Lett. 42 (1979) 47–50.

[219] A. Bohr, B.R. Mottelson, On the role of the δ resonance in the effective spin-dependent moments of nuclei, Phys. Lett. 100 (1981) 10–12.

[220] L.S. Towner, Quenching of spin matrix elements in nuclei, Phys. Rep. 155 (1997) 263–377.

[221] J. Menéndez, D. Gazit, A. Schwenk, Chiral two-body currents in nuclei: Gamow-Teller transitions and neutrinoless double-beta decay, Phys. Rev. Lett. 107 (2011) 062501.

[222] A. Ekström, et al., Effects of three-nucleon forces and two-body currents on Gamow-Teller strengths, Phys. Rev. Lett. 113 (2014) 262504.

[223] C. Patrignani, et al., (Particle Data Group), Review of particle physics, Chin. Phys. C 40 (2016) 100001.

[224] W.T. Chou, E.K. Warburton, B.A. Brown, Gamow-Teller beta-decay rates for $A \leq 18$ nuclei, Phys. Rev. C 47 (1993) 163–177.

[225] D.H. Wilkinson, Renormalization of the axial–vector coupling constant in nuclear β-decay (III), Nuclear Phys. A 225 (1974) 365–381.

[226] B.H. Wildenthal, M.S. Curtin, B.A. Brown, Predicted features of the beta decay of neutron-rich sd-shell nuclei, Phys. Rev. C 28 (1983) 1343–1366.

[227] M. Konieczka, P. Baczyk, W. Satula, β-decay study within multireference density functional theory and beyond, Phys. Rev. C 93 (2016) 042501(R).

[228] T. Siiskonen, M. Hjorth-Jensen, J. Suhonen, Renormalization of the weak hadronic current in the nuclear medium, Phys. Rev. C 63 (2001) 055501.

[229] G. Martínez-Pinedo, A. Poves, E. Caurier, A.P. Zuker, Effective g_A in the pf shell, Phys. Rev. C 53 (1996) R2602–R2605.

[230] Y. Iwata, N. Shimizu, T. Otsuka, Y. Utsuno, J. Menéndez, M. Honma, T. Abe, Large-scale shell-model analysis of the neutrinoless $\beta\beta$ decay of ^{48}Ca, Phys. Rev. Lett. 116 (2016) 112502.

[231] V. Kumar, P.C. Srivastava, H. Li, Nuclear β^--decay half-lives for fp and fpg shell nuclei, J. Phys. G: Nucl. Part. Phys. 43 (2016) 105104.

[232] M. Honma, T. Otsuka, T. Misuzaki, M. Hjorth-Jensen, Effective interaction for f5pg9-shell nuclei and two-neutrino double beta-decay matrix elements, J. Phys.: Conf. Ser. 49 (2006) 45–50.

[233] E. Caurier, F. Nowacki, A. Poves, Shell model description of the $\beta\beta$ decay of ^{136}Xe, Phys. Lett. B 711 (2012) 62–64.

[234] A. Juodagalvis, D.J. Dean, Gamow-Teller GT$_+$ distributions in nuclei with mass $A = 90 - 97$, Phys. Rev. C 72 (2005) 024306.

[235] M. Horoi, A. Neacsu, Shell model predictions for ^{124}Sn double-β decay, Phys. Rev. C 93 (2016) 024308.

[236] P. Pirinen, J. Suhonen, Systematic approach to β and $2\nu\beta\beta$ decays of mass $A = 100 - 136$ nuclei, Phys. Rev. C 91 (2015) 054309.

[237] F.F. Deppisch, J. Suhonen, Statistical analysis of β decays and the effective value of g_A in the proton–neutron random-phase approximation framework, Phys. Rev. C 94 (2016) 055501.

[238] D.S. Delion, J. Suhonen, Effective axial–vector strength and β-decay systematics, Europhys. Lett. 107 (2014) 52001.

[239] Z.M. Niu, Y.F. Niu, H.Z. Liang, W.H. Long, T. Nikšić, D. Vretenar, J. Meng, β-decay half-lives of neutron-rich nuclei and matter flow in the r-process, Phys. Lett. B 723 (2013) 172–176.

[240] T. Marketin, L. Huther, G. Martínez-Pinedo, Large-scale evaluation of β-decay rates of r-process nuclei with the inclusion of first-forbidden transitions, Phys. Rev. C 93 (2016) 025805.

[241] M.T. Mustonen, J. Engel, Global description of β^- decay in even-even nuclei with the axially-deformed skyrme finite-amplitude method, Phys. Rev. C 93 (2016) 014304.

[242] A. Faessler, et al., Overconstrained estimates of neutrinoless double beta decay within the QRPA, J. Phys. G: Nucl. Part. Phys. 35 (2008) 075104, arXiv:0711.3996v1 [nucl-th] 26 Nov 2007.

[243] J. Suhonen, O. Civitarese, Single and double beta decays in the $A = 100$, $A = 116$ and $A = 128$ triplets of isobars, Nuclear Phys. A 924 (2014) 1–23.

[244] J. Barea, J. Kotila, F. Iachello, Nuclear matrix elements for double-β decay, Phys. Rev. C 87 (2013) 014315.

[245] J. Suhonen, O. Civitarese, Probing the quenching of g_A by single and double beta decays, Phys. Lett. B 725 (2013) 153–157.

[246] F. Šimkovic, V. Rodin, A. Faessler, P. Vogel, $0\nu\beta\beta$ and $2\nu\beta\beta$ nuclear matrix elements, quasiparticle random-phase approximation, and isospin symmetry restoration, Phys. Rev. C 87 (2013) 045501.

[247] J. Hyvärinen, J. Suhonen, Nuclear matrix elements for $0\nu\beta\beta$ decays with light or heavy majorana-neutrino exchange, Phys. Rev. C 91 (2015) 024613.

[248] J.C. Hardy, I.S. Towner, V. Koslowsky, E. Hagberg, H. Schmeig, Superallowed $0^+ \rightarrow 0^+$ nuclear β-decays: a critical survey with tests of CVC and the standard model, Nuclear Phys. A 509 (1990) 429–460.

[249] N.B. Gove, M.J. Martin, Log-f tables for beta decay, Nucl. Data Tables 10 (1971) 205–317.

[250] H. Behrens, W. Bühring, Electron Radial Wave Functions and Nuclear Beta-Decay, Clarendon Press, Oxford, 1982.

[251] M. Haaranen, P.C. Srivastava, J. Suhonen, Forbidden nonunique β decays and effective values of weak coupling constants, Phys. Rev. C 93 (2016) 034308.

[252] M. Haaranen, J. Kotila, J. Suhonen, Spectrum-shape method and the next-to-leading-order terms of the β-decay shape factor, Phys. Rev. C 95 (2017) 024327.

[253] I.S. Towner, E.K. Warburton, G.T. Garvey, Hindrance phenomena in unique first- and third-forbidden β-decay, Ann. Phys. 66 (1971) 674–696.

[254] E.K. Warburton, G.T. Garvey, I.S. Towner, Unique second- and third-forbidden β decay, Ann. Phys. 57 (1970) 174–200.

[255] G. Martínez-Pinedo, P. Vogel, Shell model calculation of the β^- and β^+ partial half-lives of ^{54}Mn and other unique second forbidden β decays, Phys. Rev. Lett. 81 (1998) 281–284.

[256] J. Kostensalo, J. Suhonen, Spin-multipole nuclear matrix elements in the pn quasiparticle random-phase approximation: Implications for β and $\beta\beta$ half-lives, Phys. Rev. C 95 (2017) 014322.

[257] ENSDF at NNDC site, http://www.nndc.bnl.gov/.

[258] A.S. Barabash, Average and recommended half-life values for two neutrino double beta decay, Nuclear Phys. A 935 (2015) 52–64.

[259] G. Drexlin, V. Hannen, S. Mertens, C. Weinheimer, Current direct neutrino mass experiments, Adv. High Energy Phys. 2013 (2013) 293986.

[260] B.J. Mount, M. Redshav, E.G. Myers, Q value of ^{115}In $\rightarrow$ ^{115}Sn($3/2^+$): The lowest known energy β decay, Phys. Rev. Lett. 103 (2009) 122502.

[261] J.S.E. Wieslander, et al., Smallest known Q value of any nuclear decay: the rare β^- decay ^{115}In($9/2^+$) $\rightarrow$ ^{115}Sn($3/2^+$), Phys. Rev. Lett. 103 (2009) 122501.

[262] C.M. Cattadori, M. De Deo, M. Laubenstein, L. Pandola, V.I. Tretyak, Observation of β decay of ^{115}In to the first excited level of ^{115}Sn, Nuclear Phys. A 748 (2005) 333–347.

[263] E. Andretti, et al., Half-life of the β decay ^{115}In($9/2+$)$\rightarrow$^{115}Sn($3/2+$), Phys. Rev. C 84 (2011) 044605.

[264] M.T. Mustonen, J. Suhonen, Nuclear and atomic contribution to beta decays with ultra-low Q values, J. Phys. G: Nucl. Part. Phys. 37 (2010) 064008.

[265] J. Suhonen, M.T. Mustonen, Nuclear matrix elements for rare decays, Prog. Part. Nucl. Phys. 64 (2010) 235–237.

[266] M.T. Mustonen, J. Suhonen, Theoretical analysis of the possible ultra-low-q-value decay branch of ^{135}Cs, Phys. Lett. B 703 (2011) 370–375.

[267] N. Sugarman, Characteristics of the fission product Cs^{135}, Phys. Rev. 75 (1949) 1473–1476.
[268] B. Singh, A.A. Rodionov, Y.L. Khazov, Nuclear data sheets for $A = 135$, Nucl. Data Sheets 109 (2008) 517–698.
[269] M. Haaranen, J. Suhonen, Beta decay of ^{115}Cd and its possible ultra-low Q-value branch, Eur. Phys. J. A 49 (2013) 93.
[270] M.E. Rose, A note on the possible effect of screening in the theory of beta-disintegration, Phys. Rev. 49 (1936) 727–729.
[271] J.L. Lopez, L. Durand, Final-state electronic interactions in allowed beta decay, Phys. Rev. C 37 (1988) 535–543.
[272] J.N. Bahcall, Overlap and exchange effects in beta decay, Phys. Rev. 129 (1963) 2683–2694.
[273] M.R. Harston, N.C. Pyper, Exchange effects in β decays of many-electron atoms, Phys. Rev. A 45 (1992) 6282–6295.
[274] A. Saenz, P. Froelich, Effect of final-state interactions in allowed β decays. I. General formalism, Phys. Rev. C 56 (1997) 2132–2161.
[275] M. Haaranen, M. Horoi, J. Suhonen, Shell-model study of the 4th- and 6th-forbidden β-decay branches of ^{48}Ca, Phys. Rev. C 89 (2014) 034315.
[276] M. Honma, T. Otsuka, B.A. Brown, T. Mizusaki, New effective interaction for pf-shell nuclei and its implications for the stability of the $N = Z = 28$ closed core, Phys. Rev. C 69 (2004) 034335.
[277] M. Aunola, J. Suhonen, T. Siiskonen, Shell-model study of the highly forbidden beta decay ^{48}Ca → ^{48}Sc, Europhys. Lett. 46 (1999) 577–582.
[278] H. Heiskanen, M.T. Mustonen, J. Suhonen, Theoretical half-life for beta decay of ^{96}Zr, J. Phys. G: Nucl. Part. Phys. 34 (2007) 837–843.
[279] J. Kostensalo, M. Haaranen, J. Suhonen, Electron spectra in forbidden β decays and the quenching of the weak axial–vector coupling constant g_A, Phys. Rev. C 95 (2017) 044313.
[280] J. Kostensalo, J. Suhonen, g_A-driven shapes of electron spectra of forbidden β decays in the nuclear shell model, Phys. Rev. C 96 (2017) 024317.
[281] V.I. Tretyak, Beta decays in investigations and searches for rare effects, AIP Conf. Proc. 1984 (2017) 020026.
[282] W.Z. Wei, D.M. Mei, C. Zhang, Cosmogenic activation of germanium used for tonne-scale rare event search experiments, arXiv:1706.05324 [nucl-ex].
[283] P.A. Amaudruz, et al., (DEAP-3600 Collaboration), DEAP-3600 dark matter search, Nucl. Part. Phys. Proc. 273–275 (2016) 340–346.
[284] P. Agnes, et al., (DarkSide-50 Collaboration), First results from the darkside-50 dark matter experiment at laboratori nazionali di gran sasso, Phys. Lett. B 743 (2015) 456–466.
[285] J. Chen, Nuclear data sheets for $A = 40$, Nucl. Data Sheets 140 (2017) 1–376.
[286] F. Nowacki, A. Poves, New effective interaction for $0\hbar\omega$ shell-model calculations in the $sd − pf$ valence space, Phys. Rev. C 79 (2009) 014310.
[287] K. Kaneko, Y. Sun, T. Mizusaki, M. Hasegawa, Shell-model study for neutron-rich sd-shell nuclei, Phys. Rev. C 83 (2011) 014320.
[288] W.H. Kelly, G.B. Beard, R.A. Peters, The beta decay of K^{40}, Nuclear Phys. 11 (1959) 492.
[289] H. Horie, K. Ogawa, Effective proton–neutron interaction and spectroscopy of the nuclei with $N = 29$, Progr. Theoret. Phys. 46 (1971) 439–461.
[290] H. Horie, K. Ogawa, Proton–neutron correlations in nuclei with $N = 30$, Nuclear Phys. A 216 (1973) 407–428.
[291] E. Browne, J. Tuli, Nuclear data sheets for $A = 60$, Nucl. Data Sheets 114 (2013) 1849–2022.
[292] G.L. Keister, F.H. Schmidt, The second-forbidden beta spectra of Co^{60} and Sc^{46}, Phys. Rev. 93 (1954) 140.
[293] J. Pradler, B. Singh, I. Yavin, On the unverified nuclear decay and its role in the DAMA experiment, Phys. Lett. B 720 (2013) 399–404.
[294] C. Buck, A.P. Collin, J. Haser, M. Lindner, Investigating the spectral anomaly with different reactor antineutrino experiments, Phys. Lett. B 765 (2017) 159–162.
[295] T.A. Mueller, et al., Improved predictions of reactor antineutrino spectra, Phys. Rev. C 83 (2011) 054615.
[296] F.P. An, et al., (Daya Bay Collaboration), Measurement of the reactor antineutrino flux and spectrum at Daya Bay, Phys. Rev. Lett. 116 (2016) 061801.
[297] J.K. Ahn, et al., (RENO Collaboration), Observation of reactor electron antineutrinos disappearance in the RENO experiment, Phys. Rev. Lett. 108 (2012) 191802.
[298] Y. Abe, et al., (Double Chooz Collaboration), Improved measurements of the neutrino mixing angle θ_{13} with the double chooz detector, J. High Energy Phys. 2014 (10) (2014) 86.
[299] F.P. An, et al., (Daya Bay Collaboration), Evaluation of the reactor antineutrino flux and spectrum at Daya Bay, Phys. Rev. Lett. 118 (2017) 251801.
[300] K. Schreckenbach, G. Colvin, W. Gelletly, F. Von Feilitzsch, Determination of the antineutrino spectrum from ^{235}U thermal neutron fission products up to 9.5 MeV, Phys. Lett. B 160 (1985) 325–330.
[301] A.A. Hahn, K. Schreckenbach, W. Gelletly, F. Von Feilitzsch, G. Colvin, B. Krusche, Antineutrino spectra from ^{241}Pu and ^{239}Pu thermal neutron fission products of ^{238}U, Phys. Lett. B 218 (1989) 365–368.
[302] N. Haag, A. Gütlein, M. Hofmann, L. Oberauer, W. Potzel, K. Schreckenbach, Experimental determination of the antineutrino spectrum of the fission products of ^{238}U, Phys. Rev. Lett. 112 (2014) 122501.
[303] D.-L. Fang, B.A. Brown, Effect of first-forbidden decays on the shape of neutrino spectra, Phys. Rev. C 91 (2015) 025503.
[304] E. Ydrefors, M.T. Mustonen, J. Suhonen, MQPM description of the structure and beta decays of the odd A = 95, 97 Mo and Tc isotopes, Nuclear Phys. A 842 (2010) 33–47.
[305] X.B. Wang, A.C. Hayes, Weak magnetism correction to allowed β decay for reactor antineutrino spectra, Phys. Rev. C 95 (2017) 064313.
[306] A.C. Hayes, J.L. Friar, G.T. Garvey, G. Jungman, G. Jonkmans, Systematic uncertainties in the analysis of the reactor neutrino anomaly, Phys. Rev. Lett. 112 (2014) 202501.
[307] A.A. Sonzogni, E.A. McCutchan, A.C. Hayes, Dissecting reactor antineutrino flux calculations, Phys. Rev. Lett. 119 (2017) 112501.
[308] L. Hayen, J. Kostensalo, N. Severijns, J. Suhonen, First forbidden transitions in the reactor anomaly, 2018, arXiv:1805.12259 [nucl-th].
[309] A.A. Sonzogni, T.D. Johnson, E.A. McCutchan, Nuclear structure insights into reactor antineutrino spectra, Phys. Rev. C 91 (2015) 011301(R).
[310] J.M. Allmond, et al., $2\pi 1\nu$ states populated in ^{135}Te from ^{9}Be-induced reactions with a ^{132}Sn beam, Phys. Rev. C 90 (2014) 014322.
[311] C. Giunti, M. Laveder, Y.F. Li, Q.Y. Liu, H.W. Long, Update of short-baseline electron neutrino and antineutrino disappearance, Phys. Rev. D 86 (2012) 113014.
[312] C. Giunti, Improved determination of the ^{235}U and ^{239}Pu reactor antineutrino cross sections per fission, Phys. Rev. D 96 (2017) 033005.
[313] C. Giunti, X.P. Ji, M. Laveder, Y.F. Li, B.R. Littlejohn, Reactor fuel fraction information on the antineutrino anomaly, J. High Energy Phys. 10 (2017) 143.
[314] M.T. Mustonen, J. Suhonen, Microscopic quasiparticle-phonon description of beta decays of ^{113}Cd and ^{115}In using proton–neutron phonons, Phys. Lett. B 657 (2007) 38–42.
[315] T. Suzuki, T. Yoshida, T. Kajino, T. Otsuka, β decays of isotones with neutron magic number of $N = 126$ and r-process nucleosynthesis, Phys. Rev. C 85 (2012) 015802.
[316] Q. Zhi, E. Caurier, J.J. Cuenca-García, K. Langanke, G. Martínez-Pinedo, K. Sieja, Shell-model half-lives including first-forbidden contributions for r-process waiting-point nuclei, Phys. Rev. C 87 (2013) 025803.
[317] D.-L. Fang, B.A. Brown, T. Suzuki, Investigating β-decay properties of spherical nuclei along the possible r-process path, Phys. Rev. C 88 (2013) 034304.
[318] J. Kostensalo, J. Suhonen, Mesonic enhancement of the weak axial charge and its effect on the half-lives and spectral shapes of first-forbidden $j^+ \leftrightarrow J^-$ decays, Phys. Lett. B 781 (2018) 480–484.
[319] E.K. Warburton, B.A. Brown, Appraisal of the Kuo-Herling shell-model interaction and application to $A = 210 − 212$ nuclei, Phys. Rev. C 43 (1991) 602–617.
[320] H. Daniel, Das β-spektrum des RaE, Nuclear Phys. 31 (1962) 293.
[321] H.F. Schopper, Weak Interactions and Nuclear Beta Decay, North-Holland, Amsterdam, 1966.
[322] J. Suhonen, Calculation of allowed and first-forbidden beta-decay transitions of odd-odd nuclei, Nuclear Phys. A 563 (1993) 205–224.
[323] K. Kubodera, J. Delorme, M. Rho, Axial currents in nuclei, Phys. Rev. Lett. 40 (1978) 755–758.

[324] P. Guichon, M. Giffon, J. Joseph, R. Laverriere, C. Samour, Exchange current corrections for partial capture rates of muons in nuclei, Z. Phys. A 285 (1978) 183–189.
[325] P. Guichon, M. Giffon, C. Samour, Possible evidence for mesonic exchange correction in ^{16}N(0^-) $\leftrightarrow$ ^{16}O(0^+) β-decay and μ-capture reactions, Phys. Lett. 74B (1978) 15–17.
[326] I.S. Towner, F.C. Khanna, Role of 2p-2h states in weak $0^+ - 0^-$ transitions in $A = 16$ nuclei, Nuclear Phys. A 372 (1981) 331–348.
[327] J. Delorme, Meson degrees of freedom in nuclei, Nuclear Phys. A 374 (1982) 541c–555c.
[328] E.K. Warburton, I.S. Towner, B.A. Brown, First-forbidden β decay: Meson-exchange enhancement of the axial charge at $A \sim 16$, Phys. Rev. C 49 (1994) 824–839.
[329] E.K. Warburton, J.A. Becker, B.A. Brown, D.J. Millener, First-forbidden beta decay near $A = 40$, Ann. Phys. 187 (1988) 471–501.
[330] E.K. Warburton, First-forbidden β decay in the lead region and mesonic enhancement of the weak axial current, Phys. Rev. C 44 (1991) 233–260.
[331] K. Kubodera, M. Rho, Axial-charge transitions in heavy nuclei and in-medium effective chiral Lagrangians, Phys. Rev. Lett. 67 (1991) 3479–3482.
[332] H. Mach, E.K. Warburton, R.L. Gill, R.F. Casten, J.A. Becker, B.A. Brown, J.A. Wigner, Meson-exchange enhancement of the first-forbidden ^{96}Y^g(0^-) $\rightarrow$ ^{96}Zr^g(0^+) β transition: β decay of the low-spin isomer of ^{96}Y, Phys. Rev. C 41 (1991) 226–242.
[333] D.H. Gloeckner, Shell-model systematics of the zirconium and niobium isotopes, Nuclear Phys. A 253 (1975) 301–323.
[334] X. Ji, B.H. Wildenthal, Effective interaction for $N = 50$ isotones, Phys. Rev. C 37 (1988) 1256–1266.
[335] B.A. Brown, unpublished.
[336] C. Gaarde, et al., The ^{48}Ca(^{3}He, t)^{48}Sc reaction at 66 and 70 MeV: Reaction mechanism and Gamow-Teller strength, Nuclear Phys. A 334 (1980) 248–268.
[337] C.D. Goodman, Gamow-teller resonances, Nuclear Phys. A 374 (1982) 241c–251c.
[338] H. Akimune, et al., Direct proton decay from the Gamow-Teller resonances in ^{208}Bi, Phys. Rev. C. 52 (1995) 604–615.
[339] D.J. Horen, et al., Energy systematics of the giant gamow-teller resonance and a charge-exchange dipole spin-flip resonance, Phys. Lett. B 99 (1981) 383–386.
[340] L. Jokiniemi, H. Ejiri, D. Frekers, J. Suhonen, Neutrinoless $\beta\beta$ nuclear matrix elements using IVSD $J^\pi = 2^-$ data, Phys. Rev. C. 98 (2018) 024608.
[341] B.D. Anderson, et al., Particle-hole strength excited in the ^{48}Ca(p, n)^{48}Sc reaction at 134 and 160 MeV: Gamow-Teller strength, Phys. Rev. C 31 (1985) 1161–1172.
[342] T. Wakasa, et al., Gamow-Teller strength of ^{90}Nb in the continuum studied via multipole decomposition analysis of the ^{90}Zr(p, n) reaction at 295 MeV, Phys. Rev. C 55 (1997) 2909–2922.
[343] K. Yako, et al., Determination of the Gamow-Teller quenching factor from charge exchange reactions on ^{90}Zr, Phys. Lett. B 615 (2003) 193–199.
[344] E. Caurier, A. Poves, A.P. Zuker, Missing and quenching of Gamow-Teller strength, Phys. Rev. Lett. 74 (1995) 1517–1520.
[345] D.R. Bes, O. Civitarese, J. Suhonen, Sechematic and realistic model calculation of the isovector spin monopole excitations in ^{116}In, Phys. Rev. C 86 (2012) 024314.
[346] O. Civitarese, J. Suhonen, Strength of $J^\pi = 1^+$ Gamow-Teller and isovector spin monopole transitions in double-β-decay triplets, Phys. Rev. C 89 (2014) 044319.
[347] H. Ejiri, Renormalization of the first forbidden beta transitions and giant forbidden beta resonances, Phys. Rev. C. 26 (1982) 2628–2635.
[348] S.P. Riley, et al., Neutrino-induced deuteron disintegration experiment, Phys. Rev. C 59 (1999) 1780–1789.
[349] M. Albert, et al., Measurement of the reaction ^{12}C(ν_μ, μ^-)X near threshold, Phys. Rev. C 51 (1995) R1065–R1069.
[350] R. Maschuw, et al., (KARMEN Collaboration), Neutrino spectroscopy with KARMEN, Prog. Part. Nucl. Phys. 40 (1998) 183–192.
[351] V. Tsakstara, T. Kosmas, Low-energy neutral-current neutrino scattering on ^{128,130}Te, Phys. Rev. C 83 (2011) 054612.
[352] V. Tsakstara, T. Kosmas, Analyzing astrophysical neutrino signals using realistic nuclear structure calculations and the convolution procedure, Phys. Rev. C 84 (2011) 064620.
[353] J.S. O'Connell, T.W. Donnelly, J.D. Valecka, Semileptonic weak interactions with C^{12}, Phys. Rev. C 6 (1972) 719–733.
[354] T.W. Donnelly, J.D. Walecka, Semi-leptonic weak and electromagnetic interactions in nuclei with application to ^{16}O, Phys. Lett. B 41 (1972) 275–280.
[355] T.W. Donnelly, J.D. Walecka, Elastic magnetic electron scattering and nuclear moments, Nuclear Phys. A 201 (1973) 81–106.
[356] T.W. Donnelly, J.D. Walecka, Semi-leptonic weak and electromagnetic interactions with nuclei: Isoelastic processes, Nuclear Phys. A 274 (1976) 368–412.
[357] T.W. Donnelly, R.D. Peccei, Neutral current effects in nuclei, Phys. Rep. 50 (1979) 1–85.
[358] V.C. Chasioti, T.S. Kosmas, A unified formalism for the basic nuclear matrix elements in semi-leptonic processes, Nuclear Phys. A 829 (2009) 234–252.
[359] E. Kolbe, K. Langanke, G. Martínez-Pinedo, P. Vogel, Neutrino-nucleus reactions and nuclear structure, J. Phys. G: Nucl. Part. Phys. 29 (2003) 2569–2596.
[360] T. Katori, M. Martini, Neutrino-nucleus cross sections for oscillation experiments, J. Phys. G: Nucl. Part. Phys. 45 (2018) 013001.
[361] E. Ydrefors, J. Suhonen, Charged-current neutrino-nucleus scattering off the even molybdenum isotopes, Adv. High Energy Phys. 2012 (2012) 373946.
[362] J.D. Walecka, Theoretical Nuclear and Subnuclear Physics, Imperial College Press, London, 2004.
[363] E. Ydrefors, K.G. Balasi, J. Suhonen, T.S. Kosmas, Nuclear responses to supernova neutrinos for stable molybdenum isotopes, in: J.P. Greene (Ed.), Neutrinos: Properties, Sources and Detection, Nova Science Publishers, 2011, pp. 151–175.
[364] J.N. Bahcall, A.M. Serenelli, S. Basu, New solar opacities, abundances, helioseismology, and neutrino fluxes, Astrophys. J. 621 (2005) L85–L88.
[365] Solar neutrino data http://www.sns.ias.edu/~jnb/SNdata/sndata.html.
[366] D. Frekers, et al., The ^{71}Ga(^{3}He, t) reaction and the low-energy neutrino response, Phys. Lett. B 706 (2011) 134–138.
[367] M.B. Aufderheide, S.D. Bloom, D.A. Resler, C.D. Goodman, Comparison of Gamow-Teller strength in ^{37}Ar and ^{39}K and ^{37}Cl neutrino cross sections, Phys. Rev. C 49 (1994) 678–685.
[368] D. Krofcheck, et al., Gamow-Teller strength function in ^{71}Ga via (p, n) reaction at medium energies, Phys. Rev. Lett. 55 (1985) 1051–1054.
[369] G. Bellini, et al., (Borexino collaboration), Neutrinos from the primary proton proton fusion process in the sun, Nature 512 (2014) 383–386.
[370] R.S. Raghavan, Inverse β decay of ^{115}In$\rightarrow$^{115}Sn*: a new possibility for detecting solar neutrinos from the proton proton reaction, Phys. Rev. Lett. 37 (1976) 259–262.
[371] R.S. Raghavan, New prospects for real-time spectroscopy of low energy electron neutrino from the sun, Phys. Rev. Lett. 78 (1997) 3618–3621.
[372] M. Fujiwara, et al., Gamow-Teller strengths of the inverse beta decay transition ^{176}Yb$\rightarrow$^{176}Lu for spectroscopy of proton–proton and other sub-MeV solar neutrinos, Phys. Rev. Lett. 85 (2000) 4442–4445.
[373] M. Agostini, et al., First simultaneous precision spectroscopy of pp, ^{7}Be and pep solar neutrino with Borexino phase-II, arXiv:1707.09279.
[374] D. Frekers, et al., Precision evaluation of the ^{71}Ga(ν_e, e^-) solar neutrino capture rate from (^{3}He, t) charge exchange reaction, Phys. Rev. C 91 (2015) 034608.
[375] K. Zuber, Spectroscopy of low-energy solar neutrinos using CdTe detectors, Phys. Lett. B 571 (2003) 148–154.
[376] K. Zuber, Real time spectroscopy of solar pp-neutrino using ^{150}Nd, Phys. Lett. B 709 (2012) 6–8.
[377] H. Ejiri, S.R. Elliott, Charged current neutrino cross section for solar neutrinos, and background to the $\beta\beta(0\nu)$ experiments, Phys. Rev. C 89 (2014) 055501.
[378] H. Ejiri, S.R. Elliott, Solar neutrino interactions with double-β decay nuclei ^{82}Se,^{100}Mo, and ^{150}Nd, Phys. Rev. C 95 (2017) 055501.

[379] N.F. de Barros, K. Zuber, Solar neutrino–electron scatterings as background limitation for double-beta decay, J. Phys. G: Nucl. Part. Phys. 38 (2011) 105201.
[380] H. Ejiri, K. Zuber, Solar neutrino interactions with liquid scintillators used for double beta-decay experiments, J. Phys. G: Nucl. Part. Phys. 43 (2016) 045201.
[381] K. Hirata, et al., (Kamiokande Collaboration), Observation of a neutrino burst from the supernova SN1987A, Phys. Rev. Lett. 58 (1987) 1490–1493.
[382] R.M. Bionta, et al., (IMB Collaboration), Observation of a neutrino burst in coincidence with supernova 1987a in the large magellanic cloud, Phys. Rev. Lett. 58 (1987) 1494–1496.
[383] E.N. Alekseev, et al., Possible detection of a neutrino signal on 23 february 1987 at the baksan underground, Scintill. Telesc. INR JETP Lett. 45 (1987) 589–592.
[384] H.A. Bethe, Supernova mechanisms, Rev. Modern Phys. 62 (1990) 801–866.
[385] H.T. Janka, K. Langanke, A. Marek, G. Martínez-Pinedo, B. Müller, Theory of core-collapse supernovae, Phys. Rep. 442 (2007) 1–6.
[386] H.T. Janka, Explosion mechanisms of core-collapse supernovae, Ann. Rev. Nucl. Part. Sci. 62 (2012) 151–407.
[387] C. Giunti, C.W. Kim, Fundamentals of Neutrino Physics and Astrophysics, Oxford University Press, New York, NY, USA, 2007.
[388] G.G. Raffelt, Particle physics from stars, Ann. Rev. Nucl. Part. Sci 49 (1999) 163–216.
[389] G.G. Raffelt, Physics opportunities with supernova neutrinos, Prog. Part. Nucl. Phys. 64 (2010) 393–399.
[390] A.B. Balantekin, G.M. Fuller, Supernova neutrino-nucleus astrophysics, J. Phys. G: Nucl. Part. Phys. 29 (2003) 2513–2522.
[391] K. Scholberg, Supernova neutrino detection, Ann. Rev. Nucl. Part. Sci. 62 (2012) 81–103.
[392] K. Langanke, E. Kolbe, Neutrino-induced charged-current reaction rates for r-process nuclei, At. Data Nucl. Data Tables 79 (2001) 293–315.
[393] K. Langanke, G. Martínez-Pinedo, Nuclear weak-interaction processes in stars, Rev. Modern Phys. 75 (2003) 819–862.
[394] K. Langanke, Weak interaction, nuclear physics and supernovae, Acta Phys. Polon. B 39 (2008) 265–282.
[395] T. Suzuki, T. Kajino, Element synthesis in the supernova environment and neutrino oscillations, J. Phys. G: Nucl. Part. Phys. 40 (2013) 083101.
[396] T. Kajino, G.J. Methews, T. Hayakawa, Neutrinos in core-collapse supernovae and nucleosynthesis, J. Phys. G: Nucl. Part. Phys. 41 (2014) 044007.
[397] C. Volpe, Neutrino-nucleus interactions as a probe to constrain double-beta decay predictions, J. Phys. G: Nucl. Part. Phys. 31 (2005) 903–908.
[398] M.T. Keil, G.G. Raffelt, Monte Carlo study of supernova neutrino spectra formation, Astrophys. J. 590 (2003) 971–991.
[399] HALO-Helium and Lead Observatory, http://www.snolab.ca/halo/.
[400] K. Zuber, HALO, a supernova neutrino observatory, Nucl. Part. Phys. Proc. 265–266 (2015) 233–235.
[401] H. Ejiri, et al., The MOON project and DBD matrix elements, Carolina Symp. Neutrino Phy., J. Conf. Ser. 173 (2009) 012009.
[402] EXO-enriched xenon observatory, https://www-project.slac.stanford.edu/exo/.
[403] M. Koshiba, Observational neutrino astrophysics, Phys. Rep. 220 (1992) 229–381.
[404] J. Engel, Approximate treatment of lepton distortion in charged-current neutrino scattering from nuclei, Phys. Rev. C 57 (1998) 2004–2009.
[405] S.E. Woosley, J.R. Wilson, G.J. Mathews, R.D. Hoffman, D.S. Meyer, The r-process and neutrino-heated supernova ejecta, Astrophys. J. 433 (1994) 229–246.
[406] G.M. Fuller, W.C. Haxton, G. McLaughlin, Prospects for detecting supernova neutrino flavor oscillations, Phys. Rev. D 59 (1999) 085005.
[407] H. Akimune, et al., Direct proton decay from the Gamow-Teller resonances in ^{208}Bi, Phys. Rev. C. 52 (1995) 604–615.
[408] B. Dasgupta, A. Dighe, G.G. Raffelt, A. Tu. Smirnov, Multiple spectral splits of supernova neutrinos, Phys. Rev. Lett. 103 (2009) 051105.
[409] J. Gava, C. Volpe, Collective neutrino oscillations in matter and CP violation, Phys. Rev. D 78 (2008) 083007.
[410] A.B. Balantekin, G.M. Fuller, Constraints on neutrino mixing, Phys. Lett. B 471 (1999) 195–201.
[411] G. Martínez-Pinedo, B. Ziebarth, T. Fischer, K. Langanke, Effect of collective neutrino flavor oscillations on νp-process nucleosynthesis, Eur. Phys. J. A 47 (2011) 98.
[412] K. Nakamura, et al., (Particle Data Group), Review of particle physics, J. Phys. G: Nucl. Part. Phys. 37 (2010) 075021.
[413] D. Gazit, N. Barnea, Neutrino neutral reaction on ^{4}He: Effects of final interaction and realistic *NN* force, Phys. Rev. C 70 (2004) 048801.
[414] T. Suzuki, S. Chiba, T. Yoshida, T. Kajino, T. Otsuka, Neutrino-nucleus reactions based on new shell model Hamiltonians, Phys. Rev. C 74 (2006) 034307.
[415] N. Jachowicz, S. Rombouts, K. Heyde, J. Ryckebush, Cross sections for neutral-current neutrino-nucleus interactions: Applications for ^{12}C and ^{16}O, Phys. Rev. C 59 (1999) 3246–3255.
[416] A. Botrugno, G. Co', Excitation of nuclear giant resonances in neutrino scattering off nuclei, Nuclear Phys. A 761 (2005) 200–231.
[417] M.-K. Cheoun, E. Ha, K.S. Kim, T. Kajino, Neutrino-nucleus reactions via neutral and charged currents by the quasi-particle random phase approximation (QRPA), J. Phys. G: Nucl. Part. Phys. 37 (2010) 055101.
[418] H. Dapo, N. Paar, Neutral-current neutrino-nucleus cross sections based on relativistic nuclear energy density functional, Phys. Rev. C 86 (2012) 035804.
[419] S.K. Singh, N.C. Mukhopadhyay, E. Oset, Inclusive neutrino scattering in ^{12}C: Implications for ν_μ to ν_e oscillations, Phys. Rev. C 57 (1998) 2687–2692.
[420] E. Kolbe, K. Langanke, P. Vogel, Weak reactions on ^{12}C within the continuum random phase approximation with partial occupancies, Nuclear Phys. A 652 (1999) 91–100.
[421] N. Jachowicz, K. Heyde, J. Ryckebush, S. Rombouts, Continuum random phase approximation approach to charged-current neutrino-nucleus scattering, Phys. Rev. C 65 (2002) 025501.
[422] N. Paar, D. Vretenar, T. Marketin, P. Ring, Inclusive charged-current neutrino-nucleus reactions calculated with the relativistic quasiparticle random-phase approximation, Phys. Rev. C 77 (2008) 024608.
[423] A.R. Samana, F. Krmpotić, N. Paar, C.A. Bertulani, Neutrino and antineutrino charge-exchange reactions on ^{12}C, Phys. Rev. C 83 (2011) 024303.
[424] C. Volpe, N. Auerbach, G. Coló, T. Suzuki, N. Van Giai, Microscopic theories of neutrino-^{12}C reactions, Phys. Rev. C 62 (2000) 015501.
[425] W.C. Haxton, Nuclear response of water Cherenkov detectors to supernova and solar neutrinos, Phys. Rev. D 36 (1987) 2283–2292.
[426] R. Lazauskas, C. Volpe, Neutrino beams as a probe of the nuclear isospin and spin–isospin excitations, Nuclear Phys. A 792 (2007) 219–228.
[427] M.-K. Cheoun, E. Ha, T. Kajino, Reactions on ^{40}Ar involving solar neutrinos and neutrinos from core-collapsing supernovae, Phys. Rev. C 83 (2011) 028801.
[428] W.E. Ormand, P.M. Pizzochero, P.F. Bortignon, R.A. Broglia, Neutron capture cross sections for ^{40}Ar and β-decay of ^{40}Ti, Phys. Lett. B 345 (1995) 343–350.
[429] I. Gil-Botella, A. Rubbia, Oscillation effects on supernova neutrino rates and spectra and detection of the shock breakout in a liquid argon TPC, J. Cosmol. Astropart. Phys. 10 (2001) 009.
[430] T. Suzuki, M. Honma, Neutrino-capture reactions on ^{40}Ar, Phys. Rev. C 87 (2013) 014607.
[431] J. Kostensalo, J. Suhonen, K. Zuber, Shell-model computed cross sections for charged-current scattering of astrophysical neutrinos off ^{40}Ar, Phys. Rev. C 97 (2018) 034309.
[432] E. Kolbe, K. Langanke, Role of ν-induced reactions on lead and iron in neutrino detectors, Phys. Rev. C 63 (2001) 025802.
[433] T. Suzuki, M. Honma, K. Higashiyama, T. Yoshida, T. Kajino, Neutrino-induced reactions on ^{56}Fe and ^{56}Ni, and production of ^{55}Mn in population III stars, Phys. Rev. C 79 (2009) 061603(R).
[434] A.A. Dzhioev, A.I. Vdovin, G. Martínez-Pinedo, J. Wambach, Ch. Stoyanov, Thermal quasiparticle random-phase approximation with Skyrme interactions and supernova neutral-current neutrino-nucleus reactions, Phys. Rev. C 94 (2016) 015805.

[435] V. Tsakstara, T.S. Kosmas, Nuclear responses of ^{64,66}Zn isotopes to supernova neutrinos, Phys. Rev. C 83 (2011) 054612.
[436] M.-K. Cheoun, E. Ha, T. Hayakawa, S. Chiba, K. Nakamura, T. Kajino, G.J. Mathews, Neutrino-induced reactions for ν-process nucleosynthesis of ^{92}Nb and ^{98}Tc, Phys. Rev. C 85 (2012) 065807.
[437] K.G. Balasi, E. Ydrefors, T.S. Kosmas, Theoretical study of neutrino scattering off the stable even Mo at low and intermediate energies, Nuclear Phys. A 868–869 (2011) 82–98.
[438] E. Ydrefors, K.G. Balasi, T.S. Kosmas, J. Suhonen, The response of ^{95,97}Mo to supernova neutrinos, Nuclear Phys. A 866 (2011) 67–78.   E. Ydrefors, K.G. Balasi, T.S. Kosmas, J. Suhonen, Nuclear Phys. A 878 (2012) 1–2 (erratum).
[439] E. Ydrefors, J. Suhonen, Charged-current neutrino-nucleus scattering off ^{95,97}Mo, Phys. Rev. C 87 (2013) 034314.
[440] E. Ydrefors, K.G. Balasi, T.S. Kosmas, J. Suhonen, Detailed study of the neutral-current neutrino-nucleus scattering off the stable Mo isotopes, Nuclear Phys. A 896 (2012) 1–23.
[441] E. Ydrefors, W. Almosly, J. Suhonen, Nuclear structure and neutrino-nucleus reactions at supernova energies, Rom. J. Phys. 60 (2015) 836–846.
[442] W. Almosly, E. Ydrefors, J. Suhonen, Neutral- and charged-current supernova-neutrino scattering off ^{116}Cd, J. Phys. G: Nucl. Part. Phys. 40 (2013) 095201.
[443] W. Almosly, B.G. Carlsson, J. Dobaczewski, J. Suhonen, J. Toivanen, P. Vesely, E. Ydrefors, Charged-current neutrino and antineutrino scattering off ^{116}Cd described by Skyrme forces, Phys. Rev. C 89 (2014) 024308.
[444] W. Almosly, E. Ydrefors, J. Suhonen, Neutrino scattering off the stable cadmium isotopes: neutral-current processes, J. Phys. G: Nucl. Part. Phys. 42 (2015) 025106.
[445] W. Almosly, E. Ydrefors, J. Suhonen, Neutrino scattering off the stable cadmium isotopes: II. Charged-current processes, J. Phys. G: Nucl. Part. Phys. 42 (2015) 095106.
[446] E. Ydrefors, J. Suhonen, Y.M. Zhao, Neutrino-nucleus scattering off ^{136}Xe, Phys. Rev. C 91 (2015) 014307.
[447] P. Pirinen, J. Suhonen, E. Ydrefors, Neutral-current neutrino-nucleus scattering off Xe isotopes, Adv. High Energy Phys. 2018 (2018) 9163586.
[448] P. Pirinen, J. Suhonen, E. Ydrefors, Charged-current neutrino-nucleus scattering off Xe isotopes, Phys. Rev. C 99 (2019) 014320.
[449] J. Engel, G.C. McLaughlin, C. Volpe, What can be learned with a lead-based supernova-neutrino detector? Phys. Rev. D 67 (2003) 013005.
[450] O. Civitarese, T. Tarutina, Multipole decomposition of the cross section of the neutrino-lead scattering process ^{208}Pb(g.s.)$(\nu, \nu')^{208}$Pb*, Phys. Rev. C 94 (2016) 054603.
[451] W. Almosly, B.G. Carlsson, J. Suhonen, E. Ydrefors, Neutral-current supernova-neutrino cross sections for ^{204,206,208}Pb calculated by Skyrme QRPA, submitted to Phys. Rev. C..
[452] W. Almosly, B.G. Carlsson, J. Suhonen, J. Toivanen, E. Ydrefors, Theoretical estimates of supernova-neutrino cross sections for stable even-even lead isotopes: Charged-current reactions, Phys. Rev. C 94 (2016) 044614.
[453] P. Anselmann, et al., (GALLEX Collaboration), First results from the ^{51}Cr neutrino source experiment with the GALLEX detector, Phys. Lett. B 342 (1995) 440–450.
[454] W. Hampel, et al., (GALLEX Collaboration), Final results of the ^{51}Cr neutrino source experiments in GALLEX, Phys. Lett. B 420 (1998) 114–126.
[455] F. Kaether, W. Hampel, G. Heusser, J. Kiko, T. Kirsten, Reanalysis of the GALLEX solar neutrino flux and source experiments, Phys. Lett. B 685 (2010) 47–54.
[456] J.N. Abdurashitov, et al., (SAGE Collaboration), The Russian-American Gallium Experiment (SAGE) Cr neutrino source measurement, Phys. Rev. Lett. 77 (1996) 4708–4711.
[457] J.N. Abdurashitov, et al., (SAGE Collaboration), Measurement a the response of a gallium metal solar neutrino experiment to neutrinos from a ^{51}Cr source, Phys. Rev. C 59 (1999) 2246–2263.
[458] J.N. Abdurashitov, et al., (SAGE Collaboration), Measurement of the response of a Ga solar neutrino experiment to neutrinos from a ^{37}Ar source, Phys. Rev. C 73 (2006) 045805.
[459] J.N. Bahcall, Gallium solar neutrino experiments: Absorption cross sections, neutrino spectra, and predicted event rates, Phys. Rev. C 56 (1997) 3391–3409.
[460] C. Giunti, M. Laveder, Statistical significance of the gallium anomaly, Phys. Rev. C 83 (2011) 065504.
[461] W.C. Haxton, Cross section uncertainties in the gallium neutrino source experiments, Phys. Lett. B 431 (1998) 110–118.
[462] D.Z. Freedman, Coherent effects of a neutral weak current, Phys. Rev. D 9 (1974) 1389–1392.
[463] A. Drukier, L. Stodolsky, Principles and applications of a neutral-current detector for neutrino physics and astronomy, Phys. Rev. D 30 (1984) 2295–2309.
[464] D.K. Papoulias, T.S. Kosmas, Standard and nonstandard neutrino-nucleus reactions cross sections and event rates to neutrino detection experiments, Adv. High Energy Phys. 2015 (2015) 763648.
[465] B. Cabrera, L.M. Krauss, F. Wilczek, Bolometric detection of neutrinos, Phys. Rev. Lett. 55 (1985) 25–28.
[466] D. Akimov, et al., Observation of coherent elastic neutrino-nucleus scattering, Science 357 (2017) 1123–1126.
[467] A.J. Anderson, J.M. Konrad, E. Figueroa-Feliciano, C. Ignarra, G. Karagiorgi, K. Scholberg, M.H. Shaevitz, J. Spitz, Measuring active-to-sterile neutrino oscillations with neutral current coherent neutrino-nucleus scattering, Phys. Rev. D 86 (2012) 013004.
[468] B. Dutta, Y. Gao, A. Kubik, R. Mohapatra, N. Mirabolfathi, L.E. Strigari, J.W. Walker, Sensitivity to oscillation with a sterile fourth generation neutrino from ultralow threshold neutrino-nucleus coherent scattering, Phys. Rev. D 94 (2016) 093002.
[469] T.S. Kosmas, D.K. Papoulias, M. Tórtola, J.W.F. Valle, Probing light sterile neutrino signatures at reactor and spallation neutron source neutrino experiments, Phys. Rev. D 96 (2017) 063013.
[470] T.S. Kosmas, O.G. Miranda, D.K. Papoulias, M. Tórtola, J.W.F. Valle, Probing neutrino magnetic moments at the spallation neutron source facility, Phys. Rev. D 92 (2015) 013011.
[471] J. Barranco, O.G. Miranda, T.I. Rashba, Sensitivity of low energy neutrino experiments to physics beyond the standard model, Phys. Rev. D 76 (2007) 073008.
[472] P. deNiverville, M. Pospelov, A. Ritz, Light new physics in coherent neutrino-nucleus scattering experiments, Phys. Rev. D 92 (2015) 095005.
[473] B. Dutta, R. Mahapatra, L.E. Strigari, J.W. Walker, Sensitivity to Z-prime and nonstandard neutrino interactions from ultralow threshold neutrino-nucleus coherent scattering, Phys. Rev. D 93 (2016) 013015.
[474] M. Lindner, W. Rodejohann, X. Xu, Coherent neutrino-nucleus scattering and new neutrino interactions, J. High Energy Phys. 03 (2017) 097.
[475] F. Zwicky, Die rotverschiebung von extragalaktischen nebeln, Helv. Phys. Acta 6 (1933) 110–127.
[476] V.C. Rubin, W.K. Ford Jr., Rotation of the andromeda nebula from a spectroscopic survey of emission regions, Astrophys. J. 159 (1970) 379–403.
[477] J. Einasto, A. Kaasik, E. Saar, Dynamic evidence of massive coronas of galaxies, Nature 250 (1974) 309–310.
[478] M.S. Roberts, R.N. Whitehurst, The rotation curve and geometry of M31 at large galactocentric distances, Astrophys. J. 201 (1975) 327–346.
[479] G.R. Blumenthal, S.M. Faber, J.R. Primack, M.J. Rees, Formation of galaxies and large-scale structure with cold dark matter, Nature 311 (1984) 517–525.
[480] M. Davis, G. Efstathiou, C.S. Frenk, S.D.M. White, The evolution of large-scale structure in a universe dominated by cold dark matter, Astrophys. J. 292 (1985) 371–394.
[481] G. Hinshaw, et al., Nine-year Wilkinson microwave anisotropy probe (WMAP) observations: cosmological parameter results, Astrophys. J. Suppl. Ser. 208 (2013) 19.

[482] N. Aghanism, et al., (Planck collaboration), Planck intermediate results. LI, features in the cosmic microwave background temperature power spectrum and shifts in cosmological parameters, Astron. Astrophys. 571 (2014) A16.
[483] H.C. Cheng, J.L. Feng, K.T. Matchev, Kaluza–Klein dark matter, Phys. Rev. Lett. 89 (2002) 211301.
[484] V.K. Oikonomou, J.D. Vergados, Ch.C. Moustakidis, Direct detection of dark matter rates for various wimps, Nuclear Phys. B 773 (2007) 19–42.
[485] S. Nussinov, Technocosmology — could a technibaryon excess provide a "natural" missing mass candidate?, Phys. Lett. B 165 (1985) 55–58.
[486] S.B. Gudnason, C. Kouvaris, F. Sannino, Dark matter from new technicolor theories, Phys. Rev. D 74 (2006) 095008.
[487] J. Hubisz, P. Meade, Phenomenology of the littlest Higgs model with T-parity, Phys. Rev. D 71 (2005) 035016.
[488] A. Birkedal, A. Noble, M. Perelstein, A. Spray, Little higgs dark matter, Phys. Rev. D 74 (2006) 035002.
[489] G. Jungman, M. Kamionkowski, K. Griest, Supersymmetric dark matter, Phys. Rep. 267 (1996) 195–373.
[490] C. Amole, et al., (PICO Collaboration), Dark matter search results from the PICO-2L C_3F_8 bubble chamber, Phys. Rev. Lett. 114 (2015) 231302.
[491] R. Bernabei, et al., (DAMA Collaboration), Final model independent result of DAMA/LIBRA-phase 1, Eur. Phys. J. C 73 (2013) 2648.
[492] C. Tomei, (On behalf of the SABRE collaboration), SABRE: Dark matter annual modulation detection in the northern and southern hemispheres, Nucl. Instrum. Methods A 845 (2017) 418–420.
[493] E. Barbosa de Souza, et al., (DM-Ice collaboration), First search for a dark matter annual modulation signal with NaI(Tl) in the Southern Hemisphere by DM-Ice17, Phys. Rev. D 95 (2017) 032006.
[494] J. Amaré, et al., (ANAIS Collaboration), Assessment of backgrounds of the ANAIS experiment for dark matter direct detection, Eur. Phys. J. C 76 (2016) 429.
[495] R. Agnese, et al., (SuperCDMS Collaboration), Projected sensitivity of the SuperCDMS SNOLAB experiment, Phys. Rev. D. 95 (2017) 082002.
[496] E. Armengaud, et al., (EDELWEISS Collaboration), Constraints on low-mass WIMPs from the EDELWEISS-III dark matter search, J. Cosmol. Astropart. Phys. 05 (2016) 019, arXiv:1603.05120 [astro-ph.CO].
[497] E. Aprile, et al., XENON Collaboration, First dark matter search results from the XENON1T experiment, Phys. Rev. Lett. 119 (2017) 181301.
[498] K. Abe, et al., (XMASS Collaboration), Direct dark matter search by annual modulation in XMASS-I, Phys. Lett. B 759 (2016) 272–276.
[499] V.A. Kudryavtsev, (for the LZ Collaboration), Expected background in the LZ experiment, AIP Conf. Proc. 1672 (2015) 060003.
[500] D.S. Akerib, et al., (LUX collaboration), Results from a search for dark matter in the complete LUX exposure, Phys. Rev. Lett. 118 (2017) 021303.
[501] J. Aalbers, et al., (DARWIN Collaboration), DARWIN: towards the ultimate dark matter detector, J. Cosmol. Astropart. Phys. 1611 (2016) 017, arXiv:1606.07001 [astro-ph.IM].
[502] X. Cui, et al., (PandaX-II Collaboration), Dark matter results from 54-ton-day exposure of PandaX-II experiment, Phys. Rev. Lett. 119 (2017) 181302.
[503] H. Ejiri, K. Fushimi, H. Ohsumi, Search for spin-coupled dark matter by sudying the axial–vector excitation of nuclei, Phys. Lett. B 317 (1993) 14–18.
[504] H. Ejiri, Ch. C. Moustakidis, J.D. Vergados, Dark matter search by exclusive studies of X-rays following WIMPs nuclear interactions, Phys. Lett. B 639 (2006) 218–222.
[505] J. Monroe, P. Fisher, Neutrino backgrounds to dark matter searches, Phys. Rev. D 76 (2007) 033007.
[506] J. Billard, E. Figueroa-Feliciano, L. Strigari, Implication of neutrino backgrounds on the reach of next generation dark matter direct detection experiments, Phys. Rev. D 89 (2014) 023524.
[507] J.D. Vergados, H. Ejiri, Can solar neutrinos be a serious background in direct dark matter searches? Nuclear Phys. B 804 (2008) 144–159.
[508] L.E. Strigari, Neutrino coherent scattering rates at direct dark matter detectors, New J. Phys. 11 (2009) 105011.
[509] J.H. Davis, Dark matter vs neutrinos: The effect of astrophysical uncertainties and timing information on the neutrino floor, J. Cosmol. Astropart. Phys. 03 (2015) 012.
[510] C.A.J. O'Hare, A.M. Green, J. Billard, E. Figueroa-Feliciano, L.E. Strigari, Readout strategies for directional dark matter detection beyond the neutrino background, Phys. Rev. D 92 (2015) 063518.
[511] P. Grothaus, M. Fairbairn, J. Monroe, Directional dark matter detection beyond the neutrino bound, Phys. Rev. D 90 (2014) 055018.
[512] J.B. Dent, B. Dutta, J.L. Newstead, L.E. Strigari, Effective field theory treatment of the neutrino background in direct dark matter detection experiments, Phys. Rev. D 93 (2016) 075018.
[513] J.B. Dent, B. Dutta, J.L. Newstead, L.E. Strigari, Dark matter, light mediators, and the neutrino floor, Phys. Rev. D 95 (2017) 051701.
[514] B.A. Brown, W.D.M. Rae, The shell-model code NuShellX@MSU, Nucl. Data Sheets 120 (2014) 115–118.
[515] B.A. Brown, N.J. Stone, J.R. Stone, I.S. Towner, M. Hjorth-Jensen, Magnetic moments of the 2_1^+ states around ^{132}Sn, Phys. Rev. C 71 (2005) 044317. B.A. Brown, N.J. Stone, J.R. Stone, I.S. Towner, M. Hjorth-Jensen, B.A. Brown, N.J. Stone, J.R. Stone, I.S. Towner, M. Hjorth-Jensen, Phys. Rev. C 72 (2005) 029901 (erratum).
[516] P. Pirinen, P.C. Srivastava, J. Suhonen, M. Kortelainen, Shell-model study on event rates of lightest supersymmetric particles scattering off ^{83}Kr and ^{125}Te, Phys. Rev. D 93 (2016) 095012.
[517] A. Heger, E. Kolbe, W.C. Haxton, K. Langanke, G. Martínez-Pinedo, S.E. Woosley, Neutrino nucleosynthesis, Phys. Lett. B 606 (2005) 258–264.
[518] J.J. Cowan, F.-K. Thielemann, J.W. Truran, The R-process and nucleochronology, Phys. Rep. 208 (1991) 267–394.
[519] F.F. Deppisch, M. Hirsch, H. Päs, Neutrinoless double-beta decay and physics beyond the standard model, J. Phys. G: Nucl. Part. Phys. 39 (2012) 124007.
[520] W. Rodejohann, Neutrino-less double beta decay and particle physics, Internat. J. Modern Phys. E 20 (2011) 1833–1930.
[521] W. Rodejohann, Neutrinoless double beta decay and neutrino physics, J. Phys. G: Nucl. Part. Phys. 39 (2012) 124008.
[522] S.M. Bilenky, C. Giunti, Neutrinoless double-beta decay, a brief review, Modern Phys. Lett. A 27 (2012) 1230015.
[523] M. Doi, T. Kotani, E. Takasugi, Double beta decay and Majorana neutrino, Progr. Theoret. Phys. Suppl. 83 (1985) 1–175.
[524] M. Doi, T. Kotani, Neutrino-emitting modes of double beta decay, Progr. Theoret. Phys. 87 (1992) 1207–1231.
[525] M. Doi, T. Kotani, Neutrinoless modes of double beta decay, Progr. Theoret. Phys. 89 (1993) 139–159.
[526] S.R. Elliott, J. Engel, Double-beta decay, J. Phys. G: Nucl. Part. Phys. 30 (2004) R183–R215.
[527] S.M. Bilenky, Majorana neutrino mixing, J. Phys. G: Nucl. Part. Phys. 32 (2006) R127–R149.
[528] J. Bernabeu, A. De Rujula, C. Jarlskog, Neutrinoless double electron capture as a tool to measure the electron neutrino mass, Nuclear Phys. B 223 (1983) 15–28.
[529] Z. Sujkowski, S. Wycech, Neutrinoless double electron capture: A tool to search for Majorana neutrinos, Phys. Rev. C 70 (2004) 052501(R).
[530] J. Suhonen, Nuclear matrix elements for the resonant neutrinoless double electron capture, Eur. Phys. J. A 48 (2012) 51.
[531] M.I. Krivoruchenko, F. Šimkovic, D. Frekers, A. Faessler, Resonance enhancement of neutrinoless double electron capture, Nuclear Phys. A 859 (2011) 140–171.
[532] J.D. Vergados, Transition operators entering neutrinoless double electron capture to excited nuclear states, Phys. Rev. C 84 (2011) 044328.
[533] J. Suhonen, Double beta decays of ^{124}Xe investigated in the QRPA framework, J. Phys. G: Nucl. Part. Phys. 40 (2013) 075102.
[534] J. Kotila, F. Iachello, Phase-space factors for double-β decay, Phys. Rev. C 85 (2012) 034316.
[535] S. Stoica, M, Mirea new calculations for phase space factors involved in double-β decay, Phys. Rev. C 88 (2013) 037303.
[536] J. Kotila, F. Iachello, Phase-space factors for $\beta^+\beta^+$ decay and competing modes of double-β decay, Phys. Rev. C 87 (2013) 024313.
[537] J. Kotila, J. Barea, F. Iachello, Phase-space factors and half-life predictions for majoron-emitting $\beta^-\beta^-$ decay, Phys. Rev. C 91 (2015) 064310.
[538] F. Ahmed, A. Neacsu, M. Horoi, Interference between light and heavy neutrinos for $0\nu\beta\beta$ decay in the left–right symmetric model, Phys. Lett. B 769 (2017) 299–304.

[539] M. Mirea, T. Pahomi, S. Stoica, Values of the phase space factors involved in double beta decay, Rom. Rep. Phys. 67 (2015) 872–889.
[540] A. Neacsu, M. Horoi, An effective method to accurately calculate the phase space facxtors for $\beta^-\beta^-$ decay, Adv. High Energy Phys. 2016 (2016) 7486712.
[541] D. Fang, A. Faessler, V. Rodin, M.S. Yousef, F. Šimkovic, Running sums for $2\nu\beta\beta$-decay matrix elements within the quasiparticle random-phase approximation with account for deformation, Phys. Rev. C 81 (2010) 037303.
[542] P. Sarriguren, O. Moreno, E. Moya de Guerra, Nuclear structure calculations for two-neutrino double-β decay, Adv. High Energy Phys. 2016 (2016) 6391052.
[543] E. Caurier, F. Nowacki, A. Poves, $\beta\beta$ decay and nuclear structure, Internat. J. Modern Phys. E (2007) 552–560.
[544] A. Neacsu, M. Horoi, Shell model studies of the ^{130}Te neutrinoless double-β decay, Phys. Rev. C 91 (2015) 024309.
[545] N. Yoshida, F. Iachello, Two-neutrino double-β decay in the interacting boson-fermion model, Prog. Theor. Exp. Phys. 2013 (2013) 043D01.
[546] D.R. Bes, O. Civitarese, Matrix elements for the ground-state to ground-state $2\nu\beta^-\beta^-$ decay of Te isotopes in a hybrid model, Phys. Rev. C 81 (2010) 014315.
[547] E.A. Coello-Pérez, J. Menéndez, A. Schwenk, Gamow-Teller and double-beta decays of heavy nuclei within an effective theory, Phys. Rev. C 98 (2018) 045501.
[548] F. Šimkovic, R. Hodák, A. Faessler, P. Vogel, Relation between the $0\nu\beta\beta$ and $2\nu\beta\beta$ nuclear matrix elements reexamined, Phys. Rev. C 83 (2011) 015502.
[549] T.R. Rodríguez, G. Martínez-Pinedo, Neutrinoless $\beta\beta$ decay nuclear matrix elements in an isotopic chain, Phys. Lett. B 719 (2013) 174–178.
[550] D. Štefánik, F. Šimkovic, A. Faessler, Structure of the two-neutrino double-β decay matrix elements within perturbation theory, Phys. Rev. C 91 (2015) 064311.
[551] F. Šimkovic, R. Dvornický, D. Štefánik, A. Faessler, Improved description of the $2\nu\beta\beta$-decay and a possibility to determine the effective axial–vector coupling constant, Phys. Rev. C 97 (2018) 034315.
[552] M. Bhattacharya, et al., Electron capture decay of ^{116}In and double β decay of ^{116}Cd, Phys. Rev. C 58 (1998) 1247–1256.
[553] O. Civitarese, J. Suhonen, Is the single-state dominance realized in double-beta-decay transitions, Phys. Rev. C 58 (1998) 1535–1538.
[554] O. Civitarese, J. Suhonen, Systematic study of the single-state dominance in $2\nu\beta\beta$ decay transitions, Nuclear Phys. A 653 (1999) 321–337.
[555] F. Šimkovic, P. Domin, S.V. Semenov, The single state dominance hypothesis and the two-neutrino double beta decay of ^{100}Mo, J. Phys. G: Nucl. Part. Phys. 27 (2001) 2233–2240.
[556] P. Domin, S. Kovalenko, F. Šimkovic, S.V. Semenov, Neutrino accompanied $\beta^\pm\beta^\pm$, β^+/EC and EC/EC processes within single state dominance hypothesis, Nuclear Phys. A 753 (2005) 337–363.
[557] O. Moreno, R. Álvarez Rodríguez, P. Sarriguren, E. Moya de Guerra, F. Šimkovic, A. Faessler, Single- and low-lying-states dominance in two-neutrino double-beta decay, J. Phys. G: Nucl. Part. Phys. 36 (2009) 015106.
[558] H. Ejiri, Experimental nuclear matrix elements for two neutrino double beta decays and single beta decays, J. Phys. Soc. Japan 78 (2009) 074201.
[559] H. Ejiri, Nuclear matrix element for two neutrino double beta decay from ^{136}Xe, J. Phys. Soc. Jpn. lett. 81 (2012) 033201.
[560] H. Ejiri, Fermi surface quasi particle model nuclear matrix elements for two neutrino double beta decays, J. Phys. G: Nucl. Part. Phys. 44 (2017) 115201.
[561] J. Suhonen, S.B. Khadkikar, A. Faessler, Confined quarks and the neutrinoless $\beta\beta$ decay, Phys. Lett. B 237 (1990) 8–13.
[562] J. Suhonen, S.B. Khadkikar, A. Faessler, Calculation of the neutrinoless $\beta\beta$ decay of ^{76}Ge using a quark model with harmonic confinement, Nuclear Phys. A 529 (1991) 727–740.
[563] J. Suhonen, S.B. Khadkikar, A. Faessler, The neutrinoless double beta decay of ^{76}Ge,^{82}Se,^{86}Kr,^{114}Cd, ^{128,130}Te, ^{134,136}Xe in the framework of a relativistic quark confinement model, Nuclear Phys. A 535 (1991) 509–547.
[564] C. Barbero, F. Krmpotić, D. Tadić, Nuclear moments for the neutrinoless double beta decay, Nuclear Phys. A 628 (1998) 170–186.
[565] C. Barbero, F. Krmpotić, A. Mariano, D. Tadić, Nuclear moments for the neutrinoless double beta decay II, Nuclear Phys. A 650 (1999) 485–497.
[566] H. Päs, M. Hirsch, H.V. Klapdor-Kleingrothaus, S.G. Kovalenko, Towards a superformula for neutrinoless double beta decay, Phys. Lett. B 453 (1999) 194–198.
[567] H. Päs, M. Hirsch, H.V. Klapdor-Kleingrothaus, S.G. Kovalenko, A superformula for neutrinoless double beta decay II: the short range part, Phys. Lett. B 498 (2001) 35–39.
[568] D. Stefanik, R. Dvornicky, F. Šimkovic, P. Vogel, Reexamining the light neutrino exchange mechanism of the $0\nu\beta\beta$ decay with left- and right-handed leptonic and hadronic currents, Phys. Rev. C 92 (2015) 055502.
[569] M. Horoi, A. Neacsu, Analysis of mechanisms that could contribute to neutrinoless double-beta decay, Phys. Rev. D 93 (2016) 113014.
[570] T. Tomoda, $0^+ \rightarrow 2^+$ $0\nu\beta\beta$ decay triggered directly by the Majorana neutrino mass, Phys. Lett. B 474 (2000) 245–250.
[571] A.S. Barabash, A.D. Dolgov, R. Dvornický, F. Šimkovic, A. Yu. Smirnov, Statistics of neutrinos and double beta decay, Nuclear Phys. B 783 (2007) 90–111.
[572] B.A. Brown, M. Horoi, R.A. Sen'kov, Nuclear structure aspects of neutrinoless double-β decay, Phys. Rev. Lett. 113 (2014) 262501.
[573] J. Menéndez, N. Hinohara, J. Engel, G. Martínez-Pinedo, T.R. Rodríguez, Testing the importance of collective correlations in neutrinoless $\beta\beta$ decay, Phys. Rev. C 93 (2016) 014305.
[574] J.M. Yao, J. Engel, Octupole correlations in low-lying states of ^{150}Nd and^{150}Sm and their impact on neutrinoless double-β decay, Phys. Rev. C 94 (2016) 014306.
[575] F. Šimkovic, G. Pantis, J.D. Vergados, A. Faessler, Additional nucleon current contributions to neutrinoless double β decay, Phys. Rev. C 60 (1999) 055502.
[576] M. Kortelainen, J. Suhonen, Improved short-range correlations and $0\nu\beta\beta$ nuclear matrix elements of ^{76}Ge and ^{82}Se, Phys. Rev. C 75 (2007) 051303(R).
[577] M. Kortelainen, J. Suhonen, Nuclear matrix elements of $0\nu\beta\beta$ decay with improved short-range correlations, Phys. Rev. C 76 (2007) 024315.
[578] A. Neacsu, S. Stoica, Study of nuclear effects in the computation of the $0\nu\beta\beta$ decay matrix elements, J. Phys. G: Nucl. Part. Phys. 41 (2014) 015201.
[579] G.A. Miller, J.E. Spencer, A survey of pion charge-exchange reactions with nuclei, Ann. Phys. 100 (1976) 562–606.
[580] H. Feldmeier, T. Neff, R. Roth, J. Schnack, A unitary correlation operator method, Nuclear Phys. A 632 (1998) 61–95.
[581] M. Kortelainen, O. Civitarese, J. Suhonen, J. Toivanen, Short-range correlations and neutrinoless double beta decay, Phys. Lett. B 647 (2007) 128–132.
[582] F. Šimkovic, A. Faessler, V. Rodin, P. Vogel, J. Engel, Anatomy of the $0\nu\beta\beta$ nuclear matrix elements, Phys. Rev. C 77 (2008) 045503.
[583] R. Roth, H. Hergert, P. Papakonstantinou, T. Neff, H. Feldmeier, Matrix elements an few-body calculations within the unitary correlation operator method, Phys. Rev. C 72 (2005) 034002.
[584] T. Neff, H. Feldmeier, Tensor correlations in the unitary correlation operator method, Nuclear Phys. A 713 (2003) 311–371.
[585] F. Šimkovic, A. Faessler, H. Müther, V. Rodin, M. Stauf, $0\nu\beta\beta$-decay nuclear matrix elements with self-consistent short-range correlations, Phys. Rev. C 79 (2009) 055501.
[586] M. Horoi, S. Stoica, Shell model analysis of the neutrinoless double-β decay of ^{48}Ca, Phys. Rev. C 81 (2010) 024321.
[587] O. Benhar, R. Biondi, E. Speranza, Short-range correlation effects on the nuclear matrix element of neutrinoless double-β decay, Phys. Rev. C 90 (2014) 065504.
[588] R.A. Sen'kov, M. Horoi, Neutrinoless double-β decay of ^{48}Ca in the shell model: Closure versus nonclosure approximation, Phys. Rev. C 88 (2013) 064312.

[589] P. Vogel, Nuclear structure and double beta decay, J. Phys. G: Nucl. Part. Phys. 39 (2012) 124002.
[590] E. Caurier, F. Nowacki, A. Poves, Nuclear-structure aspects of the neutrinoless $\beta\beta$-decays, Eur. Phys. J. A 36 (2008) 195–200.
[591] J. Barea, F. Iachello, Neutrinoless double-β decay in the microscopic interacting boson model, Phys. Rev. C 79 (2009) 044301.
[592] D.-L. Fang, A. Faessler, V. Rodin, F. Šimkovic, Neutrinoless doube-β decay of deformed nuclei within quasiparticle random-phase approximation with a realistic interaction, Phys. Rev. C 83 (2011) 034320.
[593] J. Hyvärinen, J. Suhonen, Neutrinoless $\beta\beta$ decays to excited 0^+ states and the Majorana-neutrino mass, Phys. Rev. C 93 (2016) 064306.
[594] J. Hyvärinen, J. Suhonen, Analysis of the intermediate-state contributions to neutrinoless double β^- decays, Adv. High Energy Phys. 2016 (2016) 4714829.
[595] P.K. Rath, R. Chandra, K. Chaturvedi, P. Lohani, P.K. Raina, J.G. Hirsch, Neutrinoless $\beta\beta$ decay transition matrix elements within mechanisms involving light Majorana neutrinos, classical Majorons, and sterile neutrinos, Phys. Rev. C 88 (2013) 064322.
[596] P.K. Rath, R. Chandra, K. Chaturvedi, P.K. Raina, J.G. Hirsch, Deformation effects and neutrinoless positron $\beta\beta$ decay of ^{96}Ru,^{102}Pd,^{106}Cd,^{124}Xe,^{130}Ba, and ^{156}Dy, Phys. Rev. C 80 (2009) 044303.
[597] P.K. Rath, R. Chandra, K. Chaturvedi, P. Lohani, P.K. Raina, J.G. Hirsch, Uncertainties in nuclear transition matrix elements for $\beta^+\beta^+$ and $\varepsilon\beta^+$ modes of neutrinoless positron double-β decay within the projected Hartree–Fock–Bogoliubov model, Phys. Rev. C 87 (2013) 014301.
[598] P.K. Rath, R. Chandra, K. Chaturvedi, P.K. Raina, J.G. Hirsch, Uncertainties in nuclear transition matrix elements for neutrinoless $\beta\beta$ decay within the projected-Hartree–Fock-Bogoliubov model, Phys. Rev. C 82 (2010) 064310.
[599] E. Caurier, J. Menéndez, F. Nowacki, A. Poves, Influence of pairing on the nuclear matrix elements of the neutrinoless $\beta\beta$ decays, Phys. Rev. Lett. 100 (2008) 052503.
[600] J. Menéndez, T.R. Rodríguez, G. Martínez-Pinedo, A. Poves, Correlations and neutrinoless $\beta\beta$ decay nuclear matrix elements of pf-shell nuclei, Phys. Rev. C 90 (2014) 024311.
[601] R. Álvarez-Rodríguez, E. Moya de Guerra, L. Pacearescu, A. Faessler, F. Šimkovic, Deformed quasiparticle random phase approximation formalism for single- and two-neutrino double β decay, Phys. Rev. C 70 (2004) 064309.
[602] R. Chandra, J. Singh, P.K. Rath, P.K. Raina, J.G. Hirsch, Two-neutrino double-β decay of $94 \leq A \leq 110$ nuclei for the $0^+ \rightarrow 0^+$ transition, Eur. Phys. J. A 23 (2005) 223–234.
[603] S. Singh, R. Chandra, P.K. Rath, P.K. Raina, J.G. Hirsch, Nuclear deformation and the two-neutrino double-β decay in ^{124,126}Xe, ^{128,130}Te, ^{130,132}Ba and ^{150}Nd isotopes, Eur. Phys. J. A 33 (2007) 375–388.
[604] P. Sarriguren, Deformation effects on the Gamow-Teller strength distributions in the double-β decay partners ^{76}Ge and ^{76}Se, Phys. Rev. C 86 (2012) 034335.
[605] Y.K. Singh, R. Chandra, P.K. Raina, P.K. Rath, Two neutrino double-β decay of $94 \leq A \leq 150$ nuclei for the $0^+ \rightarrow 2^+$ transition, Eur. Phys. J. A 53 (2017) 244.
[606] F. Šimkovic, L. Pacearescu, A. Faessler, Two-neutrino double beta decay of ^{76}Ge within deformed QRPA, Nuclear Phys. A 733 (2004) 321–350.
[607] A.A. Raduta, A. Escuderos, A. Faessler, E. Moya de Guerra, P. Sarriguren, Two-neutrino double-β decay in deformed nuclei with an angular momentum projected basis, Phys. Rev. C 69 (2004) 064331.
[608] A.A. Raduta, C.M. Raduta, A. Escuderos, Description of the two neutrino double β decay in deformed nuclei with projected spherical single particle basis, Phys. Rev. C 71 (2005) 024307.
[609] C.M. Raduta, A.A. Raduta, Unified description of the double β decay to the first quadrupole phonon state in spherical and deformed nuclei, Phys. Rev. C 76 (2007) 044306.
[610] M.S. Yousef, V. Rodin, A. Faessler, F. Šimkovic, Two-neutrino double β decay of deformed nuclei within the quasiparticle random-phase approximation with a realistic interaction, Phys. Rev. C 79 (2009) 014314.
[611] D.S. Delion, J. Suhonen, Double-β decay within a consistent deformed approach, Phys. Rev. C 91 (2015) 054329.
[612] D.S. Delion, J. Suhonen, Two-neutrino $\beta\beta$ decays and low-lying Gamow-Teller β^- strength functions in the mass range $A = 70 - 176$, Phys. Rev. C 95 (2017) 034330.
[613] J. Terasaki, Overlap of quasiparticle random-phase approximation states for nuclear matrix elements of the neutrino-less double-β decay, Phys. Rev. C 86 (2012) 021301(R).
[614] J. Terasaki, Many-body correlations of quasiparticle random-phase approximation in nuclear matrix elements of neutrinoless double-β decay, Phys. Rev. C 91 (2015) 034318.
[615] J. Terasaki, Examination of the consistency of the quasiparticle random-phase approximation approach to double-β decay of ^{48}Ca, Phys. Rev. C 97 (2018) 034304.
[616] D.-L. Fang, A. Faessler, F. Šimkovic, $0\nu\beta\beta$-decay nuclear matrix element for light and heavy neutrino mass mechanisms from deformed quasiparticle random-phase approximation calculations for ^{76}Ge,^{82}Se,^{130}Te,^{136}Xe, and ^{150}Nd with isospin restoration, Phys. Rev. C 97 (2018) 045503.
[617] T.R. Rodríguez, G. Martínez-Pinedo, Energy density functional study of nuclear matrix elements for neutrinoless $\beta\beta$ decay, Phys. Rev. Lett. 105 (2010) 252503.
[618] V.A. Rodin, A. Faessler, F. Šimkovic, P. Vogel, Assessment of uncertainties in QRPA $0\nu\beta\beta$-decay nuclear matrix elements, Nuclear Phys. A 766 (2006) 107–131.
[619] J. Suhonen, M. Kortelainen, Nuclear matrix elements for double beta decay, Internat. J. Modern Phys. 17 (2008) 1–11.
[620] J. Barea, J. Kotila, F. Iachello, $0\nu\beta\beta$ and $2\nu\beta\beta$ nuclear matrix elements in the interacting boson model with isospin restoration, Phys. Rev. C 91 (2015) 034304.
[621] J.A. Sheikh, N. Hinohara, J. Dobaczewski, T. Nakatsukasa, W. Nazarewicz, K. Sato, Isospin invariant skyrme energy-density-functional approach with axial symmetry, Phys. Rev. C 89 (2014) 054317.
[622] M. Konieczka, M. Kortelainen, W. Satula, Gamow-Teller response in the configuration space of a density-functional-theory-rooted no-core configuration-interaction model, Phys. Rev. C 97 (2018) 034310.
[623] T. Tomoda, Double beta decay, Rep. Progr. Phys. 54 (1991) 53–126.
[624] R.A. Sen'kov, M. Horoi, Accurate shell-model nuclear matrix elements for neutrinoless double-β decay, Phys. Rev. C 90 (2014) 051301(R).
[625] R.A. Sen'kov, M. Horoi, B.A. Brown, Neutrinoless double-β decay of ^{82}Se in the shell model: Beyond the closure approximation, Phys. Rev. C 89 (2014) 054304.
[626] R.A. Sen'kov, M. Horoi, Shell-model calculation of neutrinoless double-β decay of ^{76}Ge, Phys. Rev. C 93 (2016) 044334.
[627] J. Engel, F. Šimkovic, P. Vogel, Chiral two-body currents and neutrinoless double-β decay in the quasiparticle random-phase approximation, Phys. Rev. C 89 (2014) 064308.
[628] L.-J. Wang, J. Engel, J.M. Yao, Quenching of nuclear matrix elements for $0\nu\beta\beta$ decay by chiral two-body currents, Phys. Rev. C 98 (2018) 031301(R).
[629] A. Ali, A.V. Borisov, D.V. Zhuridov, Probing new physics in the neutrinoless double beta decay using electron angular correlation, Phys. Rev. D 76 (2007) 093009.
[630] A. Faessler, A. Meroni, S.T. Petcov, F. Šimkovic, J. Vergados, Uncovering multiple CP-nonconserving mechanisms of $(\beta\beta)_{0\nu}$ decay, Phys. Rev. D 83 (2011) 113003.
[631] A. Faessler, G.L. Fogli, E. Lisi, A.M. Rotunno, F. Šimkovic, Multi-isotope degeneracy of neutrinoless double-β decay mechanisms in the quasiparticle random-phase approximation, Phys. Rev. D 83 (2011) 113015.

[632] A. Meroni, S.T. Petcov, F. Šimkovic, Multiple CP non-conserving mechanisms of $(\beta\beta)_{0\nu}$-decay and nuclei with largely different nuclear matrix elements, J. High Energy Phys. 02 (2013) 025.

[633] E. Lisi, A.M. Rotunno, F. Šimkovic, Degeneracies of particle and nuclear physics uncertainties in neutrinoless $\beta\beta$ decay, Phys. Rev. D 92 (2015) 093004.

[634] H.V. Klapdor-Kleingrothaus, I.V. Krivosheina, I.V. Titkova, Theoretical investigation of the dependence of double beta decay tracks in a Ge detector on particle and nuclear physics parameters and separation from gamma ray events, Phys. Rev. D 73 (2006) 013010.

[635] H. Horie, K. Sasaki, On energy matrices for the independent particle model, Progr. Theoret. Phys. 25 (1961) 475–492.

[636] A. Neacsu, S. Stoica, M. Horoi, Fast, efficient calculations of the two-body matrix elements of the transition operators for neutrinoless double-β decay, Phys. Rev. C 86 (2012) 067304.

[637] J. Hyvärinen, J. Suhonen, Recursive method for computing matrix elements for two-body interactions, Phys. Rev. C 91 (2015) 054308.

[638] N. Ninohara, J. Engel, Proton–neutron pairing amplitude as a generator coordinate for double-β decay, Phys. Rev. C 90 (2014) 031301(R).

[639] A. Wodecki, W.A. Kamiński, F. Šimkovic, Grand unified theory constrained supersymmetry and neutrinoless double β decay, Phys. Rev. D 60 (1999) 115007.

[640] F. Šimkovic, M. Nowak, W.A. Kamiński, A.A. Raduta, A. Faessler, Neutrinoless double beta decay of ^{76}Ge,^{82}Se,^{100}Mo, and ^{136}Xe to excited 0^+ states, Phys. Rev. C 64 (2001) 035501.

[641] P.K. Rath, R. Chandra, K. Chaturvedi, P. Lohani, P.K. Raina, Nuclear transition matrix elements for majoron-accompanied neutrinoless double-β decay within a projected Hartree–Fock-Bogoliubov model, Phys. Rev. C 93 (2016) 024314.

[642] J. Barea, J. Kotila, F. Iachello, Limits on sterile neutrino contributions to neutrinoless double beta decay, Phys. Rev. D 92 (2015) 093001.

[643] M. Horoi, S. Stoica, B.A. Brown, Shell-model calculation of two-neutrino double-β decay rates of ^{48}Ca with the GXPF1A interaction, Phys. Rev. C 75 (2007) 034303.

[644] R. Sahu, P.C. Srivastava, V.K.B. Kota, Deformed shell model results for neutrinoless positron double beta decay of nuclei in the $A = 60 - 90$ region, J. Phys. G: Nucl. Part. Phys. 40 (2013) 095107.

[645] J.G. Hirsch, O. Castaños, P.O. Hess, O. Civitarese, Selection rules in the $\beta\beta$ decay of deformed nuclei, Phys. Lett. B 534 (2002) 57–62.

[646] J.G. Hirsch, O. Castaños, P.O. Hess, O. Civitarese, Theoretical description of double β decay of ^{160}Gd, Phys. Rev. C 66 (2002) 015502.

[647] A. Shukla, P.K. Raina, R. Chandra, P.K. Rath, J.G. Hirsch, Two-neutrino positron double-beta decay of ^{106}Cd for the $0^+ \to 0^+$ transition, Eur. Phys. J. A 23 (2005) 235–242.

[648] P.K. Rath, R. Chandra, S. Singh, P.K. Raina, J.G. Hirsch, Quadrupolar correlations and deformation effect on two-neutrino $\varepsilon\beta^+$ and $\varepsilon\varepsilon$ modes of ^{156}Dy isotope, J. Phys. G: Nucl. Part. Phys. 37 (2010) 055108.

[649] J. Barea, J. Kotila, F. Iachello, Limits on neutrino masses from neutrinoless double-β decay, Phys. Rev. Lett. 109 (2012) 042501.

[650] J. Barea, J. Kotila, F. Iachello, Neutrinoless double-positron decay and positron-emitting electron capture in the interacting boson model, Phys. Rev. C 87 (2013) 057301.

[651] N. López Vaquero, T.R. Rodríguez, J.L. Egido, Shape and pairing fluctuation effects on neutrinoless double beta decay nuclear matrix elements, Phys. Rev. Lett. 111 (2013) 142501.

[652] J.M. Yao, L.S. Song, K. Hagino, P. Ring, J. Meng, Systematic study of nuclear matrix elements in neutrinoless double-β decay with a beyond-mean-field covariant density functional theory, Phys. Rev. C 91 (2015) 024316.

[653] A. Bobyk, W.A. Kamiński, P. Zareba, Study of the double beta decay of $70 \leq A \leq 100$ nuclei within the RQRPA and the self-consistent BCS+ RQRPA formalisms, Nuclear Phys. A 669 (2000) 221–238.

[654] J. Suhonen, On the double-beta decays of ^{70}Zn,^{86}Kr,^{94}Zr,^{104}Ru,^{110}Pd and ^{124}Sn, Nuclear Phys. A 864 (2011) 63–90.

[655] J. Suhonen, Nuclear matrix elements of $\beta\beta$ decay from β-decay data, Phys. Lett. B 607 (2005) 87–95.

[656] J. Kotila, J. Suhonen, D.S. Delion, Two-neutrino double-beta decay of ^{76}Ge in an anharmonic vibrator approach, J. Phys. G: Nucl. Part. Phys. 36 (2009) 045106.

[657] M. Aunola, J. Suhonen, Mean-field effects on neutrinoless double beta decay, Nuclear Phys. A 643 (1998) 207–221.

[658] J. Suhonen, Neutrinoless double beta decay to excited collective 0^+ states, Phys. Lett. B 477 (2000) 99–106.

[659] S. Stoica, H.V. Klapdor-Kleingrothaus, Neutrinoless double-β-decay matrix elements within the second quasirandom phase approximation method, Phys. Rev. C 63 (2001) 064304.

[660] O. Civitarese, J. Suhonen, Universal features of the nuclear matrix elements governing the mass sector of the $0\nu\beta\beta$ decay, Phys. Lett. B 626 (2005) 80–85.

[661] O. Civitarese, J. Suhonen, Extracting information on the $0\nu\beta\beta$ decays from the $2\nu\beta\beta$ decays, Nuclear Phys. A 761 (2005) 313–332.

[662] J. Suhonen, Nuclear-structure effects on double beta decays to 0^+ states in ^{76}Ge, Internat. J. Modern Phys. E (2011) 451–458.

[663] M.T. Mustonen, J. Engel, Large-scale calculations of the double-β decay of ^{76}Ge,^{130}Te,^{136}Xe, and ^{150}Nd in the deformed self-consistent Skyrme quasiparticle random-phase approximation, Phys. Rev. C 87 (2013) 064302.

[664] J. Suhonen, Analysis of double-β transitions in ^{78}Kr, Phys. Rev. C 87 (2013) 034318.

[665] J. Suhonen, M. Aunola, Systematic study of neutrinoless double beta decay to excited 0^+ states, Nuclear Phys. A 723 (2003) 271–288.

[666] J. Suhonen, Sub-eV neutrino masses from $0\nu\beta\beta$ decay to an excited 0^+ state, Phys. Rev. C 62 (2000) 042501(R).

[667] J. Suhonen, Theoretical investigation of the double-β processes in ^{96}Ru, Phys. Rev. C 86 (2012) 024301.

[668] J. Suhonen, Opening of the $Z = 40$ subshell gap and the double-beta decay of ^{100}Mo, Nuclear Phys. A 700 (2002) 649–665.

[669] J. Kotila, J. Suhonen, D.S. Delion, Description of the two-neutrino $\beta\beta$ decay of ^{100}Mo by pnMAVA, J. Phys. G: Nucl. Part. Phys. 37 (2010) 015101.

[670] A. Bobyk, M. Góźdź, W.A. Kamiński, P. Zareba, A. Faessler, Study of the double-beta-decay of $100 < A \leq 150$ nuclei within the QRPA, RQRPA and the SRQRPA formalisms, Eur. Phys. J. A 19 (2004) 327–332.

[671] J. Suhonen, O. Civitarese, Theoretical results on the double positron decay of ^{106}Cd, Phys. Lett. B 497 (2001) 221–227.

[672] S. Stoica, H.V. Klapdor-Kleingrothaus, Calculation of the $\beta^+\beta^+$, β^+/EC and EC/EC half-lives for ^{106}Cd with the second quasi random phase approximation method, Eur. Phys. J. A 17 (2003) 529–536.

[673] J. Suhonen, O. Civitarese, Neutrinoless double beta decays of ^{106}Cd revisited, Phys. Lett. B 701 (2011) 490–495.

[674] D. Navas-Nicolás, P. Sarriguren, Gamow-Teller properties of the double-β-decay partners ^{116}Cd(Sn) and ^{150}Nd(Sm), Phys. Rev. C 91 (2015) 024317.

[675] L.S. Song, J.M. Yao, P. Ring, J. Meng, Relativistic description of nuclear matrix elements in neutrinoless double-β decay, Phys. Rev. C 90 (2014) 054309.

[676] T.R. Rodríguez, G. Martínez-Pinedo, Calculation of nuclear matrix elements in neutrinoless double electron capture, Phys. Rev. C 85 (2012) 044310.

[677] D.-L. Fang, K. Blaum, S. Eliseev, A. Faessler, M.I. Krivoruchenko, V. Rodin, F. Šimkovic, Evaluation of the resonance enhancement effect in neutrinoless double-electron capture in ^{152}Gd,^{164}Er, and ^{180}W atoms, Phys. Rev. C 85 (2012) 035503.

[678] J. Kotila, J. Barea, F. Iachello, Neutrinoless double-electron captures, Phys. Rev. C 89 (2014) 064319.

[679] A.A. Raduta, C.M. Raduta, Double beta decay to the first 2^+ state within a boson expansion formalism with a projected spherical single-particle basis, Phys. Lett. B 647 (2007) 265–270.

[680] V.S. Kolhinen, et al., Accurate Q value for the ^{74}Se double-electron-capture decay, Phys. Lett. B 684 (2010) 17–21.

[681] J. Schwieger, F. Šimkovic, A. Faessler, W.A. Kaminski, Double β decay to excited states of several medium-heavy nuclei within the renormalized quasiparticle random phase approximation, Phys. Rev. C 57 (1998) 1738–1743.

[682] S. Rahaman, et al., Accurate q value for the ^{113}Sn double-β decay and its implication for the search of the neutrino mass, Phys. Rev. Lett. 103 (2009) 042501.

[683] V.S. Kolhinen, et al., On the resonant neutrinoless double-electron-capture decay of ^{136}Ce, Phys. Lett. B 697 (2011) 116–120.
[684] J. Suhonen, Calculation of the β and $\beta\beta$ decay observables of ^{48}Ca using QRPA with and without particle-number projection, J. Phys. G: Nucl. Part. Phys. 19 (1993) 139–160.
[685] M. Aunola, J. Suhonen, Systematic study of beta and double beta decay to excited final states, Nuclear Phys. A 602 (1996) 133–166.
[686] J. Suhonen, O. Civitarese, A. Faessler, Description of the $0^+ \rightarrow 0^+$ neutrinoless double-beta decay transition in ^{76}Ge: Particle-number-projected quasiparticle random phase approximation, Nuclear Phys. A 543 (1992) 645–660.
[687] A. Bobyk, W.A. Kamiński, P. Zareba, New bcs and renormalized qrpa formalism with application to double beta decay, Eur. Phys. J. A 5 (1999) 385–390.
[688] V.A. Rodin, A. Faessler, F. Šimkovic, P. Vogel, Uncertainty in the $0\nu\beta\beta$ decay nuclear matrix elements, Phys. Rev. C 68 (2003) 044302.
[689] F. Krmpotić, E.J.V. de Passos, D.S. Delion, J. Dukelsky, P. Schuck, Self-consistent random phase approximation within the $O(5)$ model and Fermi transitions, Nuclear Phys. A 637 (1998) 295–324.
[690] D.S. Delion, J. Dukelsky, P. Schuck, E.J.V. de Passos, F. Krmpotić, Proton–neutron self-consistent quasiparticle random phase approximation within the $O(5)$ model, Phys. Rev. C 62 (2000) 044311.
[691] S. Stoica, H.V. Klapdor-Kleingrothaus, Critical view on double-beta decay matrix elements within quasi random phase approximation-based methods, Nuclear Phys. A 694 (2001) 269–294.
[692] O. Civitarese, F. Montani, M. Reboiro, Extended proton–neutron quasiparticle random-phase approximation in a boson expansion method, Phys. Rev. C 60 (1999) 024305.
[693] M. Sambataro, β- and double-β-decay transitions in a schematic model, Phys. Rev. C 59 (1999) 2056–2064.
[694] V. Rodin, A. Faessler, Description of double β decay within the continuum quasiparticle random-phase approximation, Phys. Rev. C 77 (2008) 025502.
[695] M. Agostini, et al., (GERDA Collaboration), Results on $\beta\beta$ decays with emission of two-neutrinos and Majorons in ^{76}Ge from GERDA phase I, Eur. Phys. J. C 75 (2015) 416.
[696] N. Ackermann, et al., (EXO Collaboration), Observation of two neutrino double beta decay in ^{136}Xe with EXO-200 detector, Phys. Rev. Lett. 107 (2011) 212501.
[697] Yu. M. Gavrilyuk, A.M. Gabgepshev, V.V. Kazalov, V.V. Kuzminov, S.I. Panusenko, S.S. Ratkevich, Indication of $2\nu2$K capture in ^{78}Kr, Phys. Rev. C 87 (2013) 035501.
[698] N.I. Rukhadze, (TGV Collaboration), Double electron capture of ^{106}Cd in the TGV-2 experiment, in: O. Civitarese (Ed.), Proc. MEDEX15, APS Conf. Proc. 1686 (2015) 020020;   Nuclear Phys. A 852 (2011) 197–206.
[699] A.P. Meshik, C.M. Hohenberg, O.V. Pravdivtseva, Ya.S. Kapsta, Weak decay of ^{130}Ba and ^{132}Ba: Geochemical measurements, Phys. Rev. C 64 (2001) 035205.
[700] M. Agostini, et al., Improved limit on neutrinoless double-β decay of ^{76}Ge from GERDA Phase II, Phys. Rev. Lett. 120 (2018) 132503.
[701] C.E. Aalseth, et al., (MAJORANA Collaboration), Search for neutrinoless double-β decay in ^{76}Ge with the Majorana demonstrator, Phys. Rev. Lett. 120 (2018) 132502.
[702] N. Abgrall, et al., (LEGEND-collaboration), The large enriched germanium experiment for neutrinoless double beta decay (LEGEND), AIP Conf. Proc. 1894 (2017) 020027.
[703] K. Zuber, COBRA: Double beta decay searches using CdTe detectors, Phys. Lett. B 519 (2001) 1–7.
[704] C. Alduino, et al., (CUORE Collaboration), First results from CUORE: A search for lepton number violation via $0\nu\beta\beta$ decay of ^{130}Te, Phys. Rev. lett. 120 (2018) 132501.
[705] D.R. Artusa, et al., The LUCIFER/CUPID-0 demonstrator: searching for the neutrinoless double-beta decay with Zn^{82}Se scintillating bolometers, J. Phys. Conf. Ser. 888 (2017) 012077.
[706] H. Park, et al., The AMoRE: Search for neutrinoless double beta decay in ^{100}Mo, Nucl. Part. Phys. Proc. 273–275 (2016) 2630–2632.
[707] D. Poda, A. Giuliani, Low background techniques in bolometers for double-beta decay search, Internat. J. Modern Phys. A 32 (2017) 1743012.
[708] A. Gando, et al., (KamLAND collaboration), Search for majorana neutrinos near the inverted mass hierarchy region with KamLAND-Zen, Phys. Rev. Lett. 117 (2016) 082503;   Phys. Rev. Lett. 117 (2016) 109903 (addendum).
[709] J.B. Albert, et al., (EXO-200 collaboration), Search for neutrinoless double-beta decay with the upgraded EXO-200 detector, Phys. Rev. Lett. 120 (2018) 072701.
[710] L. Yang, et al., Status and prospects for the EXO-200 and nEXO experiments, J. Phys. Conf. Ser. 888 (2017) 012032.
[711] S. Andringa, et al., (SNO+-collaboration), Current status and future prospects of the SNO+ experiment, Adv. High Energy Phys. 2016 (2016) 6194250.
[712] T. Iida, et al., Status and future prospect of ^{48}Ca double beta decay search in CANDLES, J. Phys. Conf. Ser. 718 (2016) 062026.
[713] F.A. Danevich, et al., (Aurora experiment), Search for double beta decay of ^{116}Cd with enriched $^{116}CdWO_4$ crystal scintillators, J. Phys. Conf. Ser. 718 (2016) 062009.
[714] D. Waters, NEMO-3 and Super-NEMO collaboration, Latest results from NEMO-3 and status of the superNEMO experiment, J. Phys. Conf. Ser. 888 (2017) 012033;   Nucl. Phys. 847 (2010) 168–179.
[715] H. Ejiri, MOON (Molybdenum Observatory Of Neutrinos) for neutrino-less double beta decays, Eur. Phys. J. 162 (2008) 239–250.
[716] N. Lopez March, et al., The NEXT high pressure xenon gas TPC for neutrinoless double beta decay searches, J. Instrum. 13 (2018) C01048.
[717] K. Han, et al., (PandaX-III collaboration), Searching for neutrinoless double beta decay with high pressure gaseous time projection chambers, arXiv:1710.08908.
[718] S. Bustabad, et al., First direct determination of the ^{48}Ca double-β decay Q value, Phys. Rev. C 88 (2013) 022501.
[719] B.J. Mount, M. Redshaw, E.G. Myers, Double-β Q values of ^{74}Se and ^{76}Ge, Phys. Rev. C 81 (2010) 032501.
[720] D.L. Lincoln, et al., First direct double-β decay Q-value measurement of ^{82}Se in support of understanding the nature of the neutrino, Phys. Rev. Lett. 110 (2013) 012501.
[721] S. Rahaman, et al., Q values of the ^{76}Ge and ^{100}Mo double-beta decays, Phys. Lett. B 662 (2008) 111–116.
[722] D. Fink, et al., Q-value and half-lives for the double-β-decay nuclide ^{110}Pd, Phys. Rev. Lett. 108 (2012) 062502.
[723] S. Rahaman, et al., Double-beta decay Q values of ^{116}Cd and^{130}Te, Phys. Lett. B 703 (2011) 412–416.
[724] D.A. Nesterenko, et al., Double-β transformations in isobaric triplets with mass numbers A = 124, 130 and 136, Phys. Rev. C 86 (2012) 044313.
[725] M. Redshaw, et al., Masses of ^{130}Te and ^{130}Xe and double-β-decay Q value of ^{130}Te, Phys. Rev. Lett. 102 (2009) 212502.
[726] M. Redshaw, et al., Mass and double-beta-decay Q value of ^{136}Xe, Phys. Rev. Lett. 98 (2007) 053003.
[727] V.S. Kolhinen, et al., Double-β decay Q value of ^{150}Nd, Phys. Rev. C 82 (2010) 022501.
[728] O. Azzolini, et al., (CUPID-0 collaboration), First result on the neutrinoless double-β decay of ^{82}Se with CUPID-0, Phys. Rev. Lett. 120 (2018) 232502.
[729] A.S. Barabash, Brief review of double beta decay experiments, arXiv:1702.06340v1 [nucl-exp].
[730] A.S. Barabash, Double beta decay to excited states: review, in: MEDEX'17, AIP Conf. Proc. 1894 (2017) 020002, arXiv:1709.06890v1 [nucl-exp].
[731] S. Eliseev, et al., Resonant enhancement of neutrinoless double-electron capture in ^{152}Gd, Phys. Rev. Lett. 106 (2011) 052504.
[732] N. Barros, J. Thurn, K. Zuber, Double beta decay searches of ^{134}Xe,^{126}Xe and ^{124}Xe with large scale Xe detectors, J. Phys. G: Nucl. Part. Phys. 41 (2014) 115105.
[733] M. Agostini, et al., Limit on the radiative neutrinoless double electron capture of ^{36}Ar from GERDA Phase I, Eur. Phys. J. C 76 (2016) 652.
[734] B. Lehnert, D. Degering, A. Frotscher, T. Michel, K. Zuber, A search for the radiative neutrinoless double electron capture of ^{58}Ni, J. Phys. G: Nucl. Part. Phys. 43 (2016) 065201.

[735] P. Belli, et al., Search for double beta decay processes in ^{106}Cd with the help of $^{106}CdWO_4$ crystal scintillator, Phys. Rev. C 85 (2012) 044610.
[736] K. Abe, et al., Improved search for two-neutrino double electron capture on ^{124}Xe and ^{126}Xe using particle identification in XMASS-I, 2018, arXiv:1801.03251.
[737] E. Aprile, et al., Search for two-neutrino double electron capture of ^{124}Xe with XENON100, Phys. Rev. C 95 (2017) 024605.
[738] J. Lagoda, Current and future neutrino experiments, Acta Phys. Polon. 49 (2018) 1213.
[739] S. Pastore, A. Baroni, J. Carlson, S. Gandolfi, S.C. Pieper, R. Schiavilla, R.B. Wiringa, Quantum Monte Carlo calculations of weak transitions in $A = 6 - 10$ nuclei, Phys. Rev. C 97 (2018) 022501(R).
[740] T. Bhattacharya, V. Cirigliano, S. Cohen, R. Gupta, H.-W. Lin, B. Yoon, Axial scalar and tensor charges of the nucleon from $2 + 1 + 1$-flavor lattice QCD, Phys. Rev. D 95 (2016) 054508.
[741] E. Berkowitz, et al., An accurate calculation of the nucleon axial charge with lattice QCD, arXiv:1704.01114 [hep-lat].
[742] R. Gupta, Y.-C. Jang, H.-W. Lin, B. Yoon, T. Bhattacharya, Axial vector form factors of the nucleon from lattice QCD, Phys. Rev. D 96 (2017) 114503.
[743] B.C. Tiburzi, M.L. Wagman, F. Winter, E. Chang, Z. Davoudi, W. Detmold, et al., Double-β decay matrix elements from lattice quantum chromodynamics, Phys. Rev. D 96 (2017) 054505.
[744] T. Abe, P. Maris, T. Otsuka, N. Shimizu, Y. Utsuno, J.P. Vary, Benchmarks of the full configuration interaction, Monte Carlo shell model, and no-core full configuration methods, Phys. Rev. C 86 (2012) 054301.
[745] T. Togashi, Y. Tsunoda, T. Otsuka, N. Shimizu, Quantum phase transition in the shape of Zr isotopes, Phys. Rev. Lett. 117 (2016) 172502.
[746] C. Stumpf, J. Braun, R. Roth, Importance-truncated large-scale shell model, Phys. Rev. C 93 (2016) 021301(R).
[747] S. Pastore, J. Carlson, V. Cirigliano, W. Dekens, E. Mereghetti, R.B. Wiringa, Neutrinoless double beta decay matrix elements in light nuclei, Phys. Rev. C 97 (2018) 014606.
[748] G.R. Jansen, J. Engel, G. Hagen, P. Navratil, A. Signoracci, Ab initio coupled-cluster effective interactions for the shell model: Application to neutron-rich oxygen and carbon isotopes, Phys. Rev. Lett. 113 (2014) 142502.
[749] G. Hagen, et al., Emergent properties of nuclei from ab initio coupled-cluster calculations, Phys. Scr. 91 (2016) 063006.
[750] S.K. Bogner, et al., Nonperturbative shell-model interactions from the in-medium similarity renormalization group, Phys. Rev. Lett. 113 (2014) 142501.
[751] H. Hergert, et al., The in-medium similarity renormalization group: A novel ab initio method for nuclei, Phys. Rep. 621 (2016) 165–222.
[752] Ö. Legeza, L. Veis, A. Poves, J. Dukelsky, Advanced density matrix renormalization group method for nuclear structure calculations, Phys. Rev. C 92 (2015) 051303(R).
[753] V. Cirigliano, W. Dekens, J. de Vries, M.L. Graesser, E. Mereghetti, S. Pastore, U. van Kolck, New leading contribution to neutrinoless double-β decay, Phys. Rev. Lett. 120 (2018) 2020010.
[754] L. Graf, F.F. Deppisch, F. Iachello, J. Kotila, Short-range neutrinoless double beta decay mechanisms, Phys. Rev. D 98 (2018) 095023.
[755] M.J. Hwang, et al., A search for $0\nu\beta\beta$ decay of ^{124}Sn with tin-loaded liquid scintillator, Astropart. Phys. 31 (2009) 412–416.